



HAL
open science

Etude expérimentale de la réduction de trainée par injection de bulles dans une couche limite turbulente décollée redéveloppée

Jishen Zhang

► **To cite this version:**

Jishen Zhang. Etude expérimentale de la réduction de trainée par injection de bulles dans une couche limite turbulente décollée redéveloppée. Autre [cond-mat.other]. Ecole nationale supérieure d'arts et métiers - ENSAM, 2019. Français. NNT : 2019ENAM0057 . tel-02591699

HAL Id: tel-02591699

<https://pastel.hal.science/tel-02591699>

Submitted on 15 May 2020

HAL is a multi-disciplinary open access archive for the deposit and dissemination of scientific research documents, whether they are published or not. The documents may come from teaching and research institutions in France or abroad, or from public or private research centers.

L'archive ouverte pluridisciplinaire **HAL**, est destinée au dépôt et à la diffusion de documents scientifiques de niveau recherche, publiés ou non, émanant des établissements d'enseignement et de recherche français ou étrangers, des laboratoires publics ou privés.

École doctorale n° 432 : Sciences des Métiers de l'ingénieur

Doctorat

T H È S E

pour obtenir le grade de docteur délivré par

l'École Nationale Supérieure d'Arts et Métiers

Spécialité “ Mécanique des Fluides et Énergétique”

présentée et soutenue publiquement par

Jishen ZHANG

le 12 décembre 2019

**Experimental Study of the Bubbly Drag Reduction in the Recovery
Region of a Separated Turbulent Boundary Layer**

Directeur de thèse : **Jean-Yves BILLARD**
Co-encadrement de la thèse : **Céline GABILLET**

Jury

M. Éric CLIMENT, Professeur des Universités, HMF, IMFT
M. Mohamed FARHAT, Professeur, STI IGM LMH, EPFL
M. Jean-Yves BILLARD, Professeur des Universités, IRENav, ENSAM – École Navale
M. Antoine DAZIN, Professeur des Universités, FISE, ENSAM ParisTech
M^{me}. Céline GABILLET, Maître de Conférences, IRENav, ENSAM – École Navale
M^{me}. Gaëlle PERRET, Maître de Conférences, LOMC, Université du Havre

Président
Rapporteur
Examineur
Examineur
Examineur
Examineur

**T
H
È
S
E**

Ainsi qu'au cabaret l'homme demeure au monde.
Le plaisir et le vin se laissent avaler.
Le temps y dure peu, tant que la joie abonde.
Et puis il faut compter, payer et s'en aller.

Pierre Matthieu, *Tablettes de la vie et de la mort* (1610)

Remerciements

J'exprime la plus grande reconnaissance à Madame Céline Gabillet, mon encadrante de thèse, pour m'avoir accueilli au sein du laboratoire, d'avoir soutenu et guidé depuis ma première année de thèse. Son exigence m'a enseigné la rigueur du travail, ses compétences, son expérience professionnelle et ses conseils avisés m'ont été indispensables tout au long de ces années.

Je tiens à remercier Monsieur Jean-Yves Billard, qui m'a dirigé dans cette thèse, en particulier pour la confiance et la liberté qu'il a bien voulu m'accorder. Je remercie Monsieur Eric Climent et Monsieur Mohamed Farhat pour avoir accepté la tâche de rapporteurs. Que Monsieur Antoine Dazin et Madame Gaëlle Perret soient également remerciés d'avoir participé au jury de soutenance.

Ma profonde reconnaissance va à l'équipe du service technique (SEFER) : Jean-Michel, Alain, Jean-Charles, Steve, Laurent, Pierre et Arnaud.

Special thanks to my supervisor 村井さん for having welcome me in the Flow Control Laboratory of the University of Hokkaido and allowed me to discover the artistic side of bubbles and for his kind advice during my stay in Japan. Thanks to my co-supervisors and colleagues : 田坂さん and 朴さん, 衆示さん, 俊さん, 大地さん, 侑さん, 大輝さん, 幸太郎さん, 菅野さん, 健介さん, 亦黙さん, 栩さん, 恵実さん, Suzyさん and Martinaさん.

Mes pensées vont ensuite aux collègues de l'IRENav avec qui j'ai aiguisé mes connaissances sur la préparation du café presque parfait, sur les fines stratégies du jeu de tarot ou bien sur la distinction entre le vrai beurre et le faux ; Vennec et Yannick qui ont dépanné le réseau et le serveur avec leurs formules magiques ; Marie et Abdel qui m'ont accompagné quotidiennement pour traverser la Grande Porte Robert Surcouf ; Karine qui m'a donné d'excellents conseils sur les films italiens ; Vanilla ma précieuse collègue qui a supporté l'état turbulent de mon bureau pendant 3 ans avec sa gentillesse et sa bienveillance ; Loïc qui s'est vanté de ses talents de pâtissier et de ses anecdotes de « son époque » ; Joseph et Rozenn qui ont apporté de la joie de vivre et sans qui mes années de thèse n'auraient pas pu être aussi heureuses ...

Mes remerciements s'adressent aussi à l'équipe de la cellule pédagogique de l'Ecole Navale, Pierre, Christophe, Alexandre, Jimmy et Jean-Yves, pour m'avoir conseillé et aidé à m'épanouir dans mon travail d'enseignant. Je remercie particulièrement à mon ami Pierre pour les nombreuses discussions intéressantes qui ont rendu les 1460 heures en bateau trans-rade beaucoup moins ennuyeuses.

Je remercie également mes amis Alice, Ségolène, Thibault, Gilles, Fatih, Owenn, François, Guillaume, Maryvonne, 池子强, 徐霄, 王乐, 尚亚菲, 石婵 et 刘泽 ...

Je ne pourrais terminer sans remercier ceux qui sont chers à mon cœur, et qui m'ont toujours soutenu au cours de mes études : ma mère, mon père, mon grand-père et ma grand-mère.

Table of Contents

Table of Contents i

Nomenclature v

 1.1 Roman Symbolsv

 1.2 Greek Symbolsvii

 1.3 Abbreviationsviii

Introduction 1

1 CHAPTER I. Literature Survey & Objectives 4

 1.1 Generalities about the single-phase turbulent boundary layer..... 4

 1.1.1 Equations of conservation 6

 1.1.2 Integral length scales 7

 1.1.3 Discussion about universality of the mean stream-wise velocity profiles..... 8

 1.1.4 Discussion about universality of the turbulent shear stress profiles..... 12

 1.1.5 Discussion about the mechanism of turbulence production in the turbulent boundary layer 13

 1.2 Generalities about the single-phase turbulent flow downstream of obstacles at the wall 15

 1.2.1 Classification of obstacle perturbation 16

 1.2.2 Reattached flows 16

 1.2.3 Turbulent structure in adverse pressure gradient flows..... 17

 1.3 Bubbly turbulent boundary layer..... 17

 1.3.1 Effect of the bubble size: Micro-bubbles 18

 1.3.2 Effect of the bubble size: Intermediate-size bubbles..... 20

 1.3.3 Effect of the bubble size: Single large bubbles 22

 1.3.4 Effect of the pressure gradient..... 23

 1.3.5 summary 24

 1.4 Conclusion..... 25

2 CHAPTER II. Description of Experimental Device and Flow Conditions 26

 2.1 Experimental Device 26

 2.2 Flow Conditions 29

 2.3 Experimental Techniques 31

 2.3.1 High frequency *PIV* measuring system for the characterization of the single phase flow 31

Table of Contents

2.3.2	<i>PTV</i> measuring system for the characterization of the liquid phase in the two-phase flow	34
2.3.3	Shadowgraphy measuring system for the characterization of the gas phase in the two-phase flow.....	39
3	CHAPTER III. Characterization of the Single Phase Flow Developing Downward the Step	46
3.1	Analysis procedures	46
3.1.1	Time-Averaging	46
3.1.2	<i>POD</i> analysis.....	49
3.2	Results. Characteristics of the single phase flow	51
3.2.1	General features of the mean flow.....	51
3.2.2	General features of the fluctuating flow	55
3.2.3	validity of the universal logarithmic law	60
3.2.4	Modal decomposition and frequency analysis.....	66
3.2.5	Longitudinal evolution of the integral scales of the flow	69
3.2.6	Discussion	71
3.3	Conclusion.....	75
4	CHAPTER IV. Influence of Bubble Injection on the Flow Developing Downward the Obstacle. Characterization of the Gas Phase.....	76
4.1	Bubbly Flow conditions	76
4.2	Statistical analysis procedure of Shadowgraphy measurements	77
4.2.1	Spatial and time averaging	77
4.2.2	Uncertainties.....	79
4.2.3	Validation of measurements and statistical processing. Conservation of mass flux of the gas	79
4.3	Bubble size and shape	80
4.3.1	Distribution of equivalent diameter.....	80
4.3.2	Evolution of the bubble equivalent diameter with flow conditions.....	82
4.3.3	Evolution of the bubble aspect ratio with flow conditions	84
4.4	Gas volume fraction	85
4.4.1	General features of the gas volume fraction profiles.....	85
4.4.2	Self-similarity of y profiles of the gas volume fraction against the air injection rate ...	86
4.4.3	Self-similarity of y profiles of the gas volume fraction against the velocity.....	88
4.4.4	Self-similarity of the y profiles of the gas volume fraction against both velocity and air injection rate	92
4.4.5	Analysis of the volume fraction peak in the vicinity of the wall according to the operating conditions (U_{ref} , Qg).....	93

Table of Contents

4.4.6	Analysis of the integral scales of the bubble layer according to the operating conditions (U_{ref} , Qg)	96
4.5	Gas phase mean flow	100
4.5.1	Mean stream-wise velocity profiles	100
4.5.2	Mean wall-normal velocity profiles	102
4.6	Gas phase turbulence	104
4.6.1	<i>Rms</i> stream-wise velocity	104
4.6.2	<i>Rms</i> wall normal velocity	106
4.6.3	Turbulent shear stress	108
4.7	Conclusion	110
5	CHAPTER V. Influence of the Bubble Injection on the Flow Developing Downward the Obstacle. Characterization of the Liquid Phase Velocity Field	112
5.1	Bubbly Flow conditions	112
5.2	Statistical analysis procedure of <i>PTV</i> measurements	113
5.2.1	Spatial averaging	113
5.2.2	Time averaging	114
5.2.3	Uncertainties	115
5.2.4	Validation in single-phase flow of the <i>PTV</i> measurements of the statistical quantities by comparison to <i>PIV</i>	116
5.3	Analysis of the liquid velocity field in the bubbly flow. Comparison to the single-phase flow. 117	
5.3.1	General features of the mean and fluctuating liquid flow	117
5.3.2	Validity of the log law	124
5.3.3	Integral parameters of the liquid phase flow	129
5.4	Discussions	132
5.4.1	Stream-wise velocity drift between gas & liquid	132
5.4.2	Wall-normal velocity drift between gas & liquid	136
5.4.3	Non-dimensional analysis of the gain of drag variation	138
5.4.4	Contribution of different mechanisms	140
5.5	Conclusion	145
6	General Conclusion	147
6.1	Recommendations for future investigations	148
7	Reference	150
8	Appendices	157
8.1	Appendix A. Bubble injection network production drawing archive	157

Table of Contents

8.2	Appendix B. Comparison between <i>PTV</i> and <i>PIV</i> profiles in single phase flow.....	158
8.2.1	Mean velocity components.....	158
8.2.2	<i>Reynolds</i> stresses	159
8.2.3	Logarithmic law versus inner variables.....	162
8.2.4	Logarithmic law versus outer variables.....	164
8.2.5	Comparison of the integral parameters between <i>PTV</i> and <i>PIV</i>	166
8.3	Appendix C. Publication	168

Nomenclature

1.1 Roman Symbols

a	mm	Major axis of the bubble contour.
b	mm	Minor axis of the bubble contour.
B		Additive constant in the log law.
C		Additive constant in the log law.
Ca		Capillary number
Cc		Cross-correlation threshold for the <i>PMC</i> method.
C_D		Bubble drag coefficient.
C_f		Friction coefficient.
C_{f0}		Friction coefficient of single-phase undisturbed flow.
C_L		Lift coefficient of the bubbles.
Cr	<i>pixel</i>	Particle-mask window size for the <i>PMC</i> method.
d_b	mm	Bubble average diameter.
e_b	mm	Width of the bubble injection area.
F	l/h	Reconstruct the gas flow rate.
f_{Dx}	N/m^3	Gas-on-liquid drag force per unit volume.
f_{Lx}	N/m^3	Gas-on-liquid lift force per unit volume.
Fr_r		Froude number based on the bubble diameter and the reference velocity.
Fr_θ		Froude number based on the momentum thickness and the reference velocity.
f_{ref}	Hz	Reference frequency.
f_{vortex}	Hz	Vortex traveling frequency.
g	m/s^2	Standard gravity.
G		<i>Clauser</i> parameter.
G_0		<i>Clauser</i> parameter of single-phase undisturbed flow.
G_b		Gain factor.
h	mm	Obstacle height.
H		Shape factor.
J		Moore's bubble drag coefficient constant.
L_R	mm	Recirculation length.
l_v	m	Viscous length of the boundary layer.
n_0		Power rate of the velocity power law.
P	Pa	Static pressure.
P_e	Pa	Static pressure outside the boundary layer.
Q_g	l/h	Gas injection rate.
Q_l	l/h	Water flow rate.
Q_p	l/h	Seeding particle injection rate.
R_b^+		Bubble radius normalized by the viscous length.

Nomenclature

R_c	<i>pixel</i>	Quasi-parallel motion threshold of the particles for the relaxation <i>PTV</i> method.
Re		<i>Reynolds</i> number.
Re_θ		<i>Reynolds</i> number based on momentum thickness and reference velocity.
$Re_{\theta 0}$		<i>Reynolds</i> number based on single-phase undisturbed momentum thickness and reference velocity.
Re_*		<i>Reynolds</i> number based on momentum thickness and friction velocity.
R_n	<i>pixel</i>	Neighbor particles distance threshold for the relaxation <i>PTV</i> method.
R_s	<i>pixel</i>	Maximum possible displacement of the particles for the relaxation <i>PTV</i> method.
Thr_{ibs}		Threshold on the isolated bubbles selection.
u	<i>m/s</i>	Instantaneous stream-wise liquid velocity.
u'	<i>m/s</i>	Instantaneous stream-wise liquid fluctuation velocity.
u_b	<i>m/s</i>	Instantaneous stream-wise bubble velocity.
u_g'	<i>m/s</i>	Instantaneous stream-wise gas fluctuation velocity.
U	<i>m/s</i>	Stream-wise mean liquid velocity.
U_e	<i>m/s</i>	External stream-wise velocity.
U_g	<i>m/s</i>	Stream-wise mean gas-phase velocity.
$U_{g\ rms}$	<i>m/s</i>	Stream-wise gas-phase <i>rms</i> velocity.
U_l	<i>m/s</i>	Stream-wise mean liquid-phase velocity.
U_{ref}	<i>m/s</i>	Reference velocity.
u^*	<i>m/s</i>	Friction velocity.
Δt_{pulse}	μs	Time between pulses.
$\Delta u_2/u_*$		Shifts of semi-logarithmic profiles caused by pressure gradient.
U_{rms}	<i>m/s</i>	Mean stream-wise liquid <i>rms</i> velocity.
$\rho\langle u'\rangle^2$	<i>m/s</i>	Stream-wise <i>Reynolds</i> stress of the liquid flow.
$-\rho\langle u'v'\rangle$	m^2/s^2	<i>Reynolds</i> shear stress of the liquid flow.
$-\rho\langle u'v'_g\rangle$	m^2/s^2	<i>Reynolds</i> shear stress of the gas flow.
v	<i>m/s</i>	Instantaneous wall-normal liquid velocity.
$\rho\langle v'\rangle^2$	<i>m/s</i>	Wall-normal <i>Reynolds</i> stress of the liquid flow.
v'	<i>m/s</i>	Instantaneous wall-normal liquid fluctuation velocity.
v_b	<i>m/s</i>	Instantaneous wall-normal bubble velocity.
v_g'	<i>m/s</i>	Instantaneous wall-normal gas fluctuation velocity.
V	<i>m/s</i>	Wall-normal mean liquid velocity.
V_g	<i>m/s</i>	Wall-normal mean gas velocity.
$V_{g\ rms}$	<i>m/s</i>	Wall-normal gas-phase <i>rms</i> velocity.
V_{rms}	<i>m/s</i>	Mean wall-normal liquid <i>rms</i> velocity.
We		<i>Weber</i> number based on the reference velocity and the mean bubble diameter.
We_{u^*}		<i>Weber</i> number based on the friction velocity and the mean bubble diameter.
x	<i>mm</i>	Stream-wise coordinate. (The origin is the beginning of the obstacle.)
y	<i>mm</i>	Wall-normal coordinate.

Nomenclature

y_{α_v-max}	<i>mm</i>	y -position of gas local maximum volume fraction.
y_{drift}	<i>mm</i>	y -position where $U_g - U_l = 0$.
y_{shift}	<i>mm</i>	y -position where $U_g - U = 0$.
W		<i>Coles's</i> wake term.

1.2 Greek Symbols

α_s		Gas local surface fraction.
α_v		Gas local volume fraction.
α_{v-max}		Gas local maximum volume fraction.
$\langle \alpha \rangle$		Average gas volume fraction.
β		<i>Clauser's</i> pressure gradient parameter.
δ	<i>mm</i>	Boundary layer thickness.
δ_3	<i>mm</i>	Boundary layer stream-wise turbulence intensity thickness.
δ_4	<i>mm</i>	Boundary layer wall-normal turbulence intensity thickness.
δ_0	<i>mm</i>	Boundary layer thickness of single-phase undisturbed flow.
δ_α	<i>mm</i>	Gas layer thickness.
δ_b	<i>mm</i>	Bubble boundary thickness.
δ_*	<i>mm</i>	Boundary layer displacement thickness.
δ_{*0}	<i>mm</i>	Single-phase undisturbed boundary layer displacement thickness.
Δ	<i>mm</i>	<i>Clauser's</i> universal thickness.
Δ_b	<i>mm</i>	Gas volume fraction scale length.
ϵ	$\mu m/pixel$	Image scale factor.
η		Non-dimensional wall coordinate. (outer variable.)
Γ	m^2/s	Circulation.
γ	$1/s$	Shear rate.
λ	J	Eigenvalue of the velocity matrix for <i>POD</i> analysis
μ	$Pa \cdot s$	Dynamic viscosity.
μ_{eff}	$Pa \cdot s$	Effective viscosity.
κ		<i>von Kármán's</i> constant.
ρ	kg/m^3	Fluid density.
ϕ	m/s	Eigenvector of the velocity matrix for <i>POD</i> analysis
σ	N/m	Surface tension.
$\sigma_{particle}$	<i>pixel</i>	Standard deviation of the <i>2D</i> Gaussian distribution for the <i>PMC</i> method
τ_w	Pa	Wall shear stress.
τ_{w0}	Pa	Wall shear stress without gas injection.
θ	<i>mm</i>	Momentum thickness of the boundary layer.
θ_0	<i>mm</i>	Undisturbed momentum thickness of the boundary layer.
ν	m^2/s	Kinematic viscosity.
Ψ		<i>Coles's</i> wake parameter.

Nomenclature

Π m^2/s^3 Production of turbulent kinetic energy.

1.3 Abbreviations

<i>ALDR</i>	Air Layer Drag Reduction
<i>ANR</i>	Agence Nationale de la Recherche
<i>BDR</i>	Bubbly Drag Reduction
<i>CCD</i>	Charged-Coupled Device
<i>DOF</i>	Depth of Field
<i>DR</i>	Drag Reduction
<i>DV</i>	Drag Variation
<i>DNS</i>	Direct Numerical Simulation
<i>EEDI</i>	Energy Efficiency Design Index
<i>FDRAIHN</i>	Frictional Drag Reduction for Naval Hydrodynamics
<i>FFT</i>	Fast Fourier Transform
<i>IA</i>	Interrogation Area
<i>LDV</i>	Laser Doppler Velocimetry
<i>PIV</i>	Particle Image Velocimetry
<i>POD</i>	Proper Orthogonal Decomposition
<i>PMC</i>	Particle Mask Correlation
<i>PTV</i>	Particle Tracking Velocimetry
<i>PDF</i>	Probability Density Function

Introduction

Minimizing the hydrodynamic resistance of marine vehicles has been a goal of Engineers and designers for several decades. With over 80% of the volume of the world's trade carried by sea (*UNCTAD 2018; IMO 2019*), international maritime transport is essential for the world's economy and yet faces a challenge in respect to climate change: despite increases in operational efficiency for many ship classes, total shipping CO_2 emissions increased from 910 million tonnes to 932 million tonnes (+2.4%) from 2013 to 2015, being responsible for 2.6% of global CO_2 emissions (*Olmer et al. 2017*). Reducing greenhouse gas emissions is imperative. The Energy Efficiency Design Index (*EEDI*) regulation of the International Maritime Organisation mandates improvements in ship energy efficiency. Essentially, the *EEDI* requires new ships (since 2013) to emit less CO_2 per unit of "transport work" (gram of CO_2 per tonne-mile). Ships built between 2015 and 2019 are required to be 10% more efficient than a baseline of ships built between 1999 and 2009. Subsequently, ships built between 2020 and 2024 must be 20% more efficient, and those built in 2025 or later must be 30% more efficient than the baseline (*Olmer et al. 2017*).

The total drag can be separated into 3 contributions: 1) skin friction (or viscous) drag, 2) form drag, 3) wave-caused resistance. Skin friction is of particular importance for marine vehicles since the latter contributes up to 50% of a ship's and 60% of a submarine's total resistance (*Perlin & Ceccio 2015*). For a surface vessel, in the general circumstances, the skin friction drag is dominant at small Froude numbers ($Fr \leq 0.3$).

Therefore, skin friction reduction can result into immediate decreases in fuel consumption and consequentially gas emissions. Designers struggled since long time to minimize the overall drag while maintaining desired operational characteristics. However, the minimization of one form of resistance often leads to an increase in another. For example, the use of slender hulls can reduce both form and wave drag but may cause an increase in skin friction and a decrease in stability.

All existing *DR* (drag reduction) techniques can be divided into passive and active means. Successful application of passive drag reduction includes modification of the hull shape and surface coating and installation of a bulbous bow. These are techniques which do not require additional input of mass, momentum or energy to promote drag reduction. Active techniques, on the contrary, require continuous engagement of mass, momentum or energy supply to achieve *DR*, and primarily the skin friction reduction. The relevant methods include introducing polymers/fibres or bubble/gas into the boundary layer of the flow around the hull, addition of air layers beneath hulls etc. Among these techniques, gas-induced skin friction reduction techniques are of special interest because air injection causes no damage to the environment.

Depending on the gas flux quantities and the external velocity, air injection can result in air layer drag reduction (*ALDR*) or in bubbly drag reduction (*BDR*), accordingly. *ALDR* occurs when a continuous air layer separates the hull surface from the flowing liquid and it interrupts the momentum transfer from the flows to the wall (*Fukuda et al. 2000; Mäkiharju et al. 2013*). It is reported to lead to a local drag reduction of 80% comparing to when air layer is absent (*Elbing et al. 2013*). However, to maintain such a nearly continuous layer, the required air flux is reported to be quite sensible to the solid surface's roughness and should be approximately proportional to the square of the free stream velocity (*Elbing et al. 2008*). As discussed also in *Ceccio (2010)*, that it presents a challenging control problem to maintain the air layer during changes in navigation speed and while manoeuvring at sea

Introduction

trials. Indeed, perturbations required larger gas flux to maintain the layer (or cavity) stable ([Makiharju et al. 2010](#))

Some structural modifications on the hull bottom such as a cavity design (i.e.: back-ward facing step) behind the air injection allow a better control of the air layer. For flow over a rough wall, the air cavity would be more cost-effective than an air layer because a relatively low gas injection rate is required to achieve the drag reduction of the same order of magnitude as in air layer case. In contrast, for a smooth wall, higher gas injection rate would be required to establish an air cavity, comparing to that for an air layer, and the rate required to establish the air cavity was reported to depend on the travel speed ([Makiharju et al. 2010](#)).

Bubbly drag reduction (*BDR*), comparing to *ALDR*, requires bubble injection in the turbulent boundary layer and evokes much more complex mechanisms. Numerous experimental & numerical investigations have been conducted to better understand these mechanisms. Successful bubble drag reduction (*BDR*) was firstly discussed by [McCormick & Bhattacharyya \(1973\)](#) and net drag reduction reaching to 40% was achieved on a fully-submerged axisymmetric body of 915 mm in length at velocities ranging from 0.3 to 2.6 m/s. [Madavan et al. \(1984\)](#) have carried out *BDR* measurements in a zero pressure gradient turbulent boundary layer and found that *BDR* increases with increasing gas injection rates and decreasing reference velocities (increasing gas volumetric fraction) and when buoyancy pushed the bubbles towards the wall. It was also revealed that the bubbles' location was important: it must be with 200 wall units of the wall to promote effective *BDR* ([Pal et al. 1988](#)). Some Soviet researchers ([Bogdevich et al. 1976](#)) have observed that the drag reduction reaches its maximum at the immediate location downstream the gas injection and does not persist as bubbles move away from the wall when traveling downstream. Same was observed for bubbly drag reduction under a flat pate by [Elbing et al. \(2008\)](#). Some numerical investigations by means of direct numerical simulation (*DNS*) of turbulent bubbly flow ([Lu et al. 2005](#)) have confirmed the importance of bubbles' wall-normal location in *BDR* persistence. Unfortunately, such numerical investigations are only possible at modest *Reynolds* numbers.

Although much research has been done experimentally and numerically on both non-equilibrium and equilibrium adverse pressure gradient boundary layers in single phase flow ([Clauser 1954](#); [Bradshaw 1967](#); [Townsend 1956](#); [Skåre & Krogstad 1994](#); [Song 2002](#); [Castillo & Wang 2004](#); [Aubertine & Eaton 2005](#)), very few studies have been dedicated to bubbly drag reduction in case of pressure gradient application. The influence of the pressure gradient on the *BDR* has been firstly studied by [McCormick & Bhattacharyya \(1973\)](#). [Clark & Deutsch \(1991\)](#) have conducted *BDR* measurements on a fully-submerged axisymmetric body under zero, positive and adverse stream-wise pressure gradient and have revealed that a weak adverse pressure gradient helps maintaining bubbles in the buffer layer and thus leads to drag reduction at low speeds. On the contrary, a favorable pressure gradient inhibited the bubbly drag reduction.

To our best knowledge, the bubbly drag reduction has never been investigated in a reattached flow (recovery region) downstream an obstacle mounted at the wall, which induces separation of the boundary layer. This configuration can be encountered in the downstream region of a cavity at the hull.

The goal of this thesis is to examine experimentally bubbles interactions with a reattached turbulent boundary layer downstream of a 2D surface-mounted squared obstacle when bubbles of intermediate-size (sub-millimetric and millimetric bubbles) are injected under favorable gravity condition at the wall in the reattached flow. 4 different free-stream velocity conditions have been studied, and the air injection rate at the wall has been varied.

Introduction

This dissertation consists of 5 chapters. A brief resuming of each chapter is described as follows:

Chapter 1 provides an overview of the state-of-art covering single-phase turbulent boundary layer under zero and adverse pressure gradient single-phase recovery region downstream of surface-mounted obstacles, and bubbly drag reduction mechanisms.

In **Chapter 2**, experimental means including the water tunnel facility, obstacle geometry are described. Flow conditions with and without obstacle and gas injection configurations are mentioned. At last, instruments and means of measurement used including high frequency Particle Image Velocimetry (*PIV*), low frequency Particle Tracking Velocimetry (*PTV*) and high frequency Shadowgraphy are introduced, altogether with associated image processing techniques and system-induced data uncertainties. *PIV* was used to characterize the single phase flow at 11 stream-wise locations from the upstream of the obstacle to the recovery region, including the recirculating region. *PTV* and Shadowgraphy were used at one stream-wise location in the recovery region to characterize both the liquid-phase and gas-phase flows respectively under bubbles injection conditions.

In **Chapter 3**, analysis procedures of experimental data of turbulent boundary layers in single-phase obstacle flow are introduced. Stream-wise evolution of integral parameters of the turbulent boundary layer in the total 11 measuring sections, and the recirculation length are characterized. The time-averaged mean and fluctuating velocity profiles are equally presented. The influence of adverse pressure gradient on mean profiles and integral parameters is discussed and the logarithmic law of the wall of mean stream-wise velocity profiles is confirmed to be valid in recovery region.

Chapter 4 describes the gas-phase flow characteristics. The evolutions of mean bubble diameter, aspect ratio and the gas layer thickness in function of volumetric fraction, *Weber* number and reference velocity are illustrated and commented. The time averaged local gas volume fraction profiles are also shown and analyzed according to the air injection rate and velocity. The gas-phase mean and turbulent velocity profiles are shown and discussed in comparison with *PIV* single-phase profiles.

The characteristics of the liquid-phase flow measured in the recovery region testing section are described in **Chapter 5**. Comparison is made with the single phase flow. Bubble-induced modifications in time-averaged mean and fluctuating velocity profiles, log law parameters as well as integral quantities are discussed. A return to equilibrium boundary layer and a friction velocity reduction are mentioned. Finally, the non-dimensional analysis of the bubbly flow is introduced and the mechanisms implied into bubbly drag reduction based on relative variation of the friction coefficient are discussed.

1 CHAPTER I. Literature Survey & Objectives

In this chapter, we describe the state of the art of the turbulent boundary layer theory, pressure gradient effects on flow structures, separated and reattached flow and bubbly drag reduction. In the first section, the general features of the single phase turbulent boundary layer under pressure gradient effect will be discussed. In the second section, generalities about separated and reattached shear flows downstream of an obstacle, mounted at the wall, will be introduced. In the last section, some principle underlying mechanisms associated with bubble-induced drag reduction will be mentioned.

1.1 Generalities about the single-phase turbulent boundary layer

Turbulence surrounds our everyday lives: from a factory chimney, to an aircraft jet; from a water flow in a river, to a tossed cup of coffee. The first known observation about turbulent flow structure was found in a sketch of *Leonardo da Vinci* (**Figure I. 1**).

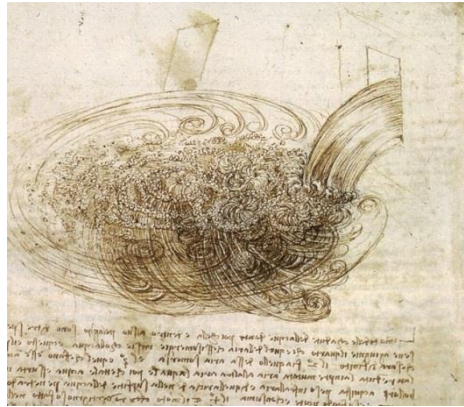


Figure I. 1 “snapshot” of water flow into a tank, *Leonardo da Vinci*, circa 1500.

However, the problems related to the origin of turbulence, that is to say, the transition from laminar to turbulent flow, remain quite complex. It was until 300 years later after the first illustration of *da Vinci*, that this phenomenon was experimentally studied by *Reynolds* (1883). The latter supposed that the turbulence appears as a result of a stability problem of laminar flows and its apparition was related to a definite value of the *Reynolds* number $Re = \frac{Ud}{\nu}$, where U and d denote the characteristic velocity and length and ν is the kinematic viscosity of the fluid. The *Reynolds* number highlights the ratio of inertia force to the friction force on the fluid particle and is a characteristic number for the similarity condition of different flows (*Schlichting* 1955). A large amount of experimental and theoretical investigations have been carried out between 1930 and 1970 for a deeper understanding of the laminar-turbulent transition (*Dryden* 1959; *Schlichting* 1955; *Tollmien & Grohne* 1961; *Shen* 1969; *Tani* 1969; *Morkovin* 1969; *Reshotko* 1976). The value of *Reynolds* number at which laminar-turbulent transition occurs (critical *Reynolds* number Re_{crit}) was found to vary greatly among flow types. Numerous investigations were conducted on the process of transition in the boundary layer on a flat plate (*Burgers* 1924; *van der Hegge Zijnen* 1924; *Dryden* 1935). The critical *Reynolds* number of the boundary layer developing along a flat plate (under zero pressure gradient) is expected to be $Re_{crit} = \left(\frac{U_e x}{\nu}\right)_{crit} = 5 \times 10^5$, where x is the distance from the leading edge of the plate. On a flat plate, in the same ways as in a pipe, the critical *Reynolds* number can be increased when the incoming flow is less perturbed.

A conceptual illustration of the laminar-turbulent transition in the boundary layer is shown in **Figure I. 2** (*Oertel* 2008). At the critical *Reynolds* number Re_{crit} , $2D$ perturbing waves named *Tollmien-*

Schlichting waves appear in the flow and lead to characteristic 3D Λ -vortex further downstream. The Λ -vortices decay and cause turbulent spots, that marks the beginning of the transition to a turbulent boundary layer flow. The transition process is complete and the boundary layer is considered fully turbulent.

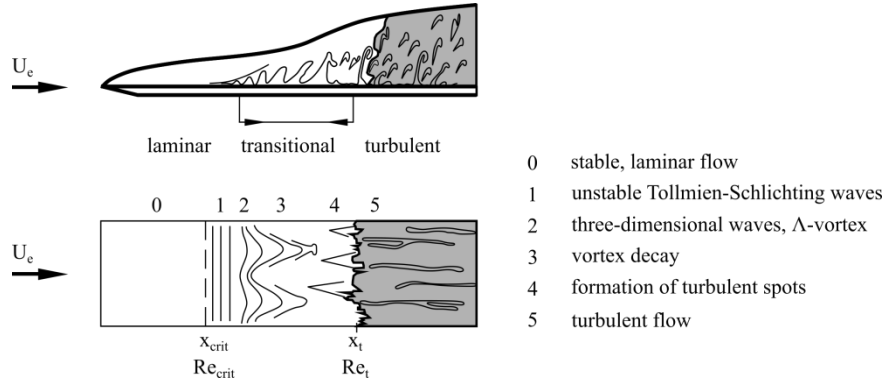


Figure I. 2 Sketch of the laminar-turbulent transition in the boundary layer of a flat plate. Extracted from Oertel 2009

Figure I. 3 represents the mean stream-wise velocity distribution $U(y)$ in the wall-normal direction achieved in a 2D fully turbulent boundary layer for stationary conditions of the flow. x is the stream-wise direction, y is the wall-normal direction.

Due to the presence of the solid wall, the no slip condition must hold at the wall with $U(y = 0) = 0$.

For a Newtonian fluid, the wall shear stress τ_w is linked to the velocity gradient at the wall and the dynamic viscosity μ of the fluid

$$\tau_w = \mu \left(\frac{\partial U}{\partial y} \right)_{y=0} \quad 1 - 1$$

U_e denotes the external velocity outside the boundary layer. Outside the boundary layer, the flow is a potential flow. According to Bernoulli's equation, the external velocity U_e is related to the static pressure P_e outside the boundary layer.

$$\frac{dP_e}{dx} = \rho U_e \frac{dU_e}{dx} \quad 1 - 2$$

The skin-friction coefficient is defined by:

$$C_f = \frac{\tau_w}{\frac{1}{2} \rho U_e^2} \quad 1 - 3$$

The boundary layer thickness δ is by convention the distance from the wall to where the mean velocity $U(y)$ reaches 99% of the external velocity and increases with x in the downstream direction.

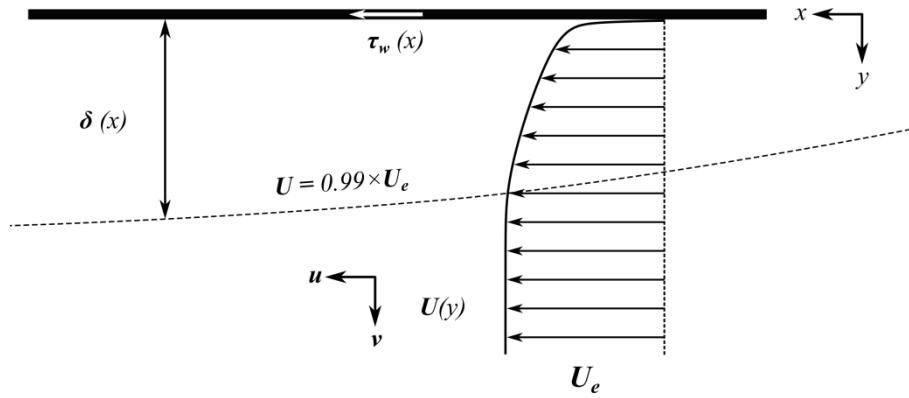


Figure I. 3 Schematic of a wall-bounded fully turbulent boundary layer.

For reasons of dimensionality, the friction velocity u_* can be defined as follows:

$$u_* = \sqrt{\frac{\tau_w}{\rho}} \quad 1 - 4$$

The friction velocity u_* can be used to characterize the turbulent flow in the near-wall region (*Chassaing 2000*). It is representative of the order of magnitude of the velocity fluctuations in the turbulent boundary layer.

1.1.1 Equations of conservation

We consider a 2D stationary turbulent boundary layer. Let us denote u and v , the instantaneous stream-wise and wall-normal velocity components. U and V are the averaged velocity respectively and u' , v' are the fluctuating velocity component respectively.

Prandtl's boundary layer theory is of great importance to simplify the conservative equations in a turbulent boundary layer. By introducing the following assumptions

$$V \ll U,$$

$$\delta \ll L, \quad 1 - 5 (a b c)$$

$$u' \sim v' \sim u^*$$

into the averaged *Navier-Stokes* equations (*Reynolds* equations), we obtain the following differential conservation equations:

$$\frac{\partial U}{\partial x} + \frac{\partial V}{\partial y} = 0$$

$$X\text{-direction: } \rho U \frac{\partial U}{\partial x} + \rho V \frac{\partial U}{\partial y} = -\frac{dP_e}{dx} + \frac{\partial}{\partial y} \left(-\rho \langle u'v' \rangle + \mu \frac{\partial U}{\partial y} \right) \quad 1 - 6 (a b c)$$

$$Y\text{-direction: } \frac{\partial P}{\partial y} = 0$$

Since the pressure is constant along the wall-normal direction in the boundary layer, the stream-wise pressure gradient is imposed equal to the external velocity gradient $\frac{dU_e}{dx}$.

The term $-\rho \langle u'v' \rangle$ is the *Reynolds* shear stress and represents the amount of momentum in the stream-wise direction due to the correlation between the stream-wise and wall-normal flow fluctuations

(*Cousteix 1989*). The total shear stress τ_{total} is composed of the viscous and turbulent shear stresses respectively:

$$\tau_{total} = \mu \frac{\partial U}{\partial y} - \rho \langle u'v' \rangle \quad 1 - 7$$

However, in the presence of flow separation & reattachment, *Prandtl's* equation is no longer valid because some assumptions are no longer true, notably the one $V \ll U$. That has pushed us to find a 2nd order simplification by taking into account the following hypothesis ($\frac{V}{U_e} \sim \frac{\delta}{L} \sim \Theta(1)$):

$$\frac{\partial U}{\partial x} + \frac{\partial V}{\partial y} = 0$$

$$X\text{-direction: } \rho U \frac{\partial U}{\partial x} + \rho V \frac{\partial U}{\partial y} = -\frac{dP_e}{dx} - \frac{\partial}{\partial x}(\rho \langle u'^2 \rangle) + \frac{\partial}{\partial x}(\rho \langle v'^2 \rangle) + \frac{\partial}{\partial y}(\tau_{total}) \quad 1 - 8 (a b c)$$

$$Y\text{-direction: } \frac{\partial P}{\partial y} = -\rho \frac{\partial \langle v'^2 \rangle}{\partial y}$$

Note that comparing to the classical *Prandtl's* momentum equation (**Eq. 1 – 6b**), two additive terms of the turbulent stress appear on the right-hand-side, which come from the contribution of stream-wise and wall-normal *Reynolds* stresses $\rho \langle u'^2 \rangle$ and $\rho \langle v'^2 \rangle$.

1.1.2 Integral length scales

Integral length scales are length scales that characterize the boundary layer globally in the wall-normal direction. They only depend on the stream-wise position x . The boundary layer is traditionally characterised by the displacement thickness δ^* , the momentum thickness, θ and the shape factor H (*Cousteix 1989*). These parameters are defined in **Eq. 1 – 9** to **1 – 11**.

$$\delta^* = \int_0^\infty \left(1 - \frac{U}{U_e}\right) dy = \int_0^\delta \left(1 - \frac{U}{U_e}\right) dy \quad 1 - 9$$

$$\theta = \int_0^\infty \frac{U}{U_e} \left(1 - \frac{U}{U_e}\right) dy = \int_0^\delta \frac{U}{U_e} \left(1 - \frac{U}{U_e}\right) dy \quad 1 - 10$$

And

$$H = \frac{\delta^*}{\theta} \quad 1 - 11$$

The displacement thickness δ^* is a distance by which the external potential field of flow is displaced outwards as a consequence of the mass deficit in the boundary layer due to the wall. The momentum thickness θ quantifies the loss of momentum in the boundary layer, as compared with potential flow. These parameters are valuable because they allow the boundary layer to be characterised quantitatively, as a result, they allow informative comparisons to be made between various boundary layers under a range of scenarii.

The shape factor H , being the ratio of δ^* to θ , is a one-parameter family of velocity profile, depending on the external pressure gradient. In the case of a flat plate, the value of the shape factor is $H \cong 2.6$ in the laminar regime and $H \cong 1.4$ in the turbulent regime. *Clauser (1954)* indicated that H varies with C_f even for constant pressure condition.

Equation 1 – 12, which derives from the integration in the y direction of the stream-wise momentum conservation **Equation 1 – 6b**, evidences that the wall shear stress τ_w is linked to the integral parameters δ^* , θ and the stream-wise pressure gradient $\frac{dP_e}{dx}$:

$$\frac{\tau_w}{\rho} = \frac{d}{dx} (U_e^2 \theta) + \delta^* U_e \frac{dU_e}{dx} \quad 1 - 12$$

1.1.3 Discussion about universality of the mean stream-wise velocity profiles

For the turbulent boundary layer developing along a wall, three distinct regions (inner, overlap and outer regions) can be found and two different length scales can be considered according to the distance from the wall.

1.1.3.1 Inner region:

In the inner part of the boundary layer (inner region), where the advection can be neglected, the characteristic length scale is the viscous length of the boundary layer

$$l_v = \frac{\nu}{u_*} \quad 1 - 13$$

The normal distance from the wall y can be scaled by l_v , leading to the well-known wall coordinate (inner variable):

$$y^+ = \frac{yu_*}{\nu} \quad 1 - 14$$

In the very near wall region of the inner region (i.e.: viscous sub-layer), where the viscous diffusion exceeds the turbulent diffusion, we have a linear velocity profile:

$$U^+ = \frac{U}{u_*} = y^+ \quad 1 - 15$$

This law is well established for a very small range of y^+ ($0 < y^+ < 5$).

Farther from the wall, still in the inner region, where the turbulent diffusion exceeds the viscous diffusion, the mean velocity profile follows a logarithmic law.

$$u^+ = \frac{1}{\kappa} \ln y^+ + B \quad 1 - 16$$

Where κ denotes the universal *von Kármán's* constant and B the intercept constant. For a flat plate ($\frac{dP_e}{dx} = 0$), the values $\kappa = 0.41$ and $B = 5.2$ are observed to be approximately independent of Re , despite a slight increase of B with increasing Re (*Dean 1978*). It was reported that B essentially depends on the roughness height (*Hama 1954*).

The logarithmic law versus inner variables is valid in the logarithmic region which extends for a flat plate in the range $30 < y^+ < 300$.

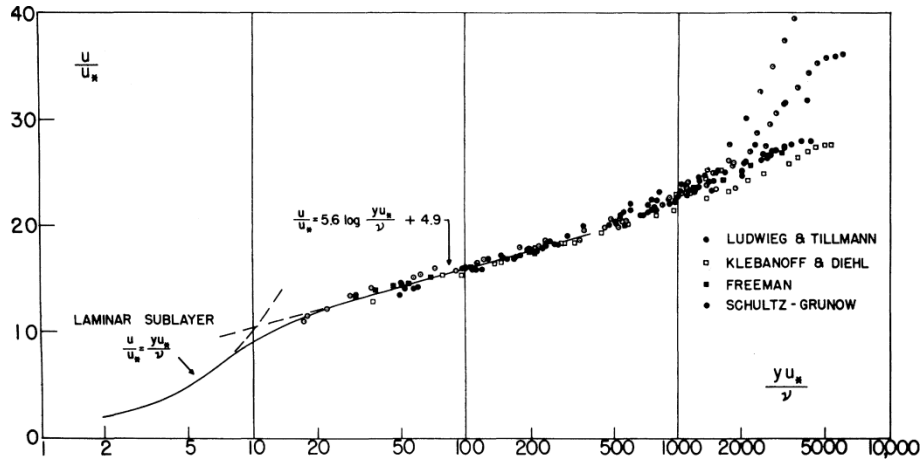


Figure I. 4 Universal velocity distribution for mean velocity profiles as a function of inner variables for a turbulent boundary layer. Extracted from Clauser 1954

Much experimental work has been done over the years on modifications of the inner region under the influence of adverse pressure gradient ($\frac{dP_e}{dx} > 0$) (Ludwig & Tillmann 1950; Stratford 1959; Herring & Norbury.1967; Klebanoff & Diehl 1952; Schultz-Grunow 1941; Bradshaw 1967; Clauser 1954).

Equation 1 – 12 evidences that an adverse pressure gradient reduces the friction coefficient C_f (Schubauer and Kabanoff 1950). Ludwig & Tillmann (1950) have proposed an empirical formula allowing estimation of C_f :

$$C_f = 0.256 \times 10^{-0.678H} \times Re_\theta^{-0.268} \quad 1 - 17$$

Where Re_θ is the Reynolds number based on the momentum thickness:

$$Re_\theta = \frac{U_e \theta}{\nu} \quad 1 - 18$$

Clauser (1954) showed that although the pressure gradients have a significant effect on the friction velocity, the universal logarithmic law is well established even when pressure gradients are present (Figure I. 4) and discussed the universality of parameters κ and B .

Direct numerical simulation (DNS) of Spalart & Watmuff (1993) indicated that the the logarithmic law may be affected by pressure gradients which can modify both the von Kármán constant κ and the B constant. Table I. 1 summarizes the values of κ and B obtained by diverse authors with increasing pressure gradients.

Case	κ	B	G	dp^+/dx^+	
1	0.42	5.8	6	-0.012	Spalart & Leonard 1987
2	0.39	5.3	5.5	-0.01	Herring & Norbury
3	0.4	5.2	6.3	-0.007	Herring & Norbury
4	0.39	4.4	6.7	0	Spalart & Leonard 1987
5	0.38	3.7	7.2	0.019	Clauser 1954; Bradshaw 1966
6	0.31	1.6	8.6	0.037	Clauser 1954; Bradshaw 1966

Table I. 1 Influence of the adverse pressure gradient on inner log fit and Clauser parameters. Pressures were normalized with $dp^+ = P_e/(\rho U_e^2)$

However, the functional dependency of these parameters on the pressure gradient is not known and it is also possible part of the modifications may be a Reynolds number effect. Indeed, it was reported that

increasing the *Reynolds* number in zero pressure gradient produces similar effects as increasing the pressure gradient (*Spalart 1988*).

Overall, the existence of a universal log law with constant κ and B values for turbulent wall-bounded flow still remains uncertain. *George (2007)* argued in his resuming review that the values of κ in boundary layers differ from those in pipe/channel flows, and the historical value of $\kappa = 0.41$ seems to be a compromise for those flow types.

It is now to discuss the outer and overlapping regions and the effects of pressure gradient:

1.1.3.2 outer region:

In the outer part of the boundary layer (outer region), the distance from the wall can be scaled by δ , leading to the non-dimensional coordinate (outer variable):

$$\eta = \frac{y}{\delta} \tag{1 - 19}$$

In the outer region of the turbulent boundary layer, the universality of the stream-wise velocity profiles $(U_e - U)/u^* = f(\eta = y/\delta)$ is not obvious.

The notion of “equilibrium boundary layer” is to be introduced. For an equilibrium turbulent boundary layer, profiles of $(U_e - U)/u^*$ as a function of y/δ are expected to be similar, regardless of the stream-wise position x , *Reynolds* number Re_x and roughness (*Clauser 1954*).

Equilibrium turbulent boundary layers are very commonly examined when studying adverse pressure gradient flows. This is because once equilibrium conditions are established, the velocity profiles of the boundary layers is said self-similar and the measurements are required at only a single stream-wise position (*Aubertine 2005*). The study of equilibrium boundary layers has led to a greater understanding of some of the basic changes which occur to boundary layers in adverse pressure gradient.

Clauser (1954) had firstly laid out the idea of equilibrium turbulent boundary layer. For a given equilibrium profile, some parameters should remain constant. Non-dimensional parameters were introduced, which were the ratio of the stream-wise pressure gradient to the viscous shear stress gradient over an integral length of the boundary layer.

Based on the displacement thickness, the parameter β is defined as follows:

$$\beta = \frac{\delta^*}{\tau_w} \frac{dP_e}{dx} \tag{1 - 20}$$

Clauser defined a new integral length scale Δ that is easier to characterize experimentally than δ , and that is considered as more universal than δ^* or θ .

$$\Delta = \int_0^\infty \left(\frac{U_e - U}{u_*} \right) dy = \delta \int_0^\infty f(\eta) d\eta \tag{1 - 21}$$

$(U_e - U)/u^* = g(y/\Delta)$ is a universal function of y/Δ , depending on the value of the *Clauser* parameter G , defined according to:

$$G = \sqrt{\frac{2}{c_f}} \times \frac{H-1}{H} \tag{1 - 22}$$

G is approximately 6.8 for a constant pressure turbulent boundary layer. *Clauser* indicated that under constant pressure condition, we have $\Delta/\delta = 3.6$. For turbulent equilibrium boundary layers, a positive

stream-wise pressure gradient induces an increase in G ($G > 6.8$), and the contrary for a negative stream-wise pressure gradient (see **Table I. 1**).

Townsend (1961) developed another definition of equilibrium boundary layer. He pointed out that an equilibrium layer was one in which the local rate of energy production and dissipation reached a state of equilibrium. The local energy production/dissipation was so large that the aspects of the turbulent motion were almost uniquely determined by the shear stress distribution and were independent of conditions outside the region. This assumption requires only absolute balance between energy production and dissipation but not the stress equilibrium and allows a zero pressure gradient boundary layer to be included into a family of equilibrium layer.

Equilibrium was reported (*Skåre and Krogstad 1994*) to be obtained when the friction coefficient remains at a low constant level of $C_f = 5.7 \times 10^{-4}$ and mean velocity profiles were documented to be self-similar. *Townsend (1976)* pointed out that the self-similar mean velocity profiles can only be obtained if the profiles of the turbulent shear stress $\frac{-\langle u'v' \rangle}{u_*^2} = f(\frac{y}{\delta})$ are also self-similar.

Some analogue results by *Cousteix (1989)* on the outer region have suggested that for each equilibrium family, the corresponding deficit mean velocity profile is uniquely a function of y/δ and the function itself varies under the influence of pressure gradient parameter β (**Figure I. 5**). It should be noticed that this observation remains true only if the *Reynolds* number approaches infinity, and the friction velocity u_* approaches zero.

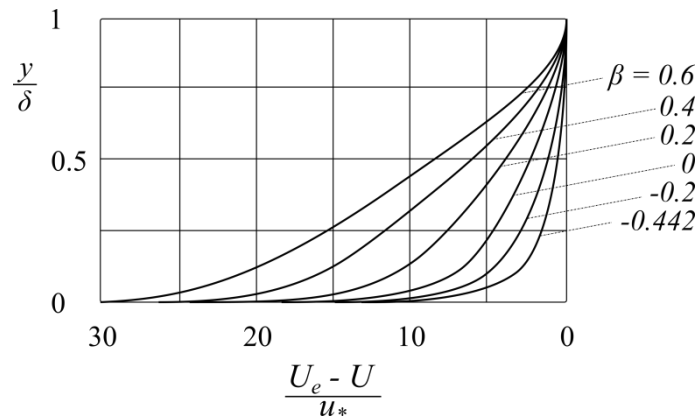


Figure I. 5 Self similar solutions of mean velocity profiles in the outer region of turbulent boundary layer as a function of β . Extracted from *Cousteix 1989*

1.1.3.3 Overlap region:

The inner and outer regions are clearly separated on the condition that the *Reynolds* $Re_\delta = u_*\delta/\nu \gg 1$. In the overlapping region, a logarithmic law is valid.

Clauser (1954) has established the validity of a logarithm law for $(U - U_e)/u_*$ as a function of y/Δ , for all equilibrium turbulent boundary layers:

$$\frac{U - U_e}{u_*} = \frac{1}{\kappa} \ln \frac{y}{\Delta} - \frac{\Delta u_2}{u_*} + 0.6 \quad 1 - 23$$

Where $\Delta u_2/u_*$ is the shift in the additive constant of the log law from the zero pressure gradient condition.

$\Delta u_2/u_*$ increases as G augments. The y/Δ validity range of the logarithmic law is reduced with the increase in G value: from $[0.002 - 0.1]$ at $G = 6.1$ to $[0.001 - 0.01]$ at $G = 19.3$.

Figure I. 6 shows the equilibrium mean velocity profiles in the overlapping region from *Clauser's* data, the slope of the semi-logarithmic curve remains constant under different pressure gradient sets and the shift in the vertical ordinate of the straight line portion (shift in $\frac{\Delta u_2}{u_*}$) is clearly seen. As can be seen in **Figure I. 6**, the logarithmic region is “shortened” as the pressure gradient increases, which is in accordance with results of reattached flow of *Bradshaw & Wong (1971)* and *Castro (1979)*, the latter argued that this might be due to the developing wake region.

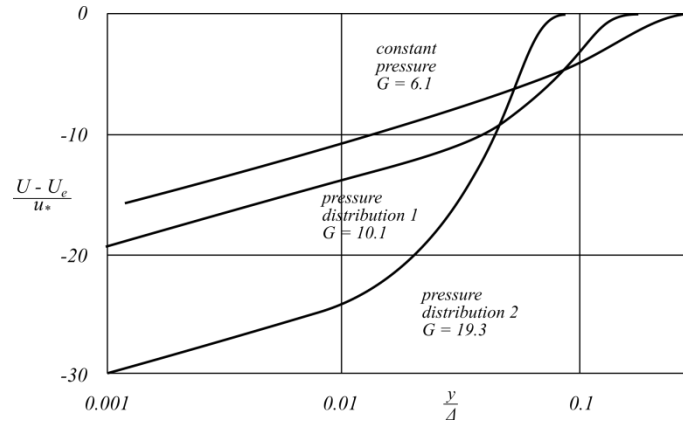


Figure I. 6 Logarithmic plot of the mean velocity profiles versus outer variables, according to G values. Extracted from *Clauser 1954*

At large distance from the wall, (typically of order 0.2δ under constant pressure), measurements diverge from the logarithmic law of the wall (*Chassaing 2000*). *Coles (1956)* has introduced the notion of a law of the wake which was an additive correction on the inner region log law (**Eq. 1 – 16**):

$$u^+ = \frac{1}{\kappa} \ln y^+ + B + \frac{\Psi}{\kappa} W(\eta) \quad 1 - 24$$

Where $W(\eta)$ denotes the wake term and is in the form of $W(\eta) = 2 \sin^2(\frac{\pi}{2}\eta)$ and Ψ the *Coles* wake parameter. *Coles (1962)* observed that Ψ equals to $0.55 - 0.6$ and becomes independent for large *Reynolds* numbers ($Re_\theta > 6000$).

1.1.4 Discussion about universality of the turbulent shear stress profiles

Integration in the wall-normal direction (y direction) of **Equation 1 – 6b** in the logarithmic region of the inner region (where advection and viscous diffusion are negligible by comparison to turbulent diffusion) yields:

$$-\langle u'v' \rangle = \frac{1}{\rho} \frac{dP_e}{dx} y + \frac{\tau_w}{\rho} \quad 1 - 25$$

The *Reynolds* stress wall-normal distributions are observed to be very sensible to the pressure gradient (**Figure I. 7**). With a positive increasing pressure gradient, the peak moves away from the wall (*Cousteix 1989*).

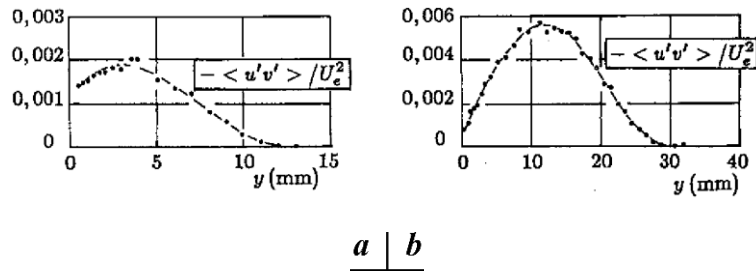


Figure I. 7 A) *Reynolds* shear stress profile under a mild adverse pressure gradient ($H = 1.59$) B) *Reynolds* shear stress profile under a steep adverse pressure gradient ($H = 2.13$). Extracted from *Cousteix 1989*

Figure I. 8 shows the evolution of the total shear stress τ profiles under the influence of pressure gradient parameter β . (As profiles are plotted in the outer region, the viscous shear stress can be neglected and the total shear stress τ equals approximately the *Reynolds* shear stress $-\rho\langle u'v' \rangle$). It can be seen that β influences the slope of *Reynolds* shear stress near the wall, for a negative value of β , the maximum *Reynolds* shear stress lays in near wall region while in case of a positive value of β , the *Reynolds* shear stress reaches the maximum far from the wall, and the wall-normal peak location moves away from the wall, as β increases.

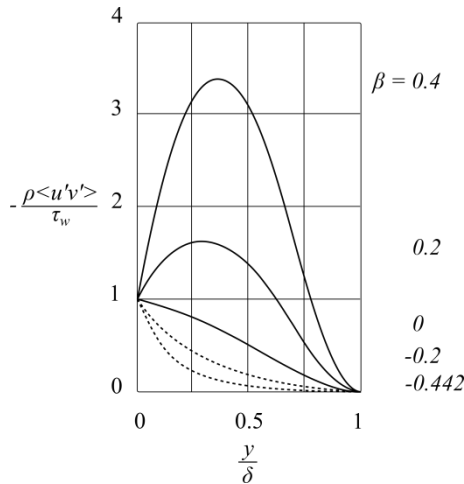


Figure I. 8 Self similar solution in the outer region of the wall-normal distribution of *Reynolds* shear stress under the influence of β Extracted from *Cousteix 1989*

1.1.5 Discussion about the mechanism of turbulence production in the turbulent boundary layer

For the turbulent boundary layer under constant pressure, the production of turbulent kinetic energy $\Pi = -\langle u'v' \rangle \frac{\partial U}{\partial y}$ is maximum in a sub-region of the inner region, where the contribution of turbulent diffusion is same order as the one of the viscous diffusion (buffer layer). The buffer layer is located in between the viscous sub-layer and the logarithmic region.

Some observations in the buffer layer of a smooth wall-bounded turbulent boundary layer have been made that attest for the existence of instantaneous vortices associated with strong turbulent stress events $u'v' < 0$ (*Sheng et al. 2009*).

Under the effect of instability (i.e.: an initial perturbation), a span-wise vortex that lifts locally vertically from the wall, breaks and gives birth to two elongated counter-rotating stream-wise vortices. Between the two vortices, the flow is subjected to an outflow jet “ejection” resulting in a local wall shear stress decrease (the wall stress minimum is located beneath the vortex roll up region); on the

other hand, wall shear stress maximum develops on the outer sides of the stream-wise vortex pair, corresponding to a “sweeping” phenomenon (inflow jet). **Figure I. 9** illustrates this scenario. The vortices (coherent structures) are localized in the buffer region ($y^+ \approx 20$), their size is of the order of $10l_v - 20l_v$. It leads to instantaneous stream-wise wall shear stress streaks that alternate between minima and maxima.

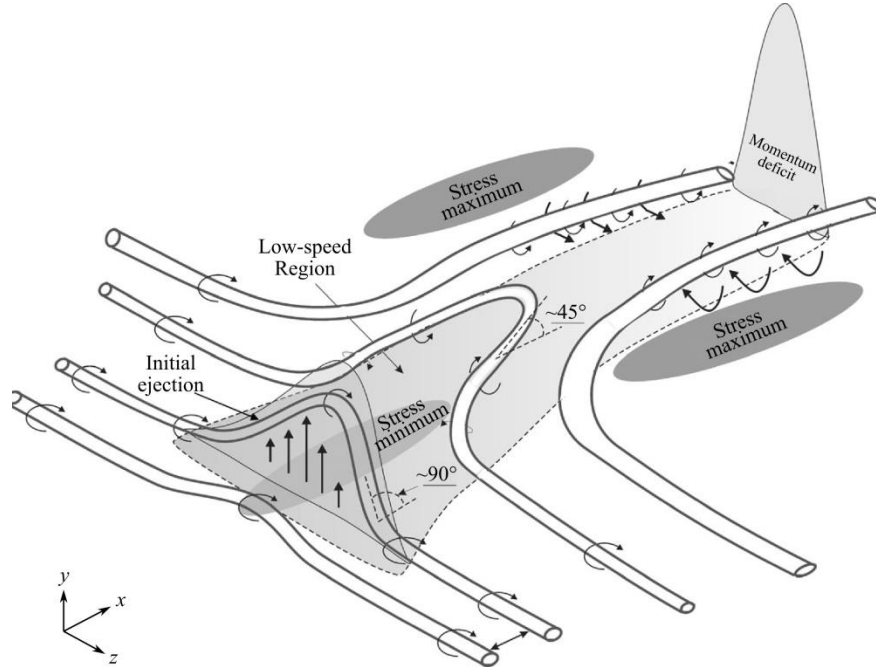


Figure I. 9 Conceptual sketch of the creation of wall shear stress streaks according to vortices generation in the buffer layer. Extracted from Sheng *et al.* 2009

Near wall distributions of turbulent stresses for a zero pressure gradient turbulent boundary layer are shown in **Figure I. 10**, according to the measurements by Sheng *et al.* (2009). The stream-wise term U_{rms} reaches a maximum value $U_{rms} \approx 3u_*$ in a region very close to the wall, roughly at $y^+ = 20$ (buffer layer). The transverse component V_{rms} increases gradually as y^+ increases and reaches a maximum value of $V_{rms} \approx 1.4u_*$. According to the continuity equation, V_{rms} should be observed to decrease as y^+ increases when $y^+ \rightarrow 0$, but such behavior is impossible to be verified experimentally (Hinze 1975). As for the Reynolds shear stress $\langle u'v' \rangle$, a constant value in the range $25 < y^+ < 60$ is observed. Following the Reynolds number or the geometry (e.g.: weak secondary flows that occur in square ducts (Kawahara 1995; Kline *et al.* 1967)), locations of peak production and magnitudes might be varying.

Another observation is the anisotropy of the distribution of U_{rms} and V_{rms} for flat plate turbulence. Wilcox (1994) suggested that the two terms in the logarithmic region follows the ratio $\frac{U_{rms}}{V_{rms}} \approx 2$. At a certain distance from the wall near the boundary layer upper limit, turbulence becomes isotropic, which means that the turbulent stresses in both directions are equal to each other (Schlichting 1955).

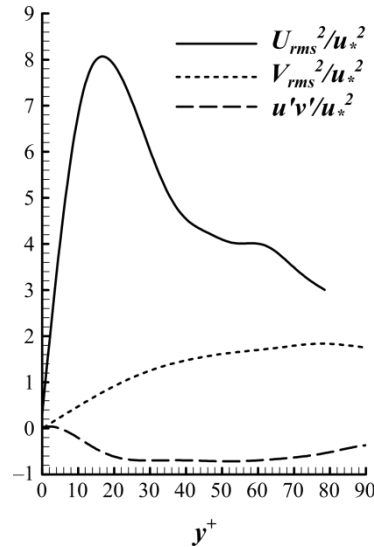


Figure I. 10 Universal distribution for mean turbulent shear stresses, normalized by u_* or u_*^2 , as a function of inner variables for a turbulent boundary layer. Extracted from *Sheng et al. 2009*

Measurements of *Skåre & Krogstad (1994)* on a non-separated flow under strong adverse pressure gradient have shown that the distribution of kinetic energy between the different turbulent stresses remains unaffected by the pressure gradient, same ratio between the different turbulent stresses is conserved comparing to that of zero pressure gradient flows.

1.2 Generalities about the single-phase turbulent flow downstream of obstacles at the wall

In the framework of the current study, we have focused on a specific flow with adverse pressure gradient which is a turbulent flow in the reattached region downstream of a 2D squared obstacle. The sudden restriction and expansion of the flow section makes the flow quite complex, comparing to flows without separation. This section is devoted to the description of general features of the flow developing downstream of obstacles at the wall. We are interested in the particularities of this flow that make the turbulent boundary layer different from the classical turbulent boundary layer with adverse pressure gradients (as described in section 1 of the chapter).

Figure I. 11 shows the configuration. A separation of the boundary layer occurs, which leads to the development of a recirculating region. Here δ_0 is the initial boundary layer at the obstacle position without the presence of the obstacle. L_R denotes the recirculation length and is strongly affected by the initial inclination of the dividing streamline and thus by the obstacle's geometry (*Bergles 1983*). However, the recirculation length is reported to vary weakly with the *Reynolds* number (*Song and Eaton 2004*). The same authors have also concluded that boundary layers at Re_θ less than 2000 – 3000 can not be considered fully turbulent.

As shown in **Figure I. 11**, downstream of the recirculating region, a new shear layer is born and spreads outwards the original shear layer. At the reattachment point, the new shear layer splits and gives birth to a new sub-boundary layer.

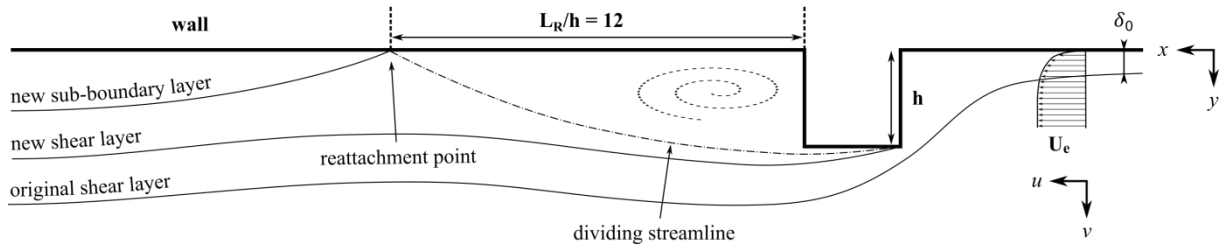


Figure I. 11 Schematic of flow over obstacle

Under these circumstances, conventional boundary layer calculation methods might be inapplicable under the perturbation effects on the turbulence structure. *Bradshaw & Wong (1971)* suggested that it was needed to define three strengths of perturbation applied to an initial shear layer flow over obstacle. The levels were characterized by the ratio of the initial boundary layer thickness δ_0 and the obstacle height h (δ_0/h).

1.2.1 Classification of obstacle perturbation

According to *Bradshaw & Wong (1971)*, the strength of the perturbation depends on how far the new shear layer bordering the recirculation flow has spread into the original shear layer and can be classified as follows:

- 1) Weak perturbation: $\delta_0/h \gg 1$
- 2) Strong perturbation: $\delta_0/h = \Theta(1)$
- 3) Overwhelming perturbation: $\delta_0/h \ll 1$

It was mentioned by the same authors that the flow structure might be easier to understand when it is under an overwhelming perturbation since this type of flow is less dependent on the initial boundary layer. Comparing to a backward-facing step flow, the flow over obstacle can be more complex as it involves two separation regions.

1.2.2 Reattached flows

The flow quite after the reattachment point differs much from a plane mixing layer (ordinary boundary layer), even at positions far downstream of the obstacle (*Bradshaw and Wong 1971*). As mentioned earlier, the split of the new shear layer at the reattachment point has resulted in roughly one-sixth of the mass flow deflecting up-stream in the case of a backward-facing step flow (*Etheridge & Kemp 1977*). *Coles (1956)* defined the reattached mean velocity profiles as a linear combination of the logarithmic law of the wall and the law of the wake.

However, it was reported in the works on reattached flow downstream of a 2D surface mounted square under a “weak” perturbation ($\delta_0/h = 0.48$; $Re_\theta = 1250$) by *Antoniou & Bergeles (1988)* that the logarithmic law (**Eq. 1 – 16**) holds true in the reattached flow, even at region near the reattached point (*Antoniou & Bergeles 1988*). *Song & Eaton. (2002)* carried out LDA & PIV measurements on separated and recovered flow with strong perturbation due to a smoothly contoured ramp and found that the logarithmic law of the wall is valid downstream of reattachment but the range of validity reduced to $y^+ < 100$ at $x/h = 13$ but extended to $y^+ = 200$ at $x/h = 23$. The return of parameter β and Clauser parameter G to their expected values at equilibrium has been observed for a reattached flow under strong perturbation $\delta_0/h = \Theta(1)$ at distance from the obstacle $x/h = 25$ (*Antoniou & Bergeles 1988*).

1.2.3 Turbulent structure in adverse pressure gradient flows

Castro & Haque (1987) pointed out in their works on turbulent structure in the recirculation region that the turbulent structure of the separated shear layer differs from that of a plane mixing layer, notably the monotonous increase of the *Reynolds* normal stresses as reattachment is approached. *Agelinchaab & Tachie (2008)* have carried out experimental investigations of channel flow over a $2D$ square obstacle and reported that the *Reynolds* stream-wise, wall-normal and shear stresses increase along the dividing streamline, reach the maxima and decreases as the reattachment approaches. *Bradshaw and Wong (1971)* explained that the *Reynolds* stresses decrease is induced by the splitting of large eddies that produce the shear stresses. Partially in the recirculation region and after the reattachment point, values of $-\langle u'v' \rangle$ are reported to increase linearly with y near the wall (*Etheridge and Kemp 1977, Agelinchaab & Tachie 2008*). Downstream of reattachment point where a new sub-boundary layer develops, the locations of peak values of $-\langle u'v' \rangle$ increasingly move away from the wall, under effect of the mixing and spreading of the new layer, values of maxima of $-\langle u'v' \rangle$ decrease rapidly (*Agelinchaab & Tachie 2008*).

In the reattached boundary layer, a stress equilibrium layer was defined (*DeGraaff & Eaton 1999*) as a near wall region where the *Reynolds* stresses are in equilibrium with the local skin friction. *Song & Eaton (2004)* suggested that in the recovery region of the separated turbulent boundary layer, the inner part of the boundary layer ($y^+ \leq 70$) recovers more rapidly than the outer layer and develops a stress equilibrium layer while the energetic large eddies in outer layer persist. Accordingly, in the stress equilibrium layer, the scaling of the *Reynolds* stress proposed by *DeGraaff & Eaton (2000)* for a flat-plate turbulent boundary layer is still valid.

1.3 Bubbly turbulent boundary layer

Most of the studies dealing with the interaction between bubbles and a turbulent boundary layer have been focused on bubbly drag reduction (*BDR*). As mentioned in the general introduction, bubbly drag reduction has been mainly addressed in the context of propulsion of marine underwater vehicles and surface ships (*Ceccio 2010*).

Up to the nineties, studies dedicated to the bubbly drag reduction were experimental studies conducted in turbulent boundary layers developing at zero pressure gradient condition and small *Reynolds* numbers. In most of these studies, global measurement of the bubbly drag induced reduction was achieved and it reveals a large discrepancy between the results according to the *Reynolds* numbers and the air injection rates. When compiling all these results, even at high *Reynolds* numbers, self-similar laws cannot be evidenced (*Sanders et al. 2006*) and are still of interest. Although some physical mechanisms are suspected in the bubbly drag reduction process, it still requires academic and numerical studies, particularly local studies, to clearly identify which of the mechanisms is dominant and find, if possible, models.

We will now discuss of the different physical mechanisms implied in the bubbly drag reduction (*BDR*).

Park (2016) has suggested a classification of effects of bubbles in boundary layer into two categories, passive static effects and active dynamic effects.

The passive static effects are characterized by modifications of fluid properties by small bubbles comparing to the boundary layer thicknesses. Such modifications include the decrease of near wall average density (*Elbing et al. 2008*) and the modification of the local viscosity (*Einstein 1906*). It requires a gas volume fraction peak near the wall. *Madavan et al. (1985)* have confirmed, in their

work with numerical modelling of bubbly boundary layer by locally varying density and viscosity, a quite good agreement with the experimental results.

The gas volume fraction peak is enhanced at low velocity, high air injection rate and favorable gravity direction (i.e.: injection under a wall) (*Madavan 1985*). Nevertheless, the gas volume fraction peak localisation in the buffer layer or in the logarithmic region depends on the bubble size and obviously plays a role.

The active dynamic effects, on the other hand, involve the modifications of the turbulent flow structure induced by the bubbles, splitting of the bubbles (*Meng & Uhlman 1989*) and deformation of the bubbles (*Kitagawa et al. 2005*).

Overall, mechanisms involved in both effects for bubbly drag reduction seem to be the issue of bubble size. Let's call d_b the equivalent bubble diameter. It can be classified roughly into three types of bubble size: micro-bubble, intermediate-size bubble and large-size bubbles. This will be introduced separately along with influence on *BDR*. We will examine only the case when gravity is favorable to *BDR*. A schematic diagram of the bubbly flow is shown in *Figure I. 12*.

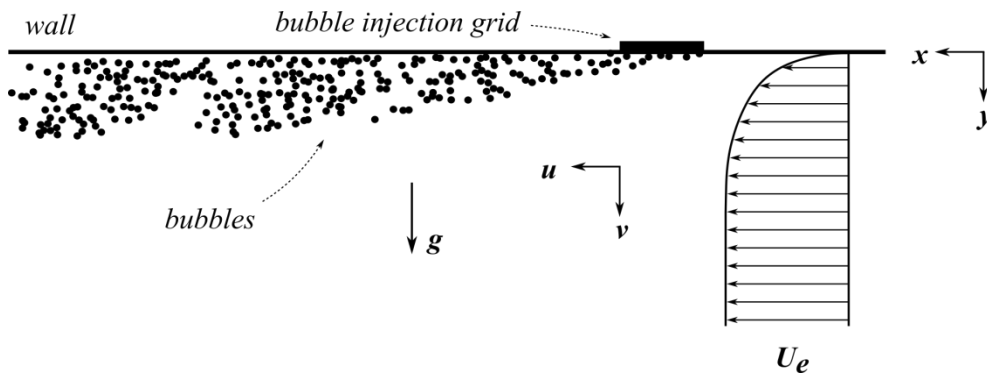


Figure I. 12 Schematic representation of the bubbly turbulent boundary layer with gravity effect in favor of bubbly drag reduction

Let us define the gain factor G_b as the ratio of Relative Drag Reduction (by comparison to the single phase flow) to the average gas volume fraction $\langle \alpha \rangle$ in the bulk flow:

$$G_b = \frac{\Delta D}{D(\alpha)} \quad 1 - 26$$

Where ΔD denotes the drag reduction as bubbles are injected and D is the initial drag without bubbles. The gain factor G_b evaluates the sensitivity of the drag reduction per unit void fraction (*Murai 2014*).

1.3.1 Effect of the bubble size: Micro-bubbles

A bubble is classified as a micro-bubble when its diameter is smaller than the near wall coherent structures.

In turbulent boundary layer flow, the buffer layer is extended roughly from 5 to 30 viscous length l_ν and is the region of high *Reynolds* stress, turbulent production and momentum transfert. To achieve *BDR* with micro-bubbles, bubbles must be able to interact with the flow structure in this region and must be smaller than the near wall stream-wise vortices responsible for the wall friction streaks (size $10 l_\nu$) (see *Figure I. 9*). For micro-bubbles, the magnitude of the gain G can be several hundreds.

Recent *DNS* results (*Ferrante & Elghobashi 2003*) highlighted a large *DR* by bubbles with dimensionless diameter $d_b^+ = 2.4$. At this size range, bubbles were reported to be trapped into the near wall stream-wise vortices of the buffer layer and created a local positive convergence $\vec{\nabla} \cdot \vec{U} > 0$, resulting in a push-away effect on the vortical structures, enhancement of the outflow jet and reduction of the global viscous drag (**Figure I. 13**). The mechanism is a compressibility effect. At higher *Reynolds* number, the stream-wise vortices are squeezed and a higher volume fraction is required to achieve same relative reduction of the viscous drag as for smaller *Reynolds* numbers (*Ferrante & Elghobashi 2005*).

However, producing such flow is difficult experimentally because the near wall vortices are very small.

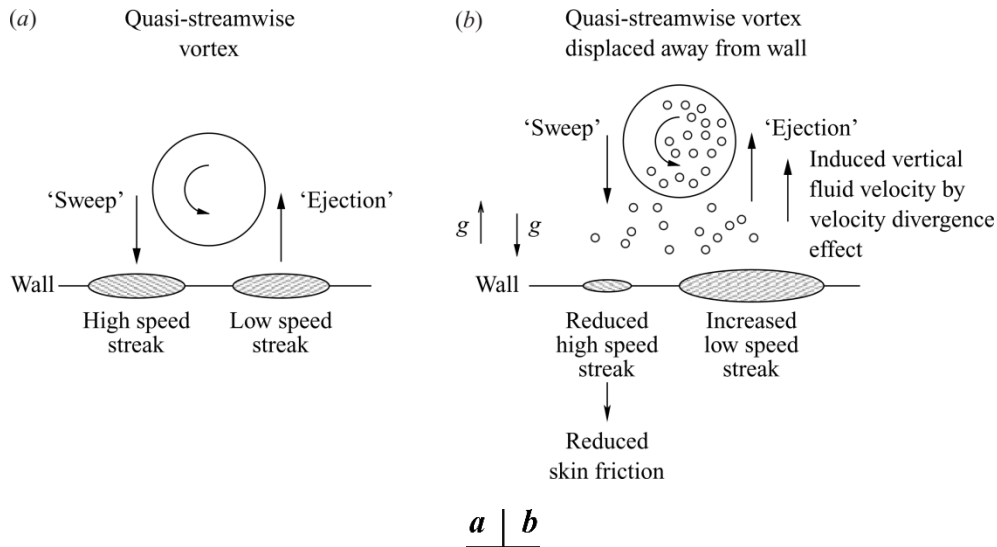


Figure I. 13 Schematic of the drag reduction mechanism in a micro-bubble turbulent boundary layer. **A)** single-phase flow. **B)** bubbly flow. Extracted from *Ferrante & Elghobashi (2004)*

Experimental studies of micro-bubbles injection into turbulent boundary layer on both flat plate (*Madavan et al. 1984; Pal, Merkle & Deutsch 1988*) and on axisymmetric bodies (*McCormick & Bhattacharyya 1973; Deutsch & Pal 1990; Clark III & Deutsch 1991*) were performed.

A substantial reduction of the momentum flux has been experimentally obtained in the inner region with micro-bubbles of mean diameter $150 \mu m$, which is of the order of the smallest turbulent scale (Kolmogorov length scale), leading to a local wall friction decrease by 25% (*Jacob et al. 2010*). The drag reduction is associated to a loss in the coherence of the turbulent structures of the buffer layer and a redistribution of the turbulent kinetic energy in favor of the small scales of the turbulence.

In the experiments of *Hara et al. (2011)* and then in the experiments of *Paik et al. (2016)*, the reduction of the wall friction is closely linked to the reduction of the turbulent shear stress induced by the important vertical fluctuating motion of the bubbles and their high concentration in the buffer layer.

The flow relaminarization caused by the change in the rheological properties of the fluid in the presence of micro-bubbles can be another mechanism. Derived from the formulation of *Einstein (1906)* for a dilute suspension and taking into account the bubble deformability by the shear stress (*Frankel & Acrivos 1970*), the effective viscosity of a dispersed bubbly flow can be estimated by the following relationship:

$$\mu_{eff} = \mu \left(1 + \frac{1 - \frac{12}{5}Ca^2}{1 + \left(\frac{6}{5}Ca\right)^2} \alpha_v \right) \quad 1 - 27$$

Where μ denotes the molecular dynamic viscosity of the liquid and α_v the local volume fraction of the gas phase ($\alpha_v < 0.1$) and Ca is the capillary number.

$$Ca = \frac{\mu\gamma d_b}{2\sigma} \quad 1 - 28$$

γ is the shear rate ($\gamma = \left| \frac{\partial U}{\partial y} \right|$), σ is the surface tension of the gas-liquid interface.

At small values of the capillary number, for bubbles smaller than the smallest structures, the effective viscosity is expected to increase. The increasing μ_{eff} will lead to an increase of the shear stress, since the latter is expressed as $\tau_{total} = \mu_{eff} \frac{\partial U}{\partial y} - \rho \langle u'v' \rangle$ (Eq. 1 – 7). However, the reduction in velocity fluctuation leads to a total reduction of τ_{total} . This phenomenon is uniquely expected in low *Reynolds* number flows (Kodama & Hinatsu, 2014). Legner (1984) suggested that the thickening of the turbulent boundary layer by the increase of the effective viscosity can be another explanation for the reduction of the wall friction.

However, for values of the capillary number above a critical value ($Ca > Ca_{crit} = 0.65$), the effective viscosity is expected to decrease, resulting in a direct reduction of the wall friction by the reduction of the viscous stress.

1.3.2 Effect of the bubble size: Intermediate-size bubbles

A bubble is classified as bubble of intermediate size when its diameter is same order of magnitude as the size of the near wall coherent structures (hence several tens of the viscous length). It leads to bubble size, same order as the inner region of the turbulent boundary layer, same order as the span-wise spacing of the wall friction streaks.

DNS results of Lu *et al.* (2005) have shown that as the bubble size increases to about $300 \mu m$ (i.e.: $54 l_v$), the deformability of bubbles forces the near-wall stream-wise vortices to squeeze towards the wall which leads to a reduction of both the vorticity of these vortices and the *Reynolds* shear stress. The role played by deformability in the BDR process has been confirmed by experimental works (van den Berg *et al.* 2005; Kitagawa *et al.* 2005). Indeed, Serizawa & Kataoka (1990) have evidenced that the deformation of the bubbles dampens the acceleration of the turbulent structures by introducing a time lag when restituting the turbulent kinetic energy to the flow.

Experimentally, supplying air flux through a porous plate seems to be the most common practice to obtain bubble sizes in the range of $100l_v - 300l_v$. The splitting of air layer and coalescence of micro-bubbles could also give birth to bubbles of mentioned size.

It was observed through experimental works of Moriguchi & Kato (2002) that drag reduction does not depend on the bubble size when the average diameter is larger than $500 \mu m$; Kawamura *et al.* (2003) have put into evidence that the drag reduction is insignificant when bubble mean diameter ranges from $500 - 2000 \mu m$. Under $500 \mu m$, the skin friction reduction effect becomes larger when bubble size is large (Kawamura *et al.* 2004). Experimental evidence in Shen *et al.* (2006) suggested that for bubbles ranging from $254 - 476 \mu m$, the drag reduction is rather determined by the effective gas volumetric flow rate which induces density variation, than by the bubble size. Therefore, it is not

obvious to conclude on the efficiency of intermediate-sized bubbles in reducing the viscous drag at the wall.

Sanders et al. (2006) have conducted large scale experiments at high *Reynolds* numbers on *HIPLATE* with bubbles of mean diameter $300 \mu m$ and suggested that, beside the local density reduction, *DR* strongly depends on the near-wall gas volume fraction, which depends on both gas injection rate and external flow speed. Drag reduction (*DR*) is achieved when bubbles stay near the wall; when bubbles migrate away from the wall beyond $y^+ = 300$, *DR* decays and disappears. Meanwhile, a bubble-free liquid layer is formed on the surface of the plate, even under buoyancy-dominant regimes. This phenomenon is considered to be the primary factor that limits the *DR* persistence. *Elbing et al. (2008)* have also carried out *DR* test on *HIPLATE* apparatus and have observed a linear dependence of the *DR* with the gas volume fraction, for a given flow velocity and a given porous plate.

As a complement of the previous studies, in the project “*FDRAIHN*” financially supported by the *ANR* (Research National Agency), the effect of intermediate bubble size on the near wall flow of a horizontal spatially developing turbulent boundary layer, under zero pressure gradient, has been characterized experimentally in the Water Tunnel of the French Naval Academy. I took part in this project, in the framework of my *Ph.D.*, by processing *PIV* measurements and by performing *LDV* measurements. Part of the results is developed in *Appendix 8.3* and I presented these results in 2016 at the 15^{ème} Journées de l’Hydrodynamique. The *Reynolds* number was $Re_\theta = 3976$, at a velocity of $U_e = 2m/s$. The bubbles were injected through needles at the upper wall and their size was varied from 40 to 300 viscous lengths, according to the local air injection rate. The global volumetric fraction in the boundary layer was varied between 0.01% and 0.11%. The 2D velocity field was characterized in the vertical plane by Particle Image Velocimetry (*PIV*) and the stream-wise velocity of the liquid was achieved at one point in the viscous sub-layer by Laser Doppler Velocimetry (*LDV*). The liquid stream-wise velocity of the two-phase flow was compared with the one of the single phase flow. *Figure I. 14* shows the relative difference of the stream-wise velocity in the viscous sub-layer and the corresponding mean bubble size according to the local air injection through each needle Q_g/n_{inj} . Q_g is the global air injection rate across the upper wall and n_{inj} is the number of needles activated at the wall. R_b^+ is the bubble radius normalized by the viscous length. Generally speaking, it was observed a reduction of the turbulent shear stress in the inner region, as the bubbles fluctuating motion in the wall-normal direction decorrelates the stream-wise and wall-normal velocity fluctuations of the liquid.

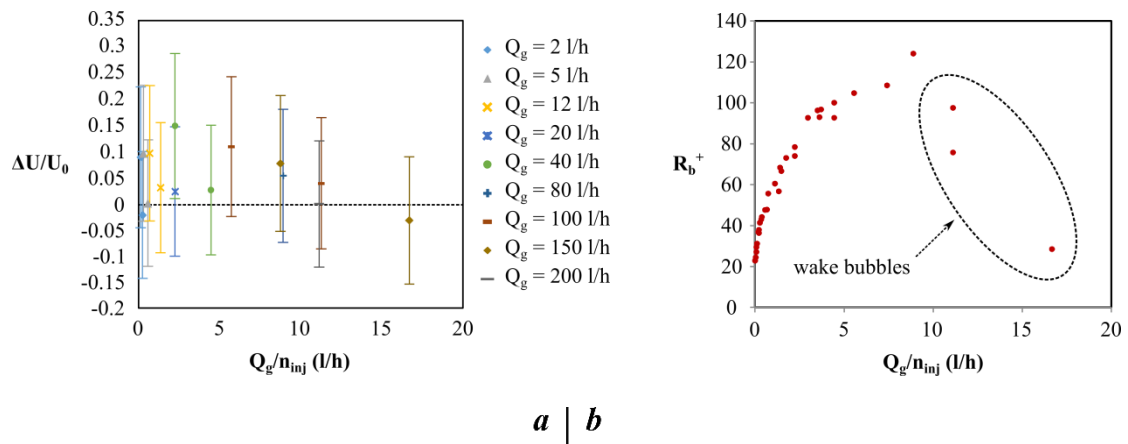


Figure I. 14 Evolution as a function of the local air injection rate through needles at 2 m/s of: A) Bubble induced relative variation in the viscous sub-layer of the mean stream-wise velocity by comparison to single phase flow B)

bubble equivalent radius normalized by the viscous length. Results extracted from project “FDRAIHN”, 15èmes Journées de l’Hydrodynamique, 2016, Zhang et al.

The results evidence two regimes: **1)** an excess of velocity in the viscous sub-layer is observed when increasing the air injection rate and the bubble size, accompanied with a deficit of the stream-wise velocity in the logarithmic region. This is in agreement with a suction effect of the boundary layer induced by bubbles buoyancy; **2)** beyond a critical bubble size (of approximately 300 viscous length), there is a fragmentation of the bubbles and small submillimetric bubbles are generated in the wake of millimetric bubbles. In this case, the stream-wise velocity is decreased in the viscous sub-layer and the boundary layer is thickened, as expected for blowing effect.

Based on these data, an estimation of the bubble induced modification of the wall shear stress was obtained in *Gabillet et al. (2016)*, taking into account the values of the local gas volume fraction measured in the viscous sub-layer. At this *Reynolds* number ($Re_\theta = 3976$), the wall shear stress is increased by the presence of the bubbles unless they fragment. It was shown that with the bubbles fragmentation, a reduction of 10% of the wall shear stress can be achieved for a bulk volumetric fraction $\langle \alpha \rangle$ of 0.8% and a near wall gas volume fraction peak of 2.4%. For a smaller *Reynolds* number ($Re_\theta = 1709$, $U_e = 1 \text{ m/s}$), no reduction of the wall shear stress was observed as no bubbles fragmentation was achieved ($d_b^+ < 160$). The increase of the gas-liquid interfacial area when fragmentation occurs requires energy which can decrease the drag force (*Meng & Uhlman 1998*).

Oishi et al. (2009) have investigated *BDR* in a channel of silicone oil by injecting millimetric bubbles at the upper wall. They confirmed the importance of gas volume fraction in *DR*, besides, the results have evidenced a complex non-linear relationship between the temporal fluctuations of-the local gas volume fraction and the local time-averaged wall friction. They have shown that *DR* is promoted by amplifying the fluctuation in the local gas volume fraction (leading to void fraction waves).

Generally speaking, for bubbles of size equivalent to the inner region, the gas volume fraction stratification (volume fraction peak near the wall) and the drift velocity between the gas and the liquid play a role in the *BDR* process. It can lead to a relative *BDR*, of several orders of magnitude the value of the near-wall average gas volume fraction.

1.3.3 Effect of the bubble size: Single large bubbles

A bubble is classified as a large bubble when its stream-wise dimension is roughly of the same order of magnitude as the thickness of the boundary layer.

For a single large bubble of diameter ranging from 2 to 90 mm, *Murai et al. (2006)* have observed a non-uniform distribution of the local skin friction in the bubble coordinate (**Figure I. 15**). The skin friction increases in the front part of the bubble and starts to decrease in the middle and rapidly falls on the minimum near the rear. *Oishi and Murai (2014)* measured the turbulent shear stress field modified by such a single bubble passage in the vicinity of the wall and discovered that a highly deformed bubble has a rotating effect and induces twins vortices at both the leading and trailing edge of the bubble, that mechanism somehow reduces the local drag. **Figure I. 15** illustrates the presence of an intense vortex at the rear. In this case, *BDR* mostly comes from this vortex and the gain factor is larger than 1, which is larger than the drag reduction expected for an air layer.

For large bubbles injected at the upper wall of a channel, *Murai et al. (2006)* have evidenced that the minimum skin friction achieved is zero when the bubble’s stream-wise length is five times larger than the channel height (i.e.: ten times larger than the boundary layer thickness). In this case, the bubble is

expected to behave as an air layer and the drag reduction is air layer drag reduction, with a gain factor of 1.

This mechanism puts into evidence that local *BDR* is a transient process, which is linked to the transient position of the gas-liquid interface near the wall.

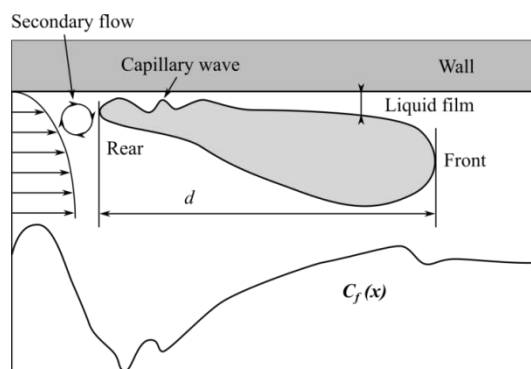


Figure I. 15 flow field around a single large bubble and instantaneous friction coefficient stream-wise distribution. Extracted from Murai 2006

Park *et al.* (2015) have confirmed that waves of gas volume fraction enhance the bubbly drag reduction. They have tested a repetitive bubble injection technique. This technique consists of supplying air through a porous plate and forming bubble swarms that provide high local transient gas volume fraction during a given time and then stop the air supply wait and repeat the process (repetitive bubble swarm). Inside each bubble swarm, the front part is led by an air film which splits into large deformable bubbles, and *DR* is achieved as the air layer isolate the wall surface from the liquid while the following bubbles enhance fluctuations of local gas volume fraction. They confirm that the near wall coherent structures, responsible of the friction streaks, are pushed away from the wall by the bubble swarms and that *BDR* achieved is more important for the repetitive injection than for a continuous injection of same time-averaged volumetric fraction.

1.3.4 Effect of the pressure gradient

Most of the previous studies of *BDR* have been conducted in channel flow with an imposed pressure gradient and a flow which is dynamically established or along flat plates for a flow which is spatially developing under zero pressure gradient conditions.

The question which is addressed here is the influence of the pressure gradient on the *BDR*.

Micro-bubble drag reduction for an adverse pressure gradient flow was believed to be firstly observed in drag measurements of McCormick & Bhattacharyya (1973). Clark & Deutsch (1991) measured the micro-bubble skin friction variation on an axisymmetric body under zero ($\partial P/\partial x = 0$), favorable ($\partial P/\partial x < 0$) and adverse ($\partial P/\partial x > 0$) stream-wise pressure gradients. They reported that although the gas injection did not alter both the pressure gradient and the axisymmetry of the flow, bubbles injection associated to a weak adverse pressure gradient leads to a substantial drag reduction at quite low speed. The authors argued that the adverse pressure gradient inhibited the “move-away” phenomenon of the bubbles and trapped them in the buffer layer. Although the reason remains unclear, the authors anticipated that the favorable pressure gradient would suppress the turbulent mixing necessary to push the bubble cloud out of the viscous sub-layer. Contrary to the adverse pressure gradient, a favorable pressure gradient inhibited the bubbly drag reduction.

1.3.5 summary

Murai (2014) made in his review paper a summary chart (Figure I. 16) of the trends observed for the bubbly induced drag modification according to the flow speed and the bubble size. He summarized results for horizontal flows: channel flow, horizontal flat plates or profiles, and model ships. Although this map does not include the effect of impact factors such as the gas volume fraction, the pressure gradient, it gives nevertheless a vision of some global trends and regions to discover. It shows that drag reduction requires small bubbles at large velocity or large bubbles at small velocity.

For intermediate conditions, bubbles injection can increase the viscous drag (Gabillet et al., 2016; Zhang et al., 2016); these corresponding points have been added on the chart of Murai. According to our recent works, three ellipses in intermediate-size bubble region are added on the Murai’s chart. It is suggested that under zero pressure gradient condition, the drag increasing region extends into flow speed lower than 2 m/s and bubble size smaller than 3 mm. Beyond 2 m/s and 3 mm in size, drag reduction is confirmed with a bubble fragmentation phenomenon.

For sub-millimetric and millimetric bubbles, in laminar flows, bubble injection at the upper wall can induce an advance in the transition from laminar to turbulent flow, thus leading to bubbly drag increase.

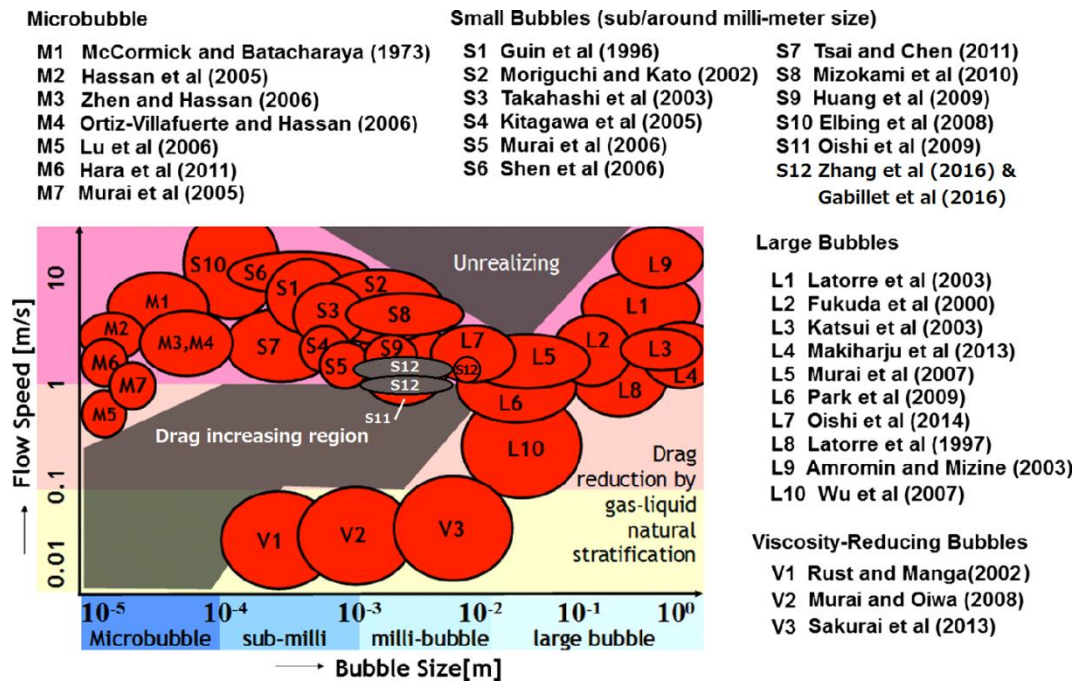


Figure I. 16 Summary schematic of success of drag reduction in function of bubble size and flow speed (Extracted from Murai 2014)

As a summary, different mechanisms can be engaged in the BDR process according to the bubble size: rheological effect, sweeping and squeezing the vertical structures, compressibility effect, decorrelation between stream-wise and wall-normal turbulent fluctuations, volume fraction gradient associated to near wall volume fraction peak, drift between liquid and gas phases, bubbles deformation, bubbles fragmentation, gas volume fraction waves.

When bubble size is extremely small, bubbles interact directly with the vortical flow structures of the buffer layer and enhance DR at quite high gain factors and persistence seems to be guaranteed. But generating bubbles of such sizes seems to be a real challenge for naval applications. Using mm-order

bubbles seems to be an easy way to achieve DR with a gain factor from 4 to 10 (*Murai et al. 2007*). However, as bubble size increases, DR suffers from the lack of persistency in the downstream flow.

1.4 Conclusion

In this chapter, we have reviewed some main characteristics of the turbulent boundary layer under zero pressure gradient and adverse pressure gradient effects and notably those of a reattached flow. Some underlying physical mechanisms associated with Bubbly Drag Reduction were introduced, under conditions in zero, favorable and adverse pressure gradients. However, as mentioned above, Bubbly Drag Reduction in reattached flow with intermediate-sized bubble injection remains unexplored.

The goal of this thesis is to examine the effect the adverse pressure gradient plays in bubbly drag reduction of reattached turbulent boundary layer flow downstream of a $2D$ surface-mounted squared obstacle with injection of intermediate-size bubbles under favorable gravity. The data in this study were gathered under the same experimental conditions than those in the project “*FDRAIHN*”: all experiments were performed in the French Navy Academy Cavitation Water Tunnel which consists of a laboratory-scale pressurized water tunnel. The bubble injecting system remained unchanged but the boundary layer thickness δ increased from 1 *cm* to 10 *cm* due to the perturbation of a $2D$ up-stream surface-mounted squared obstacle. The thickened boundary layers were roughly equivalent to those of real-scale marine vehicles. Experimental measurements were made over 4 reference velocities from 2 *m/s* to 8 *m/s*, higher than the maximum velocity tested (2 *m/s*) in the project “*FDRAIHN*”.

Bubbles were injected into the flow downstream of the reattached point and interacted with the recovered turbulent boundary layer further downstream. The bubble-size-to-boundary-layer-thickness ratios and the reference velocities were chosen to be situated in a range comparable to those of naval hydrodynamics applications.

2 CHAPTER II. Description of Experimental Device and Flow Conditions

The goal of this chapter is to give a detailed inventory of the experimental setup and the different measuring and calculation techniques used in the actual work.

Section 2.1 describes the experimental facility including the geometry of obstacle and gas & particle injectors. *Section 2.2* covers the flow condition with and without obstacle and also the particle and gas injection configurations. In *section 2.3*, the measuring techniques such as the particle image velocimetry for single phase flow measurement, the image pre-processing technique, the relaxation particle tracking velocimetry for liquid phase measurement in bubbly flow and particle mask correlation method used to identify the centroid of particles, are described. The gas phase in bubbly flow was characterized by Shadowgraphy technique which will also be covered.

2.1 Experimental Device

The experiment was performed in the recirculating closed water tunnel of the French Naval Academy. The tunnel has a test section 192 mm wide, 192 mm high and 760 mm long, as shown in *Figure II. 1*. Upstream of the test section, the tunnel is equipped with a honeycomb and a convergent section with a contraction ratio of 9. The test section is constructed using *Plexiglas* to facilitate optical observation. The lower wall of the test section is inclined with a slope of 0.395%, which makes it possible to compensate the pressure gradient in the test section. The tunnel was originally designed to study the single phase flow or the cavitating flow around foils mounted at mid-height of the test section. But for the purpose of the study, we focused on the two-phase flow developing along the upper wall of the test section. All walls in the test section are made of acrylic glass. The assembly stresses between the glass walls and the frame have caused an optical distortion on the edges. To enable visualisations with minimal distortion of the very near wall region of the flow, the upper wall was shifted downward from 2 mm in the test section.

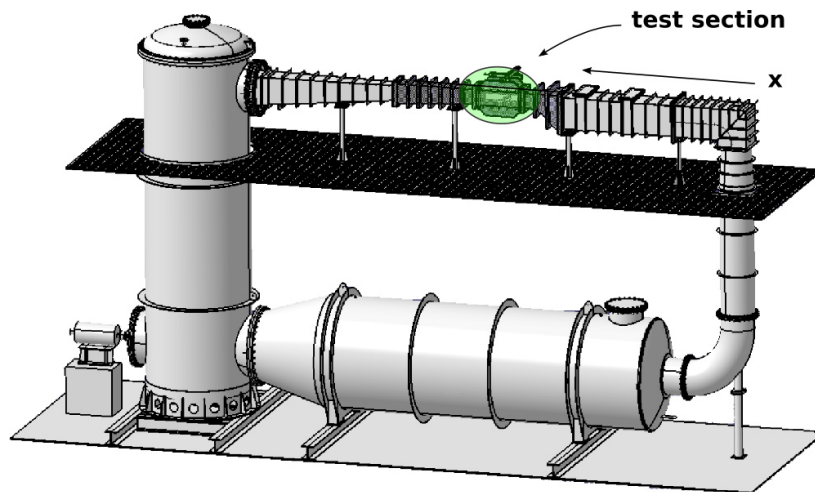


Figure II. 1 General sketch of the tunnel

A 2D square obstacle with a height h of 16 mm, which spanned the entire width of tunnel, was mounted at the upper wall of the test section, 134 mm downstream the entrance of the test section (*Figure II. 2*). The upstream rising edge corner of the obstacle is chosen by convention to be at the origin of horizontal x axis ($x = 0$). The vertical position of the upper wall is considered as the reference for the y axis ($y = 0$). u and v are the velocity components in the stream-wise and wall normal directions respectively.

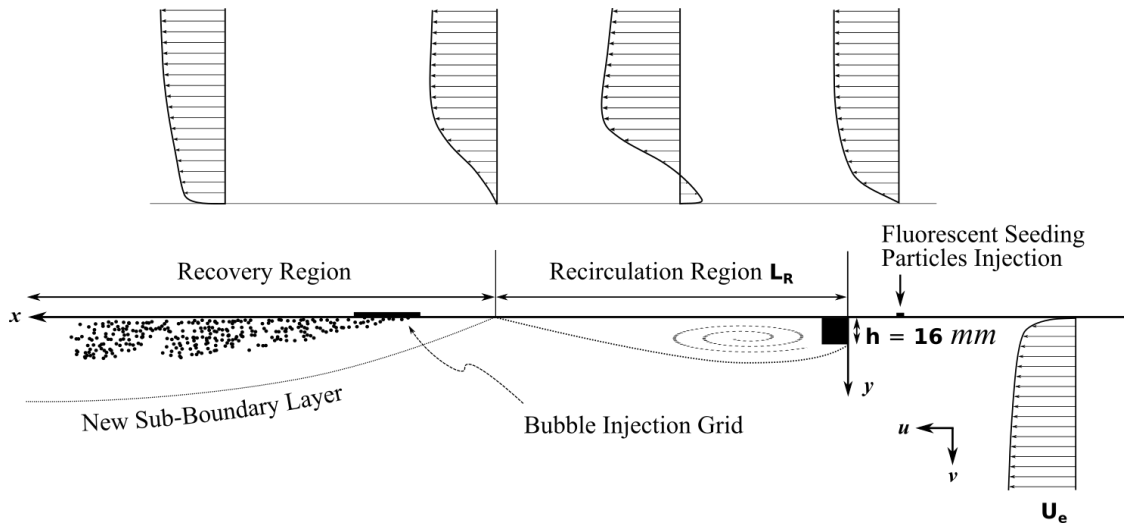


Figure II. 2 Schematic diagram of experimental setup and coordinate system: lateral view of test section with the dividing streamline downstream of the square obstacle. The bubble injection grid was located in the recovery region where a new boundary layer was created.

Figure II. 2 shows a sketch of the flow achieved in the test section with the 2D square obstacle at the upper wall. The stream-wise velocity profiles as well as the dividing streamline, expected in the single phase flow, are roughly drawn in this figure. Downstream the obstacle, there is a recirculating region characterized by a reverse flow. L_R is the distance between the upstream edge of the obstacle and the reattachment point. Downstream the reattachment point, the boundary layer is redeveloping (recovery region).

To ensure the seeding of the near wall flows for *PTV* measurements, the flow was therefore seeded by an injection pushing system with fluorescent seeding particles. Particles were injected at the upper wall at $x/h = -1.5$ upstream of the obstacle. The particle injection was operated by a linear slide actuator where a syringe pump containing fluorescent seeding particles in tap water suspension was attached to the carriage. The carriage traveled with a speed of $360 \mu\text{m/s}$ and assured a constant injection flow rate $Q_p = 0.72 \text{ l/h}$ through a needle $600 \mu\text{m}$ in diameter.

Air bubbles were injected at the wall in the recovery region. The bubble injection was carried out using a 2D grid of 57 needles of $180 \mu\text{m}$ in diameter, mounted at the upper wall (Figure II. 3). The needles were arranged in the stream-wise direction into a rectangular network of 6 transverse rows. (see Annex A for more details of the bubble injection network). The grid was embedded in the upper wall and was located in the recovery region between $x/h = 22.8$ and 27.9 with the midpoint of the grid $x/h = 25.35$. The total volume rate of gas Q_g was varied from 5 l/h to 80 l/h . Q_g was controlled by the use of 3 mass flow controllers of different measuring ranges. The air flow was regulated with Bronkhorst El-flow Prestige® flow controllers of max-range of 10.1, 48 and 336 l/h . By using the 3 controllers alternatively depending on required volume rate, a control of $\pm 10\%$ was achieved. The injection pressure was monitored with a manometer with an accuracy of $\pm 0.01 \text{ bars}$. The pressure was varied between 1.47 and 1.8 bars. The on-off control on each injection row can be operated individually by a manual valve system in the ease of varying the mean bubble size, for a given air injection rate. A picture of the control panel of air injection is shown in Figure II. 4.

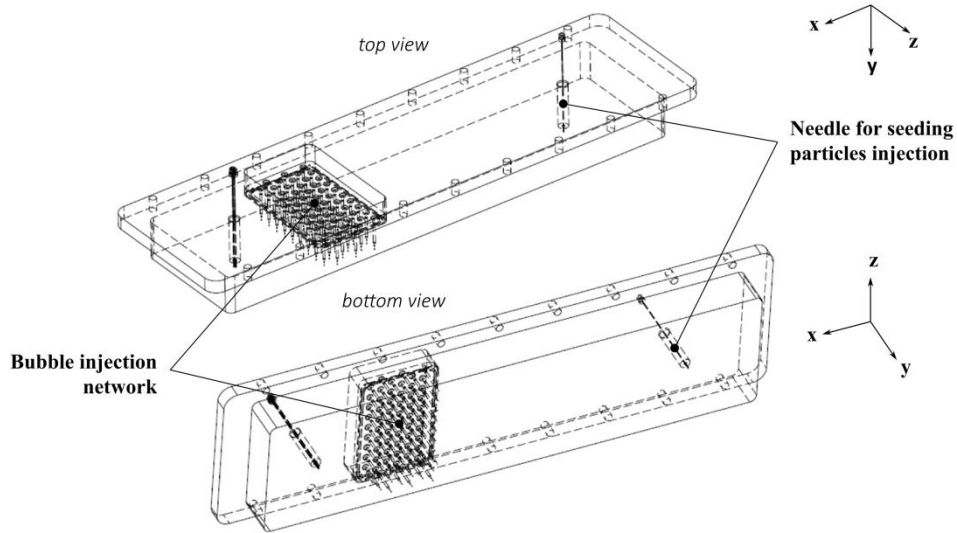


Figure II. 3 Views of the upper wall of the test section, including the bubble injection network and seeding particles needles (the obstacle is not displayed on these views).

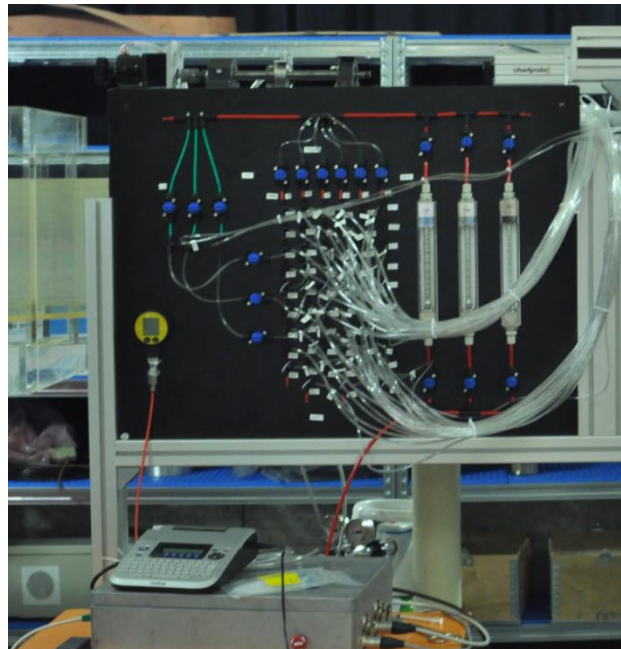


Figure II. 4 Picture of the on/off control panel of air injection

Time resolved characterization of the single-phase flow was made by *PIV*, at 11 different $x - y$ measurement sections along the symmetry axis of the tunnel, from $x/h = -1.2$ upstream of the obstacle down to $x/h = 38$ in the recovery region. Two neighbouring measurement sections were separated from 56.9 mm , giving an overlap length of 11.09 mm of the measuring sections in the stream-wise direction. The measurement sections are depicted in **Figure II. 5**. The viewing area for each station had dimension $106 \times 68 \text{ mm}^2$.

Low frequency characterization of the bubbly two-phase flow was carried out uniquely at the very downstream location ($x/h = 36.2$, which corresponds roughly with the 11^{th} measurement section in single-phase flow measurements). The viewing window had dimension $107.9 \times 107.9 \text{ mm}^2$.

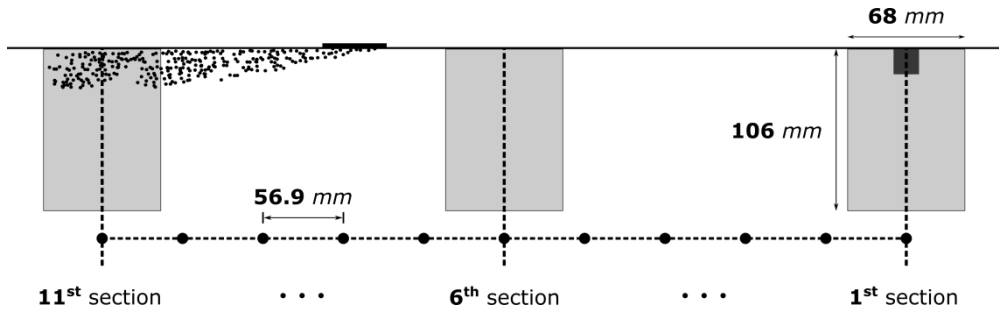


Figure II. 5 Schematic diagram of the measurement sections sequence along the tunnel. Longitudinal center of each section is represented by a point; only 3 sections are illustrated for the sake of visibility. (The single phase flow was characterized from sections 1 to 11, whereas the two-phase flow was characterized in section 11).

2.2 Flow Conditions

All measurements were made under 4 reference velocities $U_{ref} = 2, 4, 6$ and 8 m/s . The single phase flow boundary layer parameters are summarised in **Table II. 1**. They were characterized by *Laser Doppler Velocimetry* at $x = 0$ for the undisturbed flow in the absence of the obstacle.

$U_{ref} \text{ m/s}$	$Re_{\theta 0}$	δ_0/h	δ_{*0}/h	θ_0/h	G_0	C_{f0}	Power rate n_0 of the power law $\frac{U}{U_e} = \left(\frac{y}{\delta_0}\right)^{n_0}$
2	1356	0.38	0.06	0.04	6.14	$4.16e^{-3}$	0.25
4	4281	0.51	0.08	0.06	6.09	$3.19e^{-3}$	0.18
6	7280	0.72	0.10	0.07	7.15	$2.63e^{-3}$	0.17
8	9260	0.69	0.09	0.07	6.78	$2.65e^{-3}$	0.16

Table II. 1 Characteristic parameters of the single-phase undisturbed boundary layer achieved at $x = 0$ for different free stream conditions. Re_{θ} is the *Reynolds* number based on momentum thickness and U_{ref} is the reference velocity, δ^* is the displacement thickness, θ is the momentum thickness, C_f is the friction coefficient and G is the *Clauser* parameter. δ is the boundary layer thickness, determined based on the power law of the stream-wise velocity profile in the outer region, n is the power rate. Subscript 0 denotes the undisturbed flow (without the obstacle).

From 2 m/s to 6 m/s , the turbulence is developing in the boundary layer along the upper wall of the tunnel and the boundary layer expands while the power rate decreases. We notice that the downward shift of the upper wall induces a small adverse pressure gradient at the localisation of the obstacle ($G > 6.1$). The boundary layer thickness is very similar for $U_{ref} = 4, 6$ and 8 m/s .

Bradshaw et al. (1971), in their work on boundary layer relaxation, suggested that the strength of the flow perturbation can be classified by the value of δ_0/h . In our study, the ratio δ_0/h is inbetween 0.38 and 0.72, the flow is thus classified between a strongly perturbed flow and an overwhelmingly perturbed one, where classical wall boundary layer becomes wake mixing layer (as discussed in **Chap. I**).

Table II. 2 summarizes the two-phase flow's operating points. The air volumetric fraction $\frac{Q_g}{Q_g+Q_l} \approx \frac{Q_g}{Q_l}$, which is the ratio of the air injection rate to the water injection rate in the tunnel, was varied up to 0.03%.

$U_{ref} \text{ (m/s)}$	$Q_g \text{ (l/h)}$	$Q_g / Q_l \text{ (%)}$	$P \text{ (bars)}$
2	5 – 80	$1.9e^{-3} - 3.01e^{-2}$	1.49 – 1.8
4	10 – 80	$1.9e^{-3} - 1.51e^{-2}$	1.5 – 1.74
6	15 – 80	$1.9e^{-3} - 1e^{-2}$	1.52 – 1.78
8	20 – 80	$1.9e^{-3} - 7.5e^{-3}$	1.47 – 1.76

Table II. 2 Air injection conditions. Q_g is the volume rate of gas, Q_l is the volume rate of liquid, P is the injection pressure

Figure II. 6 shows the air volumetric fraction of the operating points as a function of the reference velocity. The operating points (U_{ref}, Q_g) have been chosen, in order to have same volumetric fraction for different reference velocities in the tunnel.

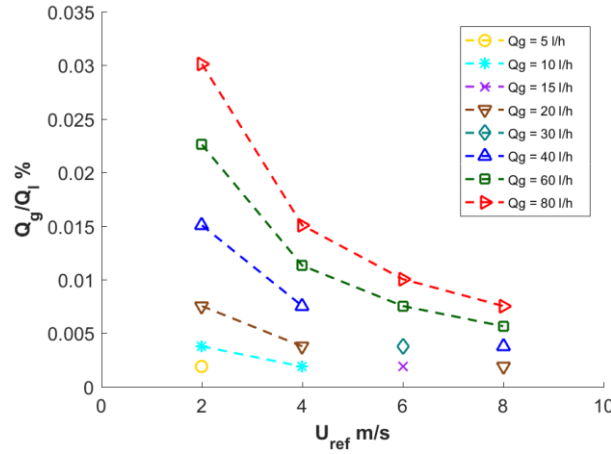


Figure II. 6 Evolution of gas flow rate Q_g , normalized by the liquid flow rate Q_l , with respect to reference velocity U_{ref} .

The injection pushing system which enables the seeding of the flow with particles generates a jet at the wall, this can modify the downstream flow structure. The influence of the induced jet has been evaluated for the single phase flow over the obstacle. For the purpose, tap water was used to promote the jet. PIV was performed both under condition with jet and without jet at each reference velocity.

Integral parameters for the single phase flow with and without jet were determined and the obtained relative differences are summarized in Table II. 3.

U_{ref} [m/s]		C [--]	B [--]	C_f [--]	u^* [m/s]	δ_* [mm]	θ [mm]	H [--]	Δ [mm]	G [--]	Re_θ [--]	Ue [m/s]
2	diff %	11.67	-9.92	4.59	2.65	7.18	6.77	0.39	4.80	-0.77	7.16	11.67
4	diff %	17.47	-10.01	4.69	3.10	0.70	1.06	-0.35	-1.58	-3.46	1.83	0.76
6	diff %	-28.38	29.41	-10.98	-5.47	-0.99	-0.75	-0.24	4.93	5.01	-0.56	0.19
8	diff %	31.41	32.76	-7.40	-4.27	-3.20	-1.48	-1.75	0.59	-2.48	-1.99	-0.52

Table II. 3 Relative difference of Integral parameters at $x = 34.9h$ for the single phase flow over the obstacle with and without jet for seeding particles injection. Relative difference is calculated following (with jet-without jet)/without jet. The relative difference (diff) encounters also for the reproducibility of the measurements.

It is observed from the previous table that there is no systematic drift of the integral parameters due to the jet. Except for the additive constants B and C of the log laws, the jet has a negligible effect on the integral parameters of the flow. This is coherent with the observation made by Bradshaw *et al.* (1971) confirming that the downstream flow is less dependent on the initial boundary layer under strong/overwhelming perturbation. It gives therefore legitimacy to the particle injection for all PTV measurements on single and bubbly phase flows.

2.3 Experimental Techniques

This section describes the different experimental techniques that have been carried out. High frequency *PIV* technique was used for the single phase flow measurements, it is described in 2.3.1. When bubbles were injected, the characterization of the liquid phase-velocity field was achieved by particles tracking velocimetry (*PTV*) applied on seeding particles: the specificities of this measuring technic and processing are discussed in 2.3.2. To top it all, the gas phase (gas fraction, gas phase velocity field, bubble size distribution) was characterized by mean of Shadowgraphy, the corresponding experimental device and processing is described in 2.3.2.2.

2.3.1 High frequency *PIV* measuring system for the characterization of the single phase flow

The total volume of the tunnel was seeded with polyamide seeding particles having mean diameters of $10 \pm 2 \mu\text{m}$ and specific density of 1.03 g/cm^3 .

A *Nd:YLF* high-frequency laser with output energy of 11.7 mJ/pulse , wavelength of 527 nm , and flash duration of 158.439 ns (first frame), was used to illuminate the flow at 500 Hz . The laser head was located at the bottom of the testing section on a rail guide system performing a linear displacement between stations along the test section. The laser sheet was generated with the use of a plano-convex cylindrical lens and the focal circle lied beneath the obstacle top surface. The flow field was imaged at 500 Hz using a 8-bit $1280 \times 800 \text{ pixel}^2$ *CMOS*-based high-speed camera with $20 \mu\text{m}$ *pixel* size. The camera was fitted with a 50 mm Zeiss Makro Planar lens. The viewing area had dimensions $68 \times 106 \text{ mm}^2$ in the *x* and *y* directions respectively.

A *Dantec*[®] commercial plane dot matrix target was used to identify the scale factor. The target features a planar $100 \times 100 \text{ mm}^2$ grid of dots (1.5 mm in diameter) equally spaced in *x* and *y* directions (spacing of 2.5 mm).

The target was settled at the centre of viewing section *n*^o 11. A 3^{rd} order *XYZ* polynomial imaging model fit was employed in order to identify the correction matrix. The scale factors in *x* and *y* directions corresponded to the coefficients on the 1^{st} order terms of *x* and *y* in the correction matrix and both scale factors were basically identical, which means that the light refraction was isotropic and the extremely low coefficients on higher order terms indicate that the optical distortion was negligible.

The whole optical measuring system was mounted on a 3-axis traverse system which allowed image data capture at the different measuring stations defined in *Figure II. 5* with the desired window size in space.

In order to improve image quality for the following *PIV* procedure, all images were firstly processed using image processing tools of *DynamicStudio 2015c*.

Image spatial pre-processing for *PIV* data is of paramount importance. The change of intensity between image pair frames due to different exposure time, the external light source from the environment, the non-even distribution of laser sheet enlightening, the particle cluster scattering and the systematic camera noise are the main sources of noises introduced during the recording process.

Digital filtering is a trade-off between filter effectiveness and image resolution. Classical method for background noise removal consists of subtracting instantaneous images by one background image with the pixel-per-pixel minimum value among all images. However, due to the global intensity fluctuation of laser sheet, residual background noise can still be found after subtraction. In this study, local background image was generated for each original image by using a combined low-pass filter and the kernel size was the same order as the particle cluster scattering area ($5 \times 5 \text{ pixel}^2$). After background

subtraction, a balancing procedure was applied in the aim of improving global uniformity of the intensity. **Figure II. 7** summarizes the different steps of the image pre-processing. An example of image pre-processing is given in **Figure II. 8**.

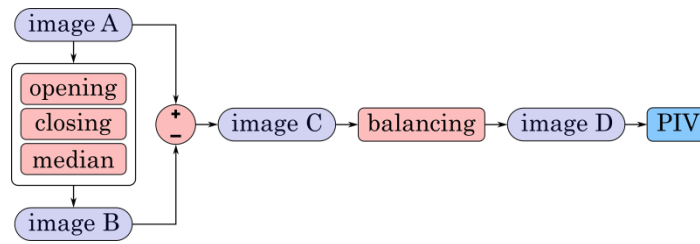


Figure II. 7 Image pre-processing for *PIV* calculation. Image A: original gray scale image, B: instantaneous background image, C: background noise removed particle images with brightness non-uniformity, D: uniform intensity image.

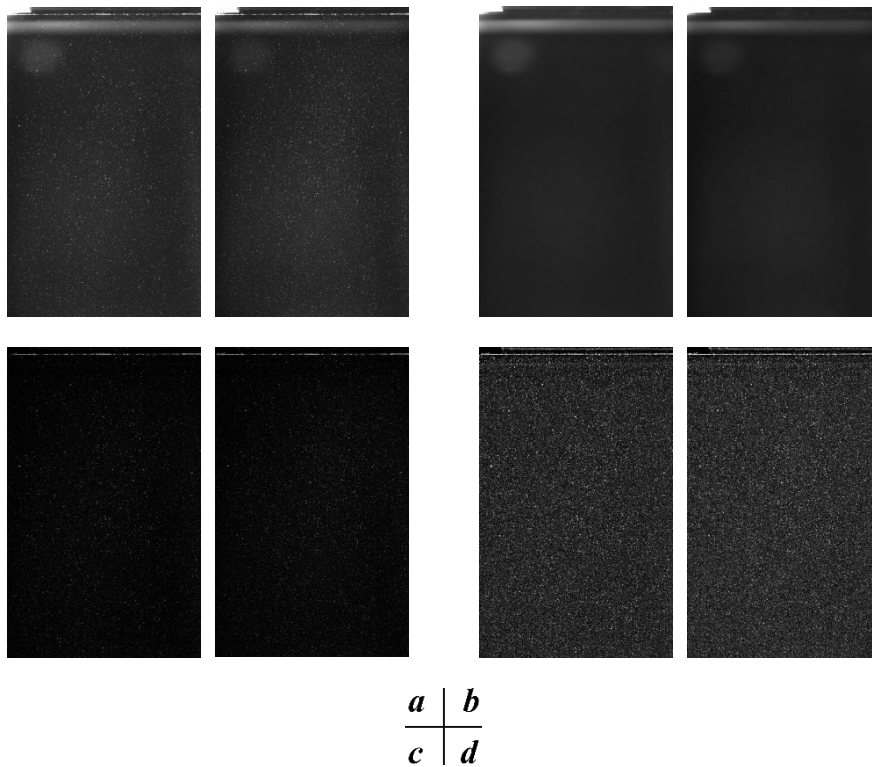


Figure II. 8 Examples of instantaneous image pairs at different steps of the image pre-processing. A: image A, B: image B, C: image C, D: image D

Velocity vectors based on pre-processed particle images were calculated using *Adaptive PIV* method implemented in *DynamicStudio*. The method uses *FFT* cross-correlation algorithm to determine the average particle displacement within an interrogation area (*IA*) and will iteratively adjust the size and shape in order to adapt to flow gradients. The *IA* size was $32 \times 16 \text{ pixel}^2$ with vector spacing interval of $16 \times 4 \text{ pixel}^2$ in *x* and *y* direction, resulting in a stream-wise and wall normal overlapping of 50% by 75%.

The limit values for *IA* shape to velocity gradients adaptation was set to 0.1 for each element in $\left| \frac{\partial U}{\partial x} \right|$, $\left| \frac{\partial U}{\partial y} \right|$, $\left| \frac{\partial V}{\partial x} \right|$, and $\left| \frac{\partial V}{\partial y} \right|$, and 0.2 for $\sqrt{\left| \frac{\partial U}{\partial x} \right|^2 + \left| \frac{\partial U}{\partial y} \right|^2 + \left| \frac{\partial V}{\partial x} \right|^2 + \left| \frac{\partial V}{\partial y} \right|^2}$.

The time between pulses was adjusted to each free stream condition so that the maximum displacement of particles did not exceed one-quarter of the width of IA . A correlation peak height of minimum 0.3 was chosen to validate the velocity vectors.

The universal outlier detection was applied to eliminate spurious vector data. A $5 \times 5 \text{ pixel}^2$ kernel was used with default values (minimum normalization level $\varepsilon = 0.1$, detection threshold $r' = 2$) (Westerweel et al. 2005).

When an IA extends into the wall (Figure II. 9), taking into account all particles in the window would result in the determination of biased velocity. The stream-wise velocity is in general over estimated (Figure II. 9a): the vector on the black dot denotes the “unbiased” velocity at the centre of the IA , while the vector on the blue circle indicates the over-estimated velocity. Wall windowing attempts to minimise this effect by masking the particles far from the wall with reflection symmetry of the wall about the IA centre point, as illustrated by Figure II. 9b. As result, only particles symmetrically distributed around the centre of the IA were taken into account, and the skewness effect was wiped out.

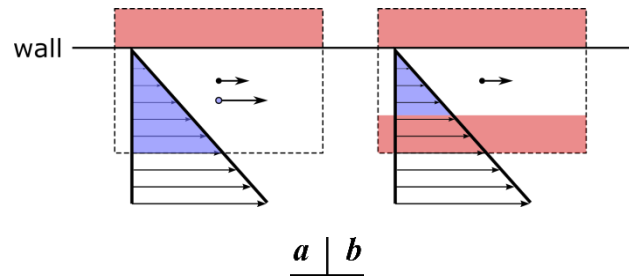


Figure II. 9 Near-wall velocity estimation without (a) and with (b) wall windowing correction. The red areas indicate the masked zone where particles are rejected. Accordingly, the blue triangles display the near wall velocity range considered

The accurate measurement of wall-normal distance of particles is crucial for velocity determination of turbulent shear flow, especially for velocity vectors near wall. When the planar laser light sheet was projected perpendicular to the smooth wall, both near-wall particles within the limits of the light sheet thickness and their reflections in the wall were captured, resulting a local mirror symmetric pattern. The wall position was then determined by finding the axis of symmetry (Figure II. 10a). However, all particles and their reflections were not evenly distributed across the axis, due to the non-zero thickness of the light sheet (Figure II. 10b). Consequently, only very bright particles were taken into account. With this method, there exists a shift in wall location due to the optical distortion in the upper wall made of acrylic glass. This shift seems to be systematic and equals 0.3452 mm upward the apparent wall location. It was adjusted based on the log law of the stream-wise velocity profiles with regard to inner variables.

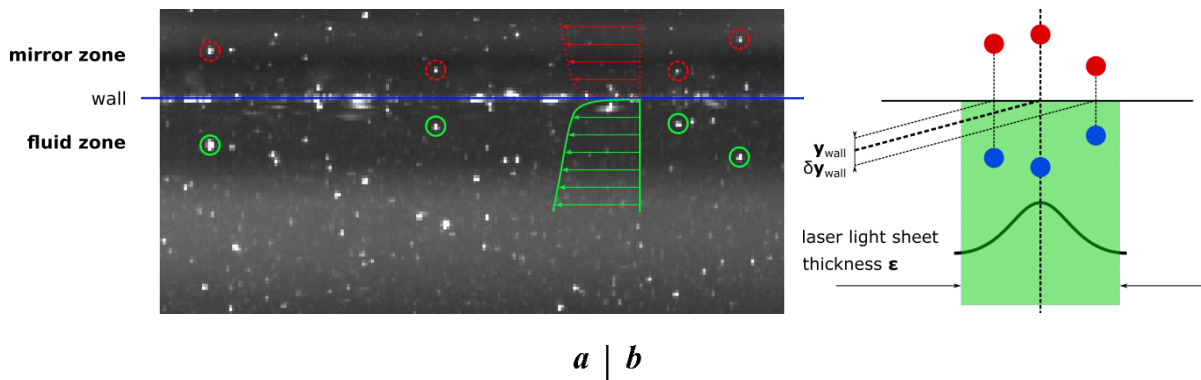


Figure II. 10 A): wall position determination. Bright particles near wall (green) and their mirror reflection image (red), B): wall position uncertainty $\delta y_{wall} = \pm 30 \mu m$

Table II. 4 summarizes the characteristics of the optical system, PIV analysis. It also resumes the random uncertainties due to the system.

Particles	Polyamide $10 \mu m$
Laser wavelength	532 nm
Lens	50 mm
Size of the viewing area (x, y)	$800 \times 1280 \text{ pixel}^2$ $68 \times 106 \text{ mm}^2$ $4.25h \times 6.63h$
Overlap of the measuring section in x direction	0.694 h
Number of measuring sections	11
Sampling rate of the doublets	500 Hz
Time between pulses (μs)	$413/U_{ref}$
Scale factor $\mu m/pixel$	85.3 $\mu m/pixel$
Final size of the PIV IA (x, y)	$32 \times 16 \text{ pixel}^2$ $0.171h \times 0.085 h$
Overlap of IA in x direction	16 pixels 0.085 h
Overlap of IA in y direction	4 pixels 0.021 h
Sub-pixel uncertainty of particles displacement in the IA δx	16.1 μm
Sub-pixel uncertainty of particles displacement in the IA δy	16.1 μm

Table II. 4 Summary of the characteristics of the high frequency PIV measuring system (IA means interrogation area)

The specific statistical analysis procedure applied to the PIV instantaneous velocity fields will be described in Chapter 3, with all the results of the PIV analysis of the single phase flow downward the obstacle.

2.3.2 PTV measuring system for the characterization of the liquid phase in the two-phase flow

In the two-phase flow, the 2 components of the velocity field of the liquid (u, v) were characterized in the vertical (x, y) plane aligned along the symmetry axis of the tunnel. The viewing area was 107.9 mm wide and 107.9 mm high and centered at $x/h = 36.2$, which overlaps the 11th section of high frequency PIV measurements.

A Phlox[®] white LED backlight array was used to supply a continuous and uniform light source aiming to enhance the bubble shadow edge. The effective illumination area was 100 mm by 100 mm. A Nd – YAG laser of 65 mJ at 532 nm, was used to illuminate the flow at 8 Hz. The laser head was located at the bottom of the testing section. A sketch of the PTV measuring setup is displayed in Figure II. 11.

It was needed to provide a rather high seeding density in order to ensure a good quality of the PTV results. Another important thing is that we don't want to catch the scattered light from the bubbles (green light). The flow was therefore seeded with fluorescent seeding particles in suspension in tap water by the injection pushing system. The seeding particles are 20 μm in mean diameter, they consist of polyamide particles with rhodamine encapsulated, made by EPF. (Müller et al. 2014)

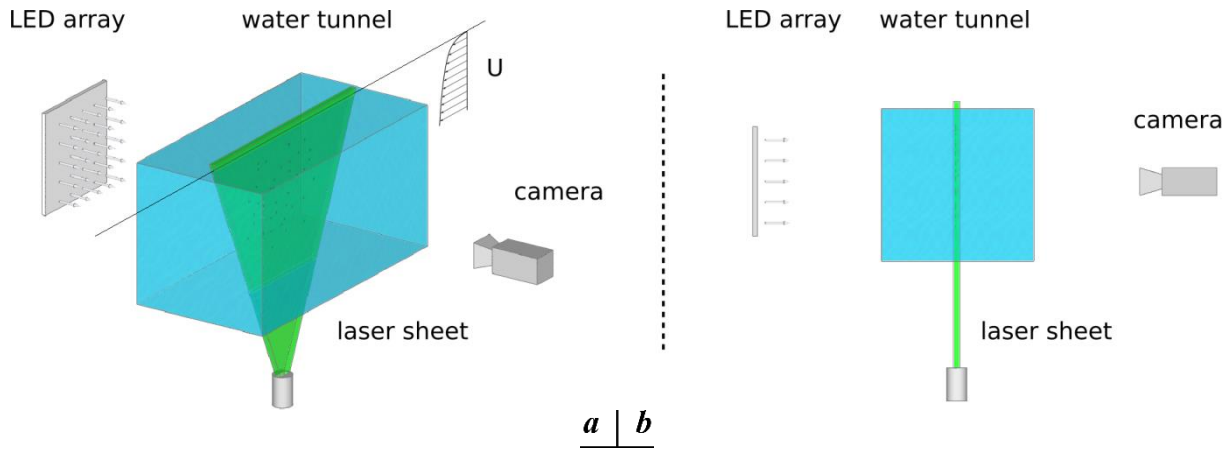


Figure II. 11 Schematic of the measurement setup for PTV characterization of the liquid phase in the two-phase flow.

The images of the bubbly flow were acquired by a CCD camera *Imperx B2020*[®] with a $7.4 \mu\text{m}$ pixel pitch that allowed acquiring a pair of images with a resolution of 2048 by 2048 pixels and a gray scale depth of 12 bit at a sampling frequency of 8 Hz. A 50 mm *Zeiss Makro Planar*[®] lens was mounted at the front of the camera. An optical filter (cutoff wavelength 570 nm) was mounted at the front of the lens and used to transmit the laser light scattered by the fluorescent seeding particles and cut the light transmitted by the bubbles. **Figure II. 12a** shows a typical image obtained in the bubbly flow. Bubbles shadows correspond to dark areas, while particles scattered light appears as small shiny areas superimposed on the background imposed by the LED backlight. The background image (**Figure II. 12b**) was subtracted to the original image, leading to a better contrast of the images (**Figure II. 12c**).

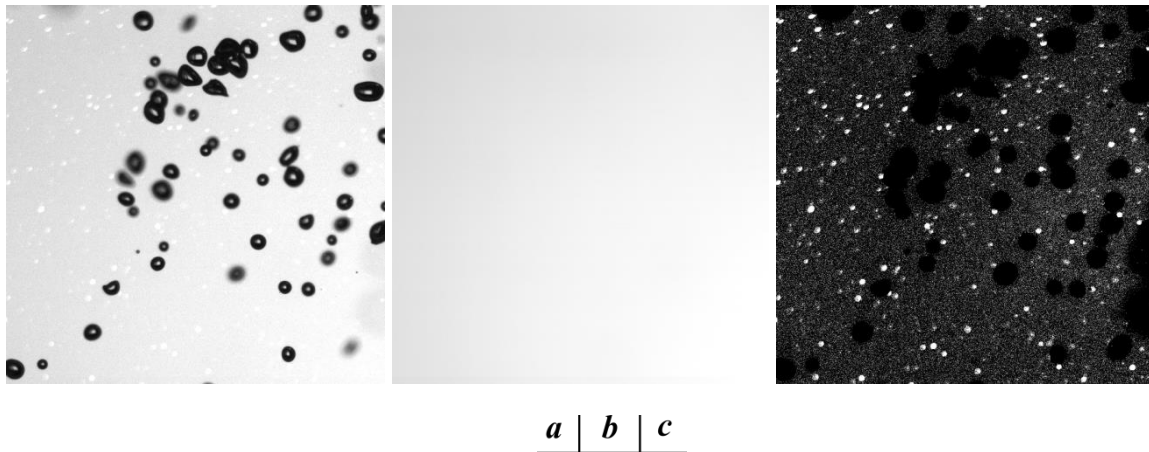


Figure II. 12 Image pre-processing steps on bubble image. a: Original bubbles and fluorescent particles image, b: background image, c: particle image after background subtraction.

The time delay between pulses was chosen in such a way that the maximum displacement of a particle on image is in the order of 10 pixels, it varies therefore from $207 \mu\text{s}$ to $51 \mu\text{s}$, depending on the reference velocity.

Table II. 5 summarizes the characteristics of the optical device for the PTV characterization of the liquid phase. For the single phase flow, the number of image pairs (*) is in average 1600 to ensure statistical convergence of the mean and rms values of the 2 velocity components. For the bubbly flow, particles superimposed on bubble shadows were removed from the statistical analysis. Thus, the

number of image pairs increases with the void fraction: it increases as the gas flow rate increases and as the velocity decreases, it varies between 1800 and 7000.

Camera serie	Pixel size (μm)	Focal length (mm)	Aperture	Viewing area (mm^2)
Imperx® B2020	7.4	50	$f2$	107.9×107.9
Viewing area ($pixel^2$)	Scale factor ($mm/pixel$)	Time delay between frames (μs)	Sampling frequency (Hz)	Number of images
2048×2048	0.0531	$413/U_{ref}$	8	1600 *

Table II. 5 Measuring conditions

2.3.2.1 Particle Mask Correlation (PMC)

PMC (particle mask correlation) was used to identify the centroid coordinates of each particle (Takehara et al., 1998). The method is based on the assumption that the intensity of light scattered by a particle resembles a 2d Gaussian distribution. By calculating the cross-correlation of a 2d Gaussian distribution and an image subzone, the centre of a particle can be identified and positioned once the cross-correlation coefficient exceeds a certain threshold.

The two-dimensional Gaussian distribution is expressed as follows:

$$T(x, y) = e^{\left(-\frac{(x-x_0)^2+(y-y_0)^2}{2\sigma_{particle}^2}\right)} \quad 2 - 1$$

Where $\sigma_{particle}$ denotes the standard deviation, x_0 and y_0 the particle pattern centre's coordinates.

The normalized cross-correlation method is implemented within *OpenCV* and is expressed as follows:

$$R(x, y) = \frac{\sum_{x',y'} (T(x',y') - I(x+x',y+y'))^2}{\sqrt{\sum_{x',y'} T(x',y')^2 \cdot \sum_{x',y'} I(x+x',y+y')^2}} \quad 2 - 2$$

Where $T(x, y)$ represents the template image, here $T(x, y)$ means the 2D Gaussian distribution. $I(x, y)$ represents the source image. The cross-correlation value $R(x, y)$ depends on the value of x, y and σ and varies between 0 and 1.

It is obvious that a particle with an intensity distribution close to a 2D Gaussian distribution of the same size will give a rather high cross-correlation while a “random-like” particle pattern will result in a relatively low cross-correlation, the same happens with two closely-located particles, in other words, the method is strongly sensitive to the parameter σ, Cr and Cc to be chosen, where Cr is the particle mask window size and Cc is the threshold value for cross-correlation.

A set of typical particle patterns (Figure II. 13) were gathered to help finding the most effective parameters in order to extract particles with various forms. The optimal parameters employed in the current study are given in Table II. 6.

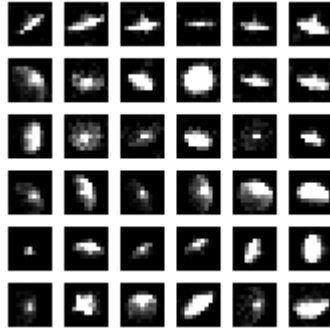


Figure II. 13 Samples of typical particle patterns with different forms and scattering intensities

	Frame 1	Frame 2
particle mask window size Cr (pixel)	7	7
$\sigma_{particle}$ (pixel)	0.91	0.91
Cross-correlation threshold Cc	0.715	0.695

Table II. 6 Optimal parameters for PMC method

An example of the particle masking procedure is shown in **Figure II. 14**. The advantage of this method is that even very dark particles can also be identified as long as their brightness pattern has a 2d Gaussian distribution form. It can be seen by the naked eye that the correlation map (**Figure II. 14a**) had well preserved the coordinate information of most tracer particles with different levels of brightness (**Figure II. 14b**). The on-pixel-accuracy position of particles was found at each local brightness peak on the correlation map (**Figure II. 14c**).

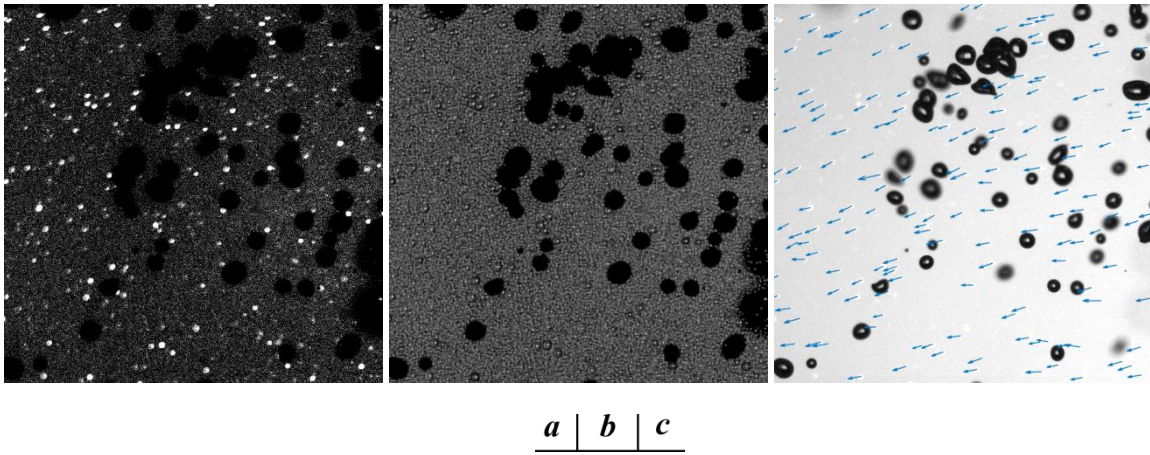


Figure II. 14 Particle identification using PMC method. A: particle image after background subtraction, B: cross-correlation map, C: particle centroids and velocity vectors map superimposed on original image

Once a particle had been identified and the maximum of its cross-correlation had been localized at pixel (x, y) , a linear two-dimensional interpolation was performed in order to obtain the particle's centroid positions with sub-pixel accuracy.

$$\Delta x = \frac{R_{x+1,y-1} + R_{x+1,y} + R_{x+1,y+1} - R_{x-1,y-1} - R_{x-1,y} - R_{x-1,y-1}}{R_{x+1,y-1} + R_{x+1,y} + R_{x+1,y+1} + R_{x-1,y-1} + R_{x-1,y} + R_{x-1,y-1}} \quad 2 - 3$$

$$\Delta y = \frac{R_{x-1,y+1} + R_{x,y+1} + R_{x+1,y+1} - R_{x-1,y-1} - R_{x,y-1} - R_{x+1,y-1}}{R_{x-1,y+1} + R_{x,y+1} + R_{x+1,y+1} + R_{x-1,y-1} + R_{x,y-1} + R_{x+1,y-1}} \quad 2 - 4$$

Where $R_{x,y}$ is the normalised cross-correlation coefficient and Δx and Δy are the sub-pixel corrections from position (x, y) .

The maximum random errors related to the sub-pixel correction are given in **Table II. 7**.

Image scale factor ($\mu\text{m}/\text{pixel}$)	53
Sub-pixel random error Δx (μm)	2.6
Sub-pixel random error Δy (μm)	2.6
Sub-pixel random error $\Delta u/U_{ref}$	1.3%
Sub-pixel random error $\Delta v/U_{ref}$	1.3%

Table II. 7 Random error for the instantaneous flow measurement by PTV (due to sub-pixel resolution)

2.3.2.2 Relaxation PTV method

The relaxation method is a two-frame tracking algorithm firstly proposed by *Barnard and Thompson (1980)* in human movement analysis and was implemented by *Wu and Pairman (1995)* in the framework of fluid mechanics. The most important advantage of the relaxation method comparing to other multi-frame tracking method is that the analysis is based on a particle matching probability that converges within several iterations, resulting in an accurate particle trajectory determination even with high-density particle images. As displayed in **Figure II. 15**, particle positions of two consecutive frames of an image pair are superimposed and are represented with black dots in the first frame and blue ones in the second. The first step is to find and label every possible inter-frame link around the target particle in frame 1. The search is done within a region defined by the radius R_s . R_s can be interpreted as a threshold on the maximum value of the velocity magnitude. As illustrated in **Figure II. 15**, two in-region particles are identified as candidate particles. Based on the hypothesis that particles in a finite volume undergo a quasi-parallel fluid motion, the second step is to preselect first-frame neighbor particles around the target particle within a circle defined by the radius R_n and translate them into new coordinates by a vector defined by the inter-particle link. For the sake of clarity, two different inter-particle links are illustrated in **Figure II. 15** (*a*: first link, *b*: second link).

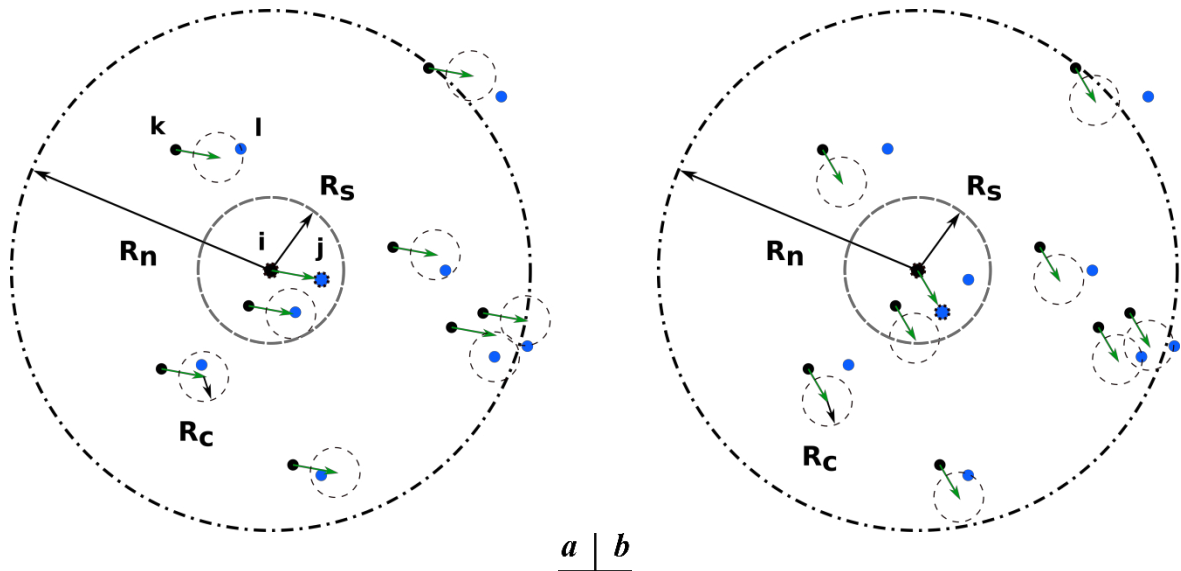


Figure II. 15 Relaxation PTV method on a quasi-parallel motion flow. *a*: 1st candidate particle probability (true), *b*: 2nd candidate particle probability (false)

It is obvious that for a target particle i in frame 1, the match probability with whichever candidate particle j in frame 2 satisfies the following relationship:

$$\sum_j p_{ij} + p_i^* = 1 \quad 2 - 5$$

Where p_{ij} denotes the match probability between particle i and j and p_i^* the no-match probability.

The value of p_{ij} for each candidate particle j is evaluated with respect to the summation of the probability p_{kl} particle detection in neighbor particle circle regions defined by R_c on frame 2. The ratio of R_c to R_n can be understood as a threshold on the velocity gradient. For a given neighbor particle k , if one or more particles l are detected, the probability p_{kl} equals to 1, otherwise 0.

$$\tilde{p}_{ij}^{(n)} = p_{ij}^{(n-1)} (A_p + B_p \sum_k \sum_l p_{kl}^{(n-1)}) \quad 2 - 6$$

The probability p_{ij} is calculated and updated through iteration loop, as indicated in **Eq. 2 – 6**, where A_p and B_p are weighting constants ($A_p = 0.3$ and $B_p = 3.0$ according to *Barnard and Thompson*) and n denotes the iteration step.

In order to satisfy **Eq. 2 – 5**, the updated probability $p_{ij}^{(n)}$ is normalized within each loop, the usual scheme is the following:

$$p_{ij}^{(n)} = \frac{\tilde{p}_{ij}^{(n)}}{\sum_j \tilde{p}_{ij}^{(n)} + p_i^{*(n-1)}} \quad 2 - 7$$

Where the no-match probability $p_i^{*(n)}$ is normalized by:

$$p_i^{*(n)} = \frac{\tilde{p}_i^{*(n-1)}}{\sum_j \tilde{p}_{ij}^{(n)} + p_i^{*(n-1)}} \quad 2 - 8$$

The update and normalization of the match probability are iterated 10 – 20 times before reaching a constant value. As a result, the match probability for the most likely inter-particle link (**Figure II. 15a**) increases almost to unity while the others (**Figure II. 15b**) tend to zero.

The optimal parameters for relaxation *PTV* method are given in **Table II. 8**.

R_s	(pixel)	12
R_c	(pixel)	1.2
R_n	(pixel)	25
$R_s/\delta t/U_{ref}$	(%)	154
Convergence threshold in probability		1×10^{-4}

Table II. 8 Optimal parameters for relaxation *PTV* method

The specific statistical analysis procedure applied to the *PTV* instantaneous velocity fields will be described in **Chapter 4**, with all the results of the *PTV* analysis of the bubbly flow downward the obstacle.

2.3.3 Shadowgraphy measuring system for the characterization of the gas phase in the two-phase flow

Characterization of the gas phase (including measurements of the bubble diameter d_b statistics, time averaged gas phase volume fraction α_v and time averaged gas phase velocity components in a vertical plane U_g, V_g) was achieved using a Shadowgraphy measuring system. It was carried out downward the bubble injection network in the recovery region of the boundary layer at the 11th section where *PTV* characterization of the liquid phase flow was done. The viewing area of the gas phase is centred at $x/h = 35$ with a dimension of $106 \times 106 \text{ mm}^2$. The setup is illustrated in **Figure II. 16**.

The flow was back-illuminated and the bubbles produced shadows. The shadow imaging of the gas bubbles was carried out using a laser-powered *ShadowStrobe* optics by *Dantec*[®]. A *Nd – YAG* laser of

65 mJ at 532 nm was used. The effective diameter of the optic head is 100 mm and the center was positioned at $y = 23.8 \text{ mm}$ from the upper wall, in order to capture the near-wall bubbles. The shadow patterns were recorded on a CCD camera EO4M equipped with a telecentric lens (TC4M-120F). The CCD camera has a $7.4 \mu\text{m pixel}$ pitch that allowed acquiring a pair of images with a resolution of 2048 by 2048 pixel and a gray scale depth of 12 bit at a sampling frequency. The images were recorded at a frequency of 8 Hz, which is identical to that for PTV measurements. The number of image pairs for each gas injection case was 2000, which enabled to process at least $2.7e^5$ bubbles for the flow condition of minimum gas volume fraction. The time between pulses was adjusted, so as to limit the maximum bubbles stream-wise displacement between two consecutive frames in the range [30% – 100%] of the bubble diameter.

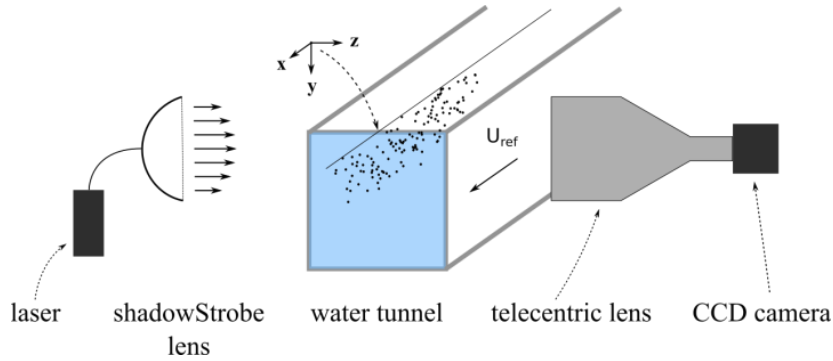


Figure II. 16 Schematic of the measurement setup for Shadowgraphy characterization of the gas phase

Table II. 9 summarizes the characteristics of the optical system of the Shadowgraphy measurements. It also resumes the random uncertainties due to the system (related to bubble size).

Laser wavelength	(back-lighting)	532 nm
Lens		telecentric
Size of the viewing area	(x, y)	2048 × 2048 pixel ² 106 × 106 mm ² 6.63h × 6.63h
Sampling rate of the doublets		8 Hz
Time between pulses Δt_{pulse}	(μs)	413/ U_{ref}
Scale factor ϵ	($\mu\text{m}/\text{pixel}$)	51.8
Uncertainty of instantaneous bubble diameter determination Δd_b (mm)		±0.1
Sub-pixel uncertainty of the instantaneous bubble centre positioning $\Delta x_b, \Delta y_b$		between 6 and 10 μm According to the bubble size
Maximum sub-pixel uncertainty of the instantaneous bubble velocity determination (by tracking method)	$\frac{\Delta u_b}{U_{ref}}, \frac{\Delta v_b}{U_{ref}}$	between 2 and 5% According to the bubble size and reference velocity
pixel uncertainty of the instantaneous bubble velocity determination (by cross correlation method)	$\frac{\Delta u_b}{U_{ref}}, \frac{\Delta v_b}{U_{ref}}$	12%

Table II. 9 Summary of the characteristics of the Shadowgraphy measuring system and random errors due to resolution

The acrylic glass window suffers from an optical distortion in the near-wall regions and could cause a scale factor variation with regard to the wall-normal direction. The scale factor ϵ is considered to be uniquely dependent on y the distance from the wall. In order to determine the scale factor $\epsilon(y)$, a steel rule with 0.5 mm graduation was placed vertically at the center line of the tunnel with its origin at the wall position. A calibration image was acquired.

A program was created in *MATLAB* to identify the graduation line positions in the image, since the line positions were known à-priori to be the distance to the wall, the scale factor function was constructed. (*Figure II. 17*)

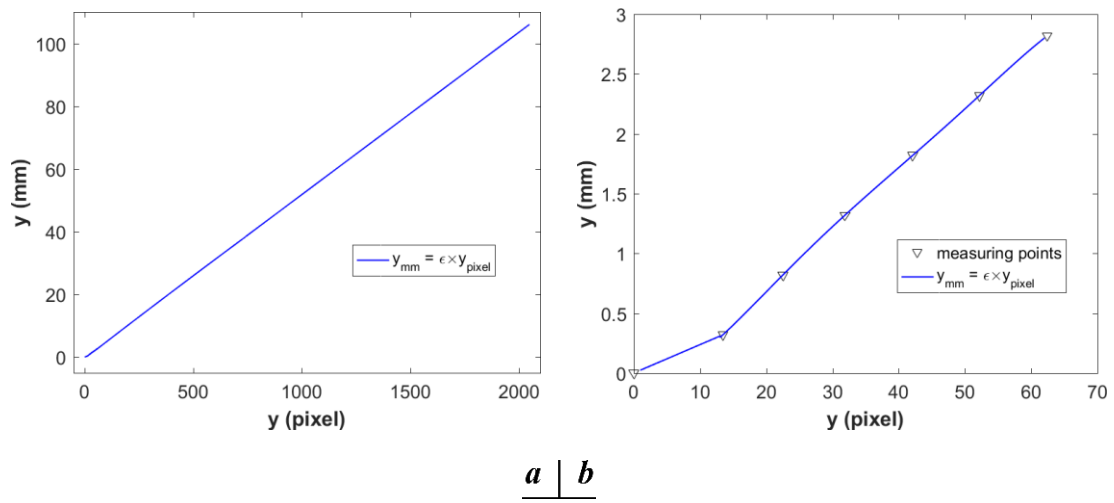


Figure II. 17 Reconstructed pixel-mm conversion with the scale factor ϵ . **A** : whole field. **B** : near wall zoomed-in view

Based on the assumption that the variation of refractive indices in the acrylic glass window is due to a non-uniform stress in the vertical direction from the mechanical assembly, the scale factor function was considered to be stream-wise (x) independent. A transformation mapping matrix was established.

All images were post-processed via a *MATLAB* program. *Figure II. 18* displays a conceptual view of the image processing sequences, dedicated to the gas phase characterization. *Figure II. 21* illustrates the different steps of the processing of an instantaneous image of bubbles shadows.

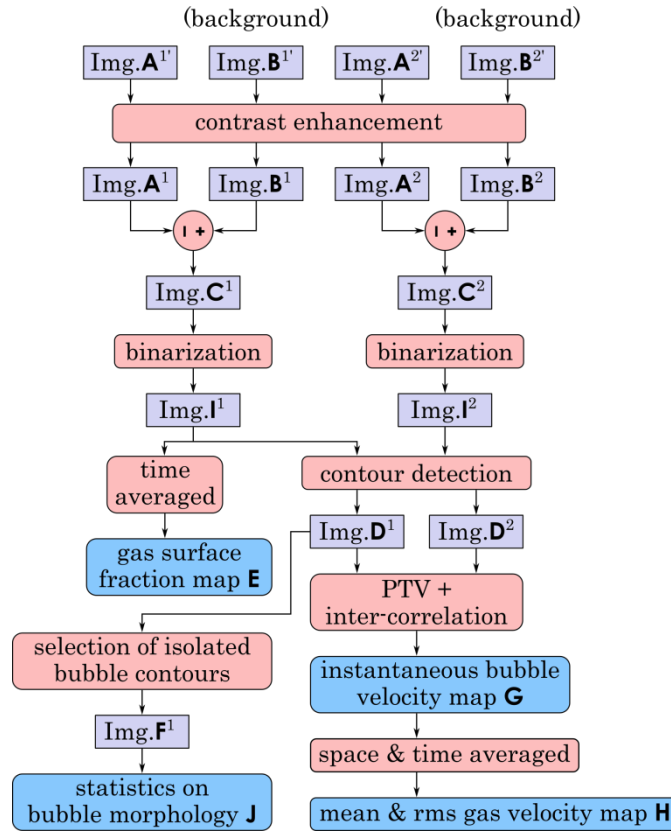


Figure II. 18 Flow chart of the image-processing for the gas phase characterization.

It is of extreme importance to ensure a same intensity level between two consecutive images within an image pair, since the bubble identification was based on an image binarization using a global intensity threshold. A weak contrast at the edge of bubbles or intensity imbalance of a same bubble between two consecutive images could result in a bubble area partial reduction, even a total bubble disappearance; this could introduce considerable measurement uncertainties in gas phase fraction, bubble tracking and geometry statistics determinations.

In our study, both the raw bubble image pairs (*Image A^{1'}, A^{2'}*) and background image pairs (*Image B^{1'}, B^{2'}*) were processed with a contrast enhancement. Bubble images were then subtracted from background images (*Image C¹, C²*). Image binarization was applied with a threshold of 40% of the gray-scale depth for both two frame images. This threshold level made it possible to detect all bubbles within the depth of field of the telecentric lens (86.39 mm) with a good accuracy.

The local gas surface fraction α_s in the vertical plane (example is shown in *Figure II. 21 G, map E*) can be estimated with the temporal average of all binarized images I . T is the measurement time, it yields:

$$\alpha_s(x, y) = \frac{1}{T} \sum_{t=0}^{t=T} I(x, y, t) \quad 2 - 9$$

The local gas volume fraction α_v was approximated based on the local gas surface fraction and the mean bubble diameter $\langle d_b \rangle$, assuming spherical shape of the bubbles:

$$\alpha_v(x, y) = \frac{2 \langle d_b \rangle}{3 DOF} \alpha_s(x, y) \quad 2 - 10$$

All bubbles' contours were detected on binarized images. To calculate the statistics of the bubbles' sizes, the overlapping bubbles were removed from the binarized bubble images, leaving only convex bubble contours. For the purpose, only isolated bubbles were selected by applying a threshold on the relative variation of the apparent measured bubble area, compared to its equivalent elliptic area:

$$Thr_{ibs} = \left| \frac{S - \frac{1}{4}\pi a \times b}{\frac{1}{4}\pi a \times b} \right| \quad 2 - 11$$

Where $Thr_{ibs} = 0.1$, S is the measured apparent area of the bubble and a, b are the major and minor axis of the bubble contour. In addition, all bubbles, the contours of which were touching the borders of the viewing area, were removed.

By this way, we obtain the statistical distributions of the 2D projection area, diameter, major and minor axes and eccentricity of isolated bubbles. The equivalent diameter d_b is estimated based on the apparent area, assuming spherical shape. The random uncertainty of the bubble diameter determination is given in the **Table II. 9**. An example of bubble size distribution is given in **Figure II. 19**. For the different operating conditions, the average bubble diameter was ranging from 0.4 to 1.23 mm. The average eccentricity a/b was 1.1, which confirms the quite spherical shape of isolated bubbles.

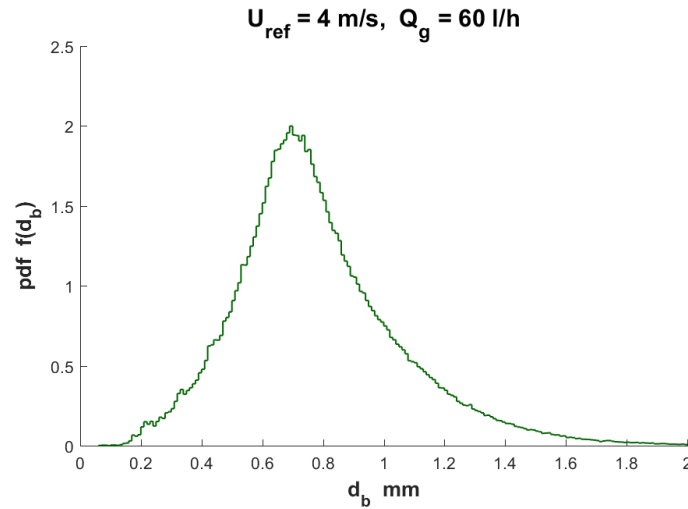


Figure II. 19 Example of bubble equivalent diameter distribution for $U_{ref} = 4 \text{ m/s}, Q_g = 60 \text{ l/h}$

To determine the gas phase velocity, all bubbles detected were used: non elliptic bubbles superimposed in the depth of field, non-elliptic bubbles resulting from clustering near the wall and isolated bubbles. Bubbles with edges touching the borders of the viewing area were removed from the statistical analysis. Once all bubbles' contours were determined on each frame at time t , the center of each bubble was positioned $(x_b^{N(t)}, y_b^{N(t)})$. N denotes the number of the bubble on frame at t . Bubble velocity was calculated with the use of a combination of tracking and cross-correlation methods.

-At first, an inter-frame link was created between bubbles of *frame 1* acquired at time t and bubbles of the next *frame 2* acquired at $t + \Delta t_{pulse}$. For each *frame-1* bubble, we went through the entire list of *frame-2* bubbles and calculated the center-to-center displacement. Two threshold values on the maximum stream-wise and wall-normal displacement were set to be 1.5 and 0.5 times the displacement at the reference velocity ($U_{ref} \times \Delta t_{pulse}$). Since the average displacement of bubbles is of the same order of magnitude than the average bubble radius, no ambiguity could be made about

multiple bubble displacements. Another criterion on the relative area variation of inter-frame linked bubbles was established with a tolerance of 20%. The stream-wise and wall-normal velocities were then calculated based on the center-to-center displacement of two inter-frame linked bubbles $N_1(t)$ and $N_2(t + \Delta t_{pulse})$.

$$u_b^{N_1(t)} = \frac{x_b^{N_2(t+\Delta t_{pulse})} - x_b^{N_1(t)}}{\Delta t_{pulse}} \quad 2 - 12$$

$$v_b^{N_1(t)} = \frac{y_b^{N_2(t+\Delta t_{pulse})} - y_b^{N_1(t)}}{\Delta t_{pulse}} \quad 2 - 13$$

The random uncertainties due to sub-pixel resolution of the visualization system of the bubbles' center localizations and associated bubbles' velocity determination by tracking are given in **Table II. 9**.

For bubbles patterns that had failed to be associated, a cross-correlation was performed locally to estimate the mean displacement of the bubble pattern. Firstly, image of *frame 1* was cropped within a window region covering entirely the bubble pattern with an extension defined by the maximum displacement thresholds, image of *frame 2* was cropped at the same position with the same rectangle dimension. The peak value of the spatial 2D cross-correlation of the two cropped windows gave the most probable displacement of the bubble pattern in the stream-wise and wall normal directions, and thus the most probable velocity components of the pattern.

Bubbles patterns, that could not be inter-frame linked by tracking but were processed by cross-correlation, correspond to bubbles clusters near the wall or bubbles patterns (**Figure II. 20**) which derive from bubble accumulation in the depth of field. Their velocity vectors represent from 7.8% to 16.2% of the vectors of the total velocity field.

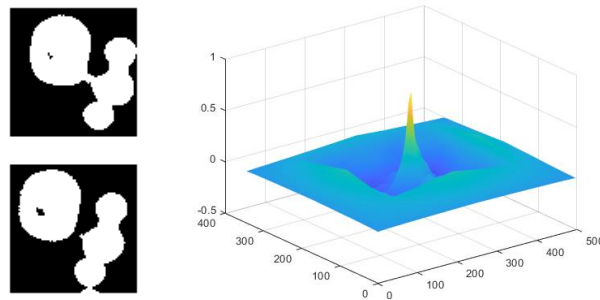


Figure II. 20 Example of bubble pattern that could not be inter-frame linked by tracking. Left up: frame 1 left down: frame 2- Right: spatial 2D cross-correlation of frame1 and 2

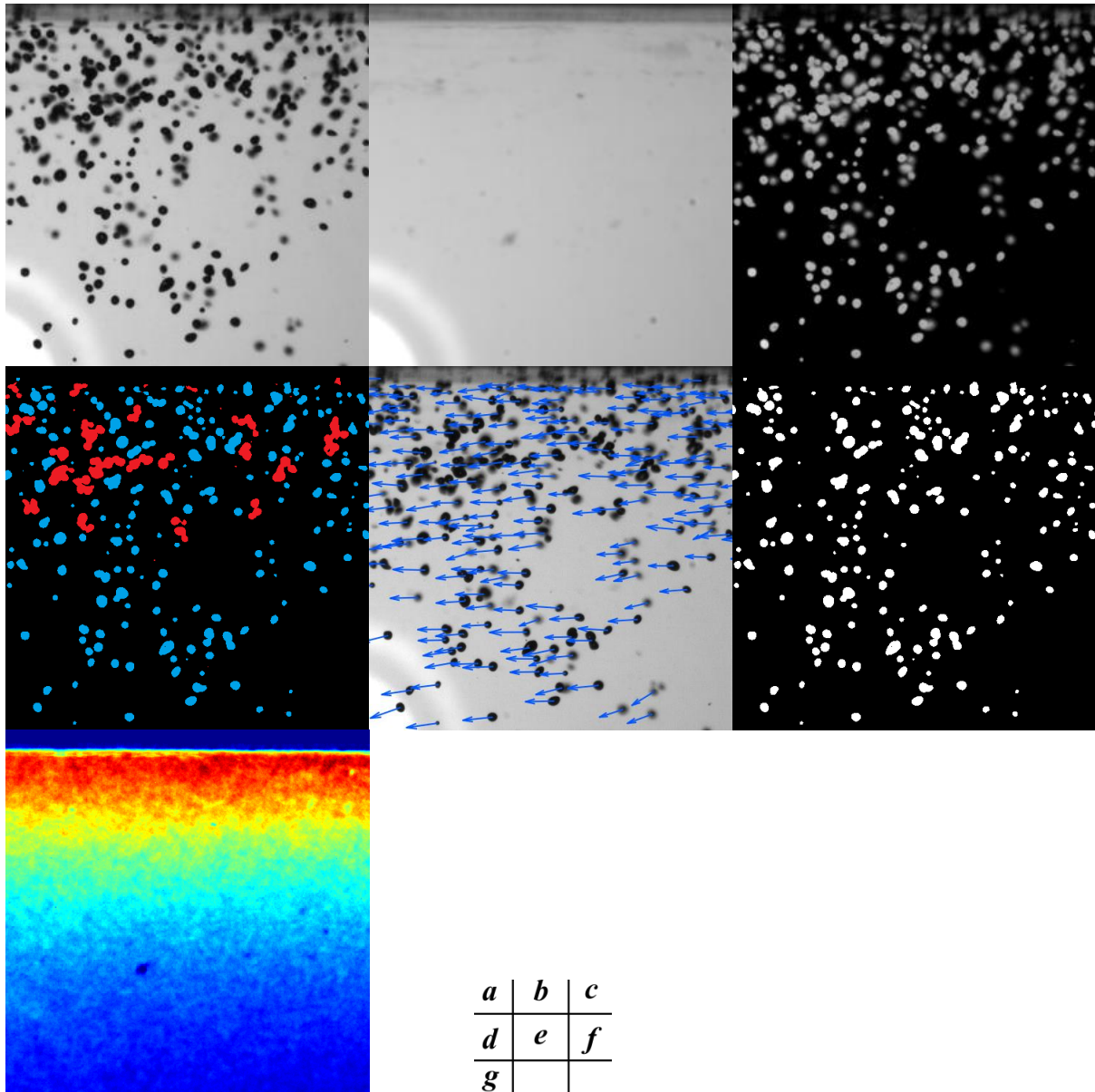


Figure II. 21 Illustration of the different image processing steps applied on instantaneous image of bubbles shadows (zoomed in the near-wall region for reason of clarity) A: contrast adjusted shadow image (*Img. A^I*). B: contrast adjusted background image (*Img. B^I*). C: reverse shadow image after background subtraction (*Img. C^I*). D: Detected gas patterns image (blue: bubbles associated by tracking, red: bubbles characterized by cross correlation) (*Img. I^I*). E: All bubbles centroids and velocity vectors map superimposed on shadow image A (*Map G*). F: Detected isolated bubbles image (*Img. F^I*). G: Time-averaged gas surface fraction map (*Map E*)

The experimental setup was introduced in this chapter, as well as the flow conditions and the use of variety of measurement techniques: high frequency *PIV* for single-phase flow characterization; low frequency *PTV* for the characterization of the liquid-phase flow in the bubbly flow; Shadowgraphy of the bubbles for the characterization of the gas-phase. Random errors associated to the different experimental techniques have been evaluated. Processing leading to the determination of instantaneous flow characteristics has been detailed. The processing for statistical analysis will be further detailed in the chapters that present the results of each experimental method.

3 CHAPTER III. Characterization of the Single Phase Flow Developing Downward the Step

The goal of this chapter is to examine the turbulent boundary layers undergoing adverse pressure gradient in the single phase flow over the 2D square obstacle. High frequency *PIV* measurements were carried out in 11 sections from the obstacle location ($x/h = -1.6$) to the recovery region's location ($x/h = 34.9$)

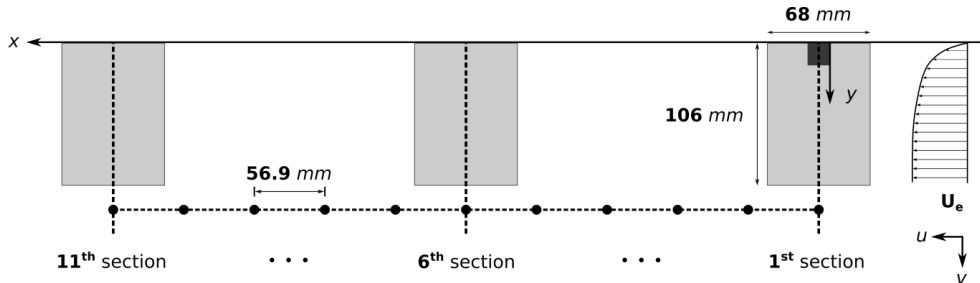


Figure III. 1 Schematic diagram of the measurement sections sequence along the tunnel for the *PIV* characterization of the single phase flow

Section 3.1 describes the data analysis procedures. It also summarizes the uncertainties on the determination of mean and *rms* velocities, integral parameters and log law deduced values. Uncertainties due to measuring system and tunnel wall positions were taken into account. Method for recirculation length calculation and vortex traveling frequency determination were also covered in the section. In **section 3.2**, the development of the single phase flow was examined both qualitatively and quantitatively. Mean velocity profiles, *Reynolds* stress profiles and overall fields are illustrated and analyzed in this section. The universality of the log law of the mean stream-wise velocity profiles is also discussed in this section, both for inner and outer variables. The frequency characteristic of the travelling vortices downstream the obstacle is presented.

At last, the stream-wise evolution of the integral parameters is discussed in this section in comparison to boundary layer in equilibrium in *Clauser's* (1954) investigations.

3.1 Analysis procedures

3.1.1 Time-Averaging

A total of 7000 image-doublets were accounted for the statistical analysis. It represents 14 s of measurement time. Vectors that had been identified as invalid were excluded. The vector validation rate was 94.35% in our study. A standard averaging procedure is applied among all the valid vectors in each *IA* of the *PIV* to determinate the local mean and *rms* values of the stream-wise velocity *u* and wall normal velocity *v*.

Random uncertainties of the mean and *rms* velocity components, induced by the sub-pixel resolution of the *PIV* system are given in **Table III. 1**. *U* and *V* denote mean values and U_{rms} and V_{rms} are the *rms* values of *u* and *v* components respectively. As a reminder, U_{ref} is the required velocity set-point, which is very close to the external velocity U_e , achieved far upstream the obstacle, in the test section.

Sub-pixel resolution of the <i>PIV</i> system (μm)		16
Random error $\Delta U/U_{ref}$	(%)	$\pm 6.73 \times 10^{-2}$
Random error $\Delta V/U_{ref}$	(%)	$\pm 6.73 \times 10^{-2}$
Random error $\Delta U_{rms}/U_{ref}$	(%)	0.75

Random error	$\Delta V_{rms}/U_{ref}$	(%)	± 0.72
Random error	$\Delta(-\overline{u'v'})/U_{ref}^2$	(%)	± 0.21
Random error	$\Delta U_e/U_{ref}$	(%)	$\pm 7.61 \times 10^{-3}$
Random error	$\Delta \frac{dP_e}{dx} / \frac{dP_e}{dx}$	(%)	$\pm 1.79 \times 10^{-2}$

Table III. 1 Uncertainties of the local mean and rms velocity components induced by the sub-pixel resolution of the PIV measuring system (errors are considered as random errors, same errors are encountered for different reference velocities U_{ref})

For a given measurement section at x , the mean external velocity $U_e(x)$ was obtained by taking into account the contribution of the local mean stream-wise velocity measured at several points, far from the wall, where the velocity is estimated to be converged (i.e.: no velocity gradient in the y direction is noticeable). The random uncertainty on U_e determination and $\frac{dP_e}{dx} = -\rho U_e \frac{dU_e}{dx}$ determination, due to the sub-pixel resolution, is also given in **Table III. 1**.

3.1.1.1 Integral length of the boundary layer

Integration in the y direction of the mean stream-wise velocity profiles $U(y)$ makes it possible to determine the classical integral length scales of the boundary layer $\delta^* \theta H$ at different x locations. For the purpose of the study, we define new integral length scales δ_3 and δ_4 , which characterize the turbulence intensities in the stream-wise and wall normal directions respectively:

$$\delta_3 = \int_0^\delta \frac{\langle u' \rangle^2}{U_e^2} dy \quad 3 - 1$$

$$\delta_4 = \int_0^\delta \frac{\langle v' \rangle^2}{U_e^2} dy \quad 3 - 2$$

The uncertainties of $\delta^* \theta \delta_3 \delta_4$ and H linked to the sub-pixel resolution of the PIV system, are given in **Table III. 2**.

	2 m/s	4 m/s	6 m/s	8 m/s
Random error $\Delta\delta^*/\delta^*$ (%)	$\pm 5.95 \times 10^{-2}$	$\pm 6.83 \times 10^{-2}$	$\pm 7.66 \times 10^{-2}$	$\pm 8.23 \times 10^{-2}$
Random error $\Delta\theta/\theta$ (%)	$\pm 7.56 \times 10^{-2}$	$\pm 8.67 \times 10^{-2}$	$\pm 9.70 \times 10^{-2}$	$\pm 1.04 \times 10^{-1}$
Random error $\Delta H/H$ (%)	$\pm 1.35 \times 10^{-1}$	$\pm 1.55 \times 10^{-1}$	$\pm 1.74 \times 10^{-1}$	$\pm 1.86 \times 10^{-1}$
Random error $\Delta\delta_3/\delta_3$ (%)	$\pm 6.45 \times 10^{-4}$	$\pm 8.44 \times 10^{-4}$	$\pm 7.90 \times 10^{-4}$	$\pm 8.66 \times 10^{-4}$
Random error $\Delta\delta_4/\delta_4$ (%)	$\pm 8.56 \times 10^{-4}$	$\pm 1.13 \times 10^{-3}$	$\pm 1.06 \times 10^{-3}$	$\pm 1.13 \times 10^{-3}$

Table III. 2 Uncertainties for the integral scales determination, induced by the sub-pixel resolution of the PIV measuring system (errors are considered as random errors and characterized here in the measurement section $n^\circ 11$)

3.1.1.2 Wall friction coefficient and Clauser parameters

The best estimate of the friction velocity can be obtained by achieving the linear law of the stream-wise velocity profile in the viscous sub-layer (**Eq. 1 – 15**). However, it is impossible to measure the near-wall velocity with the actual PIV resolution. The difficulty lies also in the fact that the ratio of U^+ and y^+ variation no longer equals to 1 when a strong stream-wise pressure gradient takes place (*Etheridge et al. 1978*).

An alternative approach consists in using—the universal logarithmic law of the mean stream-wise velocity profile versus inner variables (**Eq. 1 – 16**). We decided to attempt determining the friction velocity u_* with a linear regression of the semi-logarithmic plot of the stream-wise velocity profiles $U^+ = f(\ln y^+)$ in a y range corresponding to $10^{-3} < \frac{y}{\Delta} < 10^{-2}$, depending on the stream-wise position and the reference velocity.

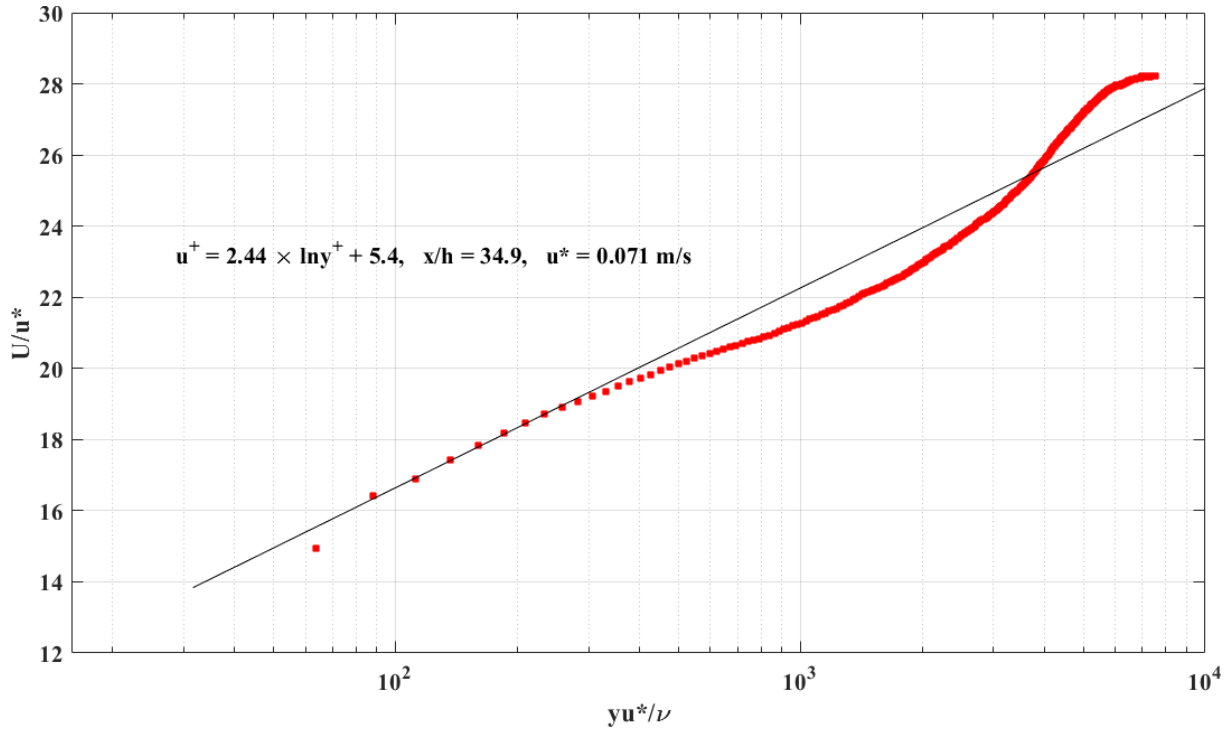


Figure III. 2 Example of friction velocity fit based on the semi-logarithmic plot of the mean stream-wise velocity profile versus inner variables ($U_{ref} = 2 \text{ m/s}$, $u^* = 0.071 \text{ m/s}$, $x/h = 34.9$)

The in-range data were processed by using the method of least squares. That process of solving for the slope and intercept for the best fit line is to calculate the sum of squared error between the line and the data and then minimize that value. The slope of the linear regression is identified as $1/\kappa$, with $\kappa = 0.41$. The additive constant B of the logarithmic law is identified as the offset of the linear regression. An example of the linear regression is shown in **Figure III. 2**.

With this value of the friction velocity imposed, the additive constant C of the logarithmic law versus outer variables (**Eq. 1 – 23**) is identified as the offset of the linear fit of the profile $\frac{U-U_e}{u_*} = g(\ln \frac{y}{\Delta})$.

We are very sensitive to the location of the wall. For *PIV* measurements based on green diffused light, the uncertainty on the wall position is $\pm 30 \mu\text{m}$, it induces an uncertainty on the determination of the friction velocity and uncertainties on the determination of the additive constants of both logarithmic laws B and C .

Uncertainties expected for u_* B C C_f are given in **Table III. 3**. The induced uncertainties on the determination of the integral parameters G Δ and β are also resumed in this table.

	2 m/s	4 m/s	6 m/s	8 m/s
$\frac{\Delta u_*}{u_*}$ (%)	1.27	1.27	1.26	1.62
$\frac{\Delta B}{B}$ (%)	5.39	5.72	6.17	7.19
$\frac{\Delta C}{C}$ (%)	3.81	4.49	4.94	10.39
$\frac{\Delta C_f}{C_f}$ (%)	5.07	5.07	5.06	6.47
$\frac{\Delta G}{G}$ (%)	1.48	1.41	1.40	1.63

$\frac{\Delta(\Delta)}{(\Delta)}$ (%)	20.74	24.01	22.98	30.07
$\frac{\Delta(\beta)}{(\beta)}$ (%)	7.91	2.24	1.04	0.84

Table III. 3 Uncertainties on u^* B C C_f G Δ and β (absolute value induced by the sub-pixel resolution of the PIV measuring system and wall position uncertainty) characterized here in measurement section $n^\circ 11$, at $x/h = 34.9$

From now on, all graphics displayed in the next sections will show error bars, due to time convergence of the statistical analysis for a confidence level of 95%.

3.1.1.3 Recirculation length

The estimates of the recirculation length L_R was established by finding the stream-wise position where the mean stream-wise velocity near the wall changed its sign. An example is given in **Figure III. 3**. It is noted that in the immediate vicinity of the wall ($y \cong 1 \text{ mm}$), the steam-wise velocity evolves linearly in the stream-wise direction. A linear trend plot was used to give the estimated position.

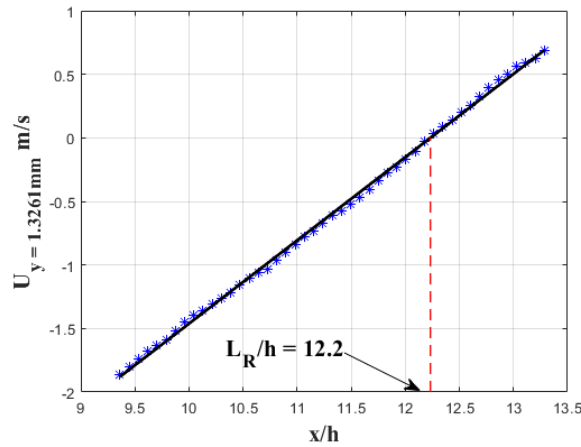


Figure III. 3 Example of linear trend estimation of reattachment point by stream-wise evolution of the mean stream-wise velocity near wall ($y = 1.33 \text{ mm}$) at $U_{ref} = 8 \text{ m/s}$

3.1.2 POD analysis

In a 2D turbulent wake flow, the spatial-temporal interaction of vortices and turbulent boundary layer can bring about complex phenomena. The analysis of the dynamics in such flow is important and requires methods based on modal analysis.

The Proper Orthogonal Decomposition (POD) is a modal decomposition technique that extracts dominant features in space and time based on representing data with an orthogonal basis. It was first introduced to the fluid dynamics by Lumley (1967) as a tool to extract coherent structures from turbulent flow fields.

A velocity vector field $U(\xi, t)$ with its temporal mean $\bar{U}(\xi)$ subtracted represent the fluctuating velocity field can be decomposed in generalised Fourier series on a set of basis functions $\phi_j(\xi, t)$.

$$U(\xi, t) - \bar{U}(\xi) = \sum_{j=1}^{\infty} a_j \phi_j(\xi, t) \quad 3 - 3$$

Where ξ denotes the spatial vector and a_j represent the projection coefficients.

POD technique provides an algorithm to represent the same set of data in terms of a minimal number of basis functions or modes to capture as much energy as possible.

The modern research on *POD* suggests extracting the spatial structure and temporal evolution separately and **Eq. 3 – 3** can be rewritten as

$$U(\xi, t) - \bar{U}(\xi) = \sum_{j=1}^N a_j(t) \phi_j(\xi) \quad 3 - 4$$

Where the projection coefficients a_j become uniquely time dependant and ϕ_j are spatial modes.

3.1.2.1 Spatial (Classical) POD method

The first step is the construction of a spatial-temporal matrix X which contains in each column a transformed ‘snapshot’ of the instantaneous flow field of the fluctuating component of the velocity vector $x(\xi, t) = U(\xi, t) - \bar{U}(\xi)$. The N snapshots are assembled columnwise in a $M \times N$ data matrix where $M = 2 \times N_x \times N_y$.

$$X = [x(\xi, t_1) \ x(\xi, t_2) \ \dots \ x(\xi, t_N)] = \begin{bmatrix} u_{1,1} & \dots & u_{1,N} \\ \vdots & \ddots & \vdots \\ u_{N_x \times N_y, 1} & \dots & u_{N_x \times N_y, N} \\ v_{1,1} & \dots & v_{1,1} \\ \vdots & \ddots & \vdots \\ v_{N_x \times N_y, 1} & \dots & v_{N_x \times N_y, N_t} \end{bmatrix} \quad 3 - 5$$

The goal of the *POD* analysis is to find the optimal basis ϕ_j in **Eq. 3 – 4**. The problem set can be transformed by finding the eigenvectors ϕ_j and the eigenvalues λ_j from

$$R\phi_j = \lambda_j \phi_j \quad 3 - 6$$

Where R is the covariance matrix of $x(\xi, t)$

$$R = \frac{1}{N-1} \sum_{i=1}^N x(\xi, t_i) x^T(\xi, t_i) = \frac{1}{N-1} X X^T \quad 3 - 7$$

The eigenvectors ϕ_j are called the *POD* modes and describe spatial coherent structures of the turbulent flow in our study.

The corresponding eigenvalues λ_j are proportional to the fluctuation kinematic energy associated with the respective *POD* modes and are arranged in the importance in terms of capturing the kinematic energy of the flow field.

3.1.2.2 Snapshots method

It is noted that the spatial vector ξ is of very large dimension M comparing to time steps N , and that makes the data covariance matrix decomposition in **Eq. 3 – 7** very time consuming. *Sirovich (1987)* rather suggested the eigenvalue decomposition on temporal correlation matrix $C = \frac{1}{N-1} X^T X$. This decomposition yields the same dominant spatial modes and non-zero eigenvalues. Since C is a symmetric, positive-semi definite matrix, all eigenvalues are real and positive.

The snapshots method consists in solving the eigenvalue problem of the temporal correlation matrix

$$C\psi_j = \lambda_j \psi_j, \ \psi_j \in \mathbb{R}^N \quad 3 - 8$$

In order to understand the spatial-temporal dynamics of the main coherent flow structures, the modal decomposition analysis in the framework of our study was carried out using *POD* method

implemented in *DynamicStudio*[®]. **Figure III. 4** shows the distribution of the cumulative kinetic energy as a function of the modes, for the different reference flow conditions.

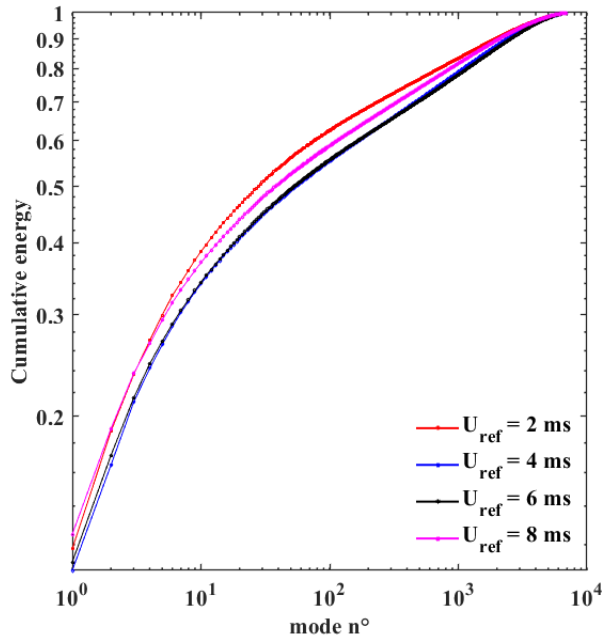
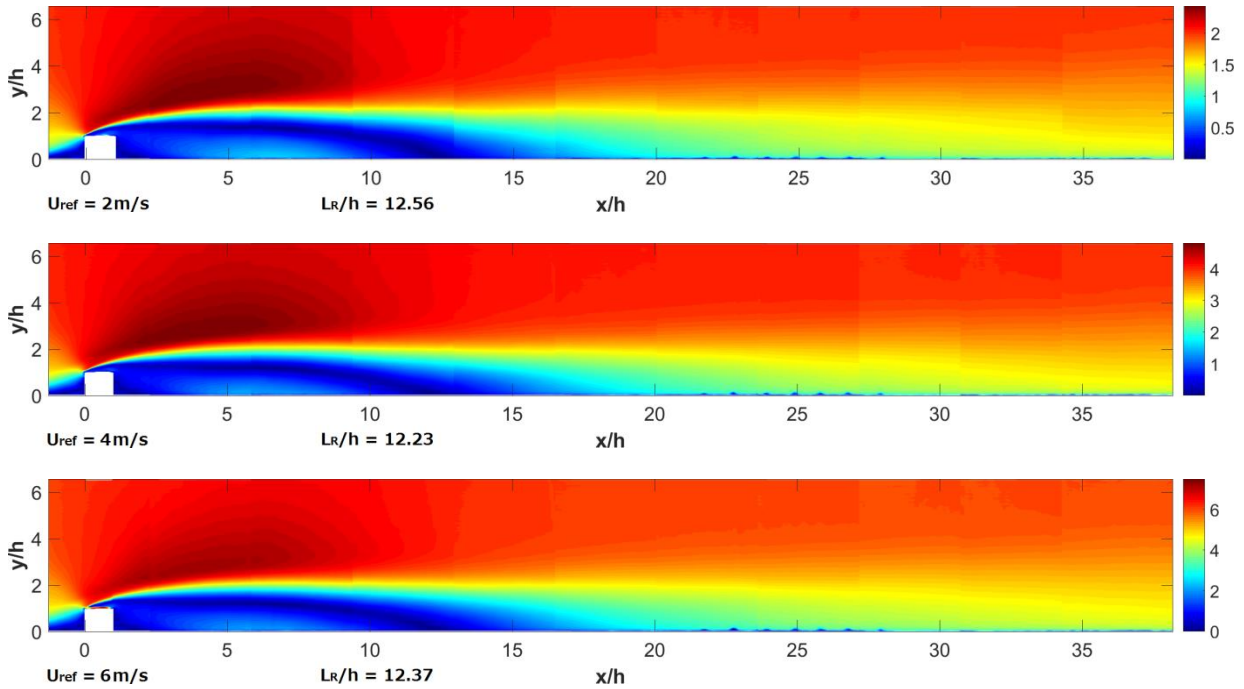


Figure III. 4 Log plot of the cumulative energy contained in all modes (1 – 7000)

3.2 Results. Characteristics of the single phase flow

3.2.1 General features of the mean flow



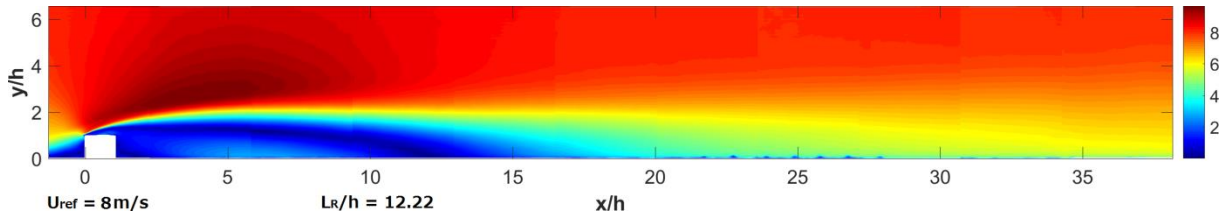


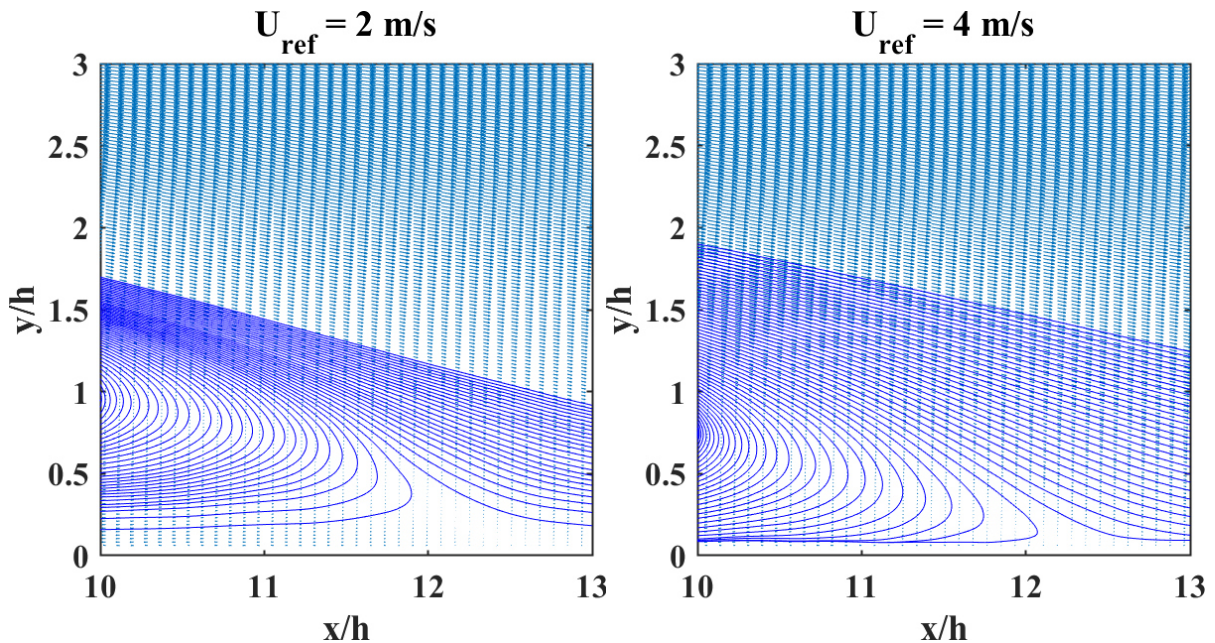
Figure III. 5 Contour plot of mean velocity magnitude: $U_{ref} = 2, 4, 6, 8 \text{ m/s}$

The isovalues contour of mean velocity magnitude obtained for the different flow conditions are shown in **Figure III. 5**.

At the inflow section $x/h = -1.32$, there is a strong deceleration in the flow field near the wall up to the leading edge of the obstacle. Separation of the flow occurs at the tip of the leading edge which gives birth to a new shear layer that borders the reverse-flow region and a new sub-boundary layer appears at the reattachment point (recovery region). In the external flow above the recovery region, the velocity accelerates up to 21% for $U_{ref} = 2 \text{ m/s}$ and 20% for $U_{ref} = 8 \text{ m/s}$ despite the weak blockage ratio $h/H = 0.1$, where H is the tunnel height.

A time-averaged vortex is formed in the wake flow downstream the obstacle. The reattachment of the separated flow on the wall plate occurs from $x/h \approx 12$, where near wall velocity becomes zero. Details will be given in the next section. In the recirculation region, the magnitude of maximum stream-wise reverse velocity was found to be 38.6% and 35% of the reference velocity at 2 m/s and 8 m/s .

In addition to the general investigations of the flow structure, recirculation length for different reference velocities has been measured **Figure III. 6**. The recirculation length was approximately 12 times as large as the obstacle height h , regardless the value of the reference velocity.



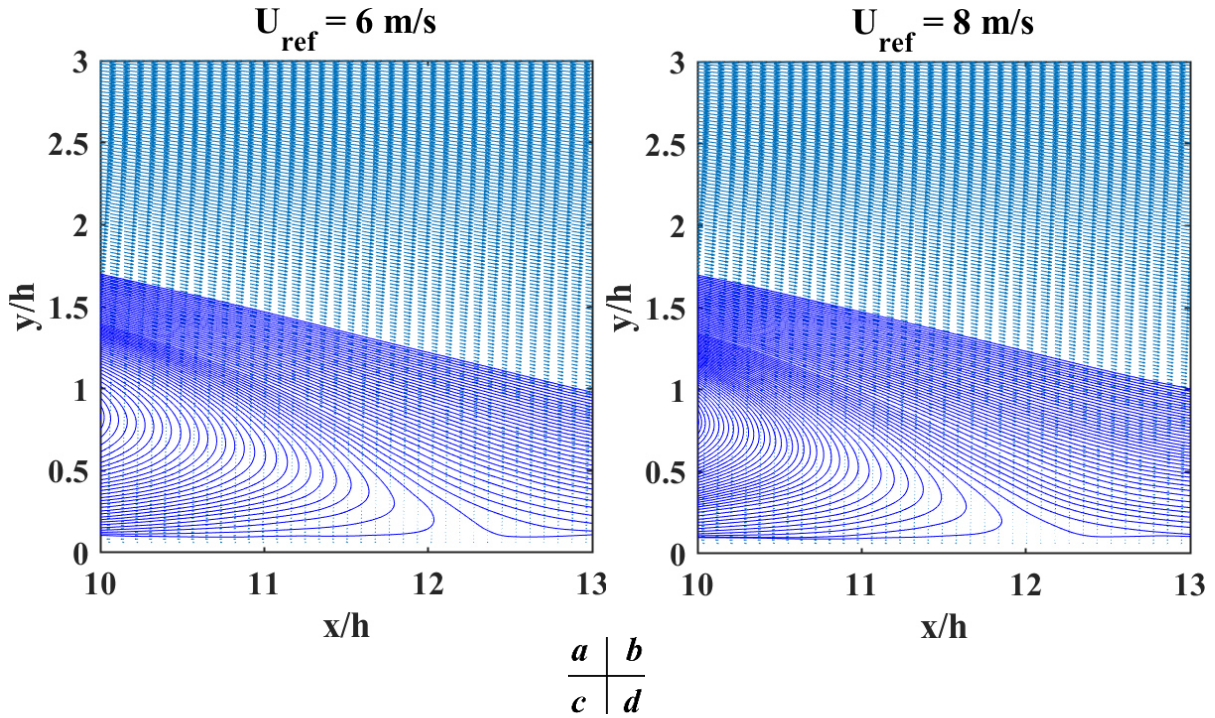


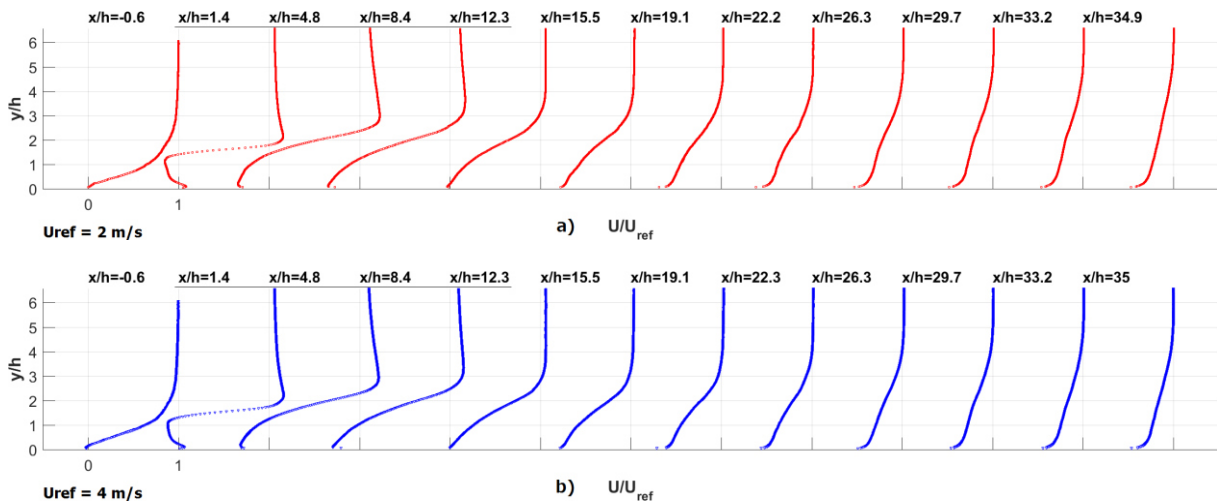
Figure III. 6 Local zoomed view of the streamlines around the reattachment point at $U_{ref} = 2, 4, 6, 8$ m/s.

	2ms	4ms	6ms	8ms
L_R (mm)	206.7 ± 5.66	201.17 ± 5.54	206.83 ± 8.97	200.23 ± 4.71
L_R/h	12.92 ± 0.35	12.57 ± 0.35	12.93 ± 0.56	12.51 ± 0.29

Table III. 4 Recirculation length versus reference velocity

The results were compared with experimental data sources from flow over square obstacle in open circuit wind tunnel (*Bergeles et al. 1983*) which show a similar recirculation length ($L_R/h = 11.5$) for an initial boundary layer δ equal to $0.48 h$, while in *Tillmann's* measurements (*1945*) for a turbulent thick boundary layer ($\delta/h = 3.3$), this length was found to be 12.5 times the obstacle height. It seems that the boundary layer thickness has little influence on recirculation length once the flow is turbulent.

Figure III. 7 and *Figure III. 8* give an overall view of the flow development. 12 stream-wise and wall normal velocity profiles from 11 measuring sections are equidistantly plotted along the stream-wise direction in up-stream, recirculation and recovery regions. Two profiles of the 1st section are illustrated.



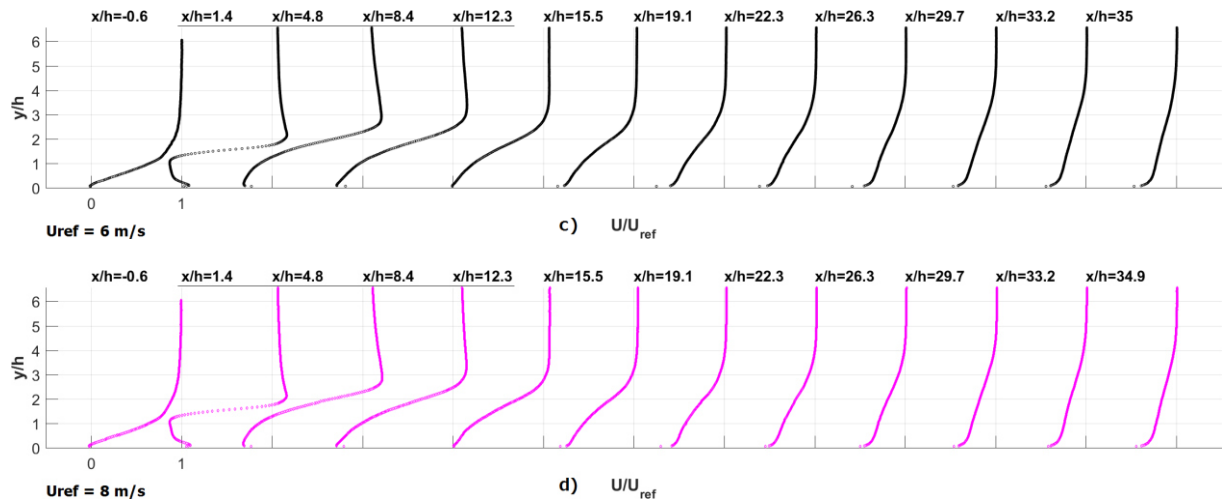


Figure III. 7 Y Profiles of the mean stream-wise velocity normalized by the reference velocity U_{ref} at different stream-wise locations.

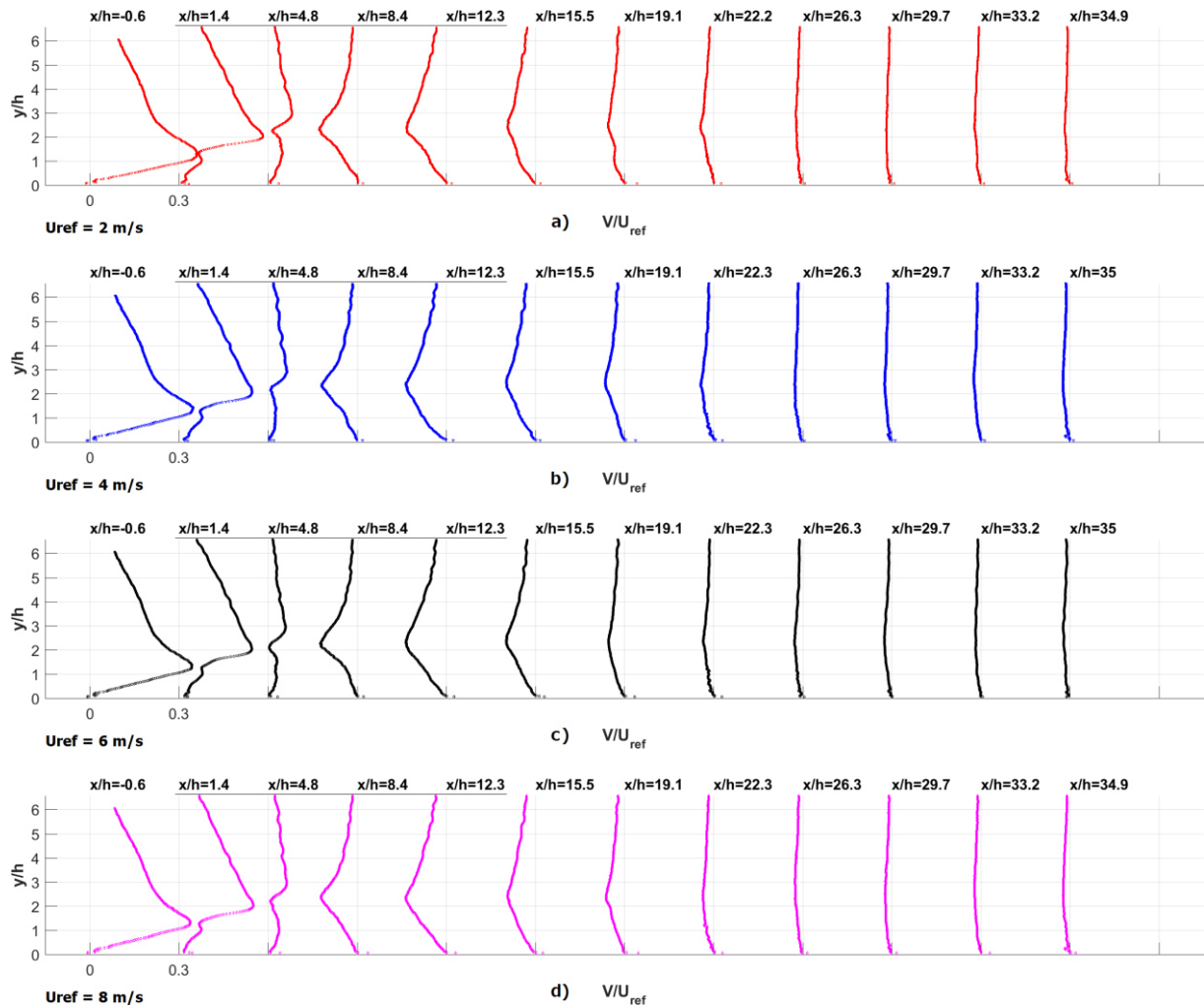


Figure III. 8 Y Profiles of the wall normal mean velocity normalized by the reference velocity U_{ref} at different stream-wise locations.

Firstly it is clear that the wake is evidenced by a deficit of the stream-wise velocity in the recirculating region. In the upstream section of obstacle $x/h = -1.1$, the upstream flow suffers a deceleration in longitudinal direction and distortion by the obstacle and the mean velocity profiles deviate from the

classical ones of flow on flat plate. In the immediate region downstream of the obstacle $x/h = 1.2$, a reverse flow promoted by the time-averaged vortex makes a negative value distribution in longitudinal component of the mean profile. The stream-wise velocity of the reverse flow reaches up to 35% of the reference velocity approximately.

It can also clearly be seen that this “momentum-deficit” region shifts outward from the wall, as x increases.

As can be observed in **Figure III. 7**, the external velocity can be very difficult to estimate at the x positions in the recirculating region, where mean stream-wise velocity fails to recover the external velocity in the visualization area due the boundary layer thickening.

Distribution of the wall-normal component of the mean velocity V (**Figure III. 8**) shows that the classical shear layer assumption that V is small compared to U is no longer valid both in the immediate upstream and in the recirculation regions. In the recirculating region, the magnitude of V can reach up to 20% of the reference velocity, which is the same order as the deficit in the stream-wise velocity. Between section $x/h = 4.8$ and $x/h = 8.4$, the flow over the vortex rushes into the inner region, which results in the reattachment at $x/h \approx 12$.

Figure III. 9 shows the external velocity U_e measured at different downstream stations for the different reference flow conditions. U_e is normalized by the corresponding reference velocity for the sake of comparison. The profiles in the stream-wise direction exhibit the occurrence of an adverse pressure gradient for $x/h > 4.8$. The pressure gradient reaches the maximum near the reattachment point and decreases downstream. The evolution in the stream-wise direction of the external pressure gradient is visible in **Figure III. 13**.

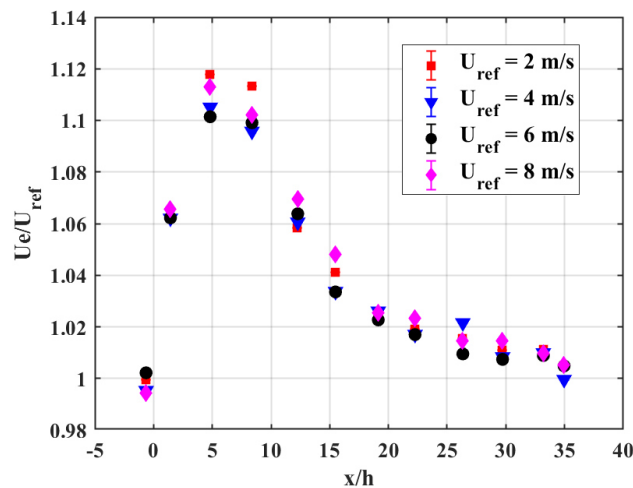


Figure III. 9 External velocity U_e along the stream-wise direction x/h

3.2.2 General features of the fluctuating flow

The isovalue contours of the *Reynolds* shear stress are plotted in **Figure III. 10** for the different flow conditions.

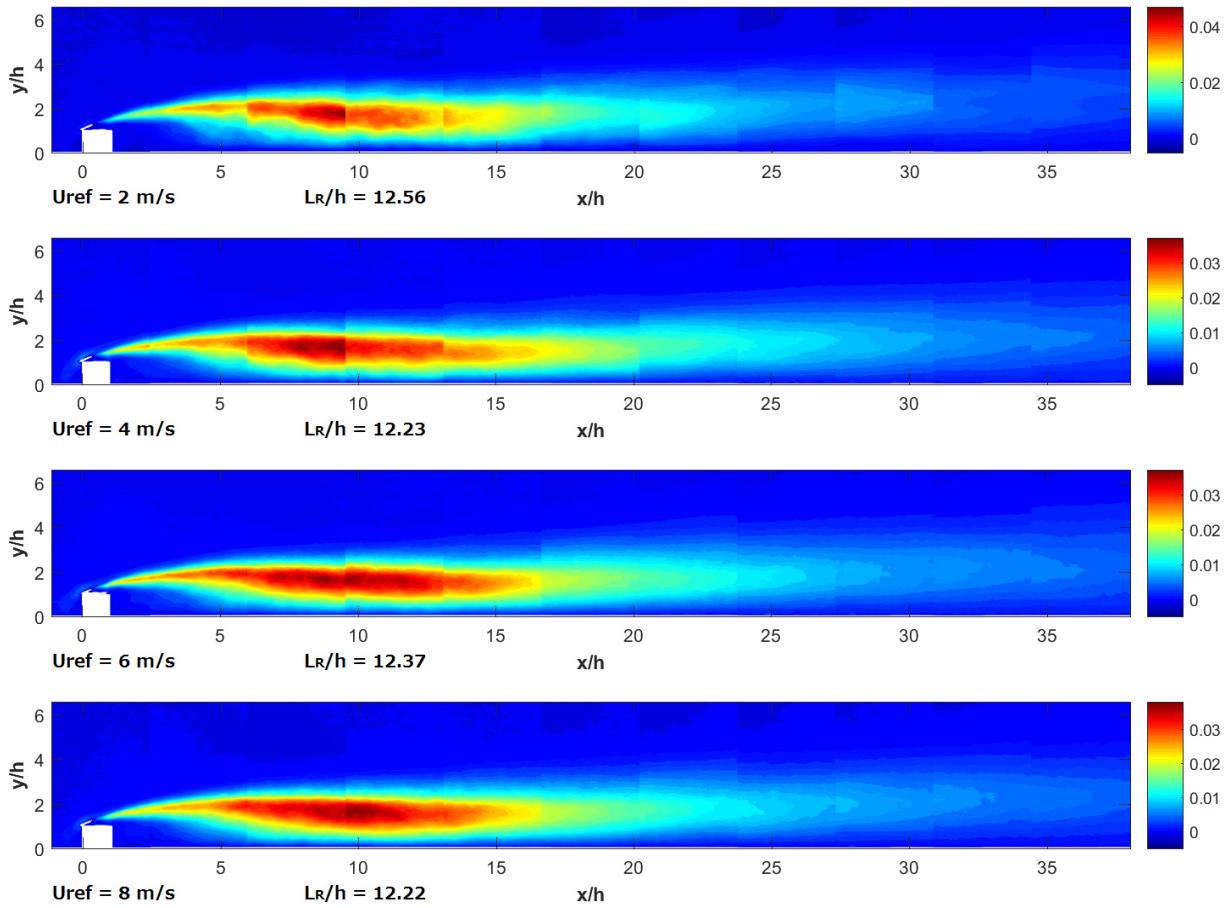
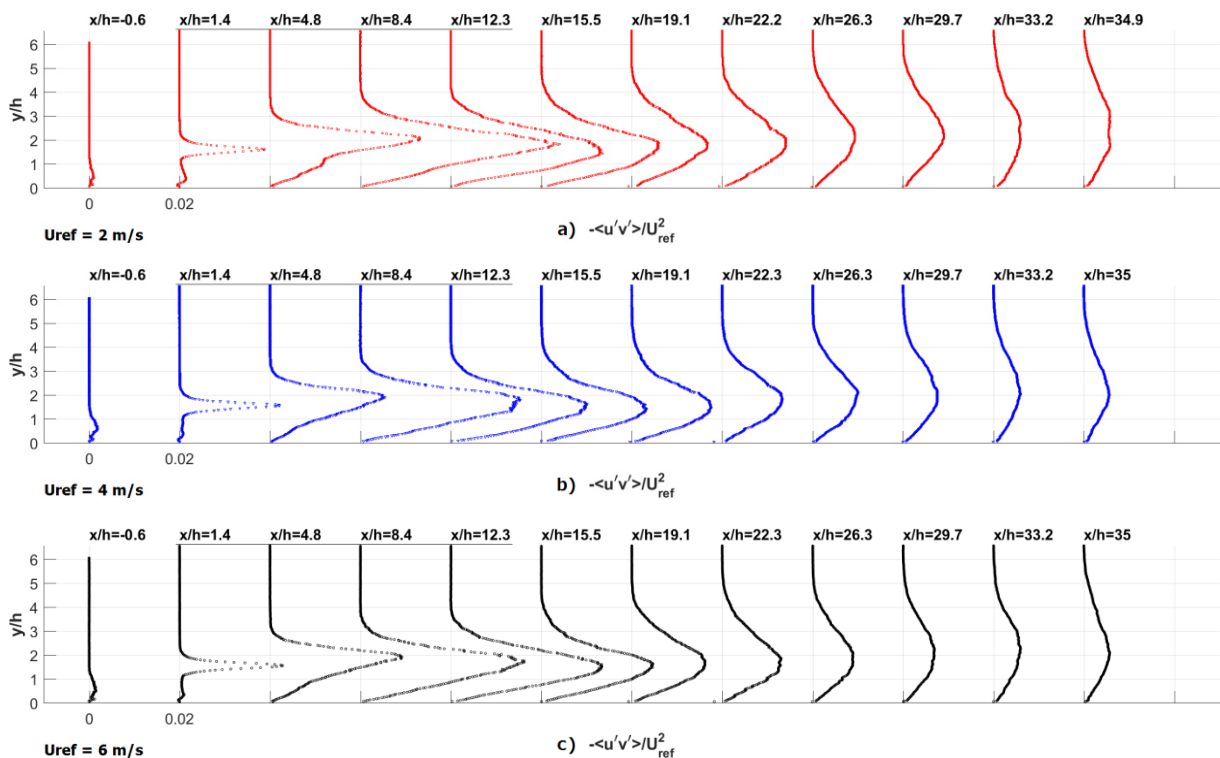


Figure III. 10 Contour plot of the Reynolds shear stress $-\langle u'v' \rangle$, normalized by the reference velocity U_{ref}^2 . $U_{ref} = 2, 4, 6, 8$ m/s

The flow that passes over the tip of the leading edge of the obstacle is strongly perturbed. It results in an extensive production of turbulent shear stress along the dividing streamline for x/h up to 10.



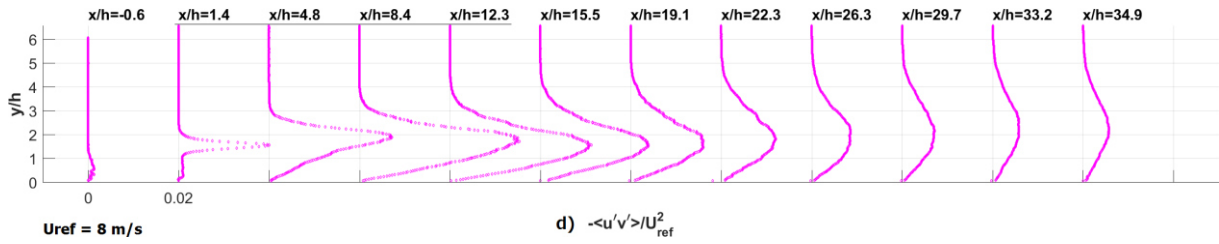


Figure III. 11 Y Profiles of the *Reynolds* shear stress $-\langle u'v' \rangle$ normalized by the reference velocity U_{ref}^2 at different stream wise locations

The profiles of the normalized *Reynolds* shear stress are shown in **Figure III. 11** for the different flow conditions. At $x/h \approx 9$ and $y/h \approx 1.7$, the *Reynolds* shear stress reaches the global maxima values. The global maxima achieved are 4.7% and 3.6% of U_{ref}^2 at $U_{ref} = 2 \text{ m/s}$ and 8 m/s respectively. The results were compared with experimental data sources from flow over square obstacle in open channel. *Agelinchaab et al. (2008)* confirm the global maxima at the same wall-normal location ($y/h \approx 1.7$) but somewhere at $x/h = 2.1$ in the stream-wise location. The maximum value is reported to be smaller in their works (1.7%), but the weak perturbation ($\delta_0/h = 9.3$) induced by the obstacle might be responsible for this discrepancy with our results.

Downstream of the reattachment point in the recovery region, locations of the peak values move away from the wall gradually, the maxima of the *Reynolds* stress decrease and the profile flattens itself as the new sub-shear layer spreads out.

What is also noticeable about the profile shape is that the *Reynolds* shear stress increases almost linearly from somewhere very near the wall all the way up to the peak, downstream the reattachment point. This phenomenon was equally observed by *Agelinchaab (2008)* and *Antoniou & Bergeles (1988)*, in flows downstream square, rectangular, semicircular blocks and prisms mounted at the wall. This is in agreement with what is expected in the inner region of a developing turbulent boundary layer for a stream-wise pressure gradient that doesn't vary in the wall normal direction: $\frac{1}{\rho} \frac{dP_e}{dx} = \frac{\partial}{\partial y} (-\langle u'v' \rangle)$.

An example of linear regression of the *Reynolds* shear stress profiles performed in the inner region is shown in **Figure III. 12**. **Figure III. 13** shows the expansion rate of the *Reynolds* shear stress in the normal direction, measured in the recovery region, for the different flow conditions. Comparison is made with the external pressure gradient $\frac{dP_e}{dx} = -\rho U_e \frac{dU_e}{dx}$ measured in each *PIV* visualization area, at different stream-wise position. There is obviously a discrepancy between $\frac{dP_e}{dx}$ and $-\rho \frac{\partial \langle u'v' \rangle}{\partial y}$. This discrepancy is maximum in the upstream part of the recovery region and decreases downstream. This can be due to different reasons: **1)** the classical assumption of the shear layer which stipulates that different quantities evolve much slower in the x direction than in the y direction is no more valid and **2)** the curvature of the velocity profile $U(y)$ can play a role.

The assumption: $\delta \ll L$ here is questionable in the recovery region. Indeed, $\delta/(x - L_R) \approx 0.2$ at the downstream position $x/h = 35$. Thus the *Prandtl* conservative equations must be corrected, by neglecting δ/L at order 2, instead of order 1 (**Eq. 1 – 8**).

In the inner region, it yields:

$$\frac{dP_e}{dx} + \frac{\partial}{\partial x} (\rho \langle u' \rangle^2) - \frac{\partial}{\partial x} (\rho \langle v' \rangle^2) - \mu \frac{\partial^2 U}{\partial y^2} = \frac{\partial}{\partial y} (-\rho \langle u' v' \rangle) \quad 3 - 9$$

Linearity of the *Reynolds* stress profiles with regard to the normal direction is checked in the inner region where viscous diffusion is negligible by comparison to turbulent diffusion or near the inflection point. It also implies that stream-wise gradients of normal *Reynolds* stress slightly depend on the normal distance from the wall.

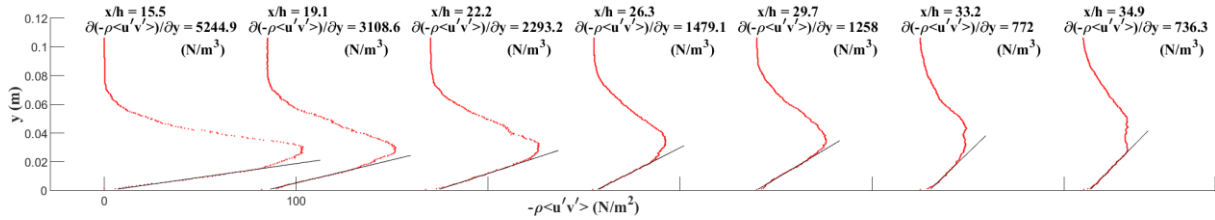


Figure III. 12 Example of linear regression plot on *y* profiles of the *Reynolds* shear stress $-\langle u'v' \rangle$ at $U_{ref} = 2 \text{ m/s}$ in the recovery region stations

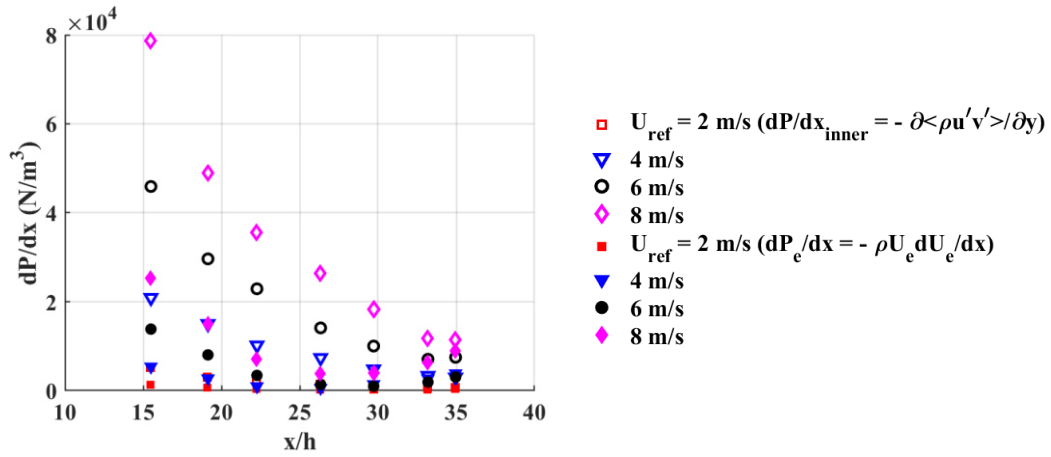


Figure III. 13 Comparison between stream wise pressure gradients achieved in the inner region due to the slope of the *Reynolds* shear stress and achieved in the external flow, as a function of the stream-wise position, for different flow conditions

The profiles of turbulence intensity of stream-wise and wall normal components of the velocity are presented in *Figure III. 14* and *Figure III. 15* respectively. The *rms* velocity components are normalized by the reference velocity.

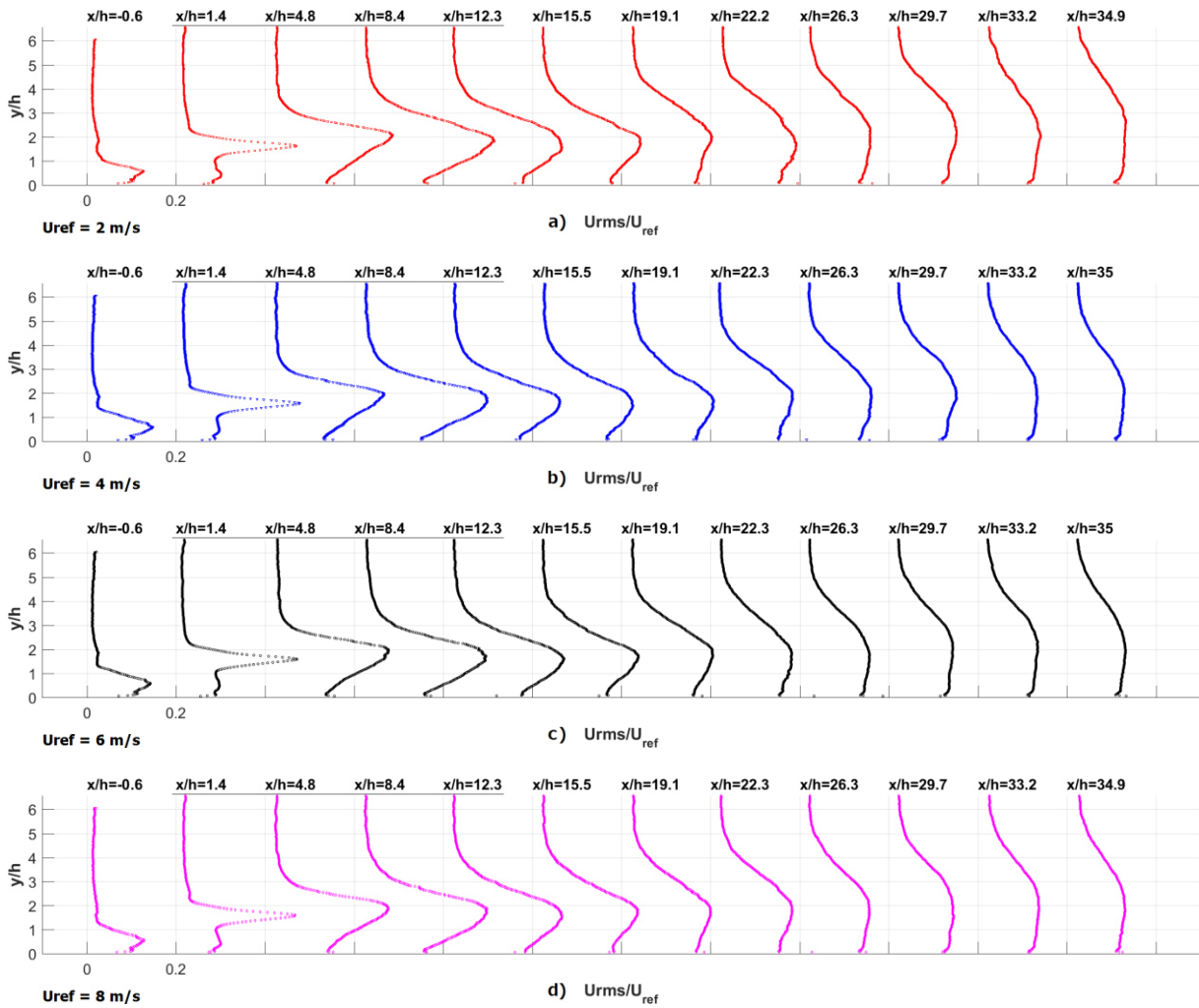
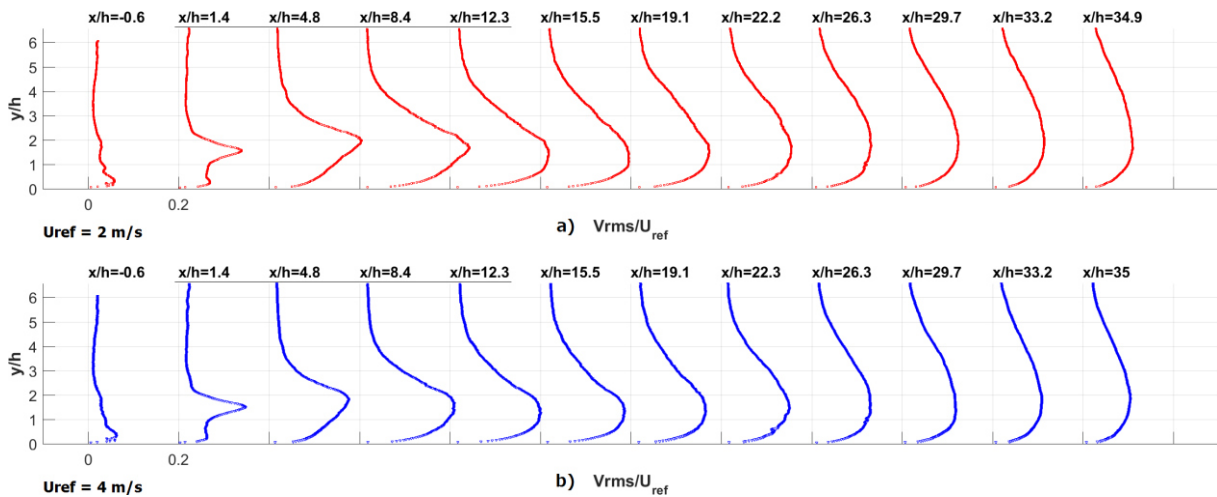


Figure III. 14 Y profiles of the rms velocities in the stream-wise direction normalized by the reference velocity U_{ref} at different stream wise locations.



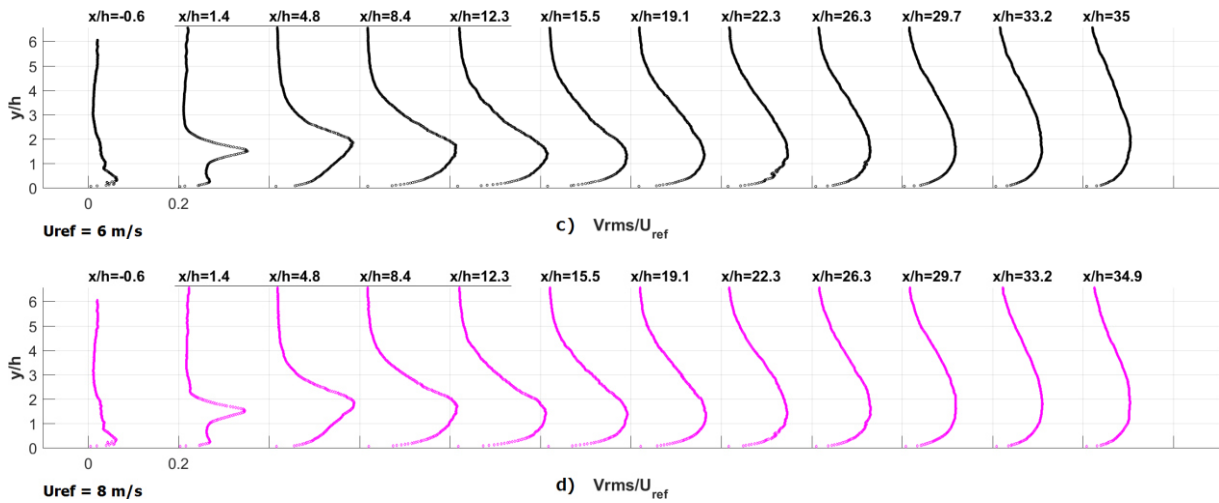


Figure III. 15 Y profiles of the rms velocities in the wall-normal direction normalized by the reference velocity U_{ref} at different stream wise locations.

The external flow depicts a turbulent intensity of about 32% and 25% for U_{rms} and V_{rms} .

As expected for turbulent shear flows, the turbulence is not isotropic in the shear layer: the fluctuating velocity components being larger in the stream-wise direction than in the normal direction.

Same trends are observed for the turbulent intensities profiles than for the *Reynolds* stress profiles. Maxima of U_{rms} are achieved at same distance from the wall than the *Reynolds* stress. The stream-wise turbulent intensity is up to 32% at $x/h \approx 8$, $y/h \approx 1.8$, which is much larger than what is expected in a classical developing boundary layer for zero pressure conditions i.e.: 9% (Cousteix 1989). Agelinchaab (2008) has reported a peak value of 28% at the vortex center location, downstream the square obstacle. In the section downstream, at $x/h = 34.9$, the maximum of stream-wise intensity is 13%, which is a bit larger than expected in a classical developing boundary layer for zero pressure conditions (i.e.: approximately 10%) (Cousteix 1989).

At $x/h \approx 8$, $y/h \approx 1.7$, the wall normal turbulent intensity reaches its maxima, which are 25% and 22% at 2 m/s and 8 m/s respectively. Agelinchaab (2008) has reported a peak value of 18% at the vortex center location. In the section downstream, at $x/h = 36$, the maximum of wall normal intensity is 11%, which is much more important than expected in a classical developing boundary layer for zero pressure conditions (i.e.: approximately 4%) (Cousteix 1989).

3.2.3 validity of the universal logarithmic law

3.2.3.1 Validity of the log law versus the inner variables

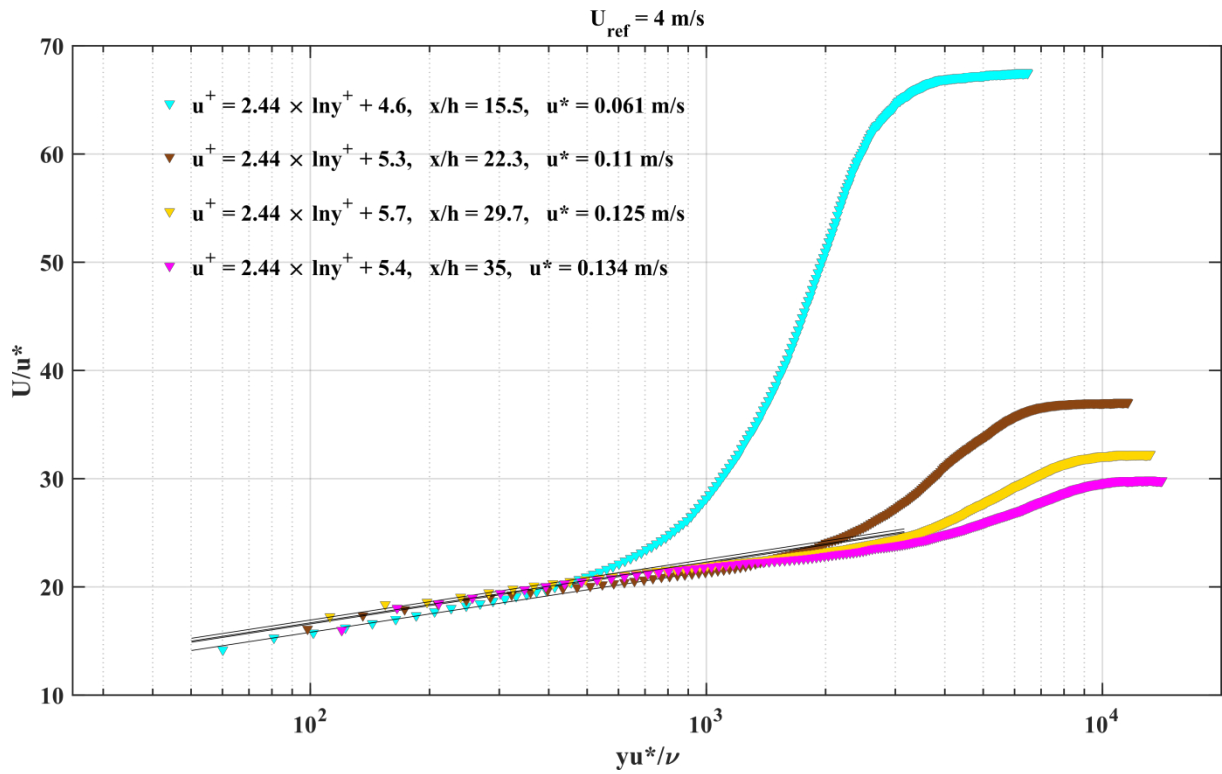
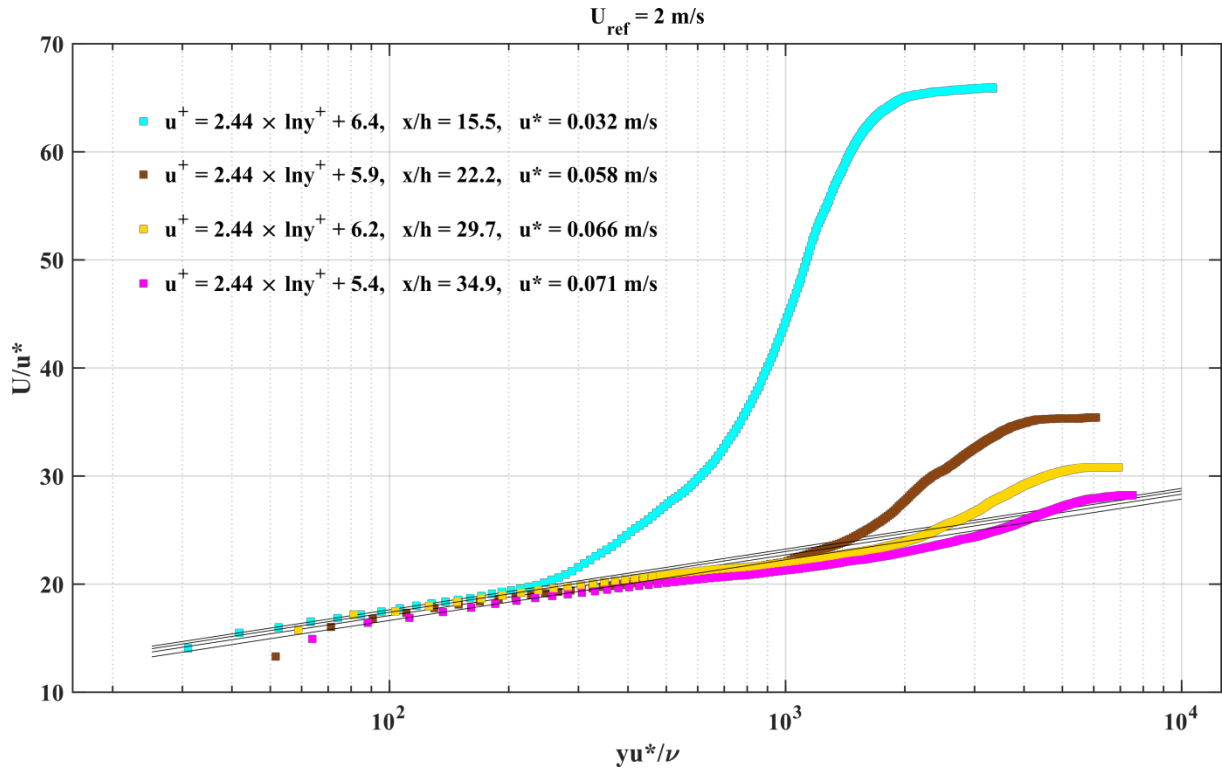
Mean velocity profiles, plotted in semi-logarithmic coordinates, for inner variables, are given in **Figure III. 16**. The figure shows the way in which the profiles of mean velocity gradually recover to the basic boundary layer profiles. For the sake of clarity, profiles at only 4 x/h stations are presented.

The log law seems to be well obeyed throughout the whole recovery region, except for stations very close to the reattachment point, by reason that profiles differ greatly from classical boundary layer shape at the early stage of new sub-layer development.

However, from profiles on $x/h = 29.7$ and $x/h = 34.9$ in **Figure III. 16**, a dip is clearly observed outside the log region. This phenomenon has been discussed in detail by Bradshaw & Wong (1972).

At the last station ($x/h = 34.9$), the profiles collapse onto the logarithmic profile (**Eq. 1 – 16**) with an additive constant B between 5.2 and 5.8.

The y^+ range of validity of the logarithmic law increases downstream with the decrease of the adverse pressure gradient (*Spalart et al. 1987*). This range of y^+ values is obviously extended when the *Reynolds* number is increased with the augmentation of the reference velocity (from $l^+ = 300$ to $l^+ = 800$ at $x/h = 34.9$ for $U_{ref} = 2$ and 8 m/s respectively).



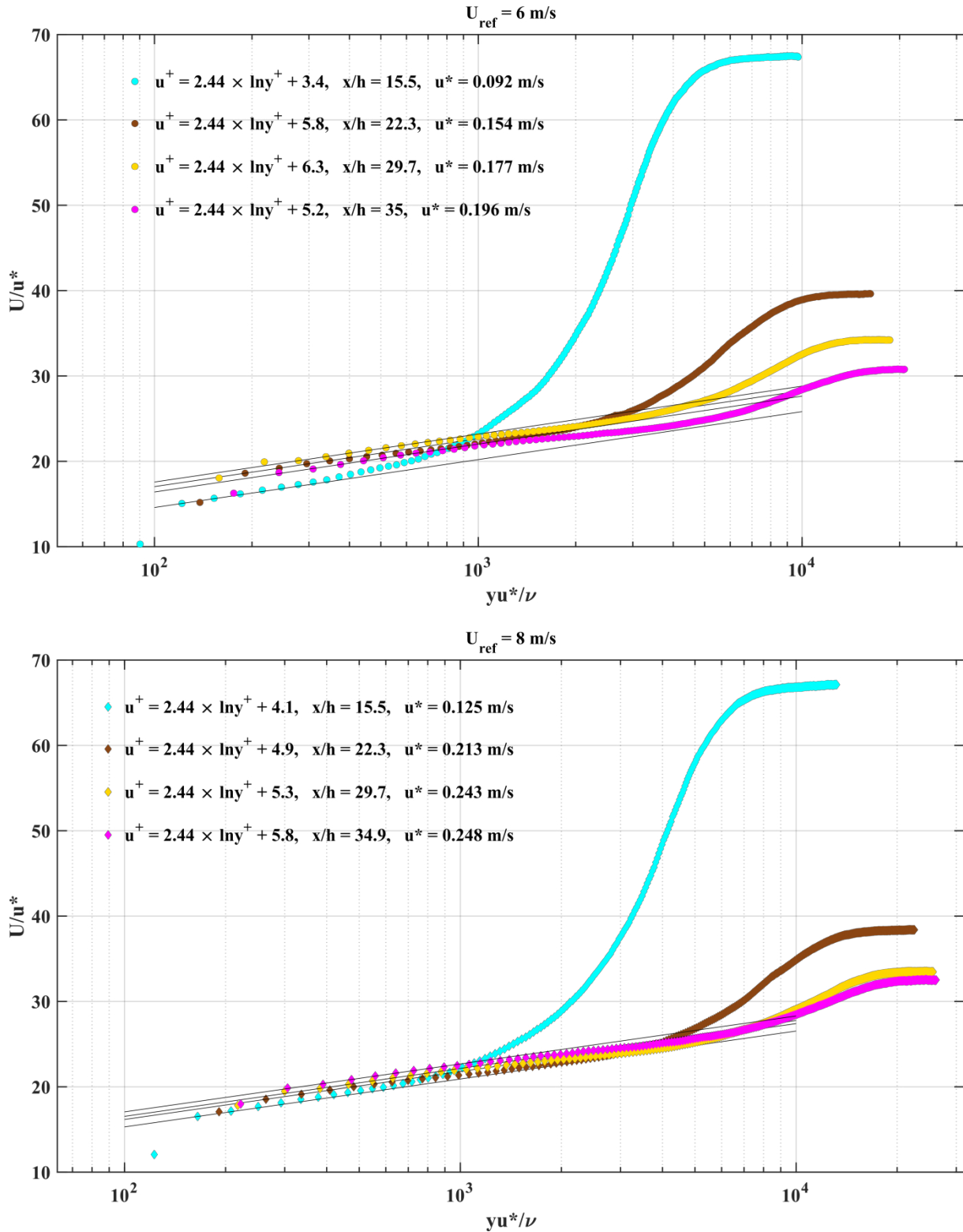


Figure III. 16 Semi-logarithmic plot of the mean stream-wise velocity profiles for inner variables at $U_{ref} = 2, 4, 6, 8 \text{ m/s}$

Based on this logarithmic-law assumption, indirect measurements of the skin friction coefficient $C_f = 2 \frac{u_*^2}{U_e^2}$ were made.

The evolutions in the stream-wise direction of the friction velocity and skin friction coefficient are shown in **Figure III. 17** for the different reference flow conditions. To check the validity of the log-law method for the determination of the friction velocity, C_f is compared to the C_f obtained by the correlation of *Ludwig-Tillmann (1949)*:

$$C_f = 0.246 \left(\frac{U_e \theta}{\nu} \right)^{-0.268} 10^{-0.678H} \quad 3 - 10$$

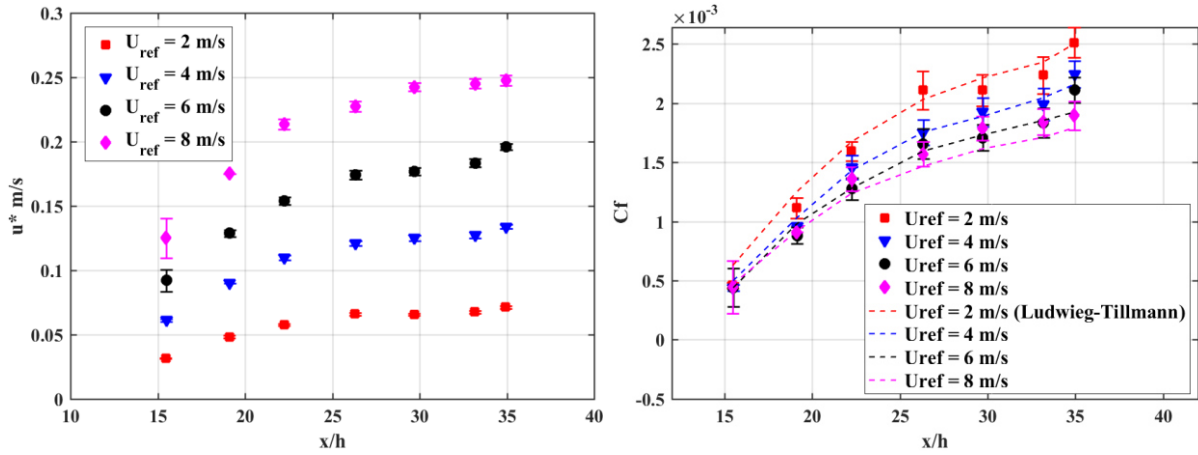


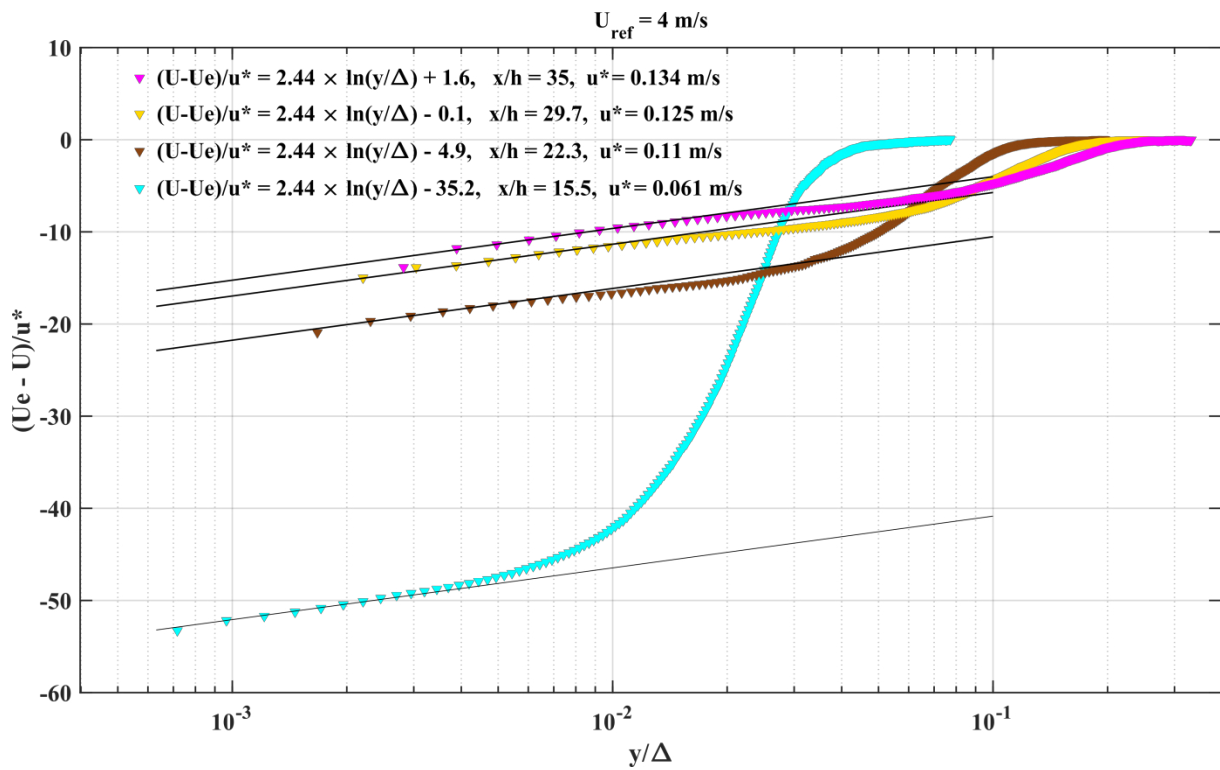
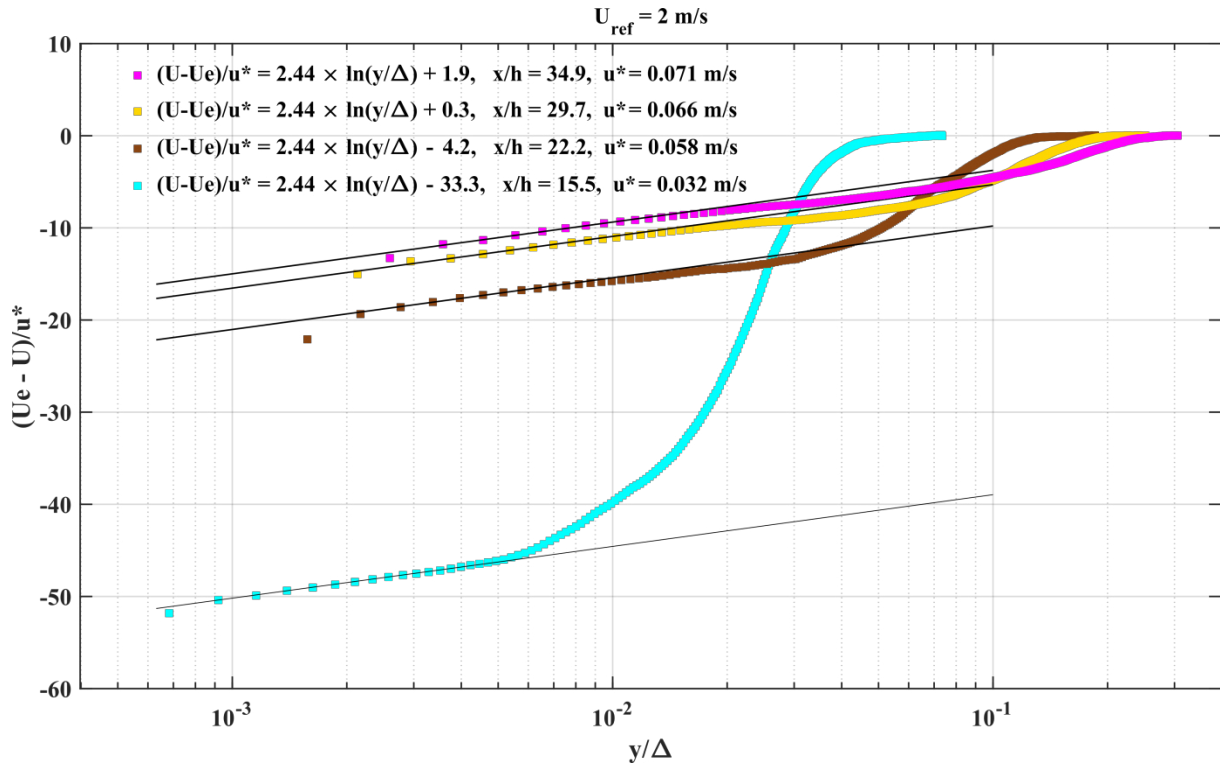
Figure III. 17 Friction velocity u^* (left) and skin friction coefficient C_f (right) along the stream-wise direction x/h (estimation based on universal logarithmic law in the inner region)

C_f increases sharply with x near the reattachment point. But its growth rate diminishes as x increases. As expected for a turbulent boundary layer that develops downstream, C_f decreases while the reference velocity increases.

Friction coefficient C_f estimated from *Ludwig-Tillmann* formula is in good agreement with the experimental results near and beyond the reattachment point. At $U_{ref} = 2$ m/s, C_f given by *Ludwig-Tillmann* formula was overestimated from 26.5%. C_f was slightly underestimated (-9.6%) at higher velocities and the discrepancy increases as x/h increases beyond the reattachment point. This trend was equally observed by *Antoniou & Bergeles (1988)*.

3.2.3.2 Validity of the log law versus the outer variables

Mean velocity profiles, plotted in semi-logarithmic coordinates, for outer variables, are given in **Figure III. 18**. The universal thickness Δ (*Eq. 1 – 21*) is estimated using the value of the friction velocity u^* determined with the log law versus inner variables. The linear evolution of $(U - U_e)/u^*$ versus $\ln(y/\Delta)$ seems to hold with the universal slope $1/\kappa$, κ being the *von Kármán* constant = 0.41. A shift in the additive constant C of the logarithmic law, owing to the steep adverse pressure gradient, can be clearly seen on the profiles. We observe that the lower the adverse pressure gradient, the higher the additive constant, which is coherent with *Clauser's* observations (*Clauser 1954*).



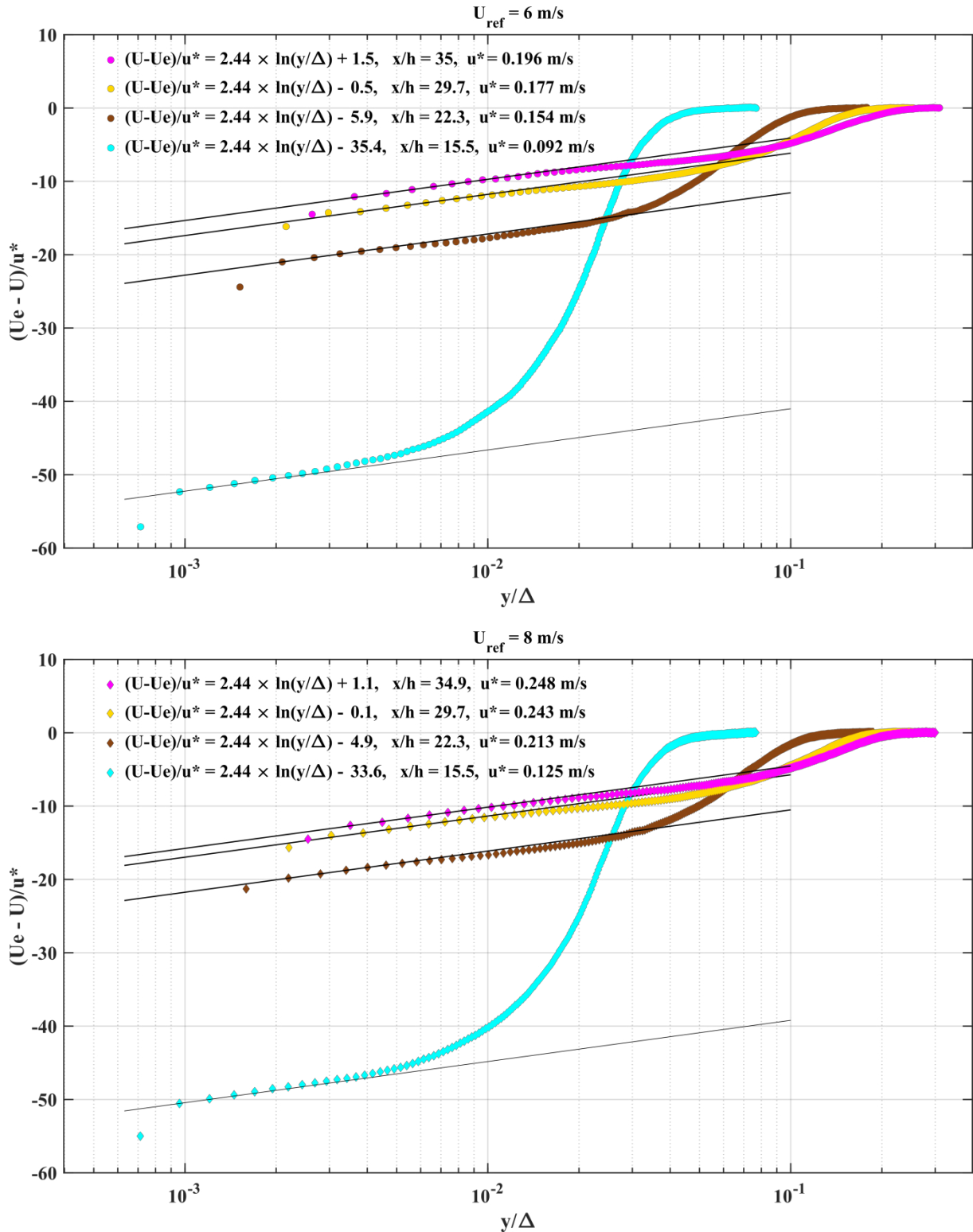


Figure III. 18 Semi-logarithmic plot of the mean stream-wise velocity profiles for outer variables at $U_{ref} = 2, 4, 6, 8 \text{ m/s}$.

3.2.4 Modal decomposition and frequency analysis

A series of isolated vortices is produced in the wake of the obstacle and travels downstream the flow when separation occurs. The travelling of the vortices is reminiscent of the *von Kármán* vortex street and the production follows a constant frequency (*Fragos et al. 2007*) which makes the downstream flow repetitive.

Figure III. 19 shows the spatial distribution of the stream-wise velocity for the four dominant modes of the *POD* decomposition at $U_{ref} = 2 \text{ m/s}$. The *POD* method was applied in the different measurement sections for each *PIV* viewing area and reconstructed for the whole field. By inspecting the flow field with mode 1, we clearly observe the formation of a large vortex series appearing to resemble a *von Kármán* vortex street as the dominant unsteady feature. The centre of the vortices locates at $y/h \approx 2$, which corresponds to the peak location of turbulent shear stress profiles. *Taira et al. (2017)* suggest that the traveling structures cannot be represented as a single mode but rather a pair of similar stationary modes. In our case, mode 1 and 2 form a pair of modes where mode 2 is geometrically similar to mode 1 but shifted in the stream-wise direction. Mode 3 and mode 4 represent the sub-harmonic spatial structures of modes 1 and 2.

Figure III. 20 shows the contour plot of mode 2 in the recirculation region for the different reference velocities. Although the centre of the vortices shifts axially downward when increasing the velocity, the spatial structure does not seem to change significantly according to the velocity.

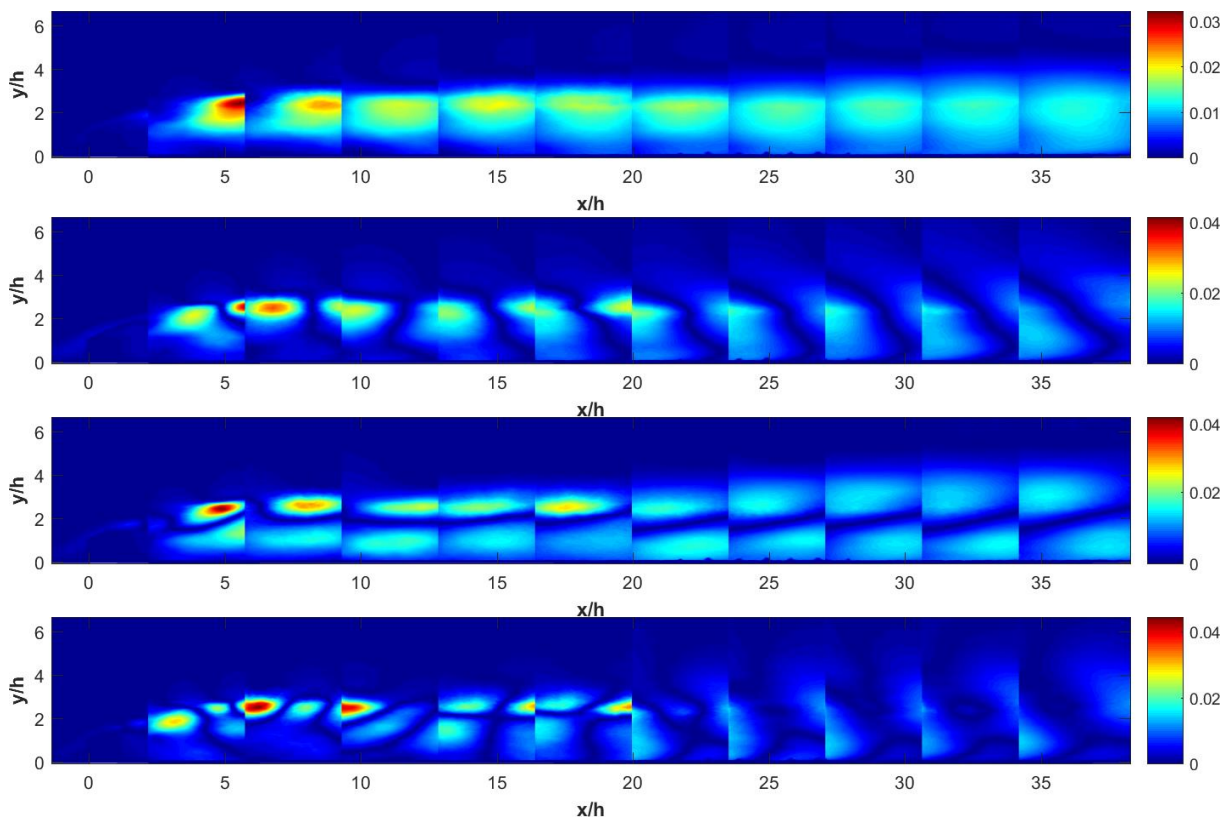


Figure III. 19 Contour plot of the stream-wise velocity for mode 1, 2, 3 and 4 at $U_{ref} = 2 \text{ m/s}$

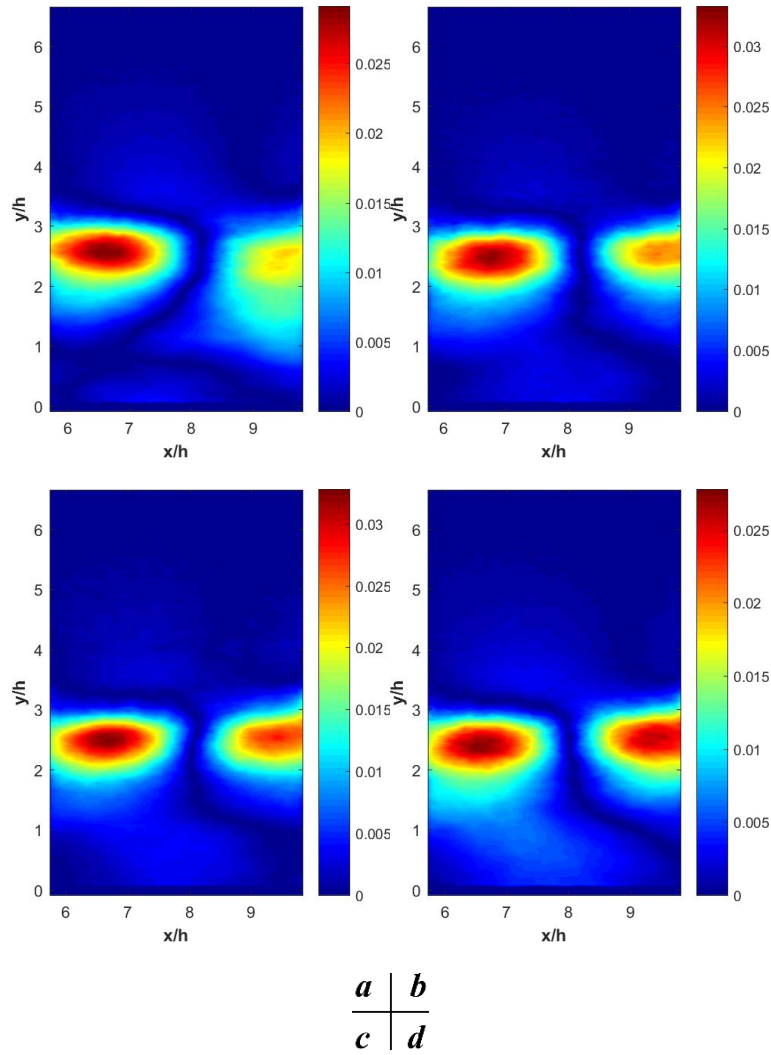


Figure III. 20 Contour plot of the stream-wise velocity for mode 2 in recirculation region at $U_{ref} = 2, 4, 6, 8 \text{ m/s}$

In energy contribution, mode 1 contains larger energy contribution than mode 2, mode 1 & 2 altogether contain 18% of the total energy. Energy contribution by mode is given in **Table III. 5**.

	Mode 1 (%)	Mode 2 (%)	Mode 3 (%)	Mode 4 (%)
2 m/s	11.79	7.07	4.77	3.44
4 m/s	10.83	5.67	4.68	3.05
6 m/s	11.2	5.94	4.38	3.15
8 m/s	12.51	6.56	4.68	2.98

Table III. 5 Energy content by four dominant modes for $U_{ref} = 2, 4, 6, 8 \text{ m/s}$

Frequency spectra of the projection coefficient a_j (**Eq. 3 – 3**) associated to mode $j = 2$ have been calculated in the recirculation region (*PIV* Section $n^\circ 3$)

Spectra are superimposed in **Figure III. 21a** for the different reference velocities. Peak frequencies at each velocity were localized in the figure, illustrating that the peak frequency increases with increase of the reference velocity.

Fragos et al. (2007) have observed a linear relationship between the vortex traveling frequency and the reference frequency: $f_{vortex} = 1/16.7 \times f_{ref}$, where $f_{ref} = U_{ref}/h$. **Figure III. 21b** shows the evolution of the peak frequency we obtained with respect to the reference frequency and comparison

to *Fragos et al. (2007)*. A good agreement of the frequency of mode 2 is found with the travelling frequency of *Fragos et al. (2007)*, leading to a constant *Strouhal* number of 1/16.7, which is imposed by the height of the obstacle.

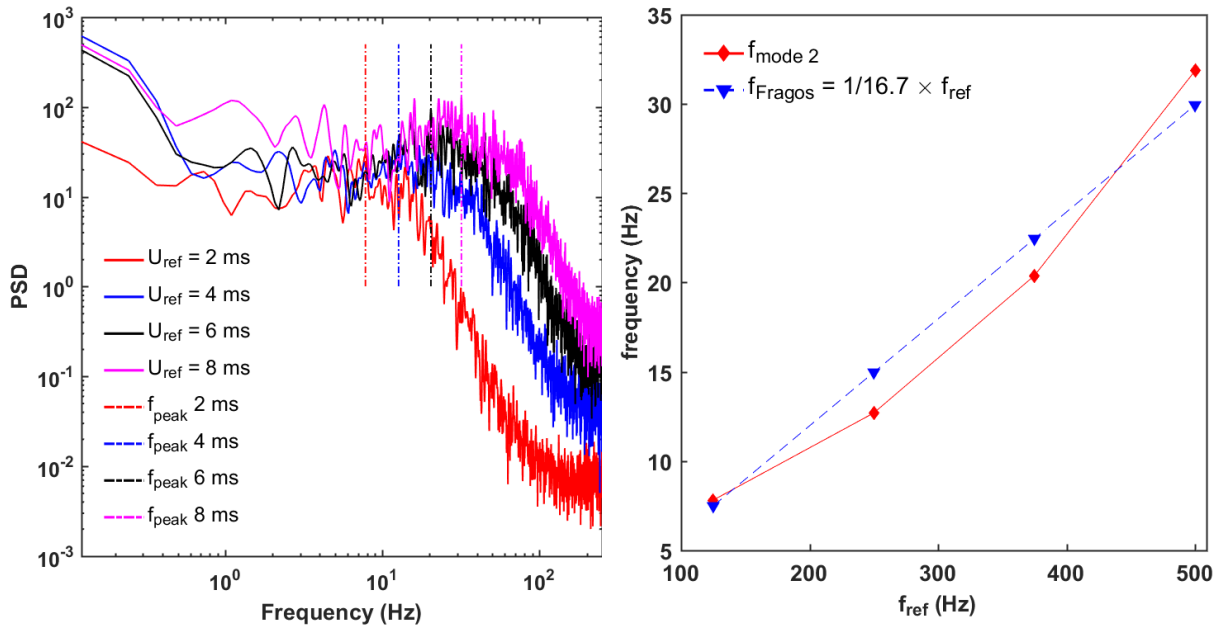


Figure III. 21 A: power spectral density of the time evolution for mode n° 2. B: peak frequency with respect to reference frequency ($f_{ref} = U_{ref} / h$) in comparison with linear relationship proposed by *Fragos et al. (2007)*

3.2.5 Longitudinal evolution of the integral scales of the flow

The variation with x of the integral length scales: displacement and momentum thickness δ^* and θ , is shown in **Figure III. 22**. Displacement thickness δ^* at $U_{ref} = 2$ m/s is seen to be larger than that at higher flow speeds. No significant difference in thickness was observed among other speeds. As expected from the study of a separation bubble over a flat plate of *Samson et al. (2012)*, δ^* is maximum at midlength of the recirculating region. According to *Samson et al.*, θ should be maximum at the reattachment point. Here, we observe a maximum of θ farther near $x/h \approx 19$, regardless of the reference velocity.

In the literature survey, the momentum thickness is reported to be lower than in our work. In the work of *Agelinchaab et al. (2008)*, θ increases monotonously as x/h increases. At $x/h \approx 19$, they obtain a dimensionless value θ/h equals to 0.42, which is smaller than the values reached in our study: 0.62 and 0.69 at 2 m/s and 8 m/s respectively; at $x/h \approx 35$, they measured a dimensionless value θ/h equals to 0.5, against 0.53 and 0.60 at 2 m/s and 8 m/s respectively in our study.

The variation with x of the universal thickness Δ and the boundary layer thickness δ is shown in **Figure III. 23**.

The boundary layer is obviously thickened downstream in the recovery region, whereas the integral boundary layer thickness Δ decreases downstream as the adverse pressure gradient diminishes. Δ offers a better universality than δ , with regard to U_{ref} .

The variation with x of the boundary layer thickness δ_3 and δ_4 is shown in **Figure III. 24**. δ_3 is maximum in the recirculating region at $x/h \approx 8$, whereas δ_4 reaches its maximum value at the reattachment point $x/h \approx 12$. Both of them decrease downstream in the recovery region. Surprisingly

δ_3 and δ_4 are more important for $U_{ref} = 2\text{ m/s}$, this is due to the fact that the boundary layer is much thicker at $U_{ref} = 2\text{ m/s}$.

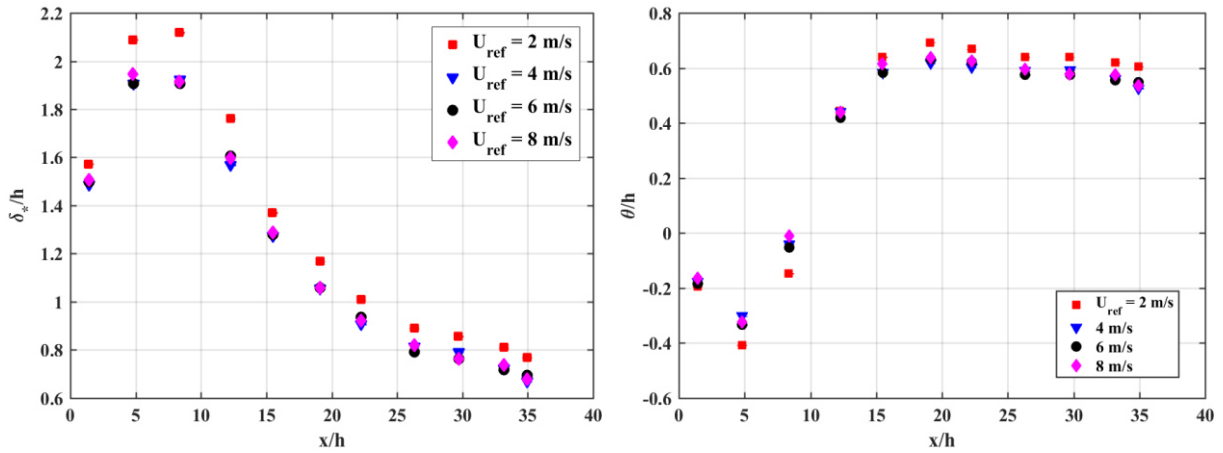


Figure III. 22 Integral length scales δ^* and θ versus x/h . Left: displacement thickness δ_x^* , right: momentum thickness θ

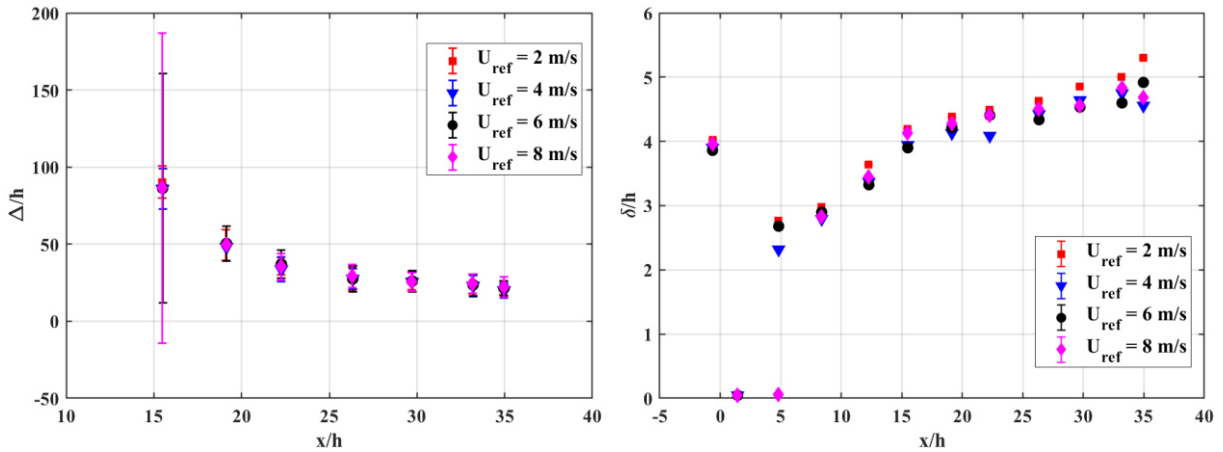


Figure III. 23 Left: integral length scale Δ , right: boundary layer thickness δ versus x/h

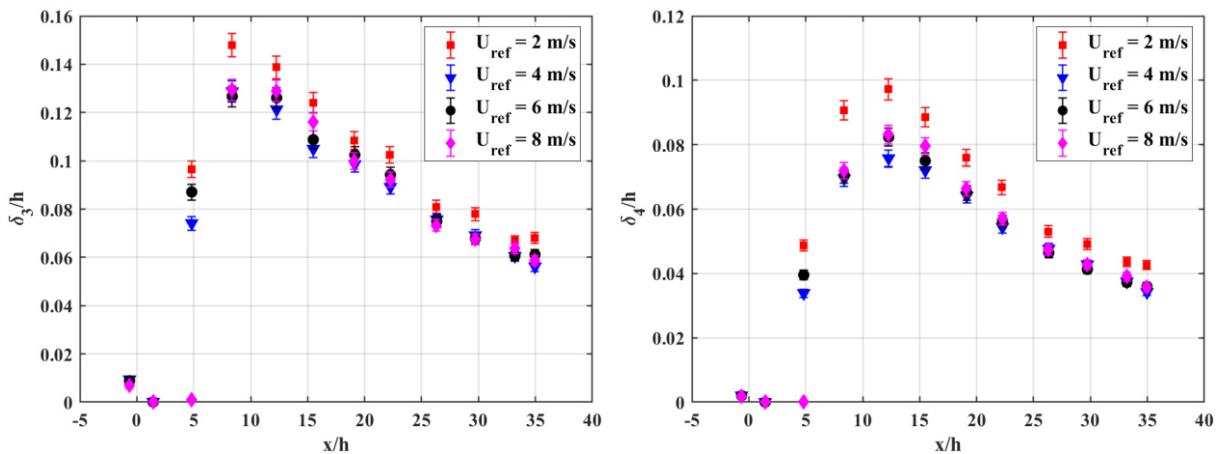


Figure III. 24 Left: stream-wise turbulent intensity thickness δ_3 , right: wall-normal turbulent intensity thickness δ_4 versus x/h . (Both δ_3 and δ_4 calculated with the use of the external velocity U_e)

The stream-wise evolution of the *Reynolds* number, based on momentum thickness and external velocity is displayed in **Figure III. 25**. The *Reynolds* number is strongly dependent on the reference

velocity but weakly dependent on the stream-wise position beyond a critical stream-wise distance ($x/h \approx 25$) that increases with the increase of the reference velocity.

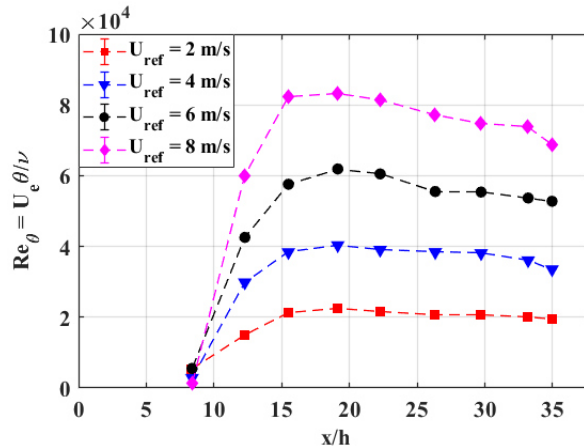


Figure III. 25 Local Reynolds number versus x/h

The longitudinal variation of the shape factor H and the *Clauser* parameter G have been plotted in **Figure III. 26**. Downstream of the reattachment point, H decreases fairly rapidly, following the decrease in the adverse pressure gradient. The stream-wise profile of H for $U_{ref} = 2 \text{ m/s}$ collapses onto other profiles while x/h increases. All the H profiles are seen to have converged to $H = 1.26$ at $x/h = 34.9$, which is similar to the results of *Agelinchaab (2008)*, and which is below $H = 1.286$, a value for a one-seventh power profile for zero gradient pressure, suggested by *von Doenhoff (1943)*.

G profiles are compared to $G = 6.8$ for constant pressure turbulent boundary layer in equilibrium. We can readily say that G at $x/h \approx 34.9$ quite fully reaches the value expected at constant pressure equilibrium.

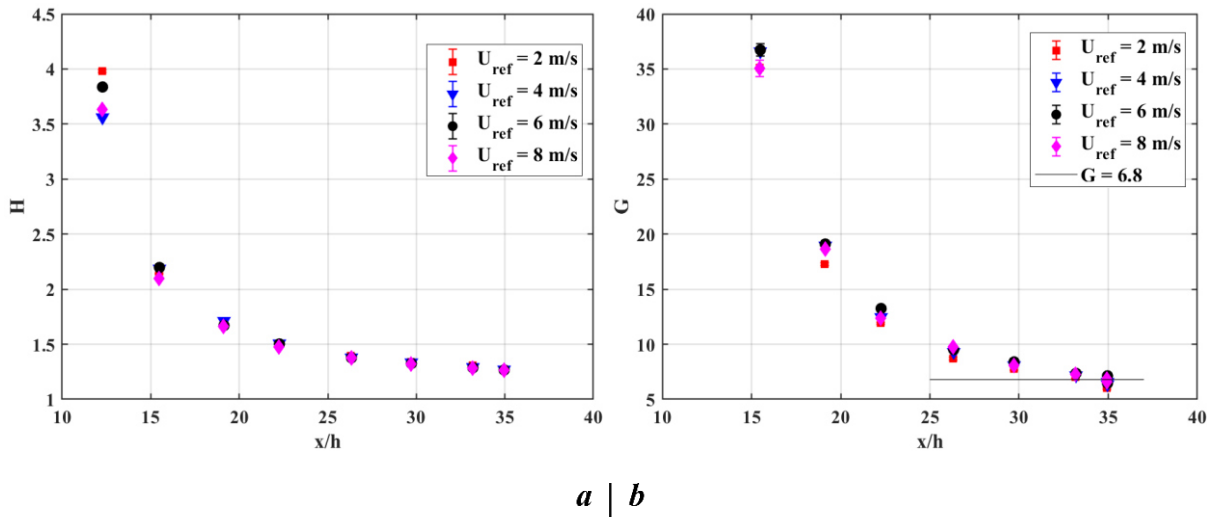


Figure III. 26 A: shape factor H and B: *Clauser* parameter G versus x/h for different flow conditions

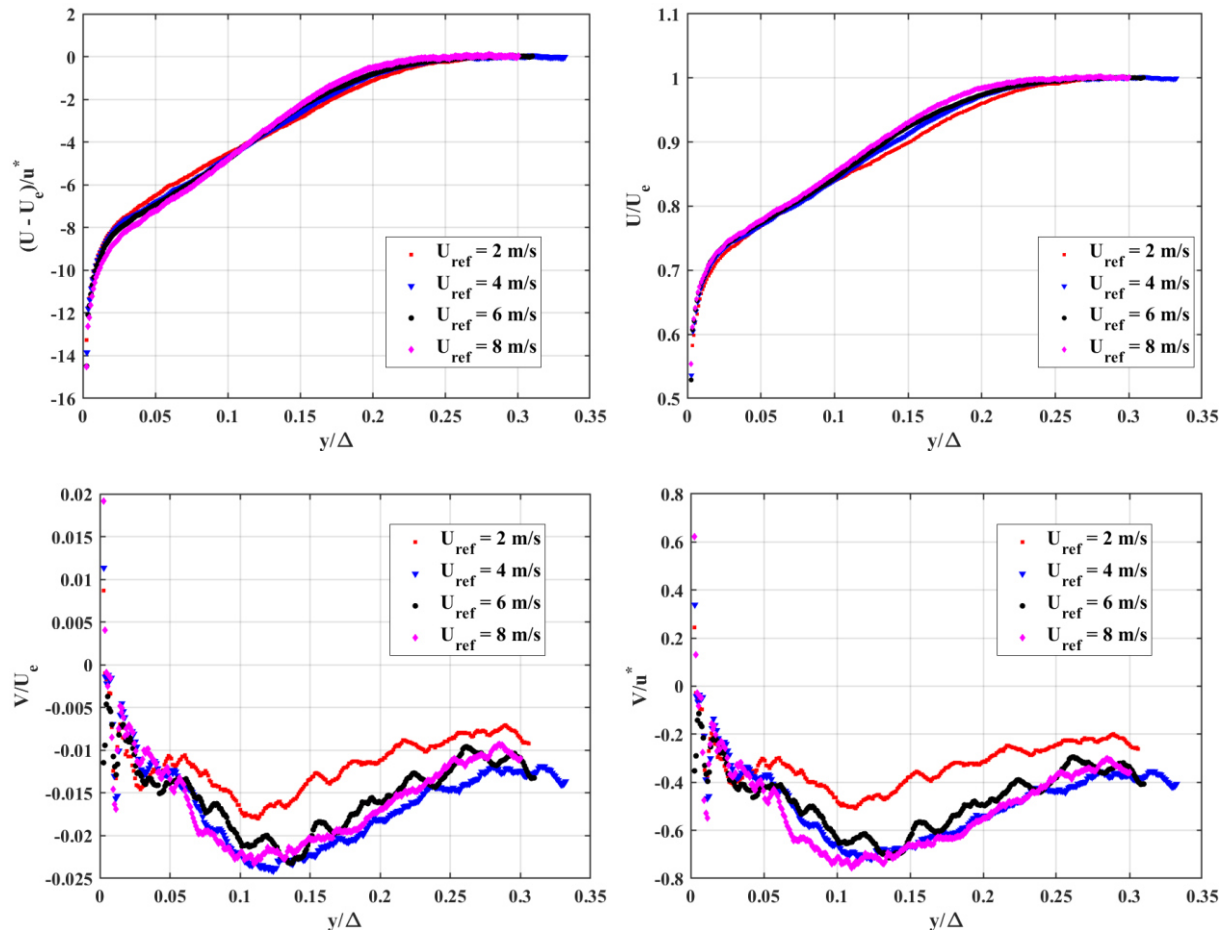
3.2.6 Discussion

For each reference velocity, we have a dependency of the *Clauser* parameter G on the stream-wise position, even in the recovery region.

Nevertheless, it seems that, for a given stream-wise position, the integral scales that characterize the mean flow (δ^* , θ , Δ , G and β) are in good agreement in the recovery region, whatever the reference velocity values: 2, 4, 6 or 8 m/s. **Figure III. 27**, **Figure III. 28** display the comparison at $x/h = 35$ of the normalized mean velocity and normalized *Reynolds* stress profiles measured for the different reference velocities.

For the purpose of comparison, the wall normal distance is normalized by the universal thickness Δ and different scalings of the velocity are tested: either with the friction velocity or with the external velocity.

According to *Coles (1962)*, in case of a flat plate, the wake parameter $\Delta U/u^*$ asymptotes to a constant value for $Re_\theta > 6000$. Here we observe that the mean stream-wise velocity profiles (**Figure III. 27a**) are still *Reynolds*-number dependent in the outer layer for $y/\Delta > 0.1$. A best self-similarity in the inner region is obtained when scaling the velocity with u^* , a best self-similarity in the outer region is achieved by scaling the velocity with U_e . For *V* profiles, despite the fact that the use of *PIV* makes it difficult to estimate correctly wall normal mean components, it demonstrated the collapse of *V* normalized by u^* through the entire outer region except for $U_{ref} = 2$ m/s, for which the flow is not fully turbulent (**Figure III. 27d**).



a	b
c	d

Figure III. 27 Comparison between the different reference velocities at $x/h = 35$ of the *Y* profiles of mean velocity components.

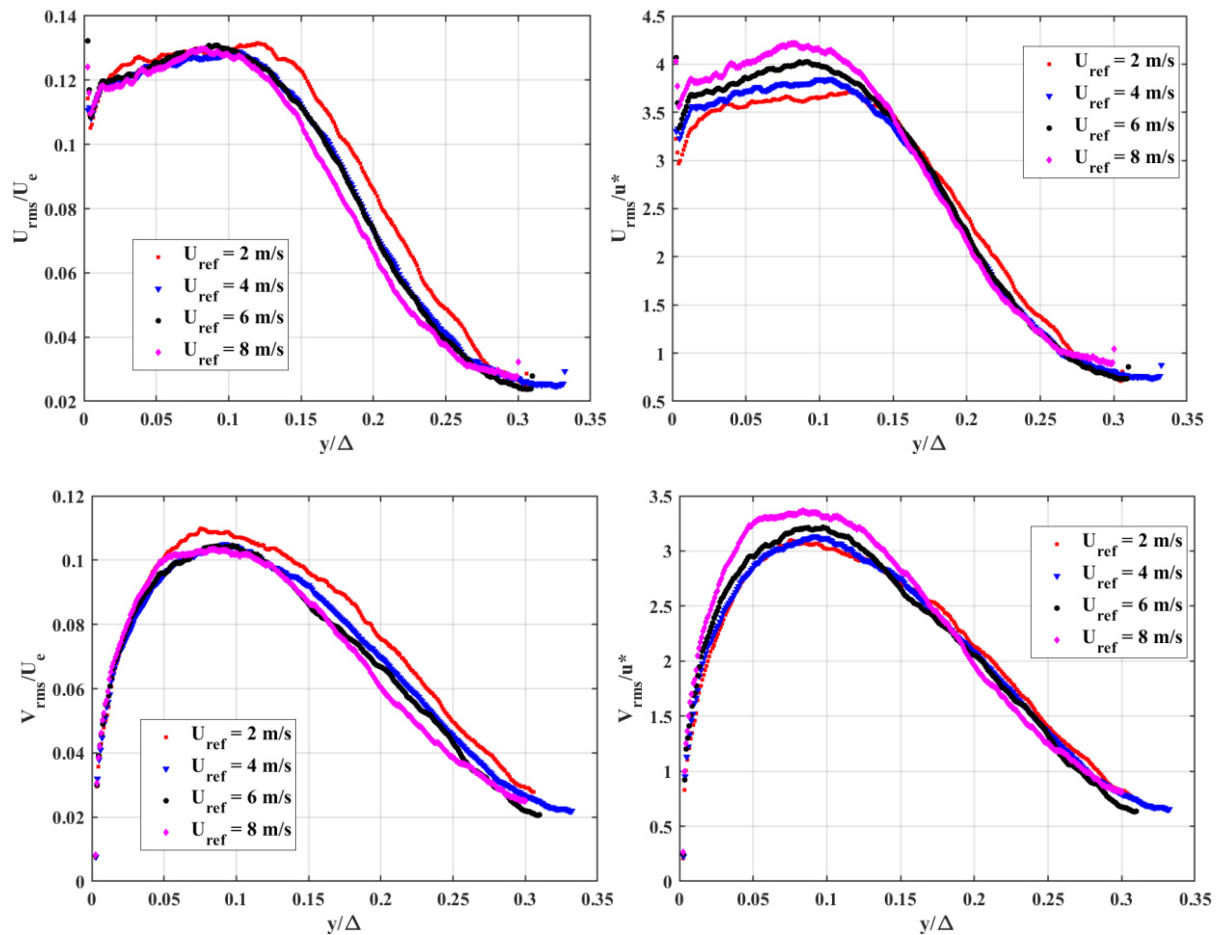
For the turbulent stresses in a flat plate flow, traditional inner scaling using u^* is shown to be valid for wall-normal and *Reynolds* shear stresses, *DeGraaf et al. (2000)* have proposed a mixed scaling u^*U_e for the stream-wise direction stress.

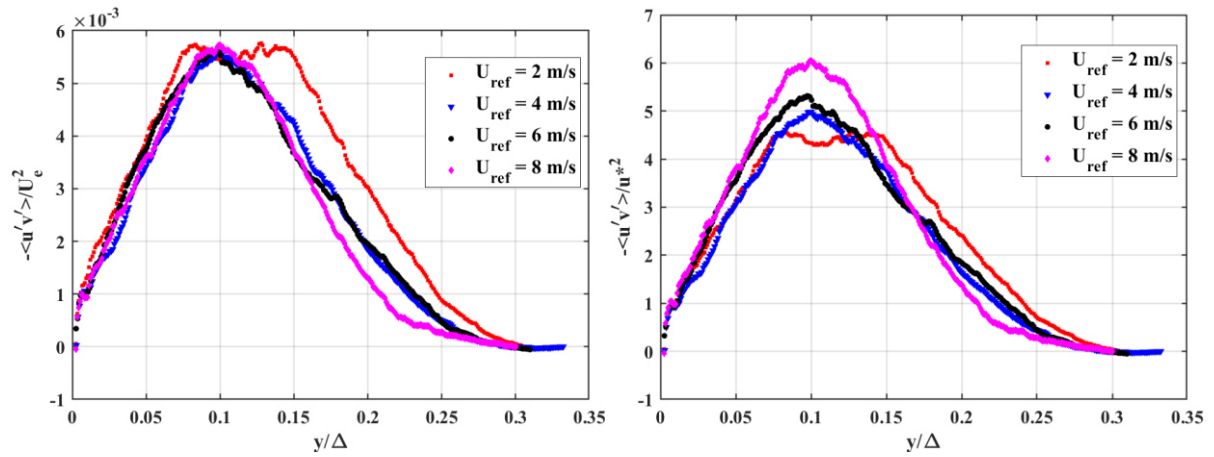
As for *Reynolds* stresses scaling, the peak value for U_{rms} V_{rms} and $\langle u'v' \rangle$ does not collapse in the *DeGraaff et al. (2000)* coordinates, inner and outer scaling U_e , u^* were used separately.

Figure III. 28a-d shows the U_{rms} and V_{rms} profiles. Same conclusions are drawn for the normal *Reynolds* stresses. The collapse of the peak values is achieved with U_e scaling. Self-similarity of the profiles is verified in the inner and outer layers of the boundary layer for $y/\Delta < 0.1$. The peak at $U_{ref} = 2 \text{ m/s}$ fails to collapse onto peaks at other velocities; but above this velocity, peak values become independent of *Reynolds* number. A better self-similarity collapse in the outer layer for $y/\Delta > 0.1$ is achieved when scaling by u^* .

Figure III. 28e-f show the $-\langle u'v' \rangle$ profiles scalings. Peak values have succeeded to collapse onto each other except for flow at 2 m/s , where a plateau appears, as mentioned earlier. At outer region, both scalings fail to collapse the stress profiles.

Generally speaking, we can conclude that we obtain a good self-similarity of the velocity profiles, which is *Reynolds* independent for $Re_\theta > 30000$, in the downstream part of our recovery region.





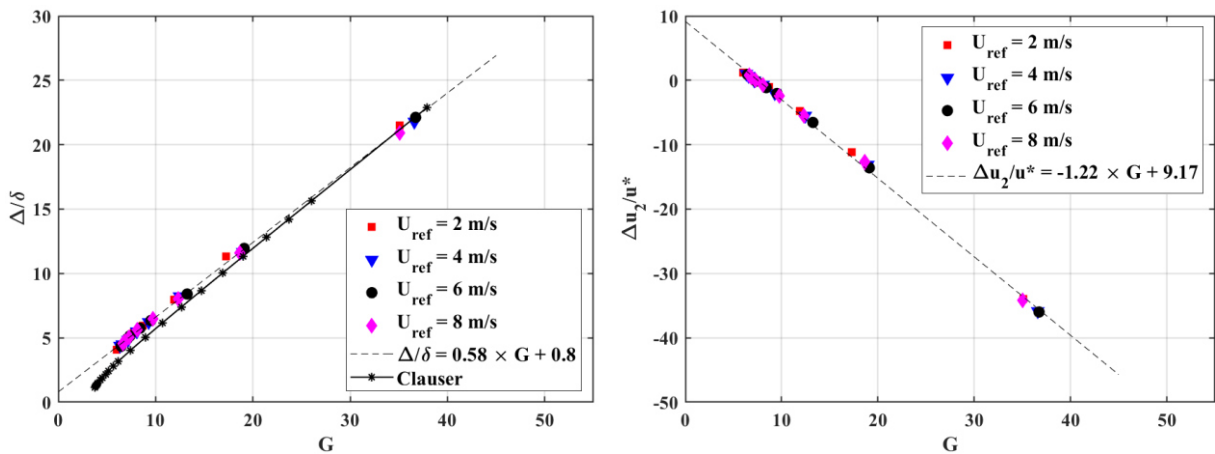
$$\begin{array}{c|c} a & b \\ \hline c & d \\ \hline e & f \end{array}$$

Figure III. 28 Comparison between the different reference velocities at $x/h = 35$ of the Y profiles of Reynolds stresses

In **Figure III. 29**, Normalized integral scales are plotted against the Clauser parameter G . We observe a linear variation of Δ/δ with regard to G (**Figure III. 29a**). Values from all velocities collapse on a line, Comparison with Clauser's data (from Cousteix 1989) shows that a good agreement is achieved for the highest values of G ($G > 30$). For smaller G values, experimental data differ from Clauser's data. For an approximate G value in zero gradient flow $G \approx 6.8$, experimental data are observed to be 31% higher than Clauser's ones.

Figure III. 29b displays also the shift in the additive constant of the log law $\frac{\Delta u_2}{u_*} = 0.6 - C$ from the zero pressure condition against the value of G . The additive constant seems to be Reynolds number (velocity) independent and to decrease linearly with G .

Figure III. 29c shows the evolution of the Clauser's pressure gradient parameter β with G . β is evaluated based on the stream-wise external velocity gradient. The Clauser's data (Cousteix 1989) were equally plotted in comparison. β depicts good agreement with Clauser's data for a large range of G . For small values of G ($G < 7$), that is to say, in the downstream part of the recovery region, β is higher than Clauser's data: 2.44 against 1.84 for Clauser.



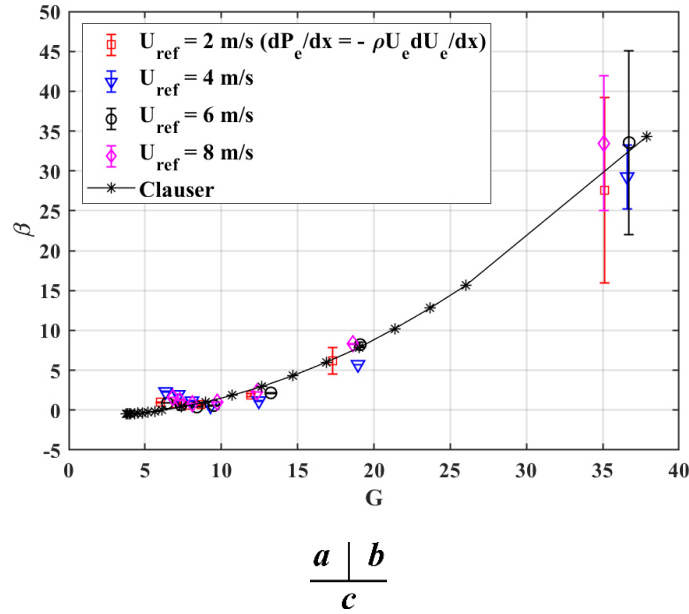


Figure III. 29 Normalized integral scales versus Clauser Parameter G A: Normalized universal thickness Δ/δ , B: Shift from the zero pressure condition of the additive constant of the log law, C: Universal parameter β .

3.3 Conclusion

The mean and fluctuating flow developing downstream the obstacle, characterized by *PIV* for the single phase flow conditions, has been analyzed in this chapter. Vortex traveling frequency, quantified with the use of *POD* method, has been shown to be reference velocity dependent. The recirculation length ($L_R = 12h$) was found to be independent on the reference velocity.

The stream-wise and wall normal evolution of the overall field have been discussed. In the recovery region, the boundary layer characteristics are strongly dependent on the stream-wise position x .

In regards to the mean stream-wise flow, the universal log law seems to be valid for velocity profiles even under steep adverse pressure gradient. In the recovery region, a self-similarity of the mean flow profiles was observed at a given stream-wise position for $Re_\theta > 30000$. The self-similarity was partially achieved on the fluctuating flow, depending on the scaling velocity.

We can conclude that the turbulent boundary layer which develops in the recovery region has reached equilibrium for a given reference velocity. Evolution of integral parameters such as Δ/δ and β has indicated that the flow is not fully relaxed in the very last testing section in the recovery region, where more works on multiphase flow characterization were carried out.

4 CHAPTER IV. Influence of Bubble Injection on the Flow Developing Downward the Obstacle. Characterization of the Gas Phase

This chapter examines the influence of the main flow velocity and the gas injection rate on the gas phase characteristics downstream the obstacle in the reattachment region by means of Shadowgraphy. We focus in this chapter on the gas volume fraction distribution, mean and *rms* velocity components of the gas phase in the vertical plane and statistics of the bubble size distribution, measured at a position $x/h = 34.3$. The flow configuration and the coordinate system used are recalled in **Figure IV. 1**.

Bubbly flow conditions are firstly summarized, followed by a description of the statistical analysis procedure of data provided by Shadowgraphy technique. The third part of this chapter is dedicated to the statistics of bubble size and shape under different operating conditions. The gas volume fraction such as self-similarity scaling of mean profiles and integral parameters characteristic of the bubble layer are examined in a fourth part. Finally, the mean and *rms* gas phased averaged velocity profiles are presented and discussed.

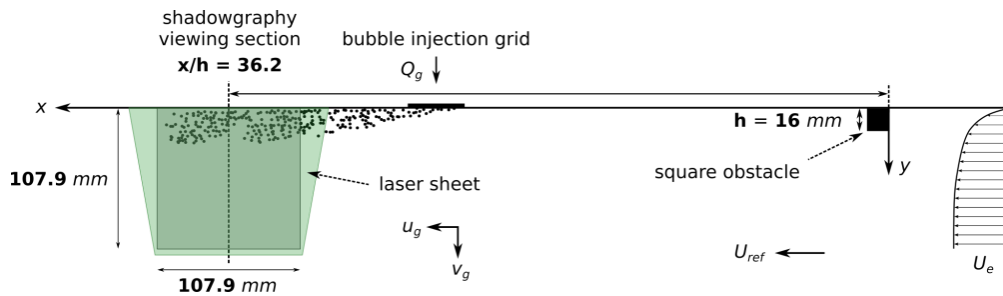


Figure IV. 1 Sketch of experimental setup and viewing section

4.1 Bubbly Flow conditions

All measurements were made under four reference velocities $U_{ref} = 2, 4, 6$ and 8 m/s . The air injection rate varied up to 80 l/h . The operating points are summarized in **Table IV. 1**.

The value of the characteristic parameters (*Reynolds* number, global gas volumetric fraction in the tunnel, average volume fraction in the boundary layer....) obtained at the stream-wise position of the viewing area ($x/h = 34.3$) are also given in **Table IV. 1**. The values of these characteristic parameters are based on integral parameters of the boundary layer in single phase flow. The average air volume fraction $\langle \alpha \rangle$ of the boundary layer is estimated, assuming that bubbles are advected at the velocity of the single phase flow, based on the following relationship:

$$\langle \alpha \rangle = \frac{Q_g}{U_e(\delta - \delta_*)e} \quad 4 - 1$$

Where e is the width of the water tunnel.

U_{ref} (m/s)	θ/h	Δ/h	Re_θ $(\frac{U_e \theta}{\nu})$	Re_* $(\frac{u^* \theta}{\nu})$	Q_g (l/h)	Q_g/Q_l (%)	$\langle \alpha \rangle$ (%)
2	0.68	23.88	21662	794	0	0	
2	0.68	23.88	21662	794	5	0.002	0.0049
2	0.68	23.88	21662	794	10	0.004	0.0098
2	0.68	23.88	21662	794	20	0.008	0.0196
2	0.68	23.88	21662	794	40	0.015	0.0392

2	0.68	23.88	21662	794	60	0.023	0.0587
2	0.68	23.88	21662	794	80	0.030	0.0783
4	0.63	23.43	40623	1381	0	0	
4	0.63	23.43	40623	1381	10	0.002	0.0049
4	0.63	23.43	40623	1381	20	0.004	0.0099
4	0.63	23.43	40623	1381	40	0.008	0.0197
4	0.63	23.43	40623	1381	60	0.011	0.0296
4	0.63	23.43	40623	1381	80	0.015	0.0395
6	0.62	24.07	60630	1988	0	0	
6	0.62	24.07	60630	1988	15	0.002	0.0053
6	0.62	24.07	60630	1988	30	0.004	0.0105
6	0.62	24.07	60630	1988	60	0.008	0.0210
6	0.62	24.07	60630	1988	80	0.010	0.0281
8	0.53	21.35	68913	2157	0	0	
8	0.53	21.35	68913	2157	20	0.002	0.0052
8	0.53	21.35	68913	2157	40	0.004	0.0105
8	0.53	21.35	68913	2157	60	0.006	0.0157
8	0.53	21.35	68913	2157	80	0.008	0.0210

Table IV. 1 Characteristics of the operating points of the bubbly flow achieved in the viewing area at $x/h = 34.3$ (characteristics of the single phase boundary layer are used here, as reference values)

Figure IV. 2 shows the averaged volume fraction $\langle \alpha \rangle$ in function of the volumetric fraction Q_g/Q_l . It can be seen that $\langle \alpha \rangle$ changes linearly with Q_g/Q_l and appears to be quite independent of the reference velocity.

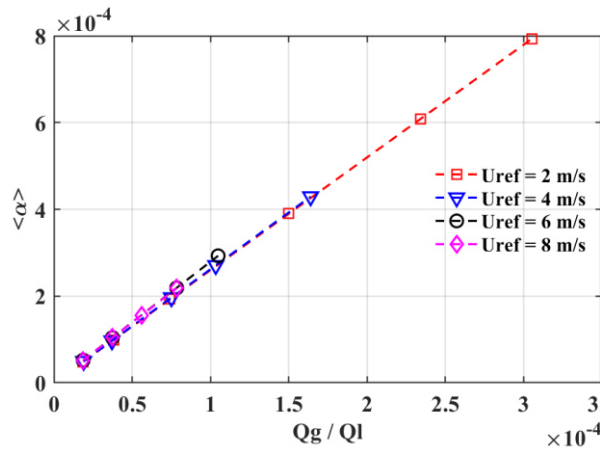


Figure IV. 2 Averaged volume fraction in function of volumetric fraction

4.2 Statistical analysis procedure of Shadowgraphy measurements

4.2.1 Spatial and time averaging

The gas phase's surface fraction and velocity components have been spatially averaged over an Eulerian grid. The Eulerian grid is the same as the one used for processing *PTV* measurements to characterize the liquid phase (*Chap. 5*). The size of the grid in the x and y directions has been optimized in order to improve the spatial resolution in the y direction and maximize the number of detected particles for *PTV* measurements. The integration window's was spread in the x direction, leading to a spatial resolution in x direction of 13.6 mm . The integration window's width in y direction was chosen to be quite identical to that of the Interrogation Area in *PIV* thus yielded a spatial resolution in the wall-normal direction of 1.4 mm . The grids overlap in the y direction, as shown in *Figure IV. 3*. The grid point spacing in the y direction was 4 pixels (i.e.: 0.212 mm).

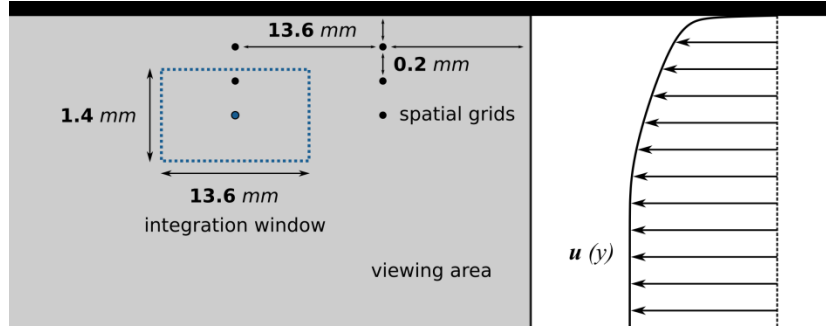


Figure IV. 3 Schematic view of integration window (blue dotted lines) and spatial grid resolution (black dots)

Each time a bubble's centroid is included in a grid, it contributes to the statistical analysis in this grid. **Figure IV. 4** shows the number of centroids n_b , cumulated in time, passing through the grid centered at $y = 0.58 \text{ mm}$ from the wall as a function of the reference velocity and as a function of the global gas volumetric rate. As a reminder, the measurement time is 250 seconds, the number of acquired images doublets is 2000, corresponding to a sampling frequency of the doublets at 8 Hz.

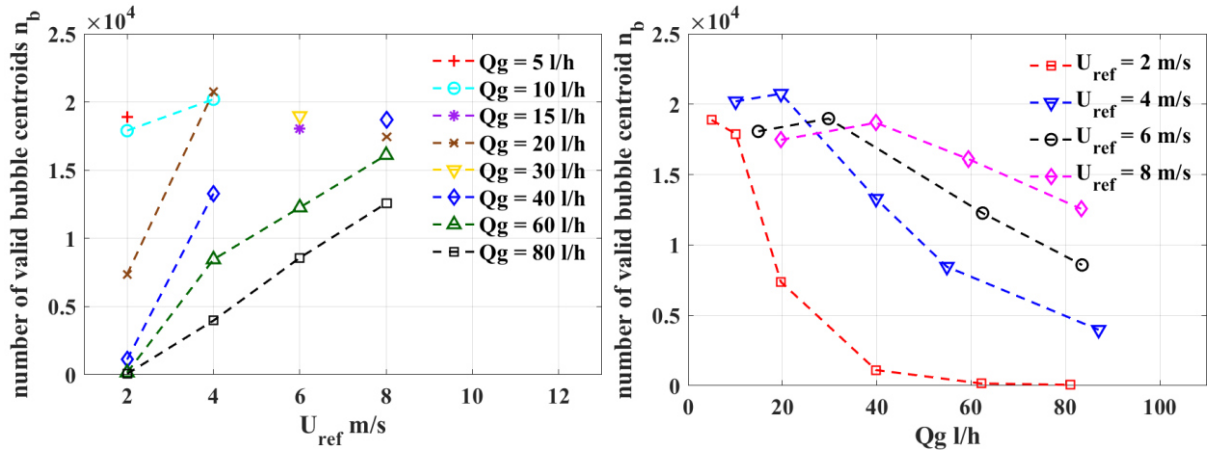


Figure IV. 4 Number of bubbles centroids, cumulated in time, passing over the grid centered at $x/h = 34.3$ and $y = 0.58 \text{ mm}$ from the wall, and validated by the image processing, according to the reference velocities and according to the global volumetric fraction

From now on, $U_g(y) = \langle u_b \rangle_{\Delta x, \Delta y, t} = \langle u_b \rangle_{n_b}$ and $V_g(y) = \langle v_b \rangle_{\Delta x, \Delta y, t} = \langle v_b \rangle_{n_b}$ are referred to time and spatial averages of the stream-wise and vertical velocity components of the bubbles at $x/h = 34.3$.

$U_{g \text{ rms}}(y) = \sqrt{\langle (u_b - U_g)^2 \rangle_{n_b}}$, $V_{g \text{ rms}}(y) = \sqrt{\langle (v_b - V_g)^2 \rangle_{n_b}}$ are the corresponding *rms* velocity components. $-\langle u'v' \rangle_g(y) = -\langle (u_b - U_g)(v_b - V_g) \rangle_{n_b}$ is the *Reynolds* shear stress of the gas phase.

$\langle d_b \rangle$ and $\sigma(\langle d_b \rangle)$ are the mean and *rms* bubble diameter which derives from the ensemble averaging of the bubble equivalent diameter, performed among all isolated bubbles observed in the viewing area for each time.

The time averaged gas surface fraction obtained at each pixel (**Eq. 2 – 9**) was averaged spatially over the Eulerian grid at $x/h = 34.3$: $\alpha_s(y) = \langle \alpha_s(x = 34.3 h, y) \rangle_{\Delta x, \Delta y}$. Let us denote $\alpha_s(y)$ its wall normal profile. The time averaged local gas volume fraction is deduced from the mean bubble diameter, the gas surface fraction and the depth of field *DOF* (**Eq. 2 – 10**):

$$\alpha_v(y) = \frac{2 \langle d_b \rangle}{3 \text{DOF}} \alpha_s(y)$$

4 – 2

Consider now the ratio between the local gas volume fraction $\alpha_v(y)$ and the gas volume fraction averaged over the boundary layer thickness $\langle\alpha\rangle$, the bubble boundary thickness δ_b was defined as the wall-normal location where:

$$\alpha_v(\delta_b) = 0.05 \langle\alpha\rangle \quad 4 - 3$$

This method is similar to the one used to estimate the boundary layer thickness, and thus suffers from the same shortcoming as δ . An alternative approach to define the bubble layer thickness can be based on an integral method. We define the gas layer thickness δ_α as the distance by which the wall is displaced outwards as a consequence of the occupied volume by bubbles, it is defined by:

$$\delta_\alpha = \int_0^\infty \alpha_v dy \quad 4 - 4$$

4.2.2 Uncertainties

Random errors of statistical quantities, related to the sub-pixel resolution of the Shadowgraphy measuring system, are evaluated in **Table IV. 2**.

Spatial resolution in x direction : $\Delta x/h$	0.85
Spatial resolution in y direction : $\Delta y/h$	0.087
Sub-pixel Random error : $\langle d_b \rangle/h$	$5.2e^{-7} - 8.1e^{-7}$
Sub-pixel Random error : $\sigma(\langle d_b \rangle)/h$	$1.3e^{-4} - 4.0e^{-4}$
Sub-pixel Random error : $\Delta U_g/U_{ref}$	$1.3e^{-4} - 3.4e^{-4}$
Sub-pixel Random error : $\Delta V_g/U_{ref}$	$1.3e^{-4} - 3.4e^{-4}$
Sub-pixel Random error : $\Delta U_{g\ rms}/U_{ref}$	$4.8e^{-4} - 3.7e^{-3}$
Sub-pixel Random error : $\Delta V_{g\ rms}/U_{ref}$	$1.2e^{-4} - 2.1e^{-3}$
Sub-pixel Random error : $\Delta(-\langle u'v'_g \rangle)/U_{ref}^2$	$3.0e^{-4} - 7.7e^{-4}$

Table IV. 2 Random error in the determination of statistical quantities, linked to the Shadowgraphy measurement system (spatial resolution of the grid, sub-pixel resolution of the Shadowgraphy optic system) at $x/h = 34.3$ (It should be pointed out that the random errors for $\Delta U_{g\ rms}/U_{ref}$, $\Delta V_{g\ rms}/U_{ref}$ and $\Delta(-\langle u'v'_g \rangle)/U_{ref}^2$ was evaluated using the peak value in $U_{g\ rms}$ and $V_{g\ rms}$ profile).

Uncertainties due to statistical convergence are not evaluated here. They will be represented as error bars on all following graphics.

4.2.3 Validation of measurements and statistical processing. Conservation of mass flux of the gas

We may reconstruct the gas flow rate F by writing the law of volume flow rate conservation in the integral form:

$$F = \int_0^\infty \alpha_v U_g e_b dy \quad 4 - 5$$

Where e_b denotes the width of the bubble injection area = 167.04 mm (**Chap. 2 Appendix 8.1**). By assuming that all bubble shadows are captured on the images, that is to say, no bubble is overlapped, the value of F should be equal to the gas injection flow rate Q_g . This method plays an important role in finding the effective measurement volume depth DOF of the bubbles, since the latter is used to define the local volume fraction α_v (**Eq. 4 - 2**)

Figure IV. 5 shows the evolution of F with respect to Q_g . For consistency purposes, the effective measurement volume depth DOF was calibrated to have the best linear fit adjustment with the curve $F = Q_g$. It yields $DOF = 86.39$ mm, which is quite in agreement with the depth of field of the telecentric lens.

This graph highlights the validity limit of the gas volume fraction measurement for some operating points. At high global volumetric fraction Q_g/Q_l where bubble-overlapping in the field of view takes place, F can be underestimated. This is the case at $U_{ref} = 2 \text{ m/s}$, beyond $Q_g \geq 40 \text{ l/h}$ (equivalent to a volumetric fraction of $Q_g/Q_l \geq 0.015\%$). For this velocity, above this critical air injection rate, the bubbles slide along the upper wall under buoyant force, it results in a significant overlapping of the bubbles apparent surface throughout the depth of field and an underestimation of the measured gas surface and volume fractions in the vicinity of the wall. For higher reference velocities 4,6 and 8 m/s , the linear relationship was respected, which validates the measurement of the gas volume fraction within the entire bubble layer.

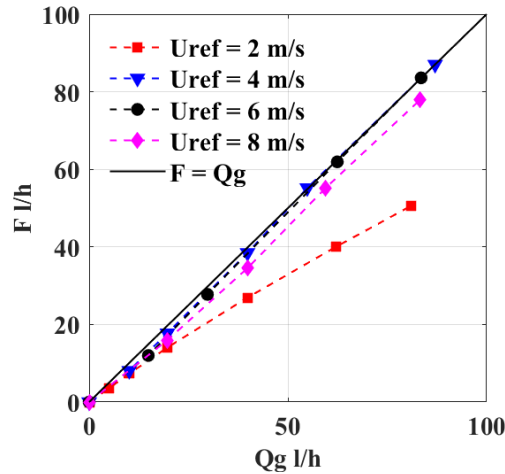


Figure IV. 5 Plot of reconstructed gas flow rate F with respect to real gas flow rate Q_g

4.3 Bubble size and shape

4.3.1 Distribution of equivalent diameter

The probability density function (PDF) of the equivalent bubble diameter is shown in **Figure IV. 6**. For all reference velocities, the most probable bubble diameter increases monotonically with increasing gas injection flow rate and decreases with increasing reference velocities.

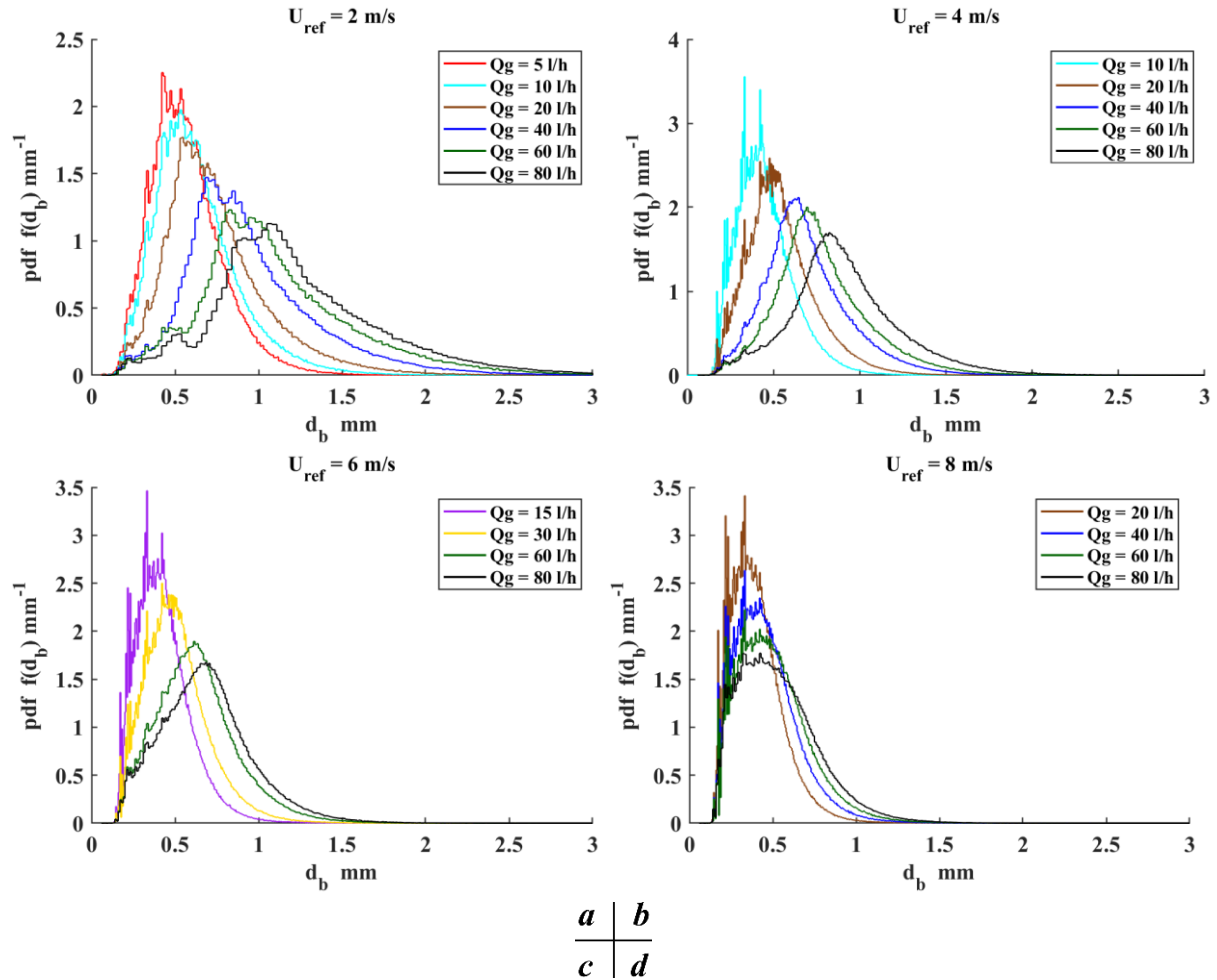


Figure IV. 6 Probability density functions of equivalent bubble diameters for different operating conditions

It can be seen, from **Figure IV. 6**, that the *PDF* of bubble diameter are asymmetrical and skewed to the left.

It has been reported in study of turbulent pipe flow under gravity and micro-gravity conditions (*Colin et al., 2012*), and also in the coalescence dominant regime (*Razzaque et al. 2003*), that the bubble size distributions follow a lognormal law. In this framework, the *PDF* of bubble diameter derives from:

$$PDF(d_b) = \frac{1}{d_b \sigma \sqrt{2\pi}} \exp\left(-\frac{(\ln(d_b) - \mu)^2}{2\sigma^2}\right) \quad 4 - 6$$

where μ is the median diameter and σ is a parameter characteristic of the width of the diameter distribution.

Figure IV. 7 shows the probability density functions of bubble diameters for two extreme cases of velocities and global air injection rates. Lognormal fits of the experimental data are also plotted. It can be seen in **Figure IV. 7a** that, at 8 m/s and $Q_g = 20$ l/h, the lognormal law fits well onto the *PDF* of bubble size distribution; at lower velocity and higher gas injection rate (**Figure IV. 7b**), the *PDF* of the bubble diameter distribution deviates from the lognormal fit. **Table IV. 3** summarizes the mean and most probable diameter characterized by original data and estimated using the fitted lognormal law. A good agreement was achieved for case 1 (**Figure IV. 7a**).

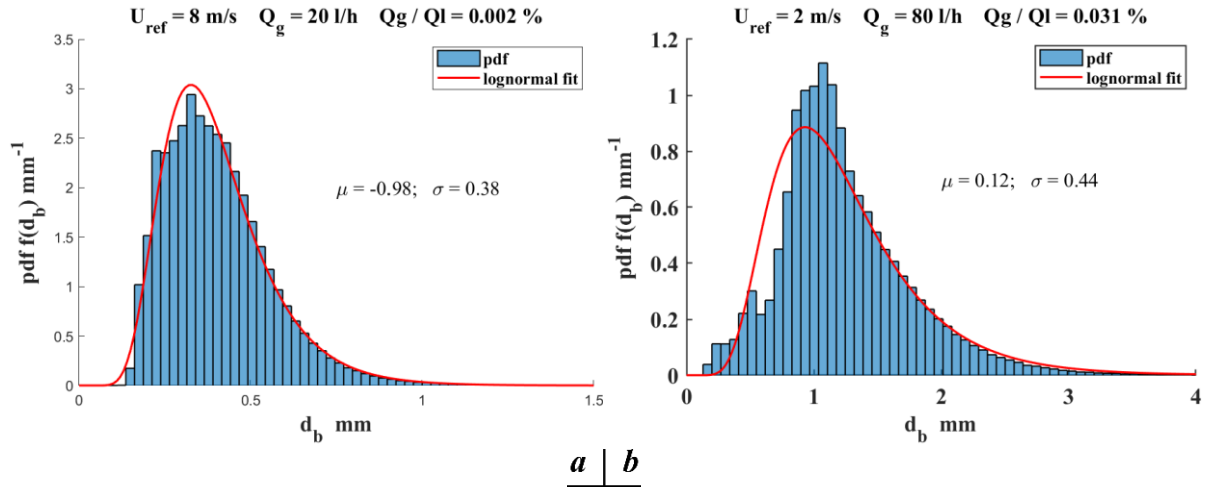


Figure IV. 7 Histograms of the bubble diameter distributions for two extreme cases of global air injection rates: a) $U_{ref} = 8 \text{ m/s}$, $Q_g = 20 \text{ l/h}$, $Q_g/Q_l = 0.002\%$ referred as case 1 b) $U_{ref} = 2 \text{ m/s}$, $Q_g = 80 \text{ l/h}$, $Q_g/Q_l = 0.031\%$ referred as case 2. Comparison to lognormal fit (red curves)

	Mean	Most probable	Mean ($e^{\mu + \frac{1}{2}\sigma^2}$)	Most probable ($e^{\mu - \sigma^2}$)
Case 1 (Figure IV. 7a)	0.40 mm	0.33 mm	0.40 mm	0.33 mm
Case 2 (Figure IV. 7b)	1.23 mm	1.07 mm	1.24 mm	0.93 mm

Table IV. 3 Arithmetic mean bubble diameters, lognormal deduced mean, and most probable bubble diameters

4.3.2 Evolution of the bubble equivalent diameter with flow conditions

The mean and *rms* of ensemble averaged bubble diameters are plotted against the global volumetric fraction Q_g/Q_l . (Figure IV. 8) For all reference velocities, the mean bubble size was observed to increase monotonically as Q_g/Q_l increases. The curves indicate that the bubble size would reach a certain limit as volumetric fraction continues to increase. As a matter of fact, the shear stress in the turbulent boundary layer will lead to a deformation and a breakage of bubbles. The *rms* values follow the same trend with regard to the volumetric fraction as for the mean values. The *rms* values for all velocities except for 2 m/s collapse onto a single curve, making think that the dispersion in bubble size was partially independent on the reference velocity.

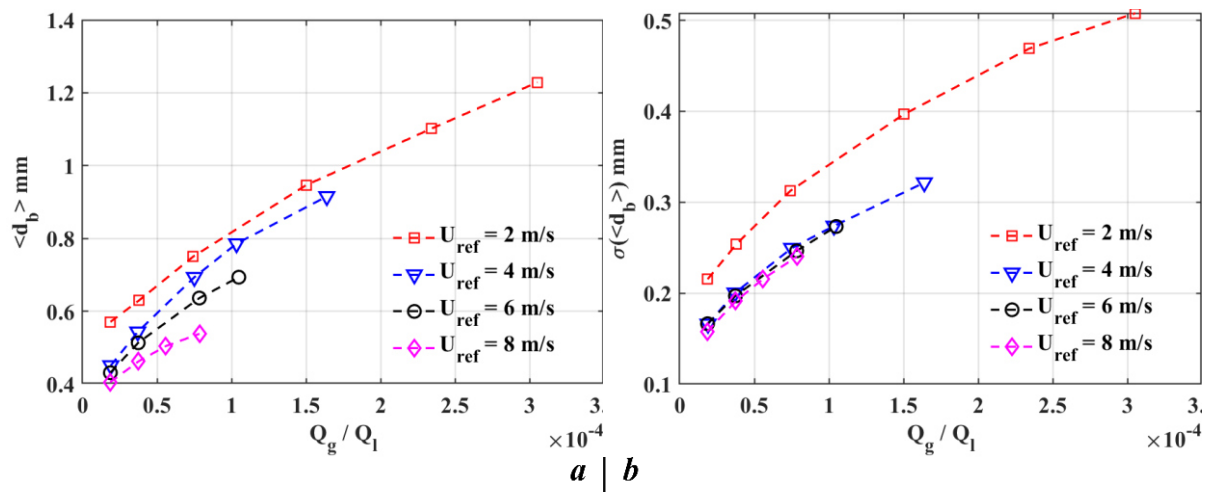


Figure IV. 8 Bubble size as a function of the reference velocity a) mean value, b) *rms* value

The evolution with respect to the reference velocity of the mean bubble diameter, scaled by the viscous length and scaled by the momentum thickness (measured in single phase flow) is shown in

Figure IV. 9. Operating points of same volumetric fractions are linked with solid lines. The mean bubble diameter $\langle d_b \rangle = \frac{\langle d_b \rangle}{\nu} u_*$ varies in a range from 40 to 140, corresponding to an equivalent dimensionless wall coordinate from buffer layer to inner log-law region. It is equally seen from **Figure IV. 9a** that d_b^+ increases with increasing velocity. This trend is consistent for all gas flow rates. For a given air injection rate, as the main flow velocity increases, the dimensionless bubble diameter seems to converge to a constant value. For a constant reference velocity, $\langle d_b \rangle$ increases as gas injection rate Q_g increases.

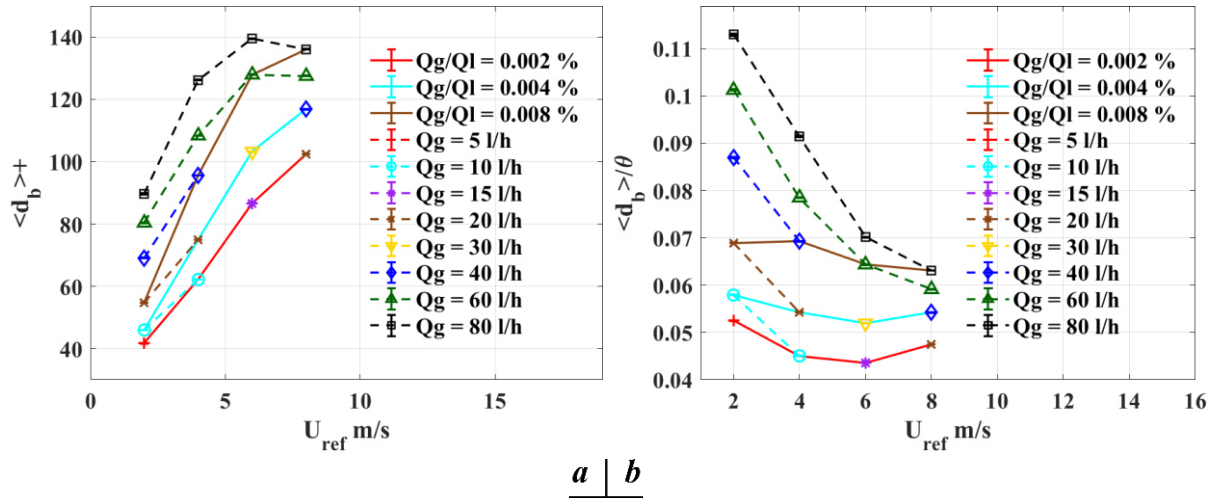


Figure IV. 9 Normalized mean bubble size as a function of the reference velocity a) scaled by the boundary layer viscous length ν/u_* , b) scaled by the momentum thickness (viscous length and momentum thickness are the ones of the single phase flow)

At constant gas flow rate Q_g , $\frac{\langle d_b \rangle}{\theta}$ is observed to decrease as the reference velocity increases. The bubble size was varied between 4% and 11% of the momentum thickness of the single phase flow. At constant volumetric fraction Q_g/Q_l , $\frac{\langle d_b \rangle}{\theta}$ is not very sensitive to U_{ref} .

Mean bubble diameter normalized by the momentum thickness is plotted against the volumetric fraction in **Figure IV. 10**. A good collapse with regard to the reference velocity is achieved. The normalized bubble diameter increases monotonically as Q_g/Q_l increases, following a 0.33 power law:

$$\frac{\langle d_b \rangle}{\theta} = 1.6 \left(\frac{Q_g}{Q_l} \right)^{0.33}$$

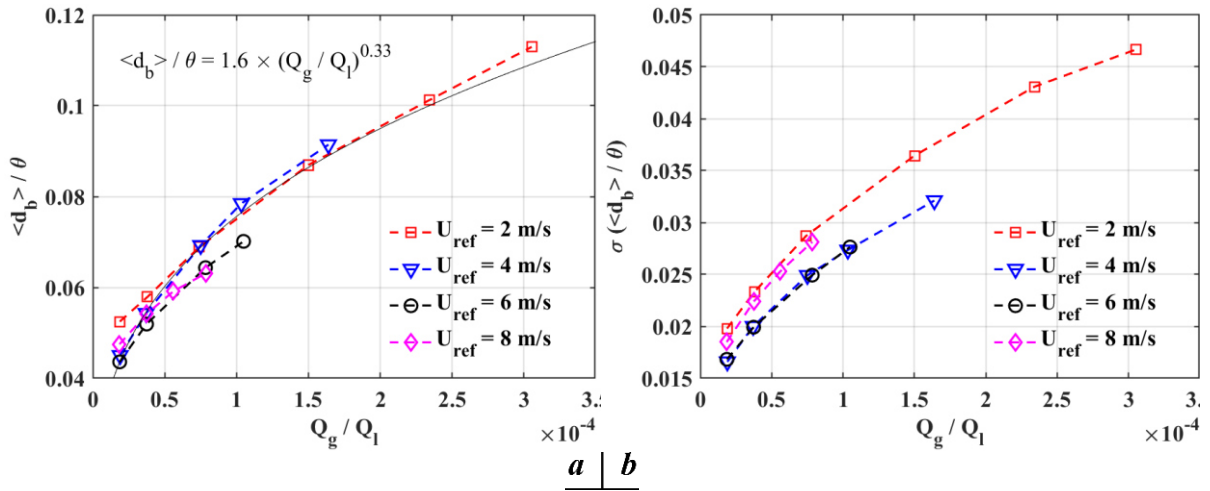


Figure IV. 10 Bubble size normalized by the boundary layer momentum thickness in single-phase flow in function of global gas volumetric fraction a) mean value, b) rms value

4.3.3 Evolution of the bubble aspect ratio with flow conditions

In this section, the shape of isolated bubbles will be approached by an elliptical geometry which is a more generalized form (Tomiyama, 2002). The semi-major and semi-minor axes a and b of the ellipse were chosen to characterize the magnitude of the flow-induced deformations of the bubbles. The bubble eccentricity factor was set to be the aspect ratio of the two semi-axes a/b .

Mean values of bubble aspect ratios $\langle a/b \rangle$ in function of the global volumetric fraction and reference velocities are shown in Figure IV. 11. It can be seen from Figure IV. 11a, that for a constant reference velocity, $\langle a/b \rangle$ increases monotonically as Q_g/Q_l increases: the higher the velocity, the higher the rate of increase, owing to inertial force. At constant Q_g , $\langle a/b \rangle$ increases (Figure IV. 11b) as U_{ref} increases.

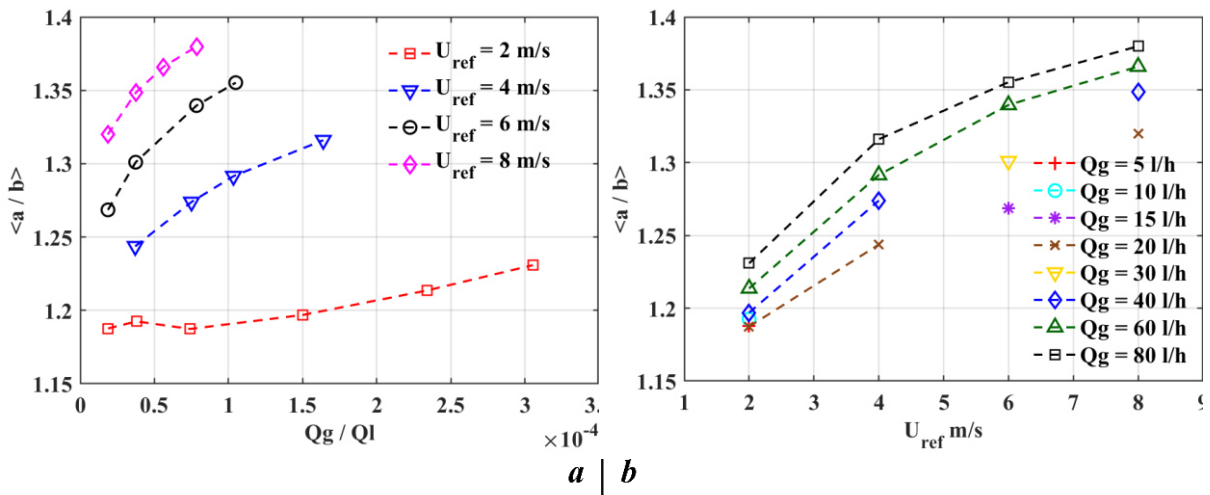


Figure IV. 11 Mean bubble eccentricity as a function of a) the volumetric fraction, b) the reference velocity

The ratio of inertial forces experienced by bubbles to the forces resulting from surface tension is characterized by the Weber number W_e .

$$W_e = \frac{\rho U^2 \langle d_b \rangle}{\sigma}$$

Where U denotes a characteristic liquid velocity, $\langle d_b \rangle$ the mean bubble diameter and σ the surface tension. The *Weber* number effects on the mean bubble aspect ratio are shown in **Figure IV. 12**. We_e was calculated based either on the reference velocity (**Figure IV. 12a**) or on the friction velocity from single-phase flow (**Figure IV. 12b**). An overall increase of $\langle a/b \rangle$ with regard to the *Weber* number was noticed from 2 m/s to 8 m/s. At constant reference velocity, a larger mean bubble diameter yields a higher level of bubble deformation. Same trends were observed in both figures. Curves of 2nd order polynomial fitting of the aspect ratio according to *Weber* number are shown in the figures. Note that we obtain quite a linear evolution of the mean aspect ratio with regard to We_{u^*} . Same linear trend with the *Weber* number is observed for bubbles rising in still liquids, for a small distortion ($a/b < 1.4$) (*Legendre, 2012*)

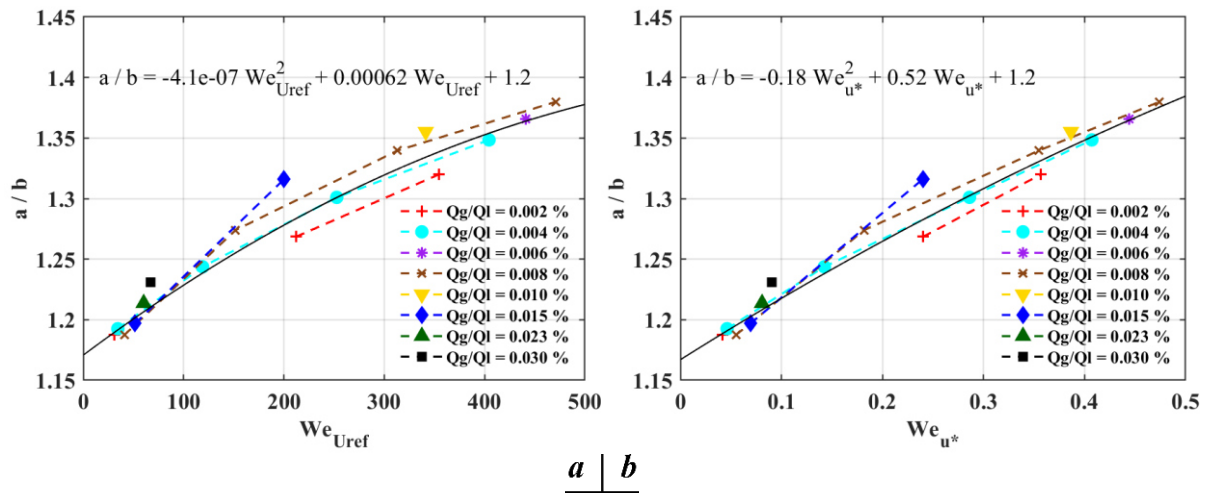


Figure IV. 12 Mean bubble aspect ratio as a function of the *Weber* number. a) We_e calculated based on reference velocity, b) We_e calculated based on the friction velocity from single-phase flow

4.4 Gas volume fraction

Much work has been focused on the scaling of gas volume fraction profiles under the influence of the gas injection rate (4.4.2) and the reference velocity (4.4.3). A universal scaling is introduced in 4.4.4. The evolution of the maximum gas volume fraction achieved near the wall and the evolution of the bubble thickness are examined extensively (4.4.5 - 4.4.6) according to non-dimensional parameters that controls the flow conditions.

4.4.1 General features of the gas volume fraction profiles

The local gas volume fraction α_v (Eq. 4 – 2) was estimated under all operating conditions. **Figure IV. 13** shows the profile of α_v in the wall normal direction for different air injection rates at constant velocities. It can be seen that α_v increases monotonically as getting close to the wall. In the near wall region where bubbles are highly concentrated (inner bubble layer), the local gas volume fraction α_v encounters a strong increase. At a y -position y_{α_v-max} in the vicinity of the wall, α_v reaches a maximum α_{v-max} , as expected for bubbles injected under a wall (*Ceccio, 2010; Sanders et al., 2006; Elbing et al., 2008*). At constant reference velocity, the increasing magnitude of α_v correlates well with the increasing gas injection rate which results in an increasing thickness of bubble layers. The magnitude of α_v at constant Q_g decreases as reference velocity increases.

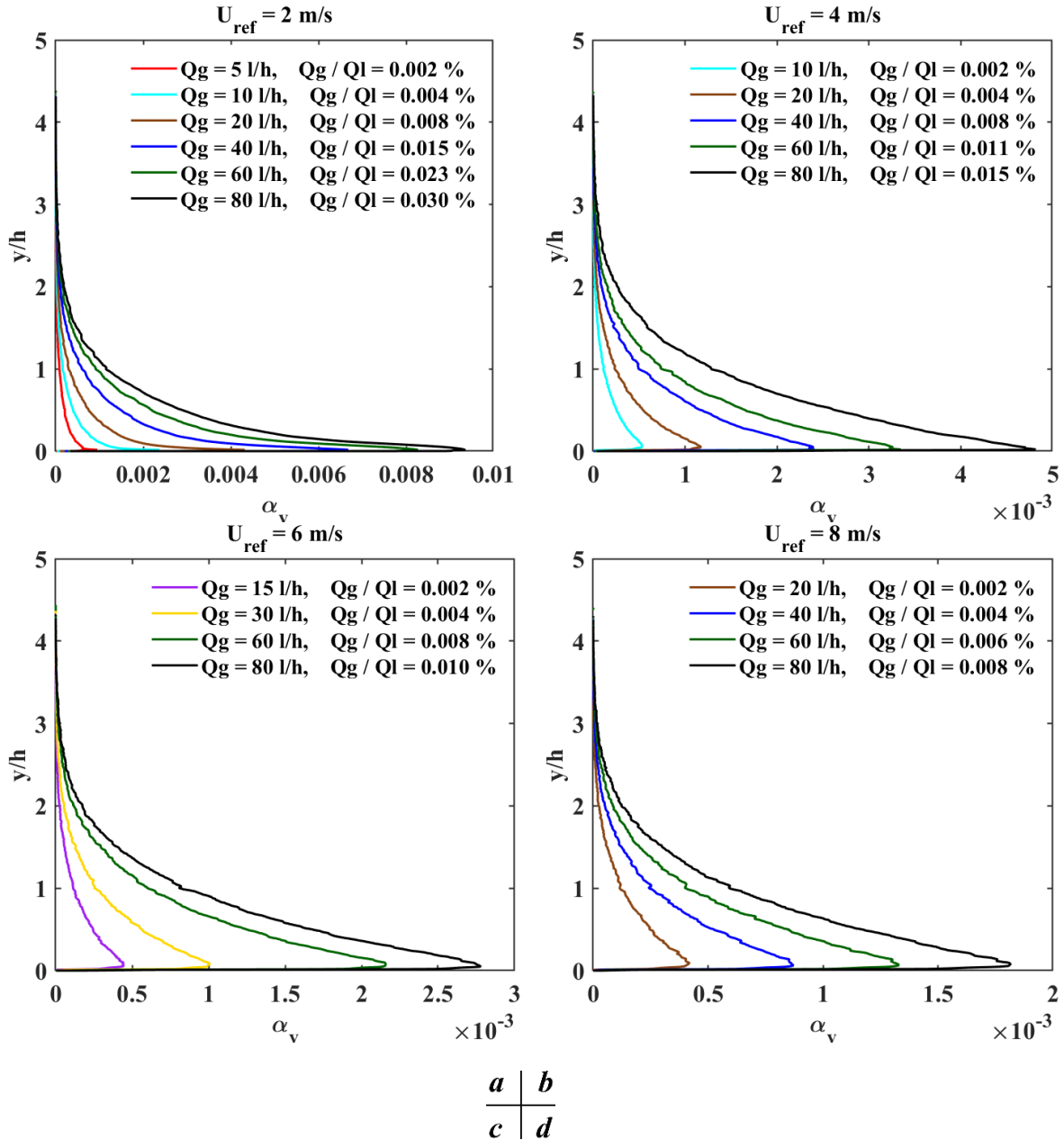


Figure IV. 13 Comparison of y -profiles of local volume fraction α_v between different gas injection rates Q_g at constant reference velocity

As discussed in previous section high concentration of wall-sliding bubbles has led to an underestimation of the local gas volume fraction α_v at $U_{ref} = 2 \text{ m/s}$. For the sake of correctness, volume fraction profiles in the vicinity of the wall at $U_{ref} = 2 \text{ m/s}$ for $Q_g/Q_l \geq 0.015\%$ (i.e.: $Q_g \geq 40 \text{ l/h}$) should be discarded.

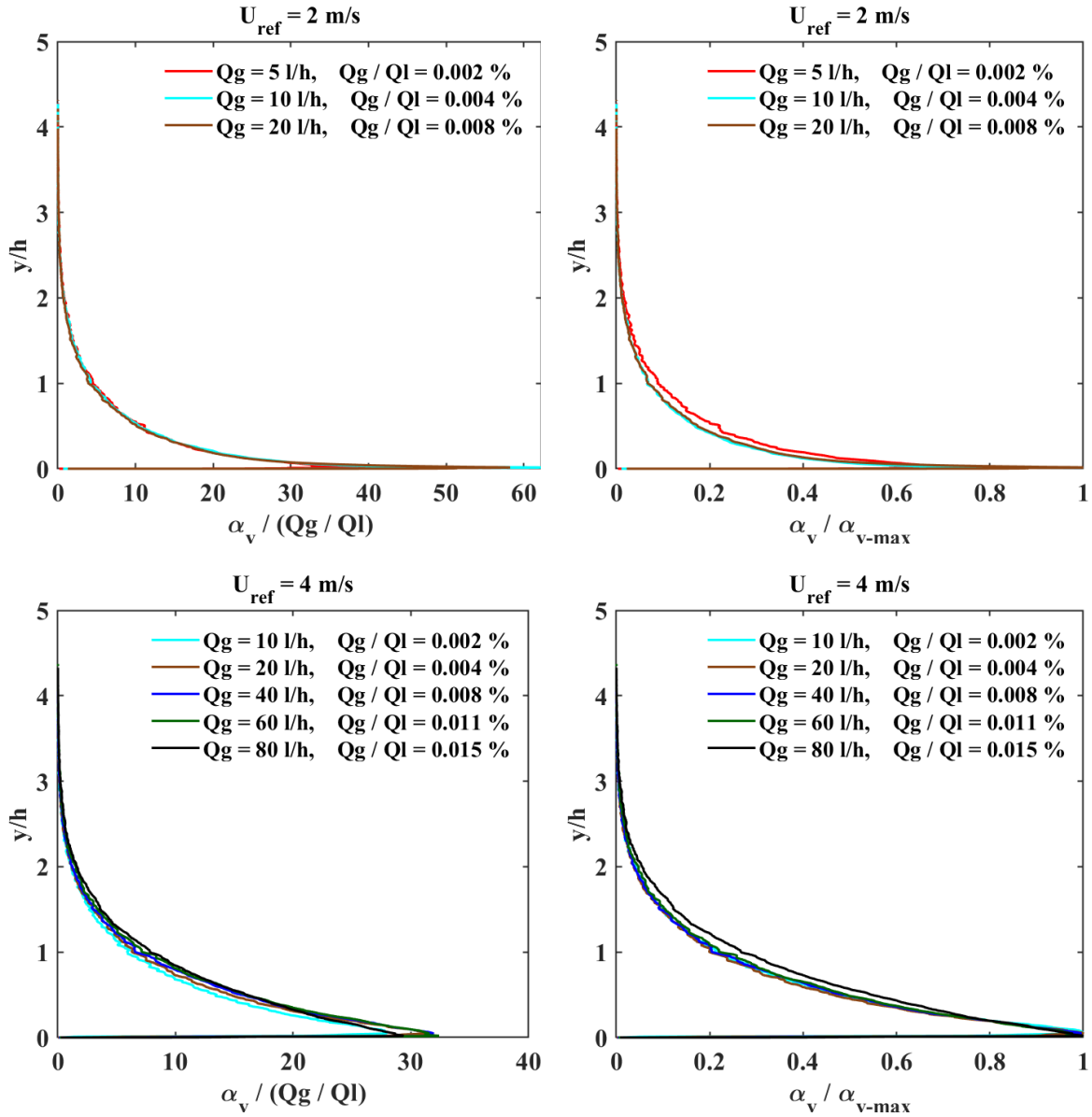
4.4.2 Self-similarity of y profiles of the gas volume fraction against the air injection rate

For analysis of self-similarity of the gas volume fraction profiles, profiles obtained for $Q_g/Q_l \geq 0.015\%$ at $U_{ref} = 2 \text{ m/s}$ have been removed, as we have shown previously that a severe bubble-overlapping took place in the field of view, owing to a wall-sliding bubble phenomenon.

To compare gas volume fraction's profiles at different air injection rate, the volume fraction can be either normalized by the global air volumetric fraction Q_g/Q_l or by the average volume fraction $\langle \alpha \rangle$ of

the boundary layer. Both representations are equivalent, as it was seen that $\langle \alpha \rangle$ evolves linearly with Q_g/Q_l , quite regardless of the reference velocity (**Figure IV. 2**). Another approach consists in normalizing the local gas volume fraction by its maximum value α_{v-max} . In **Figure IV. 14**, the profiles are illustrated scaled by the global volumetric fraction (**left column**) and by α_{v-max} (**right column**).

Self-similarity of the gas volume fraction profiles with regard to the gas injection rate is better achieved when the volume fraction is scaled by α_{v-max} than by $\frac{Q_g}{Q_l}$. A good self-similarity is obtained at $U_{ref} = 4, 6$ and 8 m/s for $\frac{Q_g}{Q_l} < 0.015\%$.



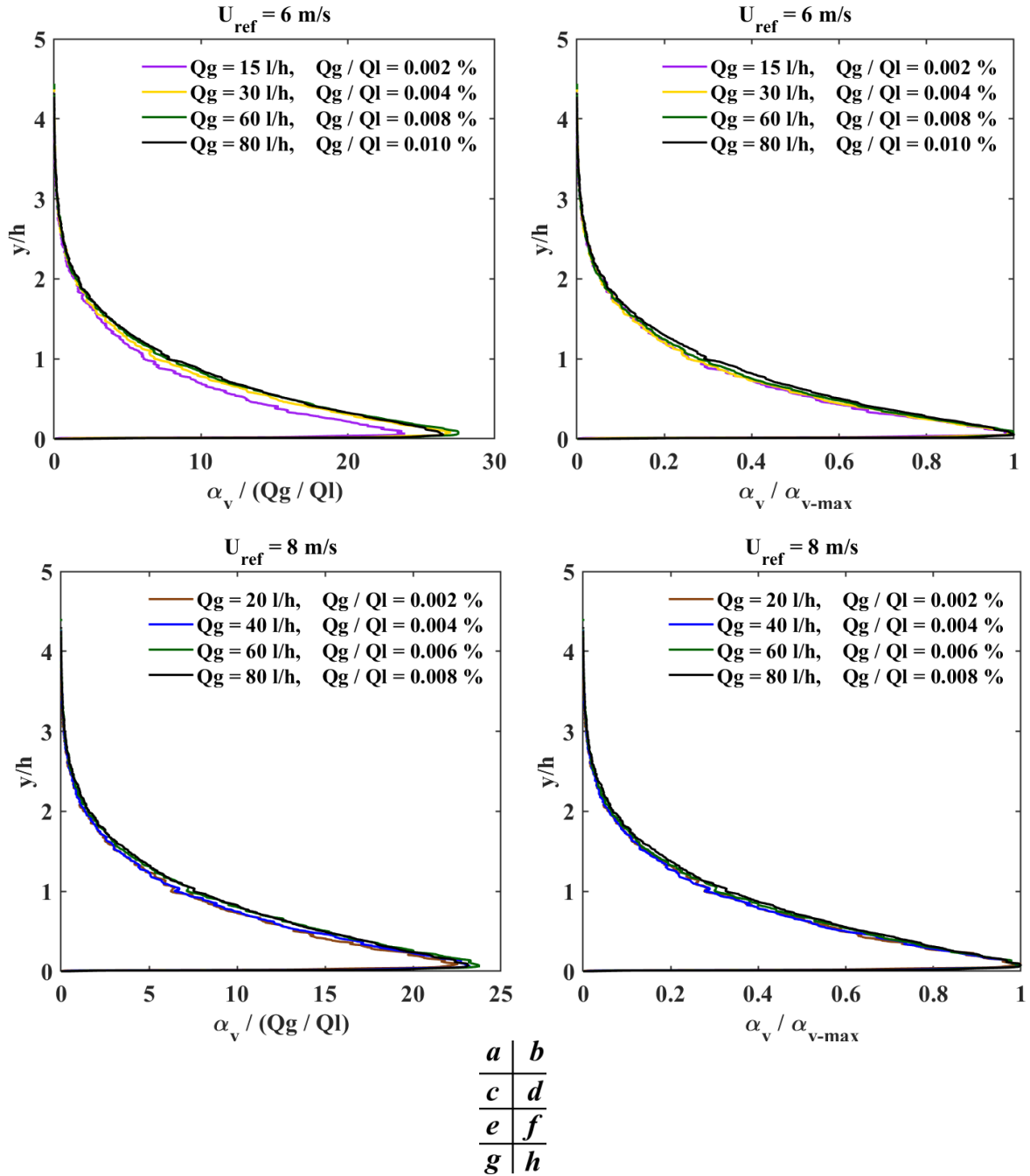


Figure IV. 14 Self-similarity of y -profiles of the volume fraction at constant reference velocity. The volume fraction is normalized by the global volumetric fraction (left column) and by α_{v-max} (right column).

4.4.3 Self-similarity of y profiles of the gas volume fraction against the velocity

The scaling analysis was performed for gas volume fraction α_v profiles at constant volumetric fractions in order to examine the self-similarity of the profiles under the influence of reference velocities (Figure IV. 15).

When scaling the gas volume fraction by $\frac{Q_g}{Q_l}$ (Figure IV. 15a,c,e), the profiles collapse well in the outer bubble layer ($y/h > 0.7$), except for the profiles at 2 m/s. At 2 m/s for all volumetric fractions, when comparison is made with other velocities, a deficit of the normalized volume fraction is observed in the outer bubble layer and an excess is observed in the inner bubble layer. At 2 m/s, peak values are nearly twice higher than those at 4 m/s. As the velocity and shear rate increase, the

turbulent mixing applied on the bubbles drive them away from the wall, making the peak value reducing at same volumetric fraction.

Owing to the gas mass conservation, the gas volume fraction α_v should satisfy the following relationship:

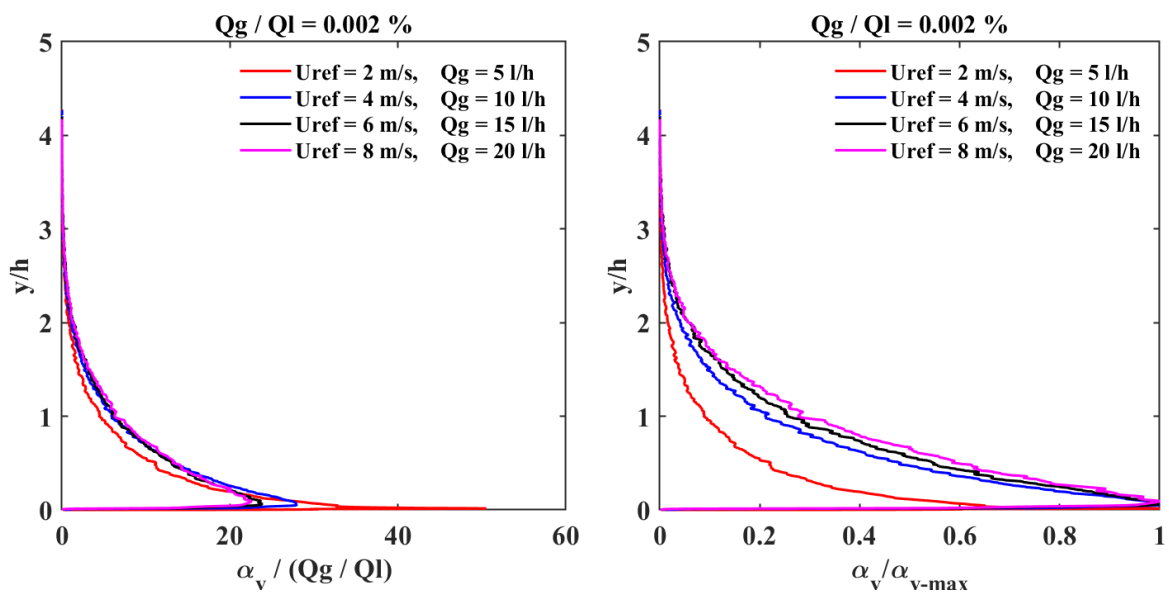
$$\int_0^\infty \frac{\alpha_v}{Q_g/Q_l} \frac{U_g}{U_{ref}} dy \sim H \quad 4 - 9$$

Where U_g denotes the stream-wise gas-phase mean velocity and H is the height of the water tunnel's section. It signifies that if U_g evolves in proportion to the liquid velocity in the bubble layer, the area under curve of profiles $\frac{\alpha_v}{Q_g/Q_l} = f(y)$ should be the same for the different reference velocities. At 4, 6 and 8 m/s where the self-similarity of $\frac{\alpha_v}{Q_g/Q_l}$ is achieved in the outer bubble layer, the peak value reduction results in a decrease of the area under the curve, letting suppose that the stream-wise velocity of the gas phase normalized by the reference velocity is augmented as the velocity in the tunnel increases. Analysis of gas-phase velocity components will be discussed in 4.5.

On the other hand, scaling the gas volume fraction by α_{v-max} has been tried (Figure IV. 15b,d,f). It provides a good collapsing of the profiles in the very near wall region but fail to collapse the profiles in the outer bubble region.

As the volume fraction's peak location $y_{\alpha v-max}$ moves away from the wall when the reference velocity increases, it is worth trying to scale the distance from the wall by a distance which is expected to evolve with the reference velocity.

In Figure IV. 16, different scales of the profiles $\frac{\alpha_v}{\alpha_{v-max}}$ are examined. The wall-normal distance is either scaled by the momentum thickness θ (left column) or by the distance of maximum gas volume fraction $y_{\alpha v-max}$ (right column). The similarity fails with both scaling factors. For θ scaling, it is not surprising: as θ decreases with the increasing U_{ref} (Table IV. 1). The scaling with $y_{\alpha v-max}$ is definitively not suited for collapsing profiles in the outer bubble region.



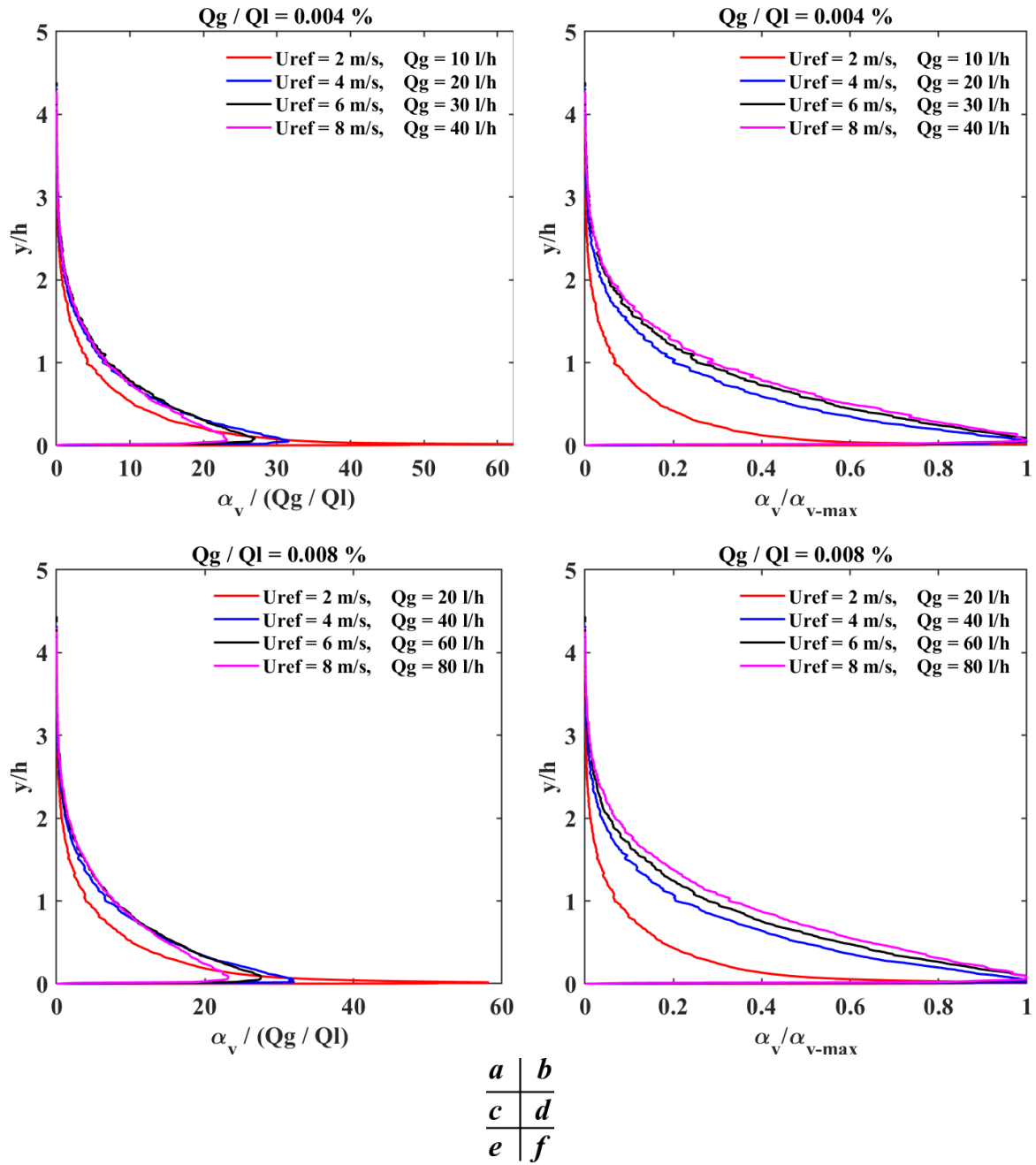
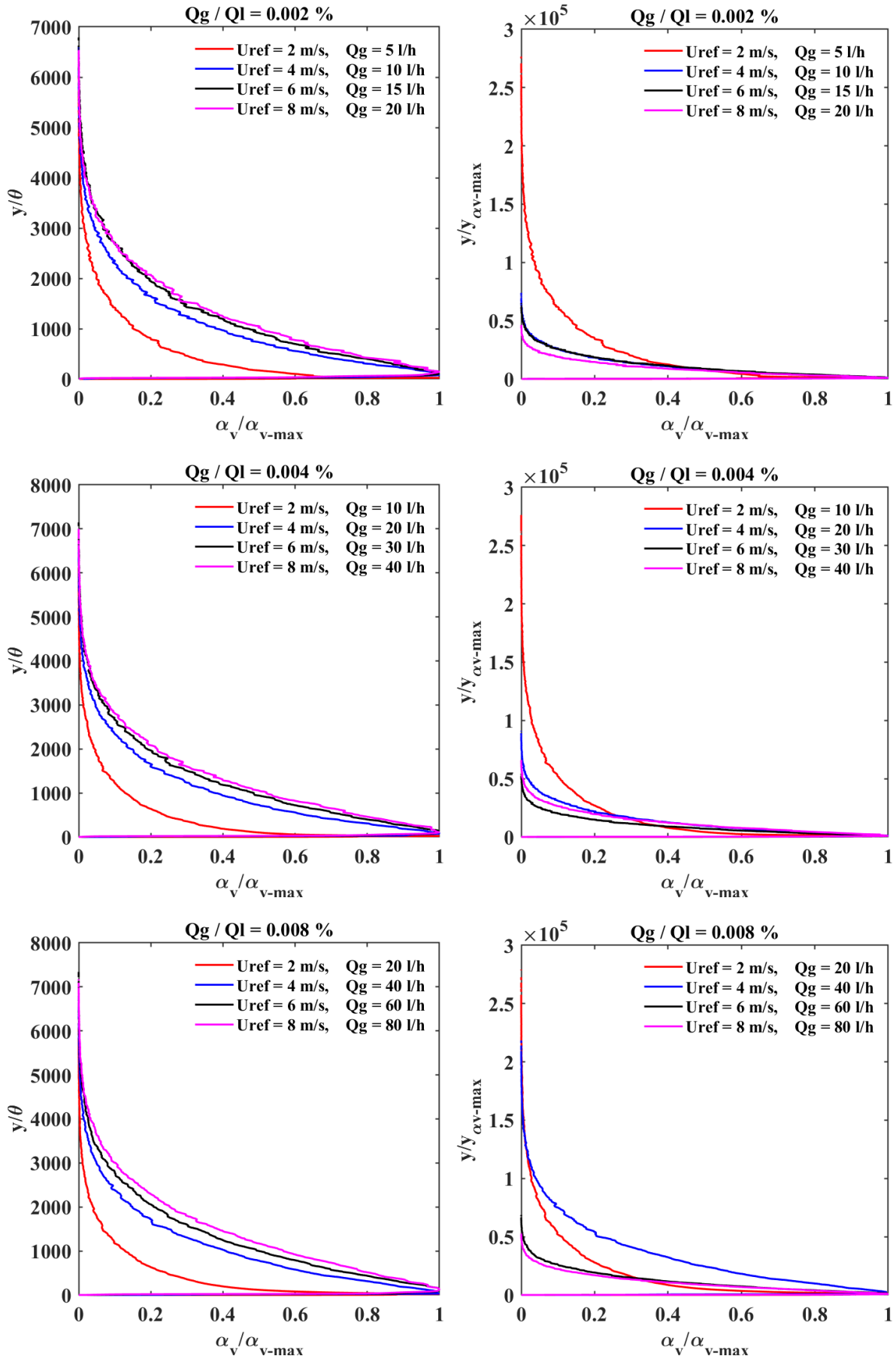


Figure IV. 15 Self-similarity of y-profiles of the volume fraction at constant volumetric fraction. The volume fraction is normalized by the volumetric fraction (left column) and maximum gas volume fraction (right column).



<i>a</i>	<i>b</i>
<i>c</i>	<i>d</i>
<i>e</i>	<i>f</i>

Figure IV. 16 Self-similarity of y -profiles of the volume fraction, normalized by the maximum gas volume fraction at constant volumetric fraction. Wall normal distances are normalized by the single-phase momentum displacement (left column) and the maximum gas volume fraction y -location (right column).

4.4.4 Self-similarity of the y profiles of the gas volume fraction against both velocity and air injection rate

In order to scale the wall-normal distance and find a good collapsing of the profiles of $\frac{\alpha_v}{\alpha_{v-max}}$, it is desirable to adjust a thickness Δ_b according to the velocity and gas injection rate. The evolution of Δ_b with the *Reynolds* number and the volumetric fraction will be shown and discussed in part *f*)

Figure IV. 17 shows the similarity of the α_v/α_{v-max} profiles with wall-normal distance scaled by Δ_b . A good collapse is achieved for data in both the inner and the outer bubble layers. It appears obvious that two distinct families of similar profiles can be identified. Profiles at 2 m/s collapse onto one family member while profiles at all higher velocities collapse onto another one.

The exponential fit of the each data family in the outer bubble layer yields the following relationship:

$$\frac{\alpha_v}{\alpha_{v-max}} = 0.9 \times \exp\left(-\left(\frac{y-y_{\alpha v-max}}{0.3 \times \Delta_b}\right)^{0.6}\right) \text{ for } y > y_{\alpha v-max} \text{ and } Re_{\theta} = 21662 (U_{ref} = 2 \text{ m/s}) \quad 4 - 10$$

$$\frac{\alpha_v}{\alpha_{v-max}} = \exp\left(-\left(\frac{y-y_{\alpha v-max}}{0.5 \times \Delta_b}\right)\right) \text{ for } y > y_{\alpha v-max} \text{ and } Re_{\theta} \geq 40623 (U_{ref} \geq 4 \text{ m/s}) \quad 4 - 11$$

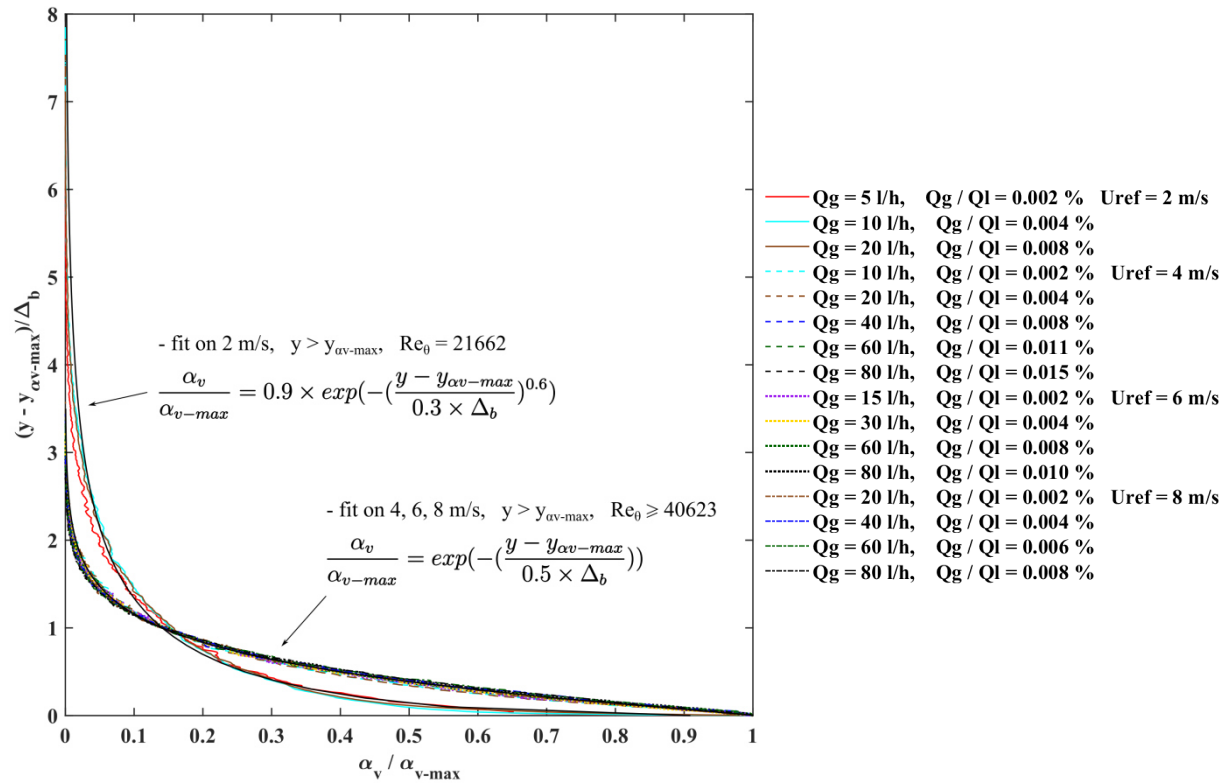


Figure IV. 17 Self-similarity in the outer bubble layer for every flow conditions of y -profiles of the volume fraction normalized by the maximum gas volume fraction near the wall. Wall normal distances are normalized by the thickness Δ_b

For $U_{ref} = 4, 6, 8 \text{ m/s}$ and for $U_{ref} = 2 \text{ m/s}$, $1.5\Delta_b$ and $1.8\Delta_b$ accordingly, are representative of the bubble layer thickness where $\frac{\alpha_v}{\alpha_{v-max}} = 5\%$.

In the inner bubble layer, no self-similarity was obtained, when plotting $\frac{\alpha_v}{\alpha_{v-max}} = f\left(\frac{y-y_{av-max}}{\Delta_b}\right)$ or $\frac{\alpha_v}{\alpha_{v-max}} = f\left(\frac{y}{y_{av-max}}\right)$.

4.4.5 Analysis of the volume fraction peak in the vicinity of the wall according to the operating conditions (U_{ref} , Q_g)

Figure IV. 18a shows the near wall α_v peak values α_{v-max} in function of Q_g/Q_l . The linear increase of α_{v-max} is observed with global volumetric fraction increasing. **Figure IV. 18b** shows the evolution of $\alpha_{v-max}/(Q_g/Q_l)$ as a function of the Reynolds number Re_θ . For a constant global volumetric fraction, as Re_θ increases, α_{v-max} decreases. From a global point of view, $\alpha_{v-max}/(Q_g/Q_l)$, as a function of Re_θ , collapses well for all operating points at different velocity (except $U_{ref} = 2 \text{ m/s}$) and different global volumetric fraction (except $\frac{Q_g}{Q_l} = 0.002\%$).

The rate of expansion A with regard to Q_g/Q_l decreases as U_{ref} increases and follows quite a linear degression in function of U_{ref} except at 2 m/s :

$$A(U_{ref}) = -1.56 \times U_{ref} + 36.14 \quad 4 - 12$$

Another linear relationship with Re_θ of the expansion rate A was found:

$$A(Re_\theta) = -2.04e^{-4} \times Re_\theta + 38.31 \quad 4 - 13$$

It yields:

$$\alpha_{v-max} = A(Re_\theta) Q_g/Q_l \quad 4 - 14$$

Figure IV. 18c shows the evolution of $\alpha_{v-max}/(Q_g/Q_l)$ as a function of dimensionless bubble size $\langle d_b \rangle^+ = \langle d_b \rangle u^*/\nu$. At a constant Q_g/Q_l , $\alpha_{v-max}/(Q_g/Q_l)$ is reported to decrease as $\langle d_b \rangle^+$ increases. Indeed, bubbles characterized by a larger size ratio to the viscous length are rather subjected to turbulent transport across the boundary layer, which makes $\alpha_{v-max}/(Q_g/Q_l)$ decreasing. On the other hand, at a constant $\langle d_b \rangle^+$, the increase of Q_g/Q_l somehow induces an increase in $\alpha_{v-max}/(Q_g/Q_l)$.

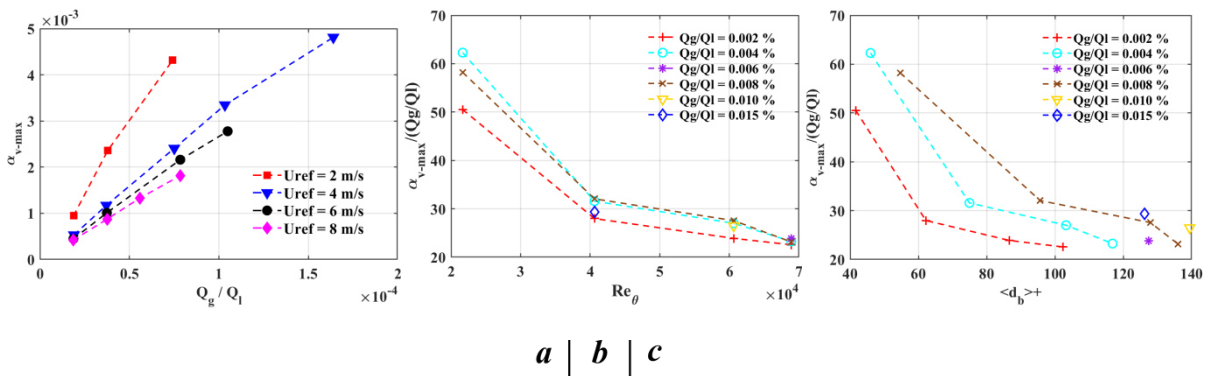


Figure IV. 18 Evolution of the maximum volume fraction near the wall according to the operating conditions: a) α_{v-max} with regard to Q_g/Q_l , b) evolution of $\alpha_{v-max}/(Q_g/Q_l)$ in function of Re_θ , c) evolution of $\alpha_{v-max}/(Q_g/Q_l)$ in function of $\langle d_b \rangle^+$

Re_θ and $\langle d_b \rangle^+$ are non dimensional parameters that rather influence the turbulent dispersion of the bubbles. Their augmentation leads to a homogenization of the volume fraction and hence a decrease in the volume fraction peak value. Competition with buoyancy effect must be analyzed. For this purpose, let us introduce the Froude number, based on the bubble diameter and the reference velocity, defined as:

$$Fr = \frac{U_{ref}}{\sqrt{g\langle d_b \rangle}} \quad 4 - 15$$

Figure IV. 19 shows the evolution of $\alpha_{v-max}/(Q_g/Q_l)$ with regard to the inverse of the Froude number. The different operating points are plotted according to the reference velocity.

The more the gravity effect (the higher $1/Fr$), the higher $\frac{\alpha_{v-max}}{Q_g/Q_l}$. Data of $\alpha_{v-max}/(Q_g/Q_l)$ collapse fairly well at higher velocities than 2m/s and show a linear dependence on $1/Fr$. A linear fit of the data except for 2 m/s yields the following relationship:

$$\frac{\alpha_{v-max}}{Q_g/Q_l} = \frac{721.6}{Fr} + 17 \quad \text{for } 40 < Fr < 120 \quad 4 - 16$$

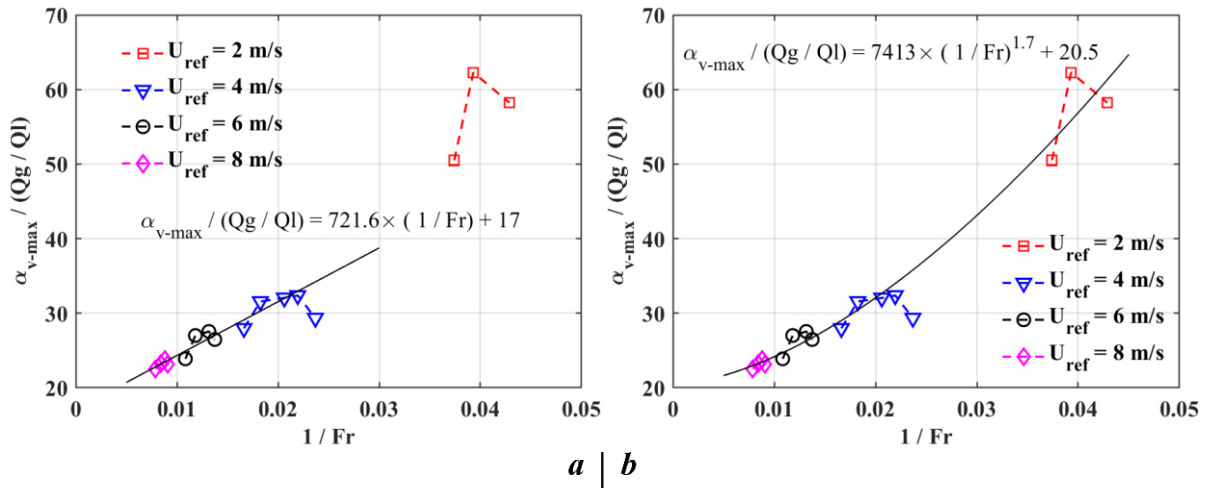


Figure IV. 19 Evolution of the maximum volume fraction near the wall according to the operating conditions: $\alpha_{v-max}/(Q_g/Q_l)$ with regard to $1/Fr$

When taking into account the data even at small Froude number (achieved for $U_{ref} = 2m/s$), the maximum value of $\alpha_{v-max}/(Q_g/Q_l)$ yields:

$$\frac{\alpha_{v-max}}{Q_g/Q_l} = \frac{7413}{Fr^{1.7}} + 20.5 \quad \text{for } 20 < Fr < 120 \quad 4 - 17$$

Figure IV. 20 shows the evolution of the distance from the wall of the volume fraction peak $y_{\alpha v-max}$ normalized by different heights, according to different non dimensional control parameters, such as Q_g/Q_l , Re_θ , $\langle d_b \rangle^+$ and Fr .

The peak distance was normalized by h , θ and $\langle d_b \rangle$ accordingly. Some qualitative remarks can be given. The peak distance is observed to increase globally as U_{ref} increases. It increases with the shear rate and turbulent dispersion, accordingly with Re_θ , $\langle d_b \rangle^+$. The y peak position shifts towards the wall

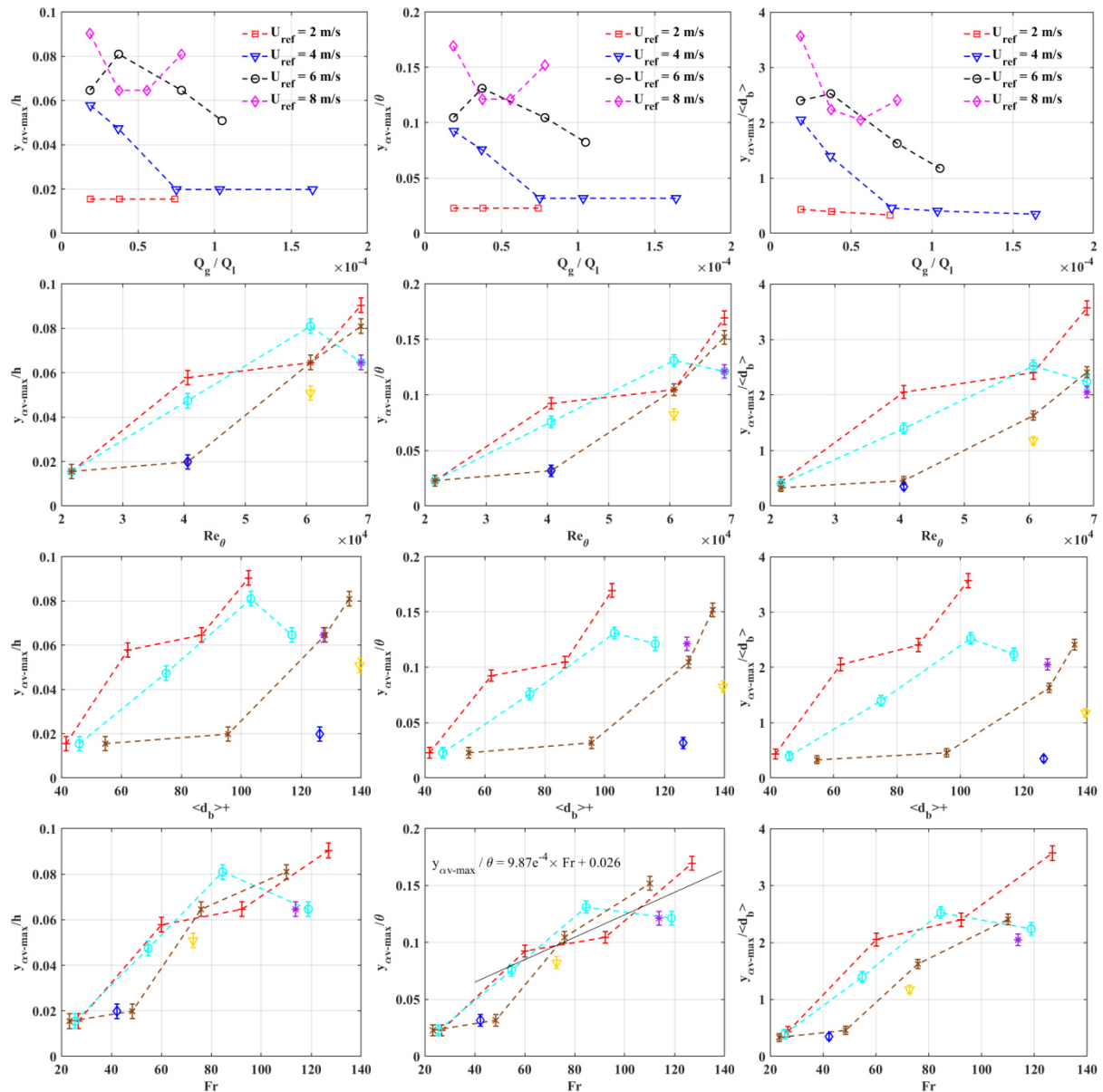
as Q_g/Q_l increases; this is a result of buoyancy enhancement owing to the expansion of the bubble size with the increase of the volumetric fraction (Eq. 4 – 7).

At 2 m/s for all volumetric fractions and at 4m/s for $\frac{Q_g}{Q_l} \geq 0.0075\%$, y_{av-max} is observed to be close to the wall and remains independent of Q_g/Q_l variation and U_{ref} variation. For these operating conditions, the buoyancy effect prevails and the volume fraction peak is located at a distance quite equal to $\langle d_b \rangle / 2$, which means that most of the bubbles are sliding along the wall.

The similarity of the peak wall normal distance according to control parameters of the flow has been examined. It is better achieved when the peak distance is normalized by the momentum thickness θ and when considering the Froude number. It yields the following relationships:

$$\frac{y_{av-max}}{\langle d_b \rangle} \approx 0.4 \quad \text{for } Fr < 50 \quad 4 - 18$$

$$\text{And } \frac{y_{av-max}}{\theta} \approx 9.87e^{-4}Fr + 0.026 \quad \text{for } Fr > 50 \quad 4 - 19$$



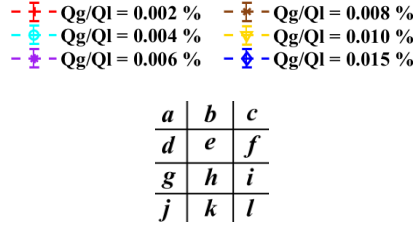


Figure IV. 20 Evolution of y_{av-max} , normalized by $h \theta$ and $\langle d_b \rangle^+$ in function of Q_g/Q_l , Re_θ , $\langle d_b \rangle^+$ and Fr

Now we are going to examine y_{av-max} that is normalized in the inner coordinate. **Figure IV. 21** shows the evolution of y_{av-max} normalized by the viscous length ν/u^* , as a function of Re_θ , Fr_θ and Fr . Generally speaking, $y_{av-max}u^*/\nu$ increases as reference velocity increases and collapses better for different air volumetric fractions when being plotted versus the Froude number Fr . The following linear relationship is observed:

$$\frac{y_{av-max}u^*}{\nu} \approx 9.87e^{-4}Fr - 43 \quad \text{for } Fr > 50 \quad 4 - 20$$

Values of $y_{av-max}u^*/\nu$ range from $20 < y^+ < 400$, and that corresponds to the buffer and logarithmic layer of the liquid mean stream-wise velocity profile.

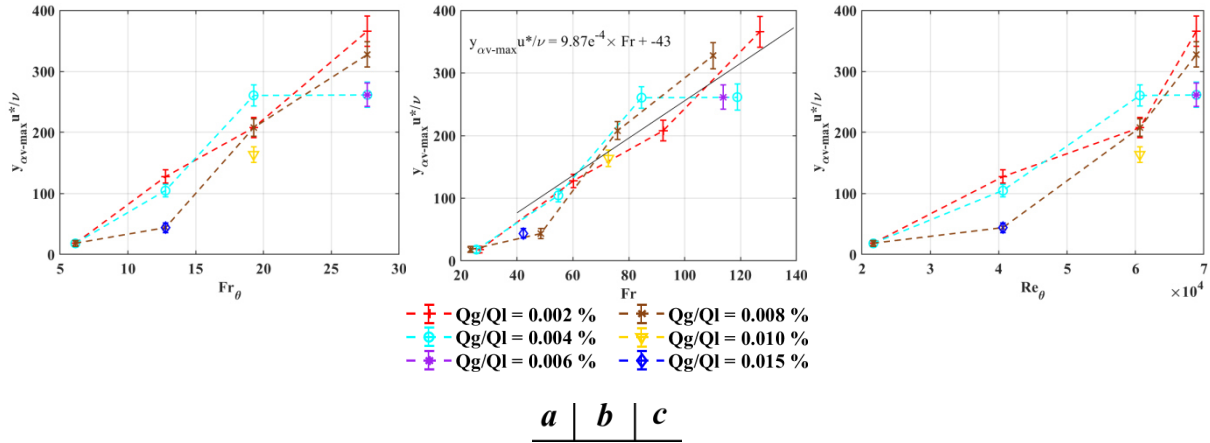


Figure IV. 21 Evolution of y_{av-max} , normalized the viscous length ν/u^* in function of Fr_θ , Re_θ , $\langle d_b \rangle^+$ and Fr (NB: viscous length and momentum thickness used for the normalization are those of the single phase flow)

4.4.6 Analysis of the integral scales of the bubble layer according to the operating conditions (U_{ref} , Q_g)

Figure IV. 22 shows the gas layer thickness δ_α with respect to Q_g/Q_l . Different scaling of δ_α (with h , with the momentum thickness θ or with the *Clauser's* universal thickness Δ) are tested on different graphics.

The gas layer thickness values collapse well against Q_g/Q_l when being scaled by the obstacle's height h , except at $U_{ref} = 2m/s$ for $\frac{Q_g}{Q_l} \geq 0.008\%$. It evidences a linear relationship of δ_α according to the volumetric fraction.

$$\frac{\delta_\alpha}{h} \approx 22 \frac{Q_g}{Q_l} \quad \text{for } Re_\theta \geq 40000 \quad 4 - 21$$

(This law was obtained by fitting a slope onto data at 4 m/s).

When using θ or Δ for the scaling of δ_α , two families of similarities appears according to U_{ref} (or Re_θ) which leads to two different linear fits.

$$\frac{\delta_\alpha}{\theta} \approx 24 \frac{Q_g}{Q_l} \quad \text{for } Re_\theta = 22000 \quad 4 - 22$$

$$\frac{\delta_\alpha}{\theta} \approx 35 \frac{Q_g}{Q_l} \quad \text{for } Re_\theta \geq 40000 \quad 4 - 23$$

$$\frac{\delta_\alpha}{\Delta} \approx 0.68 \frac{Q_g}{Q_l} \quad \text{for } Re_\theta = 22000 \quad 4 - 24$$

$$\frac{\delta_\alpha}{\Delta} \approx 0.91 \frac{Q_g}{Q_l} \quad \text{for } Re_\theta \geq 40000 \quad 4 - 25$$

Altogether with previous remarks about similarities of volume fraction y -profiles (**Figure IV. 17**), we can conclude that the gas layer characteristics are separated into 2 equilibrium families that might be somehow related to the natures of the single-phase flow itself.

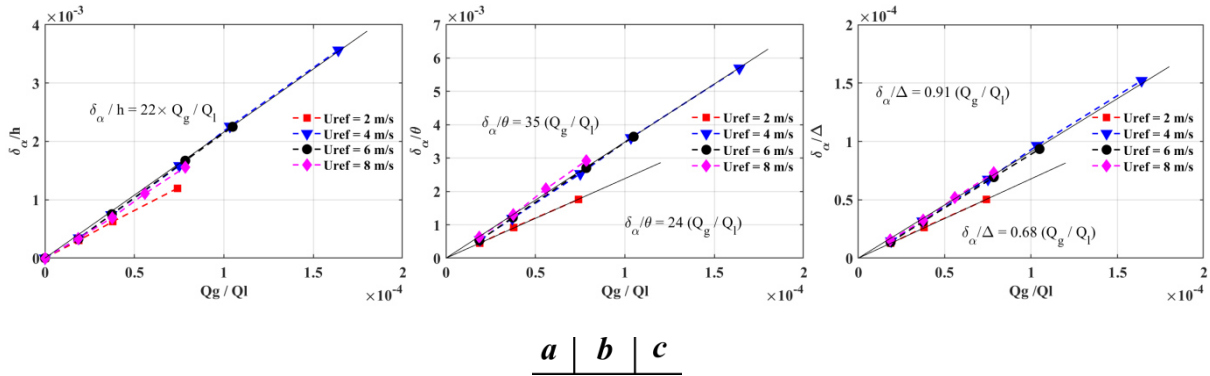


Figure IV. 22 Evolution of δ_α in function of Q_g/Q_l . δ_α is normalized: A) by h , B) by θ and C) by Δ

$\langle \alpha \rangle$ is the averaged volume fraction within a region bounded by the classical single-phase boundary layer (**Eq. 4 – 1**). It can be considered as a volumetric fraction inside the boundary layer. Thus, the ratio of $\delta_\alpha/\langle \alpha \rangle$ can be representative of an equivalent gas layer thickness. **Figure IV. 23** shows the evolution of $\delta_\alpha/\langle \alpha \rangle$, normalized by h, θ, Δ , with regard to Q_g/Q_l .

The equivalent gas layer thickness obviously increases when Q_g/Q_l augments. Nevertheless, for the operating points which are dominated by buoyancy effect and characterized ($\frac{\nu_{av-max}}{d_b} < 1$), $\frac{\delta_\alpha}{\langle \alpha \rangle}$ seems to converge to a constant value which depends on the velocity, regardless of the value of the volumetric fraction (this is verified at 2 m/s and at 4 m/s for the highest volumetric fraction). For these points, an increase in Q_g/Q_l leads to an increase of α_{v-max} , rather than an expansion of the gas layer.

Apart the case of $U_{ref} = 2 \text{ m/s}$, which is buoyancy dominated, $\frac{\delta_\alpha}{\langle \alpha \rangle}/h$ is decreased when U_{ref} augments. The gas layer's thickness evolves in the same way as the single-phase turbulent boundary layer's thickness when increasing the velocity.

The evolution of $\frac{\delta_\alpha}{\langle \alpha \rangle}/\theta$ and $\frac{\delta_\alpha}{\langle \alpha \rangle}/\Delta$ with regard to the velocity is not so obvious. A maximum is reached for the maximum velocity at $U_{ref} = 8 \text{ m/s}$, which is in agreement with an increase of the gas layer to the boundary layer ratio when increasing the contribution of turbulence induced bubble dispersion.

Note that due to the sensitivity of $\frac{\delta_{\alpha}}{\theta}$ to the global volumetric fraction, no similarity of the normalized equivalent gas layer thickness in function of *Froude* or *Reynolds* numbers was found against the global volumetric fraction. That's the reason why, the curves $\frac{\delta_{\alpha}}{\theta} = f(Re_{\theta}, Fr)$ are not displayed in this report.

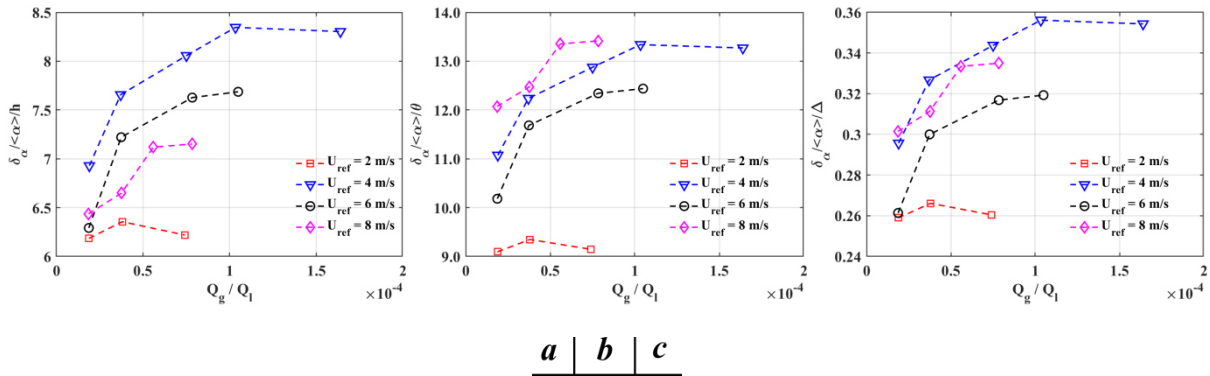


Figure IV. 23 Evolution of the equivalent gas layer's thickness $\frac{\delta_{\alpha}}{\langle \alpha \rangle}$ in function of Q_g / Q_l . $\frac{\delta_{\alpha}}{\langle \alpha \rangle}$ is normalized: A) by h , B) by θ and C) by Δ

As mentioned in 4.2.1, it is difficult to obtain a reliable bubble boundary thickness δ_b , since the edge at which $\alpha_v = 0.95 \langle \alpha \rangle$ is roughly determined due to a locally insufficient number of bubbles. **Figure IV. 24** shows the bubble boundary thickness δ_b with respect to Q_g / Q_l . At the smallest velocity, δ_b scaled by h , θ and Δ is decreased with the global volumetric fraction, as a result of increase in the bubble size and buoyancy dominant effect. At the largest velocity, on the contrary, it depicts an increase of the normalized δ_b values with respect to the volumetric fraction, as expected for inertia induced dominant effects. For intermediate velocities, δ_b seem to be quite insensitive in regards to Q_g / Q_l .

Figure IV. 25 shows the evolution of δ_b / θ according to the *Reynolds* and *Froude* numbers. Generally speaking, it confirms that the ratio of the bubble boundary thickness to θ increases with the velocity (i.e.: with Re_{θ} and Fr numbers).

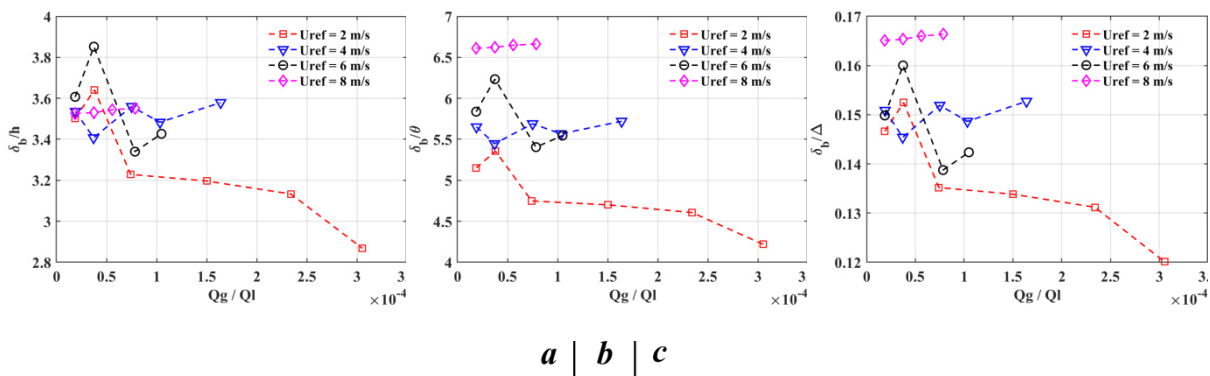


Figure IV. 24 Evolution in function of Q_g / Q_l of δ_b normalized a) by h , b) by θ and c) by Δ

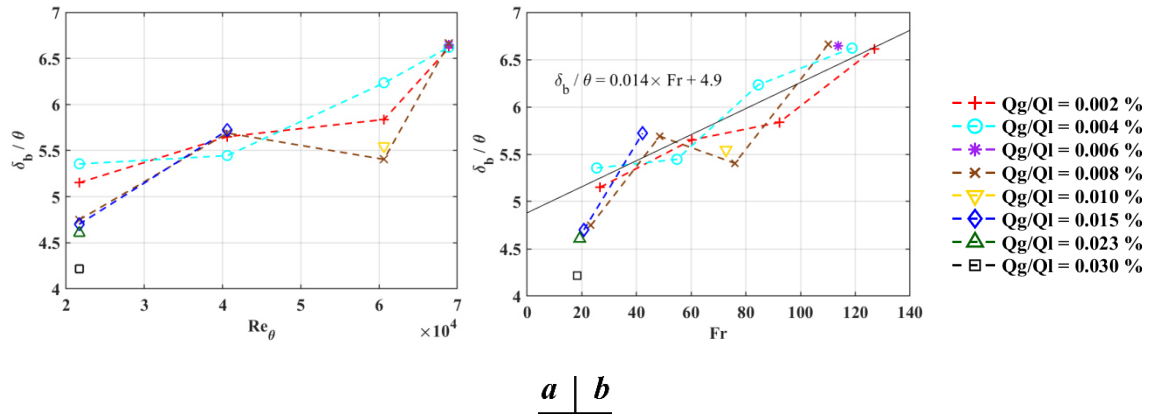


Figure IV. 25 Evolution of δ_b normalized by θ in function of a) Re_θ , and b) Fr

As shown in **Figure IV. 25**, δ_b/θ follows a linear increase with increasing Fr , in region of weak Fr number, δ_b/θ encounters a drop out of the linear fit.

$$\frac{\delta_b}{\theta} = 0.014 Fr + 4.9 \quad \text{for } Fr > 25 \quad 4 - 26$$

Figure IV. 26 shows the evolution of the dimensionless thickness Δ_b with respect to Q_g/Q_l .

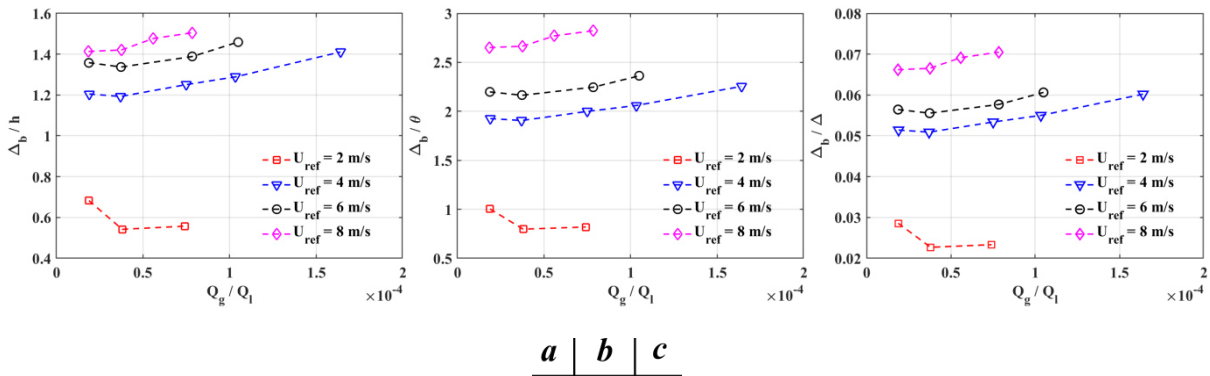


Figure IV. 26 Evolution in function of Q_g/Q_l of Δ_b normalized a) by h , b) by θ and c) by Δ

We can introduce another Froude number, based on the momentum thickness and the reference velocity.

$$Fr_\theta = \frac{U_{ref}}{\sqrt{g\theta}} \quad 4 - 27$$

Figure IV. 27 shows the similarity of Δ_b against the volumetric fraction under the influence of Re_θ , Fr and Fr_θ . For the purpose Δ_b is normalized by θ . The dimensionless thickness Δ_b in function of Fr_θ and Re_θ collapses rather well for $\frac{Q_g}{Q_l} \leq 0.008\%$. For the reference velocities $U_{ref} = 4, 6$ and 8 m/s , $\frac{\Delta_b}{\theta}$ follows a linear law with regard to Fr_θ .

$$\frac{\Delta_b}{\theta} = 0.054 \times Fr_\theta + 1.2 \quad \text{for } Re_\theta \geq 40000 \text{ (ie: } Fr_\theta \geq 13) \quad 4 - 28$$

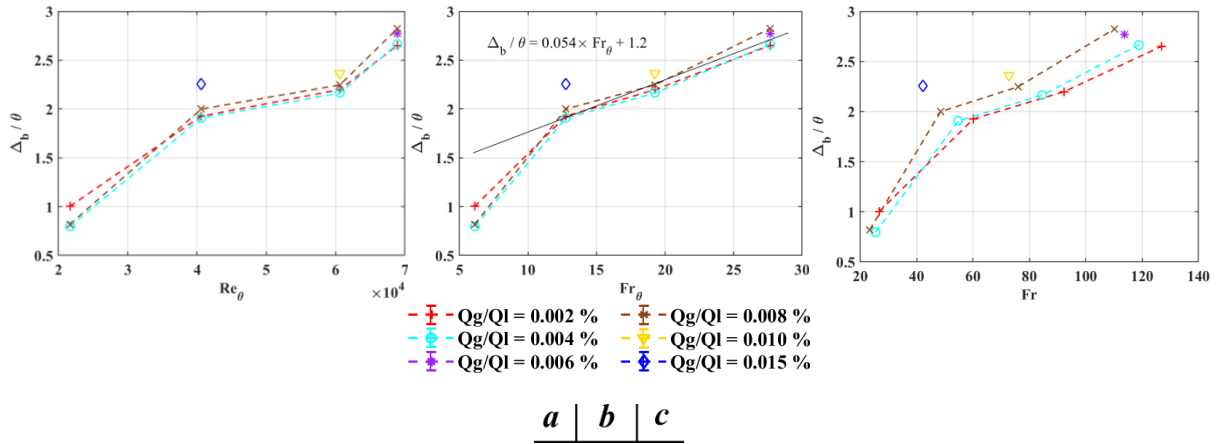


Figure IV. 27 Evolution of Δ_b normalized by θ a) in function of Re_θ , b) in function of Fr_θ and c) in function of Fr

4.5 Gas phase mean flow

In this section, wall normal profiles of the mean velocity components of the gas phase will be examined. For all the profiles, the velocity is normalized by the reference velocity and the y -coordinate is scaled by the height of the obstacle h .

Error bars linked to statistical convergence have been added on these profiles. Error bars are representative of the confidence interval, for a confidence level of 95%.

4.5.1 Mean stream-wise velocity profiles

Figure IV. 28 gives the evolution of the mean gas stream-wise velocity profiles at constant reference velocities under different air injection rates. Profiles in single-phase flow are plotted in dotted lines for the sake of comparison. When being compared to velocity profiles in single-phase flow, the gas phase profiles exhibit smaller velocity magnitudes far from the wall ($y > y_{shift}$) and larger velocity magnitudes in the near wall region ($y < y_{shift}$). y_{shift} moves slightly away from the wall as the reference velocity increases: $y_{shift}/h = 0.1$ to 0.2 from reference velocity 2 m/s to 8 m/s accordingly.

For $y/h > 1.5$, there is an inflection point in the gas stream-wise velocity profile. Above this point, the rate of increase of the velocity magnitude with the distance augments. The inflection point moves away from the wall when the reference velocity increases. Above the inflection point and for $y < y_{shift}$, profiles of the gas phase stream-wise velocity separate according to the gas injection rate. The higher the air injection rate, the smaller the gas velocity.

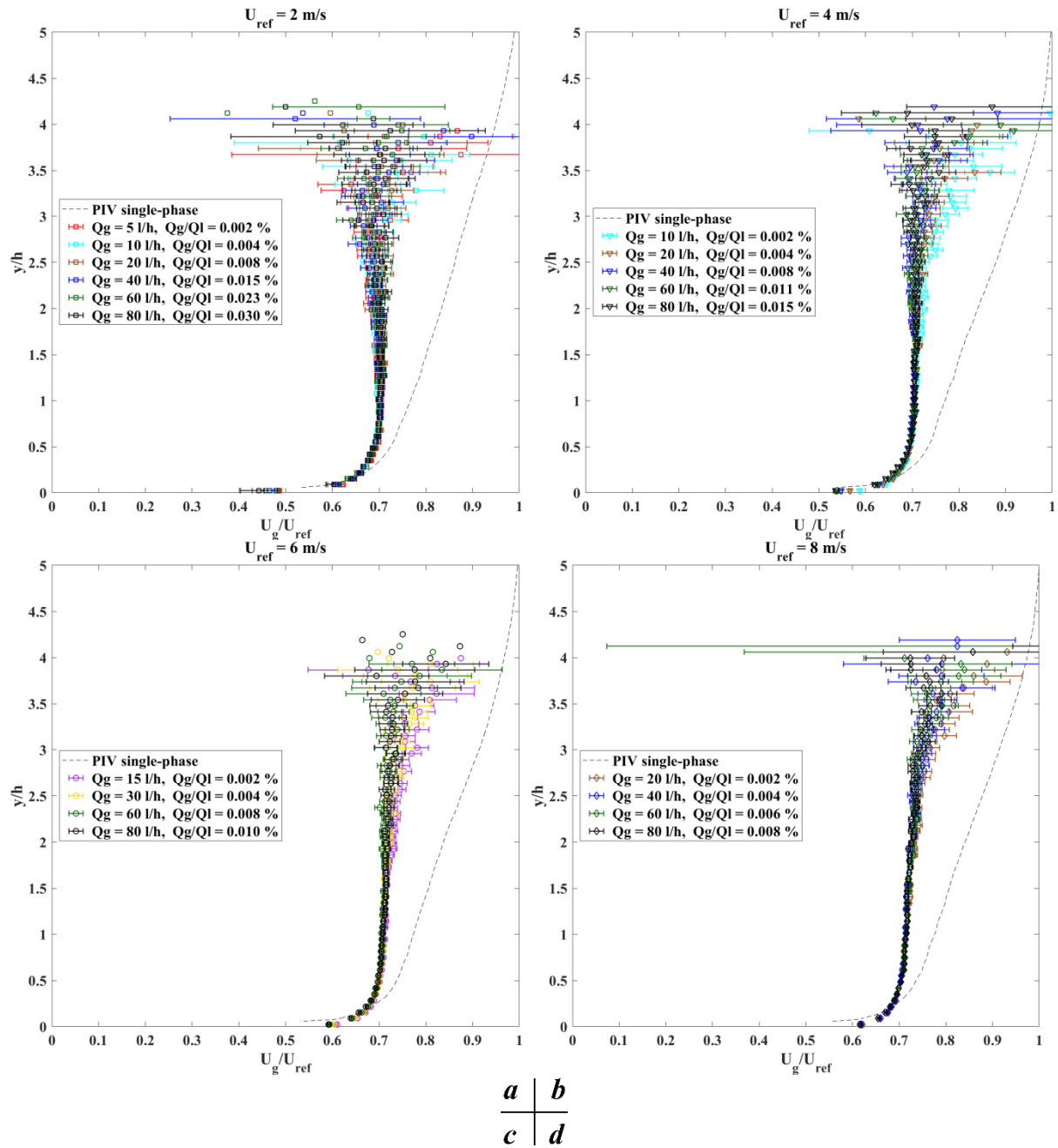


Figure IV. 28 Mean gas stream-wise velocity profiles, normalized by the reference velocity (y -coordinate normalized by h) at constant reference velocity, with single-phase PIV data in comparison

Figure IV. 29 shows the evolution of the mean gas stream-wise velocity profiles at constant volumetric fractions under different reference velocities. Over the whole range of y -coordinate, a higher reference velocity results in a higher ratio of the gas phase stream-wise velocity to the reference velocity.

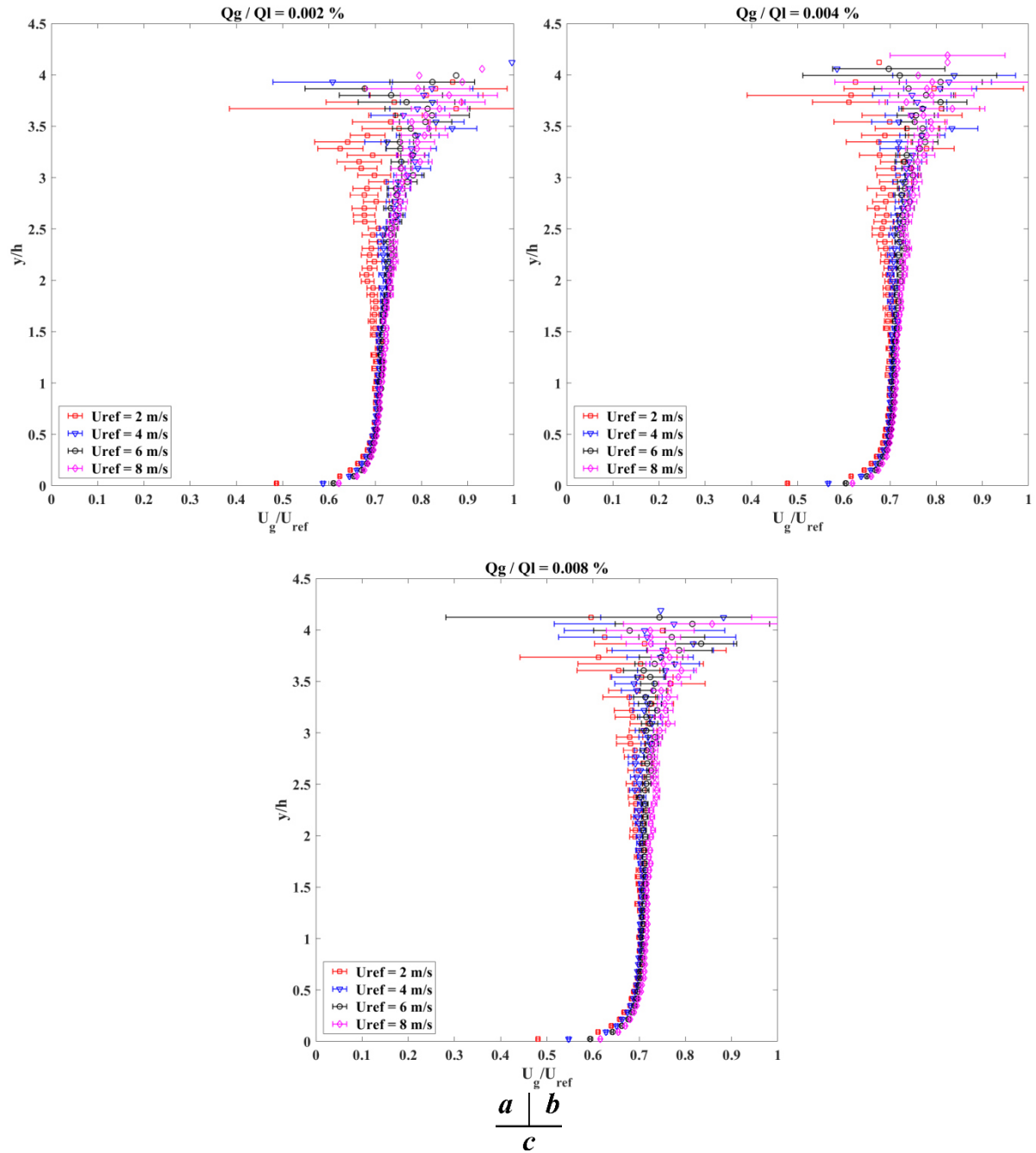


Figure IV. 29 Mean gas stream-wise velocity profiles, normalized by the reference velocity (y -coordinate normalized by h) at constant global volumetric fractions

4.5.2 Mean wall-normal velocity profiles

Figure IV. 30 displays the evolution of the mean gas wall-normal velocity profiles at constant reference velocities under different air injection rates. Profiles in single-phase flow are plotted in dotted lines for the sake of comparison. A good agreement was observed among profiles of all Q_g . It is noticeable that the wall normal velocity magnitude grows almost linearly with the wall distance, which is quite different than in single-phase flows. The mean wall normal gas velocity is positive, which means that bubbles globally move away from the wall. At the edge of the bubble layer, the normal gas velocity reaches a value of the order of $0.1 U_{ref} - 0.2 U_{ref}$ but the large confidence interval of the mean velocity at this position makes it difficult to determinate an accurate value.

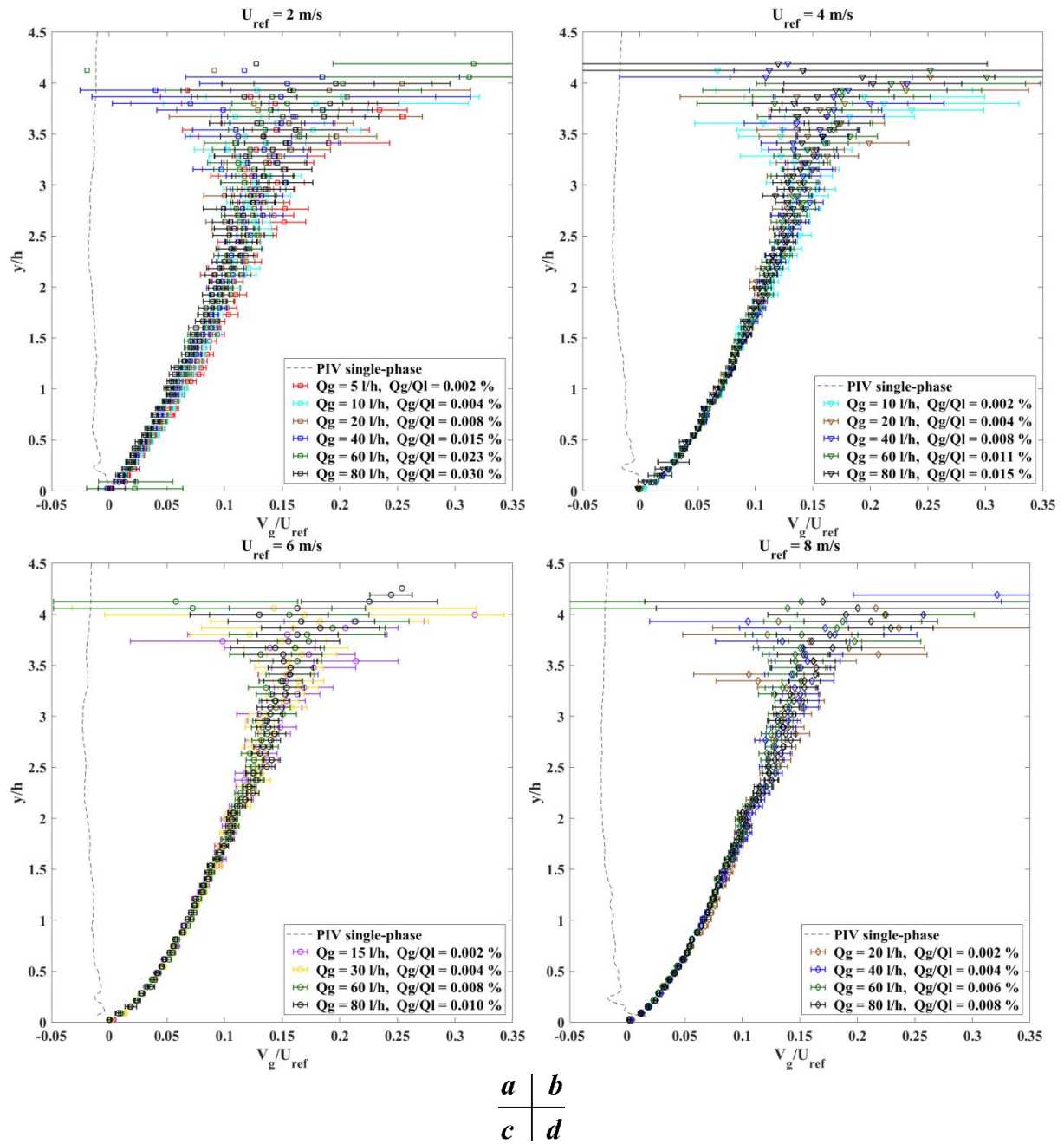


Figure IV. 30 Mean gas wall-normal velocity profiles, normalized by the reference velocity (y -coordinate normalized by h) at constant reference velocity, with single-phase PIV data in comparison

Figure IV. 31 shows the evolution of the mean gas wall-normal velocity profiles at constant volumetric fractions under different reference velocities. Over the whole range of y -coordinates, no visible influence of the reference velocity can be observed.

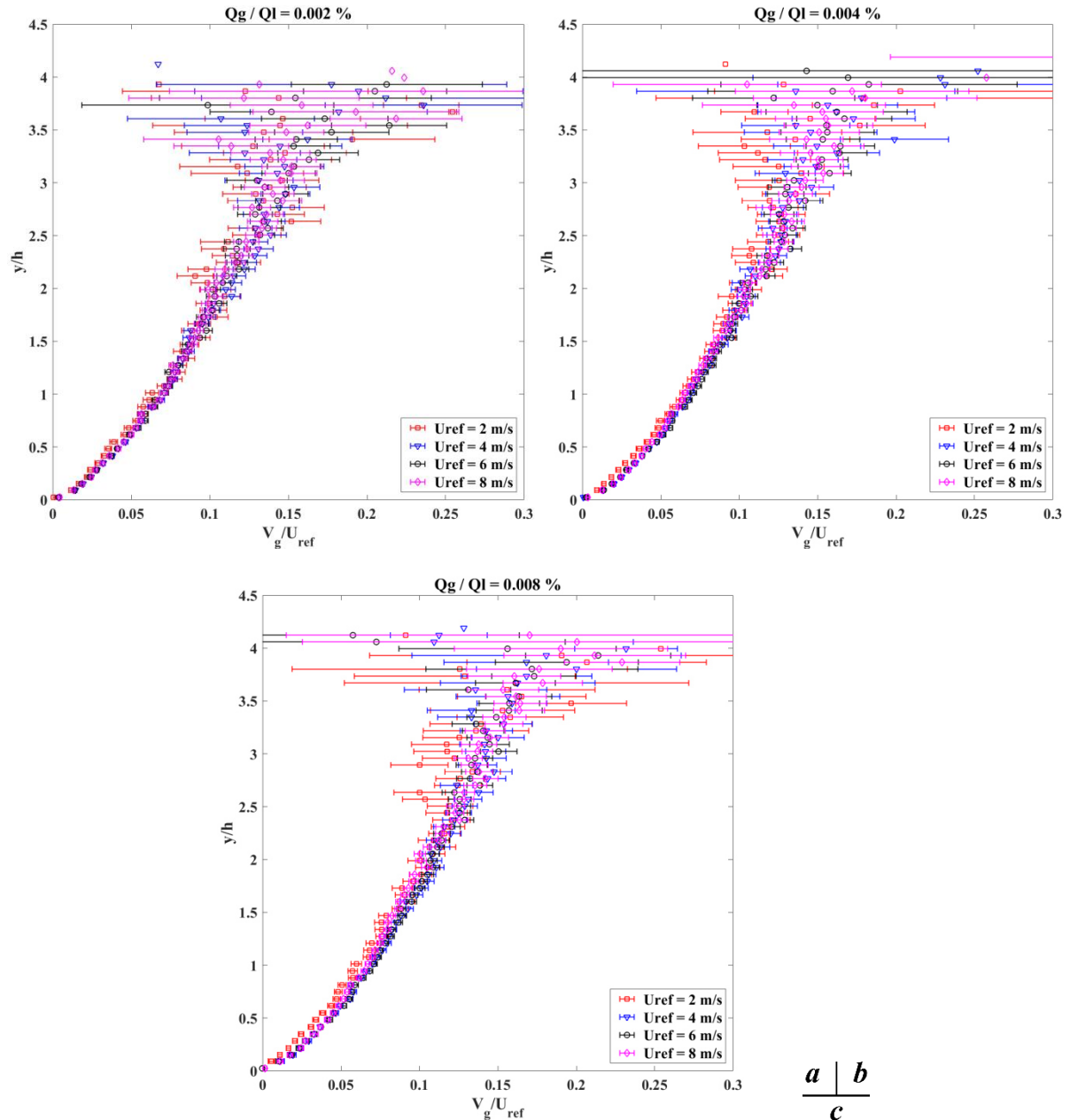


Figure IV. 31 Mean gas wall-normal velocity profiles, normalized by the reference velocity (y -coordinate normalized by h) at constant global volumetric fractions

4.6 Gas phase turbulence

In this section, wall normal profiles of the *rms* velocity components as well as wall-normal profiles of the turbulent shear stress of the gas phase will be examined. For all the profiles, the velocity is normalized by the reference velocity and the y -coordinate is scaled by the height of the obstacle h .

Error bars linked to statistical convergence are not added on these profiles, to ensure readability of the plots. Statistical convergence is difficult to achieve at the edge of the bubble layer, leading to dispersed points of the profiles in this region.

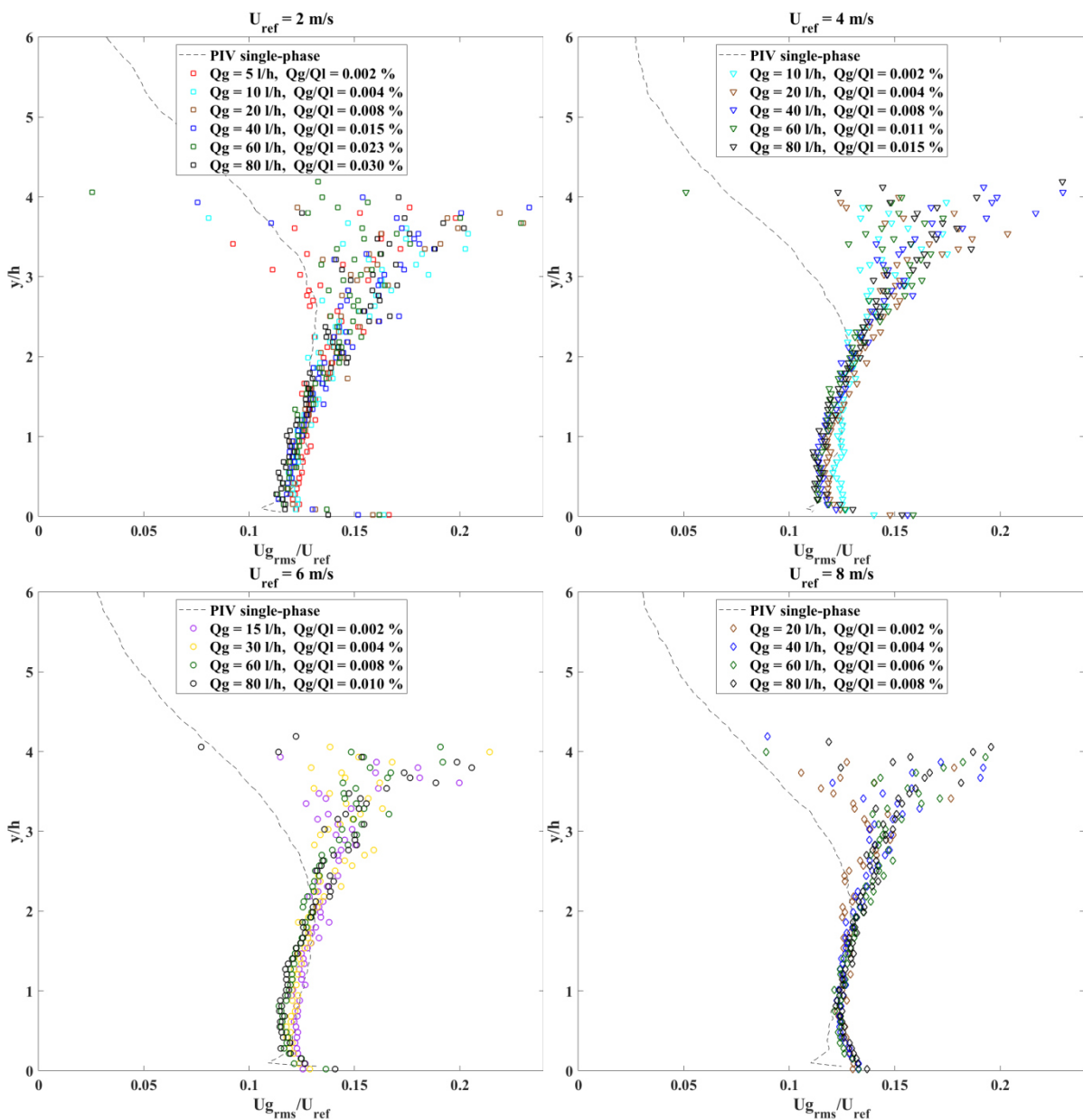
4.6.1 *Rms* stream-wise velocity

Figure IV. 32 shows the stream-wise *rms* velocity profiles of the gas at constant reference velocities under different air injection rates. *Rms* profiles in single-phase flow are plotted in dotted lines for the

sake of comparison. **Figure IV. 33** shows the evolution of the stream-wise *rms* velocity profiles at constant volumetric fractions under different reference velocities.

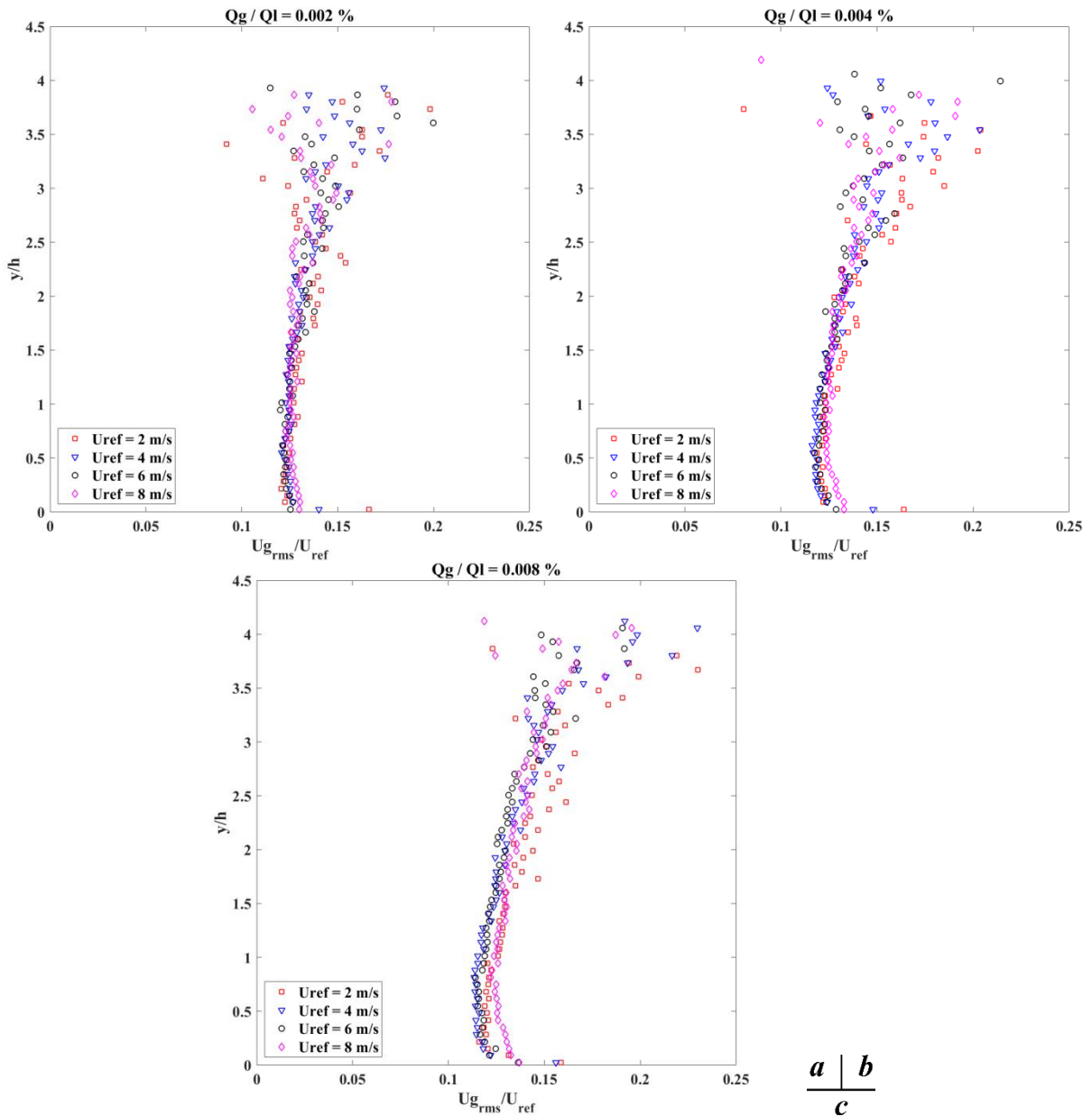
Overall, same shape of the profiles as in the single-phase flow is achieved up to $y/h \approx 2$ but the *rms* stream-wise velocity of the gas is slightly larger than the *rms* velocity of the single phase flow. Also, the gas phase *rms* velocity exhibits a peak in the very near wall region. For all reference velocities, the gas *rms* stream-wise velocity doesn't reach its maximum as in single phase flow for $2 < y/h < 3$ but keeps on increasing up to the edge of the bubbles layer.

For small reference velocities ($U_{ref} \leq 6m/s$), a diminution of the *rms* velocity magnitude with the increase of Q_g is observed below the inflection point of mean stream-wise velocity profiles ($y/h < 2$). For this range of y values, **Figure IV. 33** evidences that the ratio of the *rms* stream-wise velocity to the reference velocity augments when the reference velocity is increased. The higher the global volumetric fraction, the more noticeable this change in the *rms* velocity with the reference velocity.



$$\begin{array}{c|c} a & b \\ \hline c & d \end{array}$$

Figure IV. 32 *Rms* gas stream-wise velocity profiles, normalized by the reference velocity (y -coordinate normalized by h) at constant reference velocity, with single-phase *PIV* data in comparison



$$\begin{array}{c|c} a & b \\ \hline c & \end{array}$$

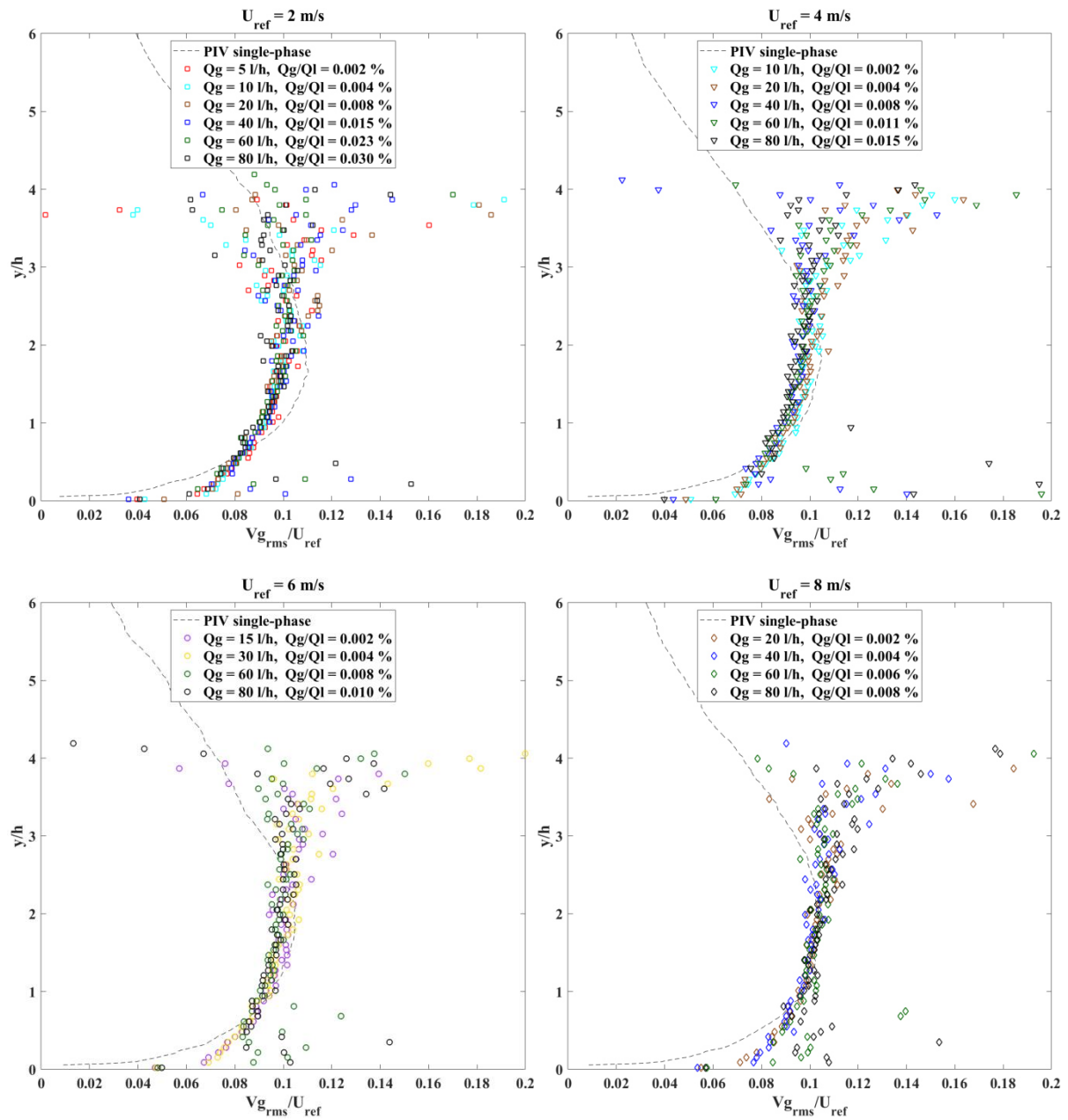
Figure IV. 33 *Rms* gas stream-wise velocity profiles, normalized by the reference velocity (y -coordinate normalized by h) at constant global volumetric fractions

4.6.2 *Rms* wall normal velocity

Figure IV. 34 is a plot of the wall-normal *rms* velocity profiles of the gas at constant reference velocities under different air injection rates. *Rms* profiles in single-phase flow are plotted in dotted lines for comparison. Figure IV. 35 shows the evolution of the wall-normal *rms* velocity profiles of the gas at constant volumetric fractions under different reference velocities. As compared with the single-phase profiles, the gas *rms* velocity profiles result in higher values for $y/h \leq 0.7$. In the range $0.7 \leq y/h \leq 2.5$, at 2 m/s, the gas *rms* velocity profiles exhibit deficit comparing to the single-

phase flow profile. For this range of y values and for large velocity ($U_{ref} \geq 6\text{ m/s}$), a good agreement is obtained between the single phase and the gas phase *rms* wall normal velocity profiles. Same trend of increasing *rms* values when moving away from the wall, from $y/h = 2.5$ up to the edge of the bubbles layer, is observed for the wall normal velocity component as for the stream-wise velocity component.

Overall, no obvious influence of gas injection rate is observed on the gas *rms* wall normal velocity profiles, except in the near wall region ($\frac{y}{h} < 0.7$) where the *rms* wall normal velocity is likely to increase as the volumetric fraction augments. At constant volumetric fraction, as was observed for the stream-wise component, when increasing the reference velocity, the gas *rms* velocity ratio to the reference velocity of the wall normal component is augmented.



$$\frac{a}{c} \mid \frac{b}{d}$$

Figure IV. 34 *Rms* gas wall normal velocity profiles, normalized by the reference velocity (y -coordinate normalized by h) at constant reference velocity, with single-phase PIV data in comparison

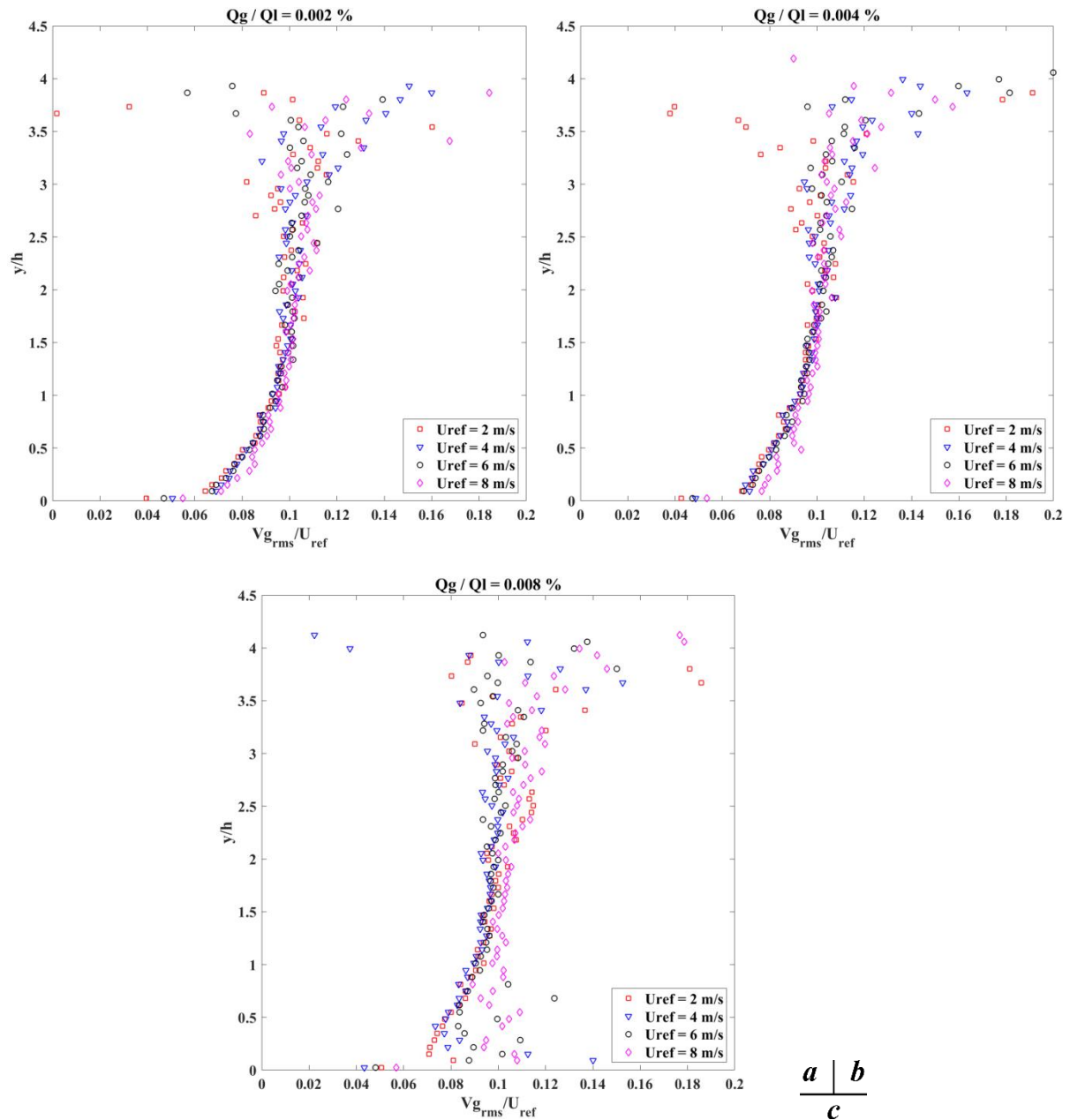


Figure IV. 35 *Rms* gas wall-normal velocity profiles, normalized by the reference velocity (y -coordinate normalized by h) at constant global volumetric fractions

4.6.3 Turbulent shear stress

Figure IV. 36 shows the gas turbulent shear stress profiles at constant reference velocities under different air injection rates. *Rms* profiles in single-phase flow are plotted in dotted lines for the sake of comparison. Figure IV. 37 displays the evolution of the gas turbulent shear stress profiles at constant volumetric fractions under different reference velocities.

Generally speaking, the turbulent shear stress of the gas phase is much smaller than the one of the single phase, which means that the stream-wise and wall-normal velocity components are much less

correlated for the gas phase than for the liquid phase in the single phase flow. No obvious influences on the gas turbulent shear stress of the gas injection rate or of the reference velocity are evidenced.

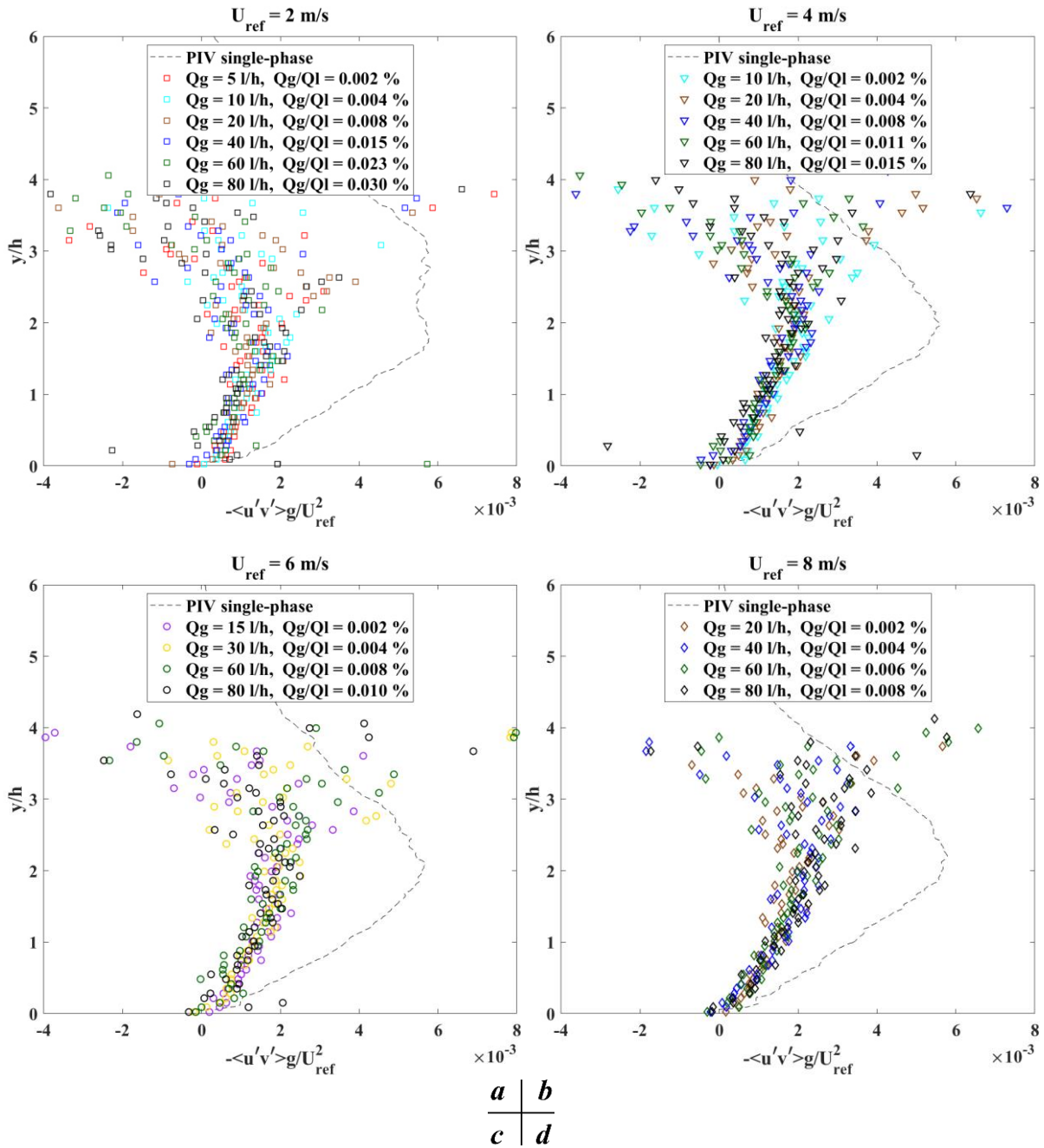


Figure IV. 36 Gas turbulent shear stress profiles normalized by the reference velocity (y -coordinate normalized by h) at constant reference velocity, with single-phase *PIV* data in comparison

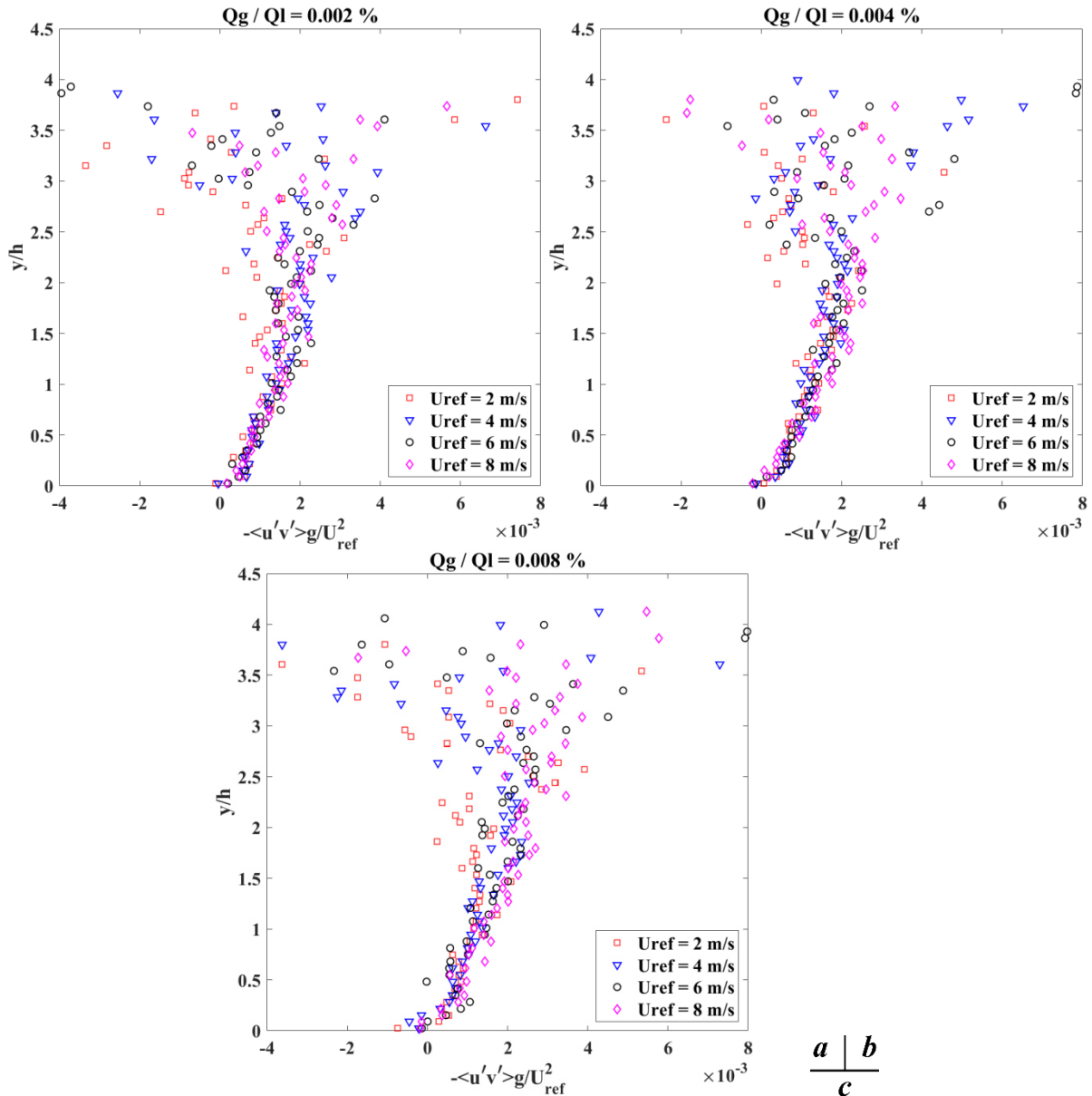


Figure IV. 37 Gas turbulent shear stress profiles, normalized by the reference velocity (y -coordinate normalized by h) at constant global volumetric fractions

4.7 Conclusion

The gas-phase flow characteristics measured in the recovery region downward the obstacle were examined in this chapter.

It is concluded that the bubble diameter distribution does not differ from that in a turbulent pipe flow and can be approximately described by a log-normal law. The bubble mean diameter scaled by the momentum thickness of the single phase flow has shown a power-law-dependency on the global volumetric fraction but remains quite indifferent with regard to the reference velocity. The variation of the bubble aspect ratio with the *Weber* number was examined and a 2nd order polynomial relationship has been established.

The gas phase flow is characterized by a maximum of volume fraction achieved near the wall in a region that we have called the inner bubbles layer. A self-similarity of wall normal profiles of the volume fraction has been obtained under different conditions of gas injection rate and reference velocity conditions in the outer bubble layer. For the purpose, the gas volume fraction has been scaled

by its maximum value reached near the wall α_{v-max} . A new length Δ_b has been found to scale the wall normal distance in order to collapse well the gas volume fraction profiles. Two distinct families, classified by the *Reynolds* numbers, have been revealed, in which self-similar profiles follow an exponential law in the outer bubbles layer.

The scaling length Δ_b is found to be of unique dependency of θ and Fr_θ . α_{v-max} is found to expand linearly with the volumetric fraction Q_g/Q_l . Its expansion rate varies under the gravity effect and evolves as a power law with regard to $1/ Fr$, with Froude number Fr defined based on the bubble size. The distance of maximum gas volume fraction y_{av-max} evolves linearly with the Froude number for $Fr > 50$; otherwise, y_{av-max} is roughly equal to the bubble radius.

A good similarity of the gas layer thickness δ_α normalized by the momentum thickness was obtained against different reference velocities. It depends linearly of the volumetric fraction Q_g/Q_l .

The mean gas velocity profiles differ greatly from those of the single phase flow. In the stream-wise direction, the gas move faster than the single phase in the inner bubbles layer and slower than the liquid phase in the outer bubble layer. Profiles of the wall-normal mean velocity have revealed that the bubbles move away from the wall, leading to larger positive values of the wall normal velocity than for the single phase flow. The turbulent shear stress has shown a decrease as compared to single phase, showing a decorrelation between the stream-wise and wall-normal mean components. Overall, the gas injection rate has quite little modification on the mean profiles, the same for the *rms* and the turbulent shear stress profiles. An increase in the reference velocity leads to an increase in the ratio of the mean stream-wise gas velocity to the reference velocity.

A detailed examination of the liquid-phase characteristics is proposed in the next chapter.

5 CHAPTER V. Influence of the Bubble Injection on the Flow Developing Downward the Obstacle. Characterization of the Liquid Phase Velocity Field.

This chapter aims at describing the characteristics of the liquid phase's flow achieved downward the obstacle, with bubbles injection.

The 2 components of the velocity field of the liquid (u, v) are characterized by *PTV* in a vertical (x, y) plane aligned along the symmetry axis of the tunnel in a viewing area 107.9 mm wide and 107.9 mm high, centered at $x/h = 36.2$. As evidenced in the previous chapter, this stream-wise position is localized in the recovery region of the single-phase flow developing downward the obstacle.

The flow configuration and the coordinate system used are recalled in **Figure V. 1**. The *PTV* measurement system and *PTV* processing used to determinate the instantaneous velocity components (u, v) of each particle has been described in details in **Chapter 2**.

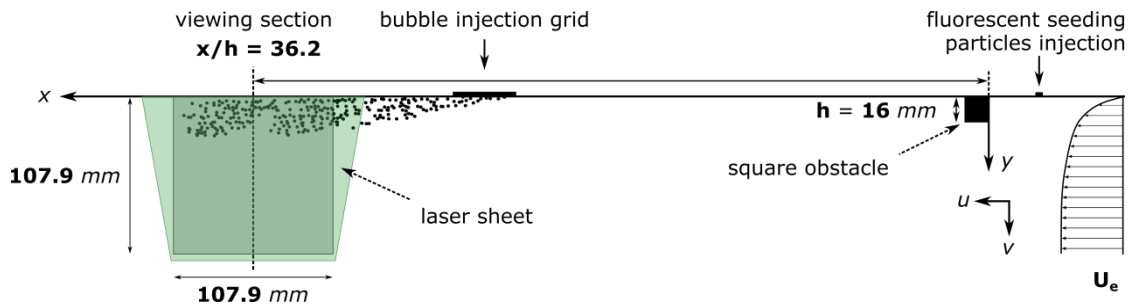


Figure V. 1 Schematic diagram of experimental setup and viewing section

Four reference velocities, same as in single-phase flow, are tested. **Section 5.1** summarizes the bubbly flow conditions. **Section 5.2** is dedicated to the description of the statistical analysis procedure implemented for the *PTV* method and comparison is made between *PTV* and *PIV* results for the single-phase flow. **Section 5.3** shows the results obtained by *PTV* in the bubbly flow at $x/h = 34.3$. The velocity components of the liquid phase are compared to those of the single-phase flow, and influences of the gas injection rate and reference velocity are discussed.

5.1 Bubbly Flow conditions

All measurements were made under four reference velocities $U_{ref} = 2, 4, 6$ and 8 m/s . The air injection rate varied up to 80 l/h . The operating points are summarized in **Table V. 1**.

The value of the characteristic parameters (*Reynolds* number, ratio of the bubble size to the length scales of the boundary layer, global volumetric fraction in the tunnel, average air volume fraction in the boundary layer $\langle \alpha \rangle$...) are based on integral parameters of the boundary layer in single-phase flow obtained at the stream-wise position of the viewing area ($x/h = 34.3$).

U_{ref} (m/s)	$\frac{Re_{\theta}}{U_e \theta}$ $\left(\frac{u^* \theta}{\nu}\right)$	$\frac{Re^*}{\left(\frac{u^* \theta}{\nu}\right)}$	Q_g (l/h)	Q_g/Q_l (%)	d_b (mm)	d_b/θ	d_b^+ $(d_b u^*/\nu)$	$\langle \alpha \rangle$ (%)
2	21662	794	0	0				
2	21662	794	5	0.002	0.57	0.052	41,4	0.0049
2	21662	794	10	0.004	0.62	0.057	45,6	0.0098
2	21662	794	20	0.008	0.74	0.068	54,3	0.0196

2	21662	794	40	0.015	0.96	0.088	69,7	0.0392
2	21662	794	60	0.023	1.11	0.102	81,2	0.0587
2	21662	794	80	0.030	1.24	0.114	90,8	0.0783
4	40623	1381	0	0				
4	40623	1381	10	0.002	0.45	0.045	61,8	0.0049
4	40623	1381	20	0.004	0.54	0.054	74,7	0.0099
4	40623	1381	40	0.008	0.69	0.069	94,9	0.0197
4	40623	1381	60	0.011	0.78	0.078	107,3	0.0296
4	40623	1381	80	0.015	0.91	0.091	125,4	0.0395
6	60630	1988	0	0	0	0		
6	60630	1988	15	0.002	0.43	0.043	86,2	0.0053
6	60630	1988	30	0.004	0.51	0.051	101,6	0.0105
6	60630	1988	60	0.008	0.63	0.063	126,1	0.0210
6	60630	1988	80	0.010	0.68	0.069	137,6	0.0281
8	68913	2157	0	0	0	0		
8	68913	2157	20	0.002	0.40	0.047	101,6	0.0052
8	68913	2157	40	0.004	0.46	0.054	115,7	0.0105
8	68913	2157	60	0.006	0.50	0.059	126,5	0.0157
8	68913	2157	80	0.008	0.53	0.062	134,5	0.0210

Table V. 1 Characteristics of the operating points of the bubbly flow achieved in the viewing area at $x/h = 34.3$ (characteristics of the single-phase boundary layer are used here, as reference values)

5.2 Statistical analysis procedure of *PTV* measurements

Mean and *rms* velocity components in the vertical plane as well as turbulent shear stress of the liquid were determined using the *PTV* based on relaxation method associated to the Particle Mask Correlation method for fluorescent seeding particles identification, described in *Chap. 2*. The combination of these two methods allows the accurate analysis of turbulent shear flow subjected to a high velocity gradient. Particle superimposed on bubble shadows were removed from the statistical analysis.

5.2.1 Spatial averaging

The instantaneous local velocity components are integrated over same Eulerian spatial grid, as the one used for spatial averaging of the gas velocity. The Eulerian grid is displayed in *Figure V. 2*.

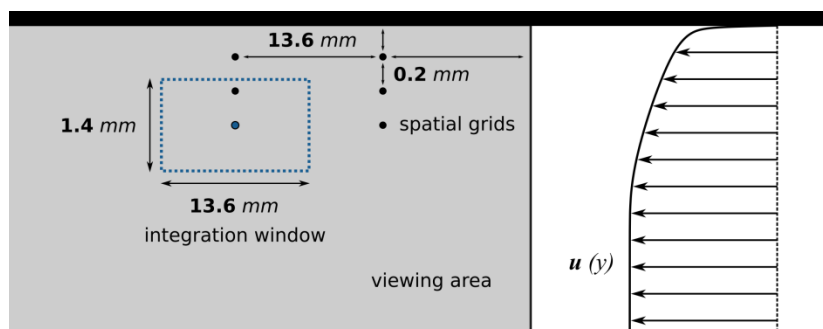


Figure V. 2 Schematic view of integration window (blue dotted lines) and spatial grid resolution (black dots)

The size of the grid in the x and y directions has been optimized in order to improve the spatial resolution in the y direction and maximize the number of detected particles to minimize the error linked to the statistical convergence. The grid's width in y direction was chosen to be quite identical to that of the Interrogation Area of *PIV*. The grids overlap in the y direction, as shown in **Figure V. 2**. Values of the spatial resolution of the *PTV* statistical analysis are summarized in **Table V. 2**. The nearest point from the wall achieved by the *PTV* system is at $= 0.21mm$.

5.2.2 Time averaging

The measuring time (i.e.: the number of pairs of images) used for the statistical analysis of the velocity field measured by *PTV* has been adjusted according to the reference velocity and air injection rate. The more bubble shadows are seen on the image, the fewer particles can be validated. **Figure V. 3** displays the number of image pairs used as a function of the reference velocity. The number of images pairs for the *PTV* analysis varied between 1500 and 7000, it was increased with the air injection rate following a linear scaling according to the global air volumetric fraction Q_g/Q_l .

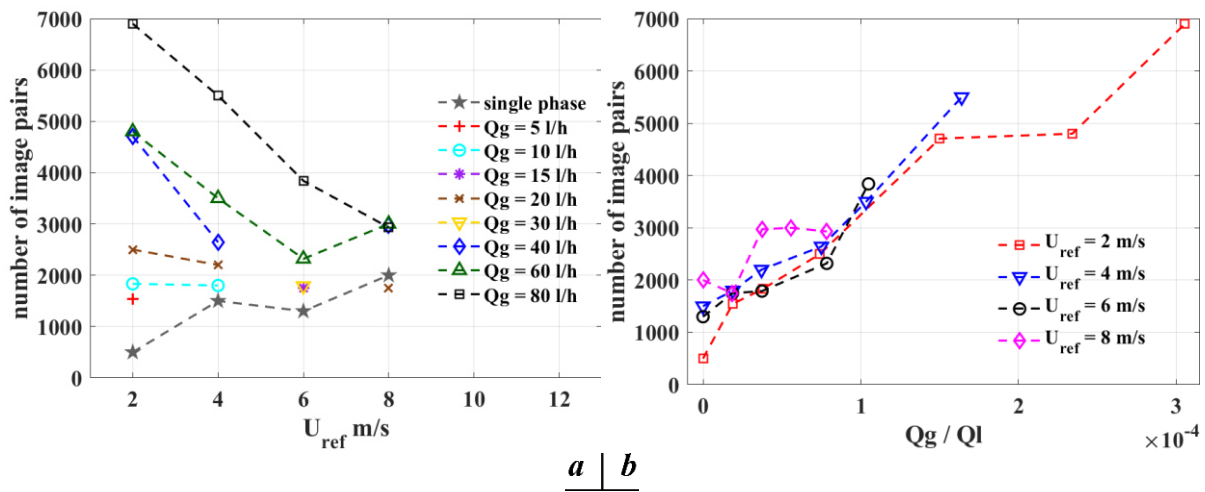


Figure V. 3 Number of image pairs according to the reference velocities (a) and volumetric fraction (b)

Figure V. 4 illustrates the number of valid particles passing through the grid centered at $y = 0.42 mm$ from the wall. For the bubbly flow, by increasing the measurement time, the number of validated particles is at least as much larger in the two-phase flow as in the single-phase flow.

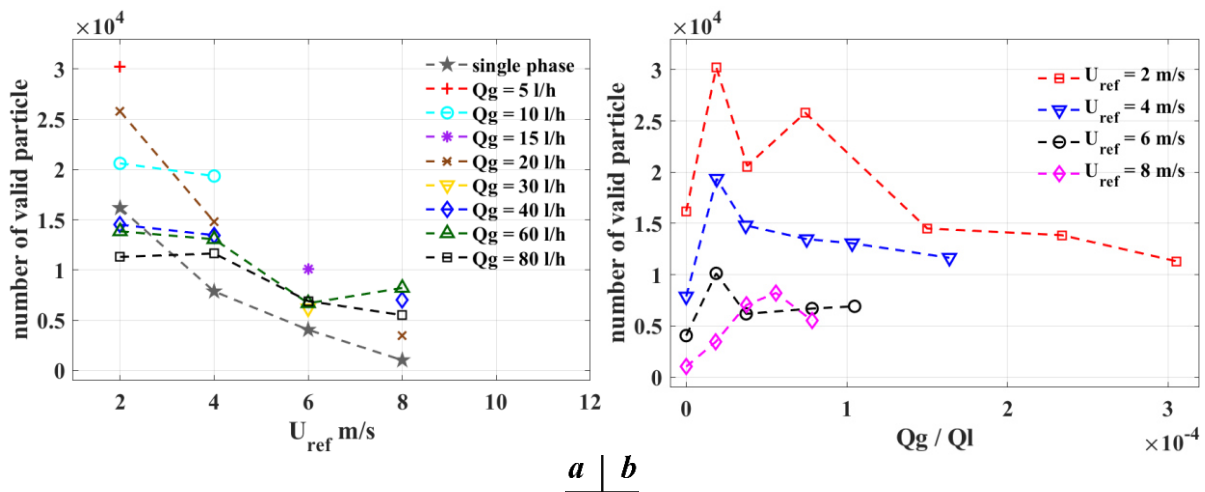


Figure V. 4 Number of valid particles located in the *PTV* grid centered at $y = 0.42 mm$ from the wall according to the reference velocities (a) and volumetric fraction (b)

5.2.3 Uncertainties

Random errors of statistical quantities, related to the sub-pixel resolution of the *PTV* measuring system, are evaluated in **Table V. 2** for the single-phase flow. For the two-phase flow, the number of particles being higher, the random errors are expected to decrease. U and V denote local mean values and U_{rms} and V_{rms} are the local *rms* values of u and v components respectively, averaged over the spatial grid and averaged in time. Integration of the profiles $U(y)$ and $U_{rms}^2(y)$ and $V_{rms}^2(y)$ along the grid points in the y direction makes it possible to determinate the integral length scales δ_* , θ , δ_3 and δ_4 .

As for the *PIV* measurements, the friction velocity was achieved, based on a linear regression of the semi-logarithmic plot of the *PTV* stream-wise velocity profiles $U = f(\ln y)$ in the inner region. The uncertainty on the position of the wall by *PTV* was $35 \mu m$. The induced uncertainties on the determination of the friction velocity u^* , friction coefficient C_f and parameters G , β and Δ are listed in **Table V. 3**.

Spatial integration in x direction : $\Delta x/h$ (i.e.: width of the grid in x direction)	0.85
Spatial integration in x direction : $\Delta x u^*/v$	991.7 – 3435.8
Spatial integration in y direction : $\Delta y/h$ (i.e.: width of the grid in y direction)	0.087
Spatial integration in y direction : $\Delta y u^*/v$	99.2 – 343.8
Overlap of the grid in y direction	84%
Spatial resolution in y direction : $\Delta y u^*/v$ (i.e.: grid spacing in y direction)	15.5 – 53.7
Sub-pixel Random error : $\Delta \bar{U}/U_{ref}$	$8.07e^{-5}$
Sub-pixel Random error : $\Delta \bar{V}/U_{ref}$	$8.07e^{-5}$
Sub-pixel Random error : $\Delta U_{rms}/U_{ref}$	0.0013
Sub-pixel Random error : $\Delta V_{rms}/U_{ref}$	$2.79e^{-5}$
Sub-pixel Random error : $\Delta(-\overline{u'v'})/U_{ref}^2$	$1.65e^{-4}$
Sub-pixel Random error : $\Delta Ue/U_{ref}$	$1.09e^{-5}$
Sub-pixel Random error : $\Delta \delta^*/\delta^*$	$9.87e^{-5}$
Sub-pixel Random error : $\Delta \theta/\theta$	$1.27e^{-5}$
Sub-pixel Random error : $\Delta \delta_3/\delta_3$	0.0703
Sub-pixel Random error : $\Delta \delta_4/\delta_4$	0.0696

Table V. 2 Random error in the determination of statistical quantities, linked to the *PTV* measurement system (spatial resolution, sub-pixel resolution) at $x = 34.3$ (It should be pointed out that the random errors for $\Delta U_{rms}/U_{ref}$, $\Delta V_{rms}/U_{ref}$ and $\Delta(-\overline{u'v'})/U_{ref}^2$ was evaluated using the peak value in the corresponding U_{rms} and V_{rms} profile of the single-phase flow).

$\frac{\Delta u_*}{u_*}$ (%)	3.74
$\frac{\Delta B}{B}$ (%)	24.76
$\frac{\Delta C}{C}$ (%)	199.28
$\frac{\Delta C_f}{C_f}$ (%)	14.95
$\frac{\Delta G}{G}$ (%)	3.86
$\frac{\Delta(\Delta)}{(\Delta)}$ (%)	3.74

$\frac{\Delta(\beta)}{(\beta)}$ (%)	0.47
-------------------------------------	------

Table V. 3 Uncertainty on the determination of $u^*, C_f, B, C, G, \Delta, \beta$ for the *PTV* measurement system at $x/h = 34.3$ (uncertainty is evaluated for the single-phase flow, same order is expected for the two-phase flow)

The uncertainties linked to the statistical convergence of velocity profiles and integral parameters will be visible on the next graphics, as error bars.

5.2.4 Validation in single-phase flow of the *PTV* measurements of the statistical quantities by comparison to *PIV*

In *Appendix 8.2*, profiles in the y direction of mean and *rms* velocity components, as well as profiles of the *Reynolds* shear stress are compared between *PIV* and *PTV* for the single-phase flow at $x/h = 34.3$.

To enable the comparison, *PIV* measurements are performed with the pushing system operating, thus generating a jet of water, whereas *PTV* measurements are performed with generating a jet of fluorescent particles suspended in water.

Generally speaking, *PTV* measurements exhibit an increase of V positive value associated to a deficit of the stream-wise mean velocity in the outer layer by comparison to *PIV*. This can be due to the fact that fluorescent Rhodamine particles are heavier than the water.

Turbulence intensities are underestimated by *PIV*, and better estimated by *PTV*. The underestimation of the velocity fluctuations is mainly due to the spatial average of the velocity in the interrogation windows in the *PIV* evaluation. (*Raffel et al. 2018, Lecuona et al. 2003*) The *Reynolds* shear stress profiles and the logarithmic laws plotted versus inner variables are very close between *PIV* and *PTV*.

The integral values for both *PIV* and *PTV* are documented in *Table V. 4*. Differences in % (*dif*) between *PIV* and *PTV* are evaluated.

An overall excess of the integral length scales has been found for *PTV* as compared to *PIV*. It is not surprising that similarity is obtained for both u^* and B , as they are the values that are firstly compared in the log-fit procedure. The increase in the additive constant C of the logarithmic law versus outer variable for *PTV* measurements is in agreement with a velocity defect more pronounced in the outer layer for *PTV*. The increase in δ^* and θ from *PIV* to *PTV* seems to be of the same order of magnitude, which results in a rather fair agreement in H . Boundary layer thicknesses characteristic of turbulent intensities in stream-wise and wall-normal direction δ_3 and δ_4 exhibit significant value underestimation for *PIV* by comparison to *PTV*.

The low relative error in *Clauser* parameter G confirmed also that the similarity in flow equilibrium condition has been obtained both for *PIV* and *PTV*.

	U_{ref}	C	B	C_f	u^*	δ^*	θ	H	δ_3	δ_4	Δ	G	Re_θ	Ue
	[m/s]	[--]	[--]	[--]	[m/s]	[mm]	[mm]	[--]	[mm]	[mm]	[mm]	[--]	[--]	[m/s]
<i>PIV</i>	2	1.9	5.4	0.0025	0.071	12.25	9.66	1.27	1.10	0.70	345.39	5.95	19339	2.01
<i>PTV</i>	2	2.8	5.2	0.0027	0.073	14.01	10.88	1.29	1.58	1.05	382.12	6.09	21662	2.00
<i>dif %</i>		52.4	4.7	6.7922	2.822	14.33	12.58	1.56	43.6	50	10.64	2.32	12	0.50
<i>PIV</i>	4	1.6	5.4	0.0022	0.134	10.64	8.43	1.26	0.91	0.56	317.35	6.21	33531	4.00
<i>PTV</i>	4	2.4	5.3	0.0023	0.138	12.74	10.01	1.27	1.45	0.95	374.95	6.31	40623	4.07
<i>dif %</i>		50.1	2.2	2.7436	3.352	19.76	18.82	0.79	59.3	69.6	18.15	1.61	21	1.96

<i>PIV</i>	6	1.5	5.2	0.0021	0.196	11.12	8.81	1.26	0.99	0.59	342.12	6.40	52920	6.03
<i>PTV</i>	6	2.4	5.2	0.0022	0.202	12.63	9.89	1.28	1.30	0.85	385.15	6.62	60630	6.16
<i>dif %</i>		57.9	0.1	1.8724	2.992	13.62	12.28	1.20	31.3	44.1	12.58	3.55	15	2.04
<i>PIV</i>	8	1.1	5.8	0.0019	0.248	10.93	8.67	1.26	0.94	0.58	355.03	6.71	69461	8.04
<i>PTV</i>	8	1.7	5.9	0.0020	0.254	10.69	8.53	1.25	1.31	0.71	341.61	6.46	68913	8.11
<i>dif %</i>		59.2	1.9	3.4123	2.542	2.15	1.61	0.55	39.4	22.4	3.78	3.74	1	0.84

Table V. 4 Integral and log-law-deduced parameters. Comparison between *PIV* and *PTV* in single-phase flow at $x/h = 34.3$.

5.3 Analysis of the liquid velocity field in the bubbly flow. Comparison to the single-phase flow.

We firstly present and discuss the general features of the bubbly flow. Then, we focus on the validity of the logarithmic law. Third part is dedicated to the presentation of the integral parameters, as a function of the air injection rate.

5.3.1 General features of the mean and fluctuating liquid flow

In this part, y profiles of the mean velocity components and *Reynolds* stress components are analysed.

Figure V. 5 displays the evolution with respect to the air injection rate of the mean stream-wise external velocity for the different reference velocities. It can be seen that the mean external velocity does not reveal any obvious variation when the flow is subjected to the gas injection.

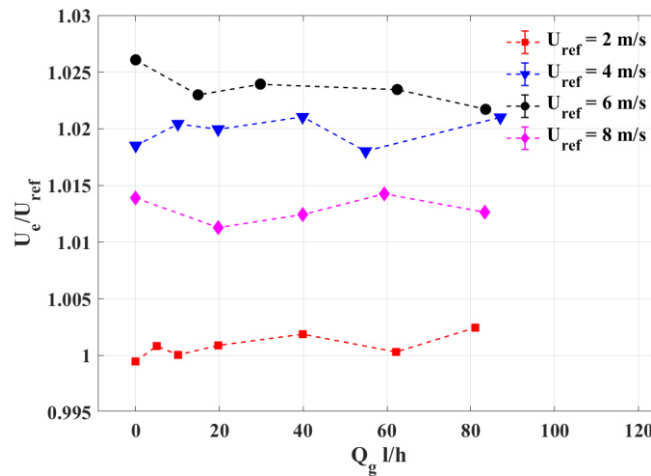


Figure V. 5 Plot of the external velocity scaled by the reference velocity, versus gas flow rate Q_g

Profiles of the mean velocity components are plotted in the following figures. *Figure V. 6* shows the mean stream-wise velocity profiles for different reference velocities. Different air injection rates are superimposed. The profiles in the bubbly flow are not very different from the single-phase profiles, except for $U_{ref} = 8$ m/s.

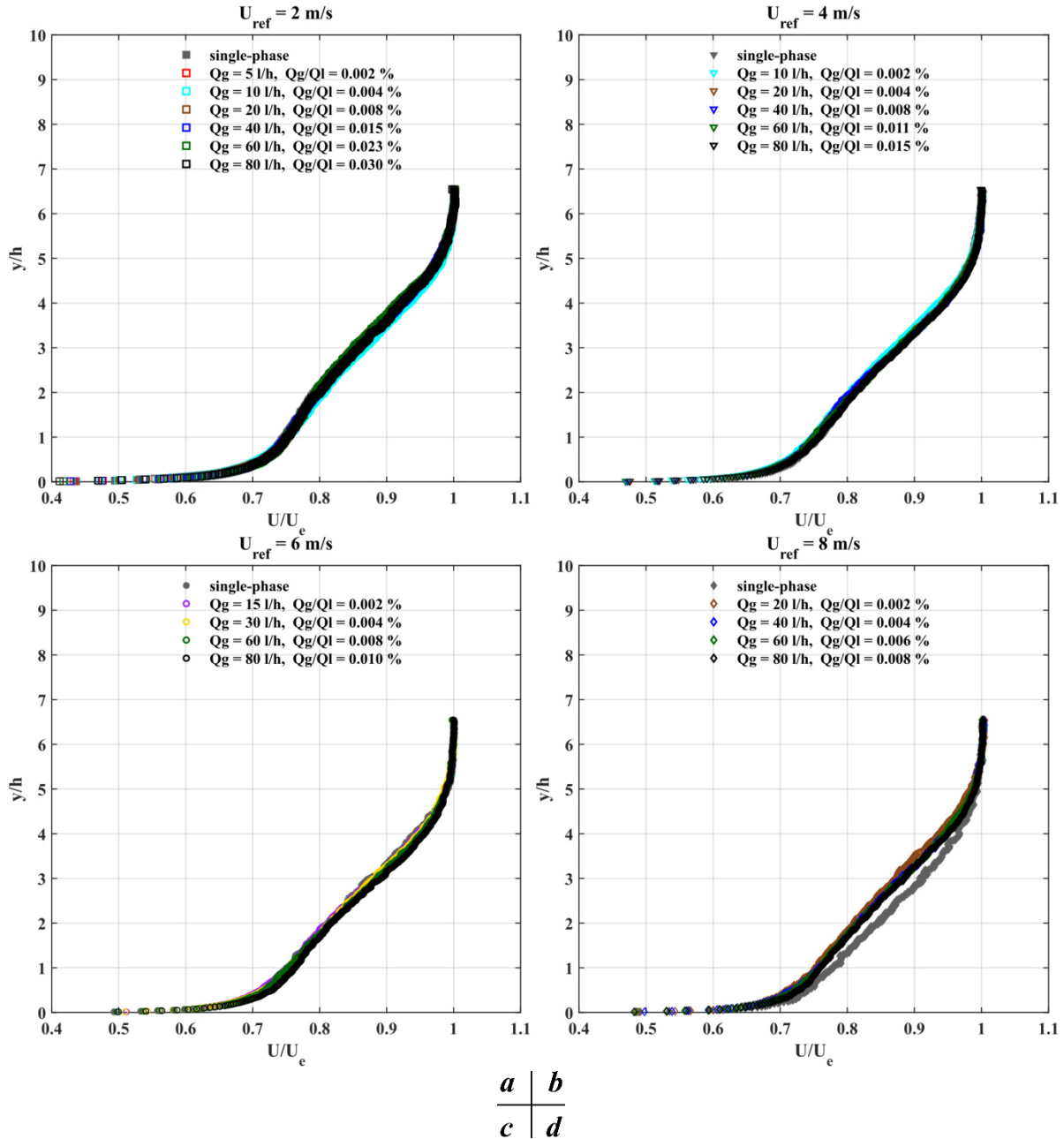


Figure V. 6 Mean stream-wise velocity U profiles normalized by the external velocity U_e for different air injection rates.

Figure V. 7 shows the mean wall-normal velocity profiles at different gas flow rate for different reference velocities. For all reference velocities, air injection does not modify the \bar{V} values at the outer boundary but modifies drastically the profile shape in the boundary layer. As discussed earlier, correct \bar{V} values are very difficult to obtain by *PTV* with Rhodamine particles. Nevertheless, these profiles exhibit some trends.

In particular, an increase in the air injection rate induces a decrease in V positive values, which can be interpreted as bubble induced driven flow towards the wall. For $U_{ref} = 2 \text{ m/s}$, this trend is inverted beyond $Qg = 40 \text{ l/h}$ ($Qg/Ql > 0.015\%$), which means that an increase of the air volumetric fraction beyond this value leads to a decrease in the bubble driven flow.

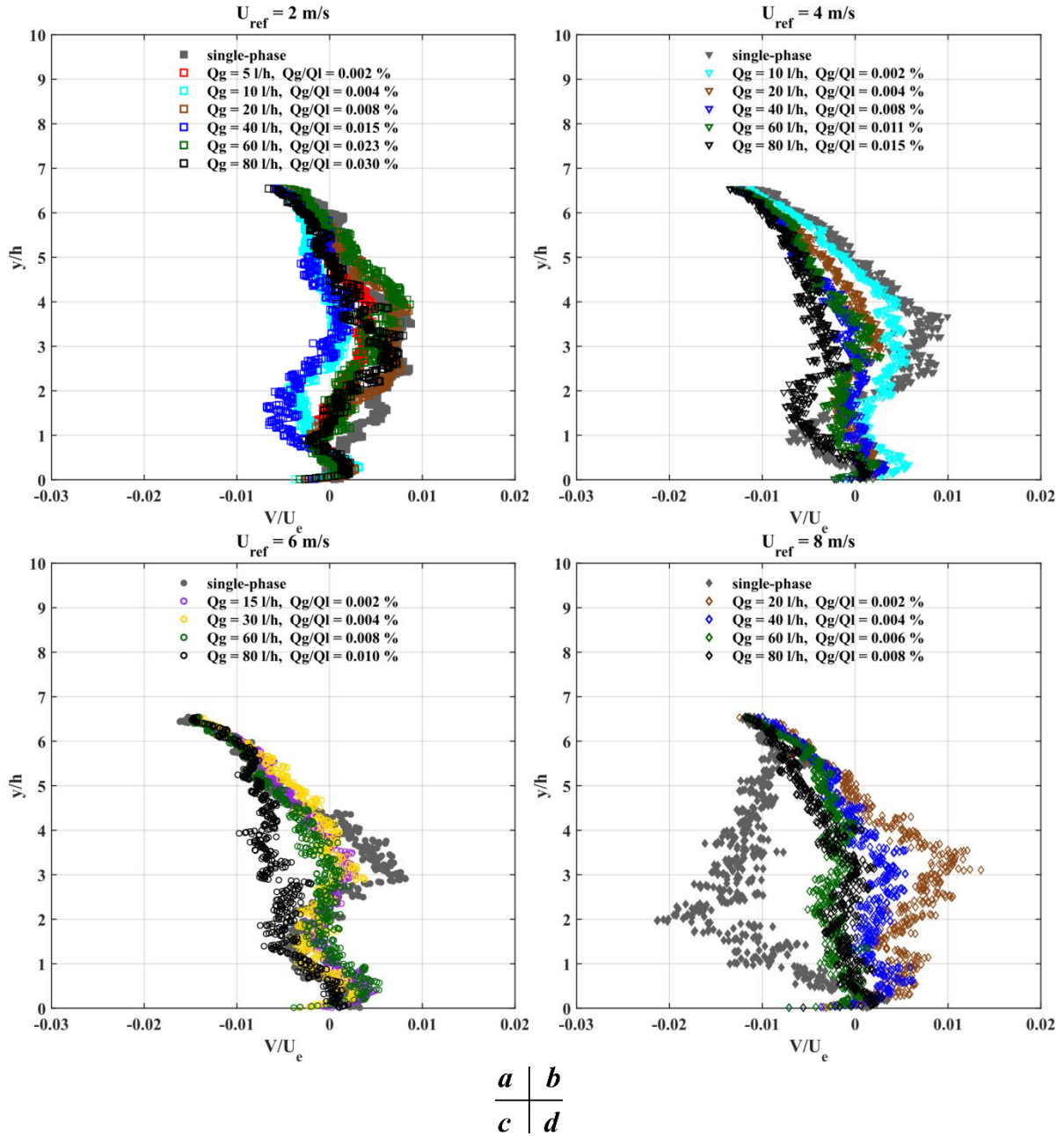


Figure V. 7 Mean wall-normal velocity V profiles normalized by the external velocity U_e for different air injection rates.

Profiles of the stream-wise and wall-normal turbulent intensity U_{rms}/U_e and V_{rms}/U_e are presented in **Figure V. 8** and **Figure V. 9** respectively. Profiles of the normalized turbulent shear stress $-\langle u'v' \rangle / U_e^2$ are displayed in **Figure V. 10**. We firstly describe trends observed in the outer region of the boundary layer.

Maxima are achieved at a wall distance $y/h = 2 - 3$. Beneath that point at the low-velocity side, the stream-wise turbulent intensity is uniformly distributed, as in single-phase flow.

At $U_{ref} = 4$ and 6 m/s , bubbles injection leads to a decrease in the maxima of the stream-wise and wall-normal fluctuating velocity components, as well as a decrease in the maxima of the turbulent shear stress. For these reference velocities, a shift of the maxima of the turbulent shear stress towards the wall is observed, when increasing the air injection rate. This is in agreement with the bubble driven

flow towards the wall previously evidenced on V profiles. Same is observed at $U_{ref} = 2 \text{ m/s}$ for $Q_g/Q_l < 0.015\%$.

At $U_{ref} = 2 \text{ m/s}$ beyond $Q_g/Q_l = 0.015\%$, the trend is inverted: an augmentation of the air injection rate induces an increase in the maxima of the stream-wise and wall-normal fluctuating velocity components, as well as an increase in the maxima of the turbulent shear stress in agreement with bubble driven flow away from the wall.

At $U_{ref} = 8 \text{ m/s}$, the trends observed in the two-phase flow between different runs at different air injection rates are in agreement with the ones observed at 4 and 6 m/s (ie: decrease in the V positive values, decrease in the maxima of Rms stream-wise and wall normal components, decrease in the maxima of turbulent shear stress when increasing the air injection rate). But at $U_{ref} = 8 \text{ m/s}$, we have a doubt as to whether the single-phase flow measured by PTV was fully stabilized. Indeed, we observe contradictory trends, ie: an increase in V positive values of the two-phase flow, by comparison to the single-phase flow, a shift of the maxima of the turbulent shear stress away from the wall which explains the strong stream-wise velocity deficit in the boundary layer. Therefore, measurements of the single-phase flow at $U_{ref} = 8 \text{ m/s}$ in the outer region of the boundary layer will be considered with caution.

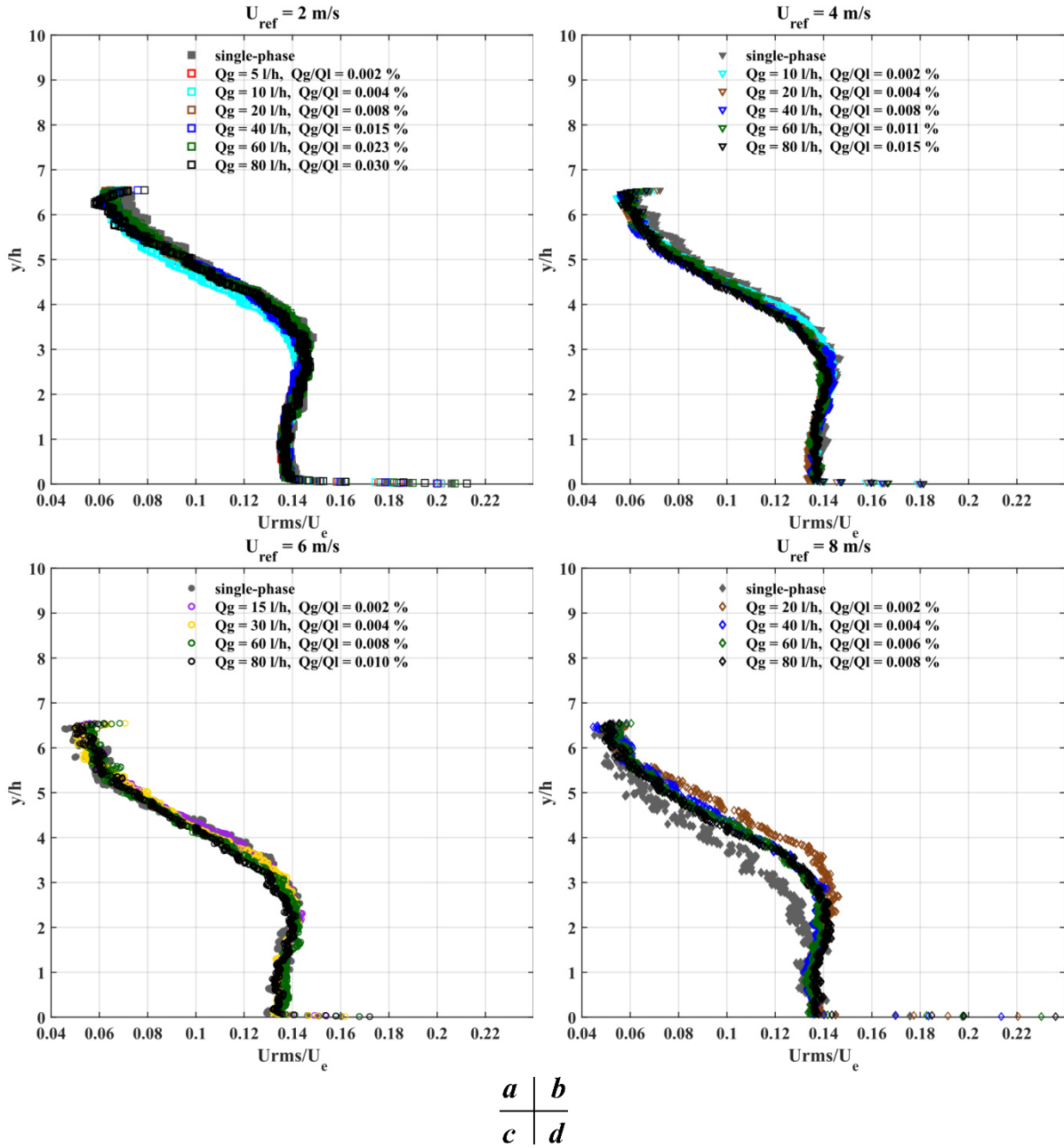


Figure V. 8 U_{rms} profiles normalized by the external velocity U_e .

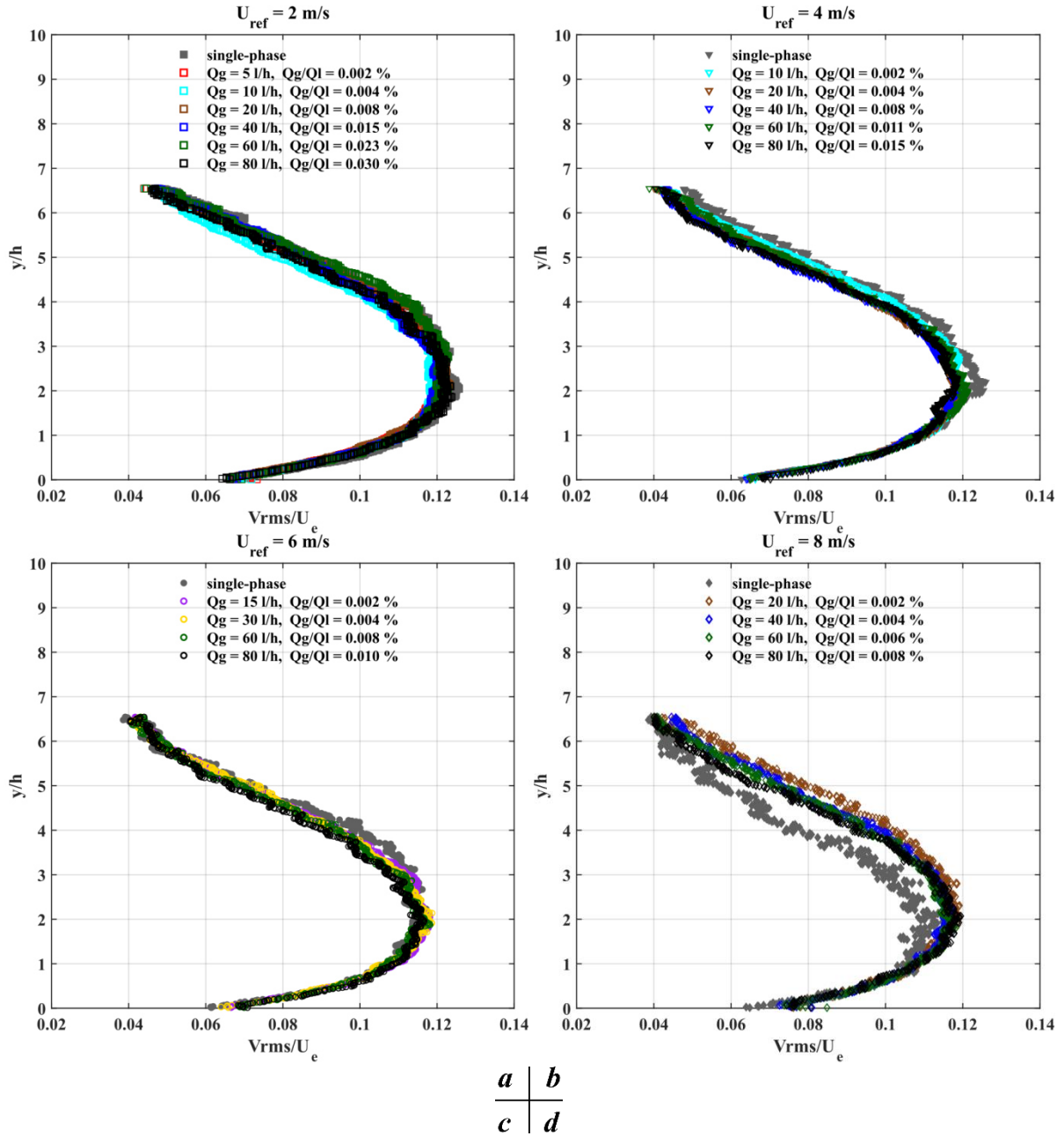


Figure V. 9 V_{rms} profiles normalized by external velocity U_e .

As can be seen on **Figure V. 10**, in the region characterized by wall distance ($y^+ > 400$ and $y/h < 2$), the turbulent shear stress seems to evolve linearly with the wall-normal distance, as expected in the single-phase flow.

Figure V. 11 shows the evolution of $-\rho \frac{\partial \langle u'v' \rangle}{\partial y}$ as a function of the air injection rate, for the different reference velocities. The slope of the $-\langle u'v' \rangle$ in the inner region doesn't seem to depend significantly on the air injection rate at each reference velocity.

From **Figure V. 10**, it is noticeable, that bubble injection is observed to increase $-\langle u'v' \rangle$ in the buffer layer and in the beginning of the logarithmic layer ($10 < y^+ < 200$) at different reference velocities except at $U_{ref} = 2 \text{ m/s}$ at which case the trend is inverted. This region corresponds to the inner

bubble layer ($y < y_{av-max}$). The contribution of the bubbles turbulent wakes in the measured turbulent shear stress will be discussed in part *V5d* and will give an insight into these modifications.

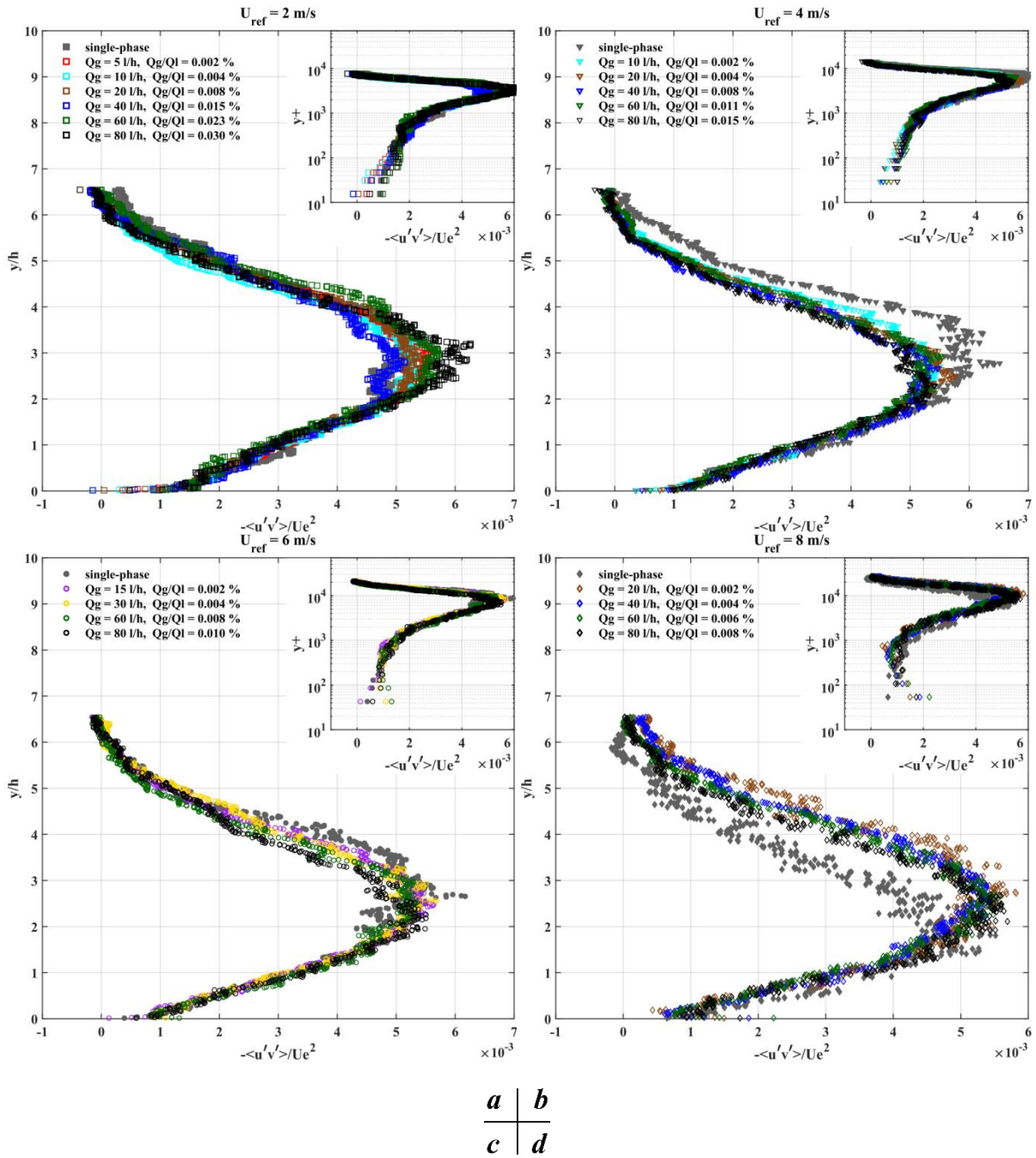


Figure V. 10 $-\langle u'v' \rangle$ profiles normalized by the external velocity U_e^2

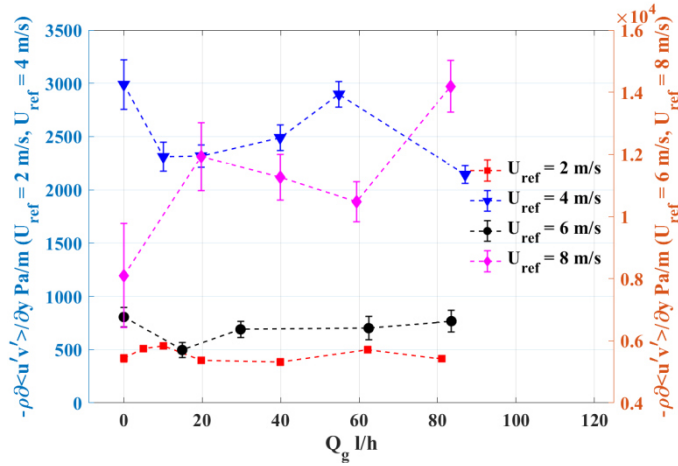


Figure V. 11 Slope of $-\langle u'v' \rangle$ in near wall region, versus gas flow rate Q_g

5.3.2 Validity of the log law

5.3.2.1 Log law with regard to the inner variables

The semi-log plots of the mean stream-wise velocity profiles for inner variables are shown in **Figure V. 12 – Figure V. 15**. The friction velocity u^* is deduced assuming that the logarithmic law (**Eq. 1 – 16**) and the *von Kármán* constant $\kappa = 0.41$ are still valid in the two-phase flow, letting the additive constant B free to adjust. For the logarithmic fit of the velocity profiles, the same range of y^+ in the inner log region as for single-phase flow is applied onto bubbly flow velocity profiles. The method, which is still of questionable legality, allows to illustrate the modification on frictional velocity under the impact of air injection in the boundary layer.

Although very small, the two-phase flow evidences a decrease in the friction velocity, for the different reference velocities except at $U_{ref} = 2 \text{ m/s}$. This reduction of the friction velocity is more important as the air injection increases and it is observed that gas injection increases the log law's upper limit. For the case at $U_{ref} = 2 \text{ m/s}$, the two phase flow exhibits an increase of the friction velocity, which is reduced when increasing the air injection rate.

A decrease in the friction velocity is accompanied with an increase in the additive constant B .

We note that the velocity profile obtained by *PTV* in the single-phase flow at $U_{ref} = 8 \text{ m/s}$, which is questionable in the outer region of the boundary layer, is likely to be valid in the inner region. Indeed, the value of the wall friction velocity obtained by *PTV* for this measurement point remains in good agreement with the value measured by *PIV* (2% of variation between *PIV* and *PTV* in the single-phase flow which is in the range of systematic measurement error between the two methods and which is much less than variations between two-phase and single-phase flow).

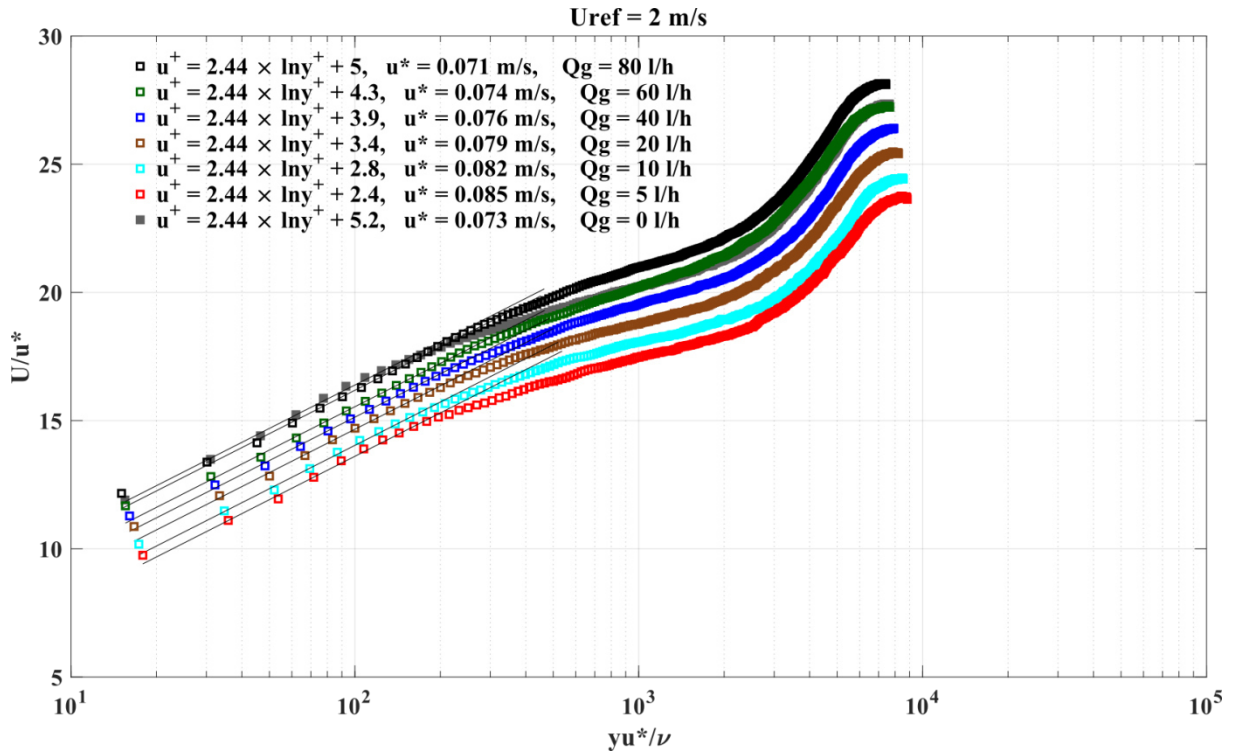


Figure V. 12 Semi-logarithmic plot of mean velocity profiles at $U_{ref} = 2 \text{ m/s}$ (inner variables)

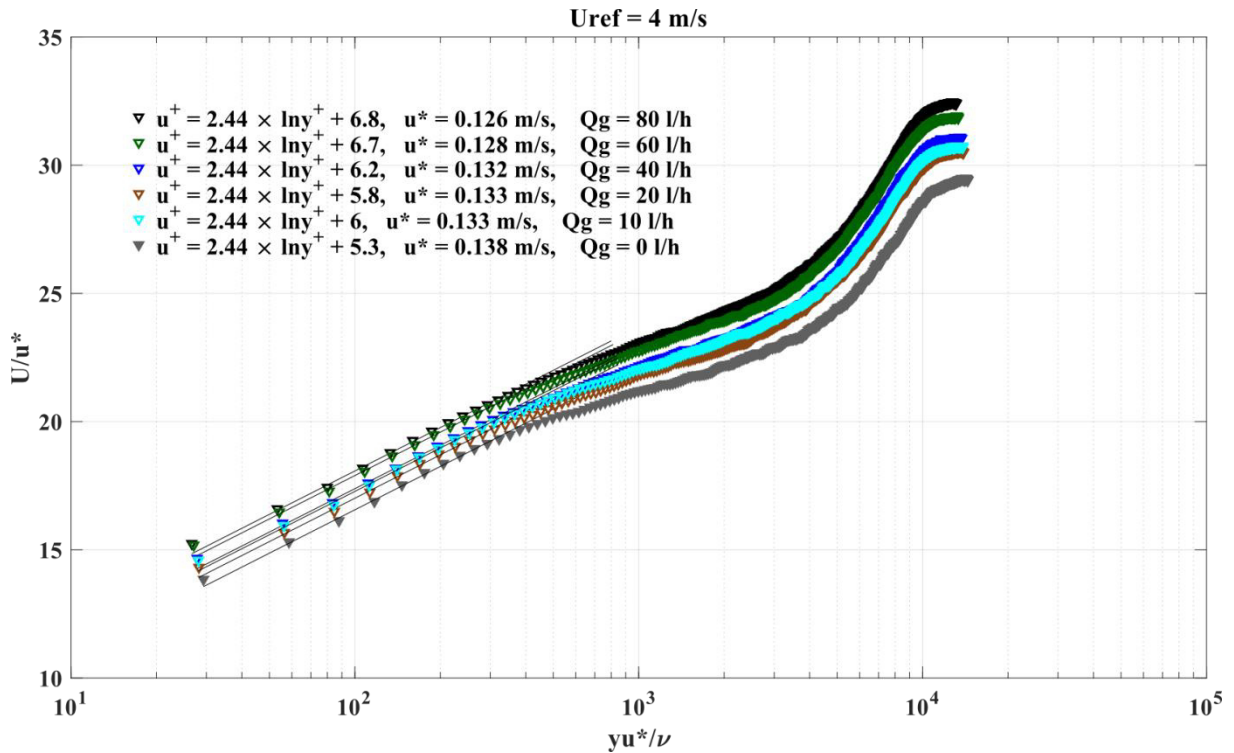


Figure V. 13 Semi-logarithmic plot of mean velocity profiles at $U_{ref} = 4 \text{ m/s}$ (inner variables)

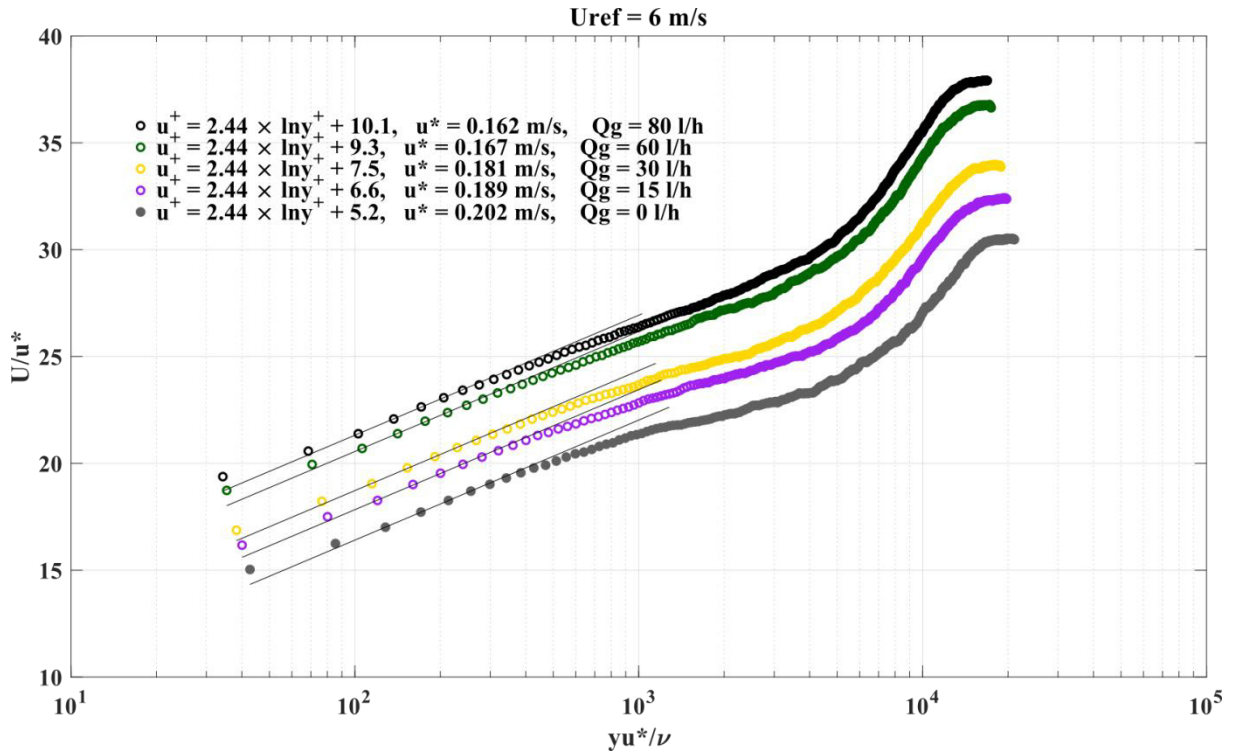


Figure V. 14 Semi-logarithmic plot of mean velocity profiles at $U_{ref} = 6 \text{ m/s}$ (inner variables)

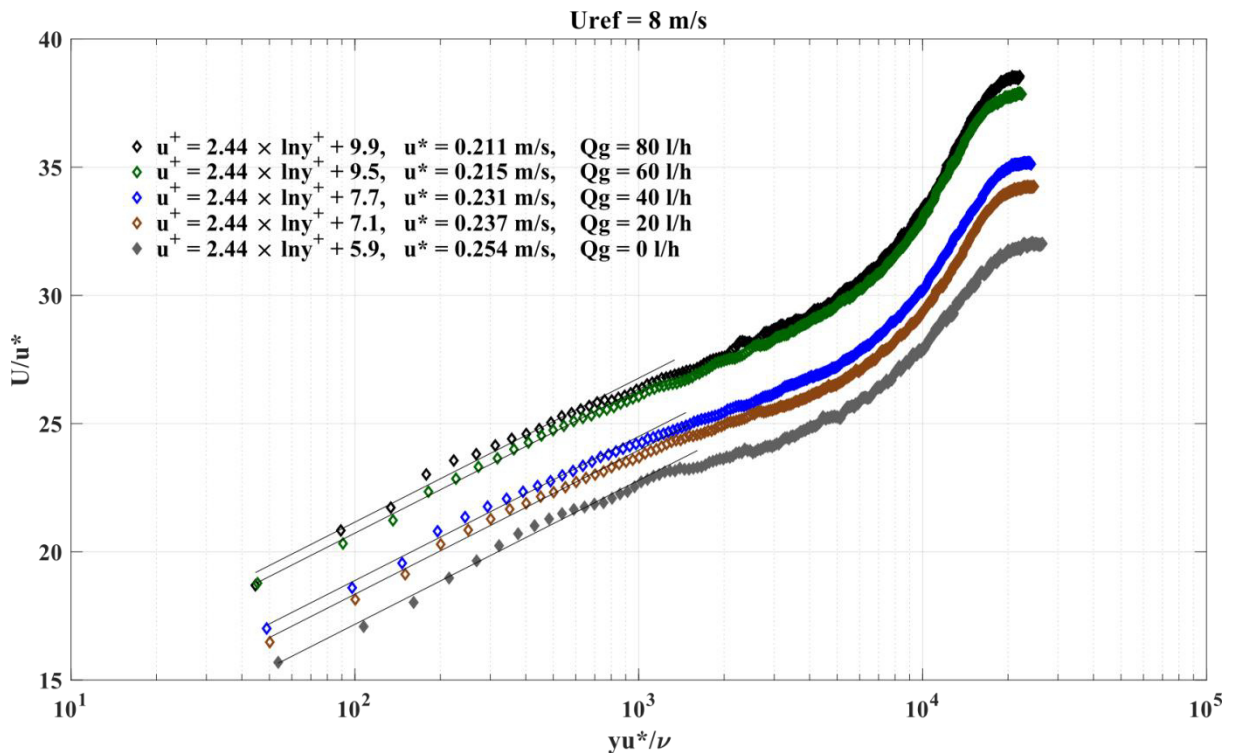


Figure V. 15 Semi-logarithmic plot of mean velocity profiles at $U_{ref} = 8 \text{ m/s}$ (inner variables)

5.3.2.2 Log law with regard to the outer variables

Figure V. 16 - Figure V. 19 show the mean stream-wise velocity profiles plotted on semi-logarithmic scales for outer variables. They evidence the outer layer modifications subject to air injection. Although one cannot deduce much from the profile plot alone, it is still possible to observe a drop of

the additive constant C , when the friction velocity is decreased in the two-phase flow. The more important the air injection rate, the less the friction velocity and the less the constant C .

For $U_{ref} = 4, 6$ and 8 m/s , log region range of validity with respect to y/Δ is enlarged when increasing the gas injection rate.

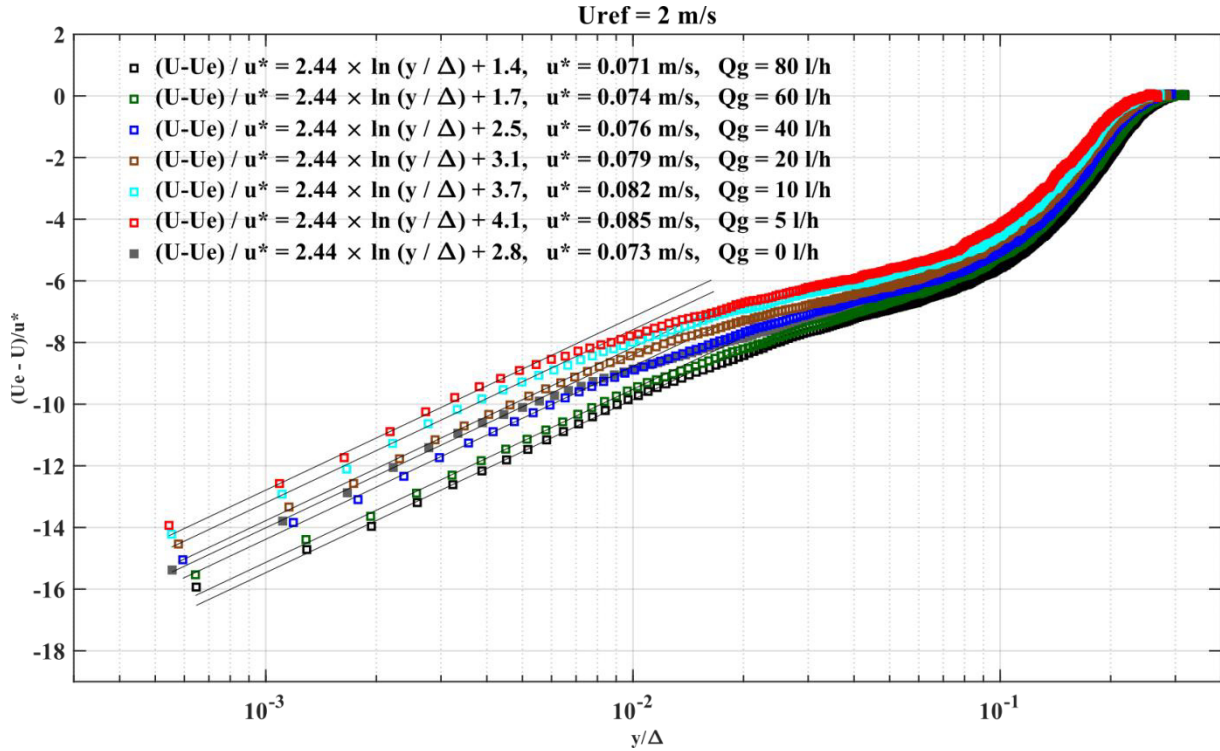


Figure V. 16 Semi-logarithmic plot of mean velocity profiles at $U_{ref} = 2 \text{ m/s}$ for outer variables

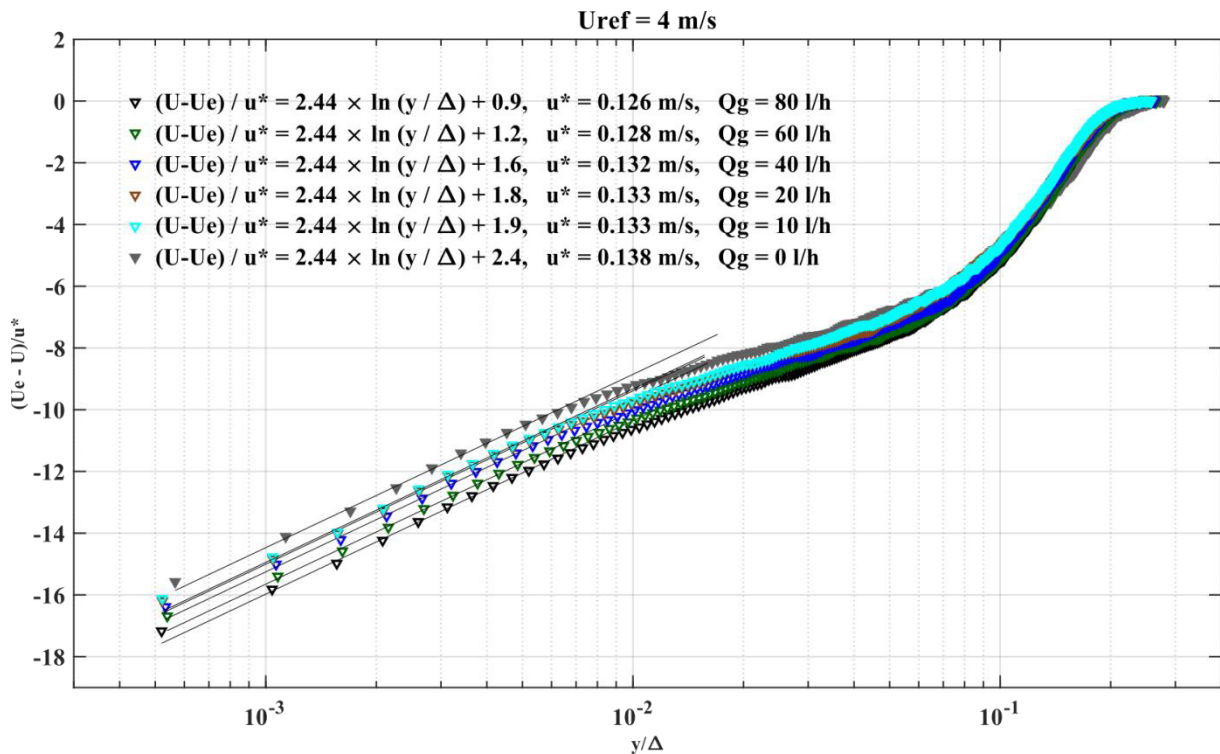


Figure V. 17 Semi-logarithmic plot of mean velocity profiles at $U_{ref} = 4 \text{ m/s}$ for outer variables

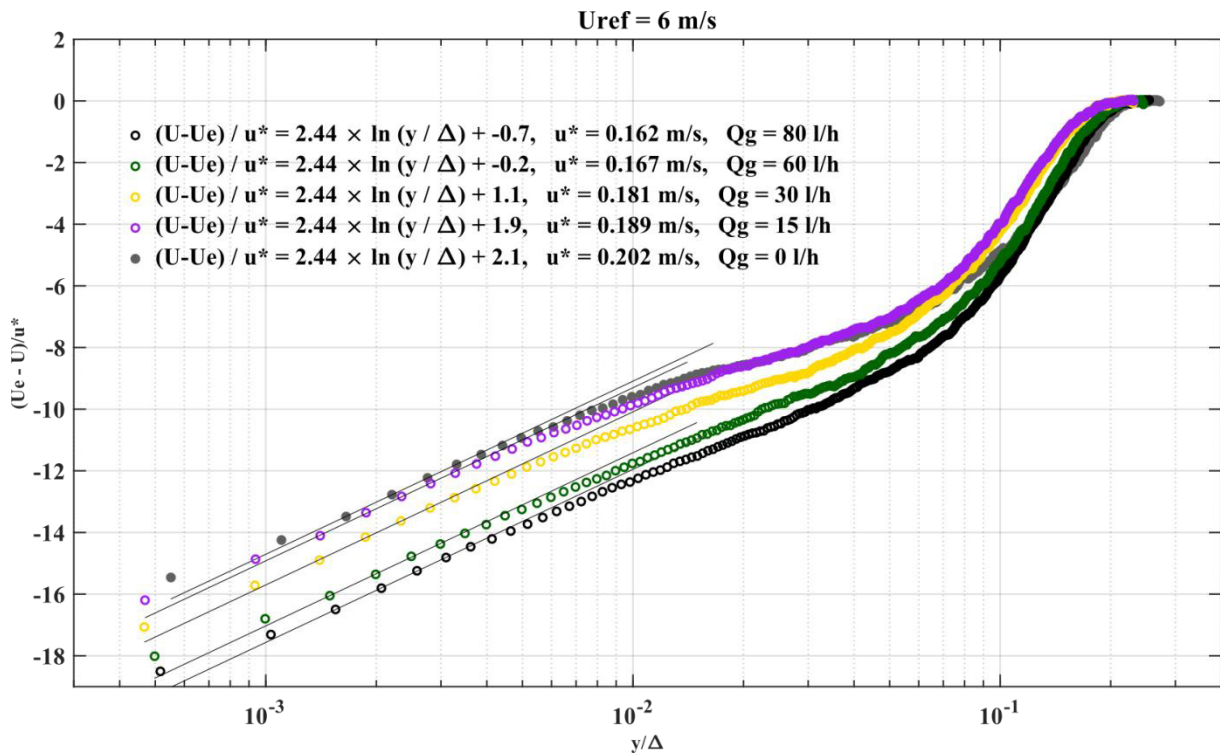


Figure V. 18 Semi-logarithmic plot of mean velocity profiles at $U_{ref} = 6 \text{ m/s}$ for outer variables

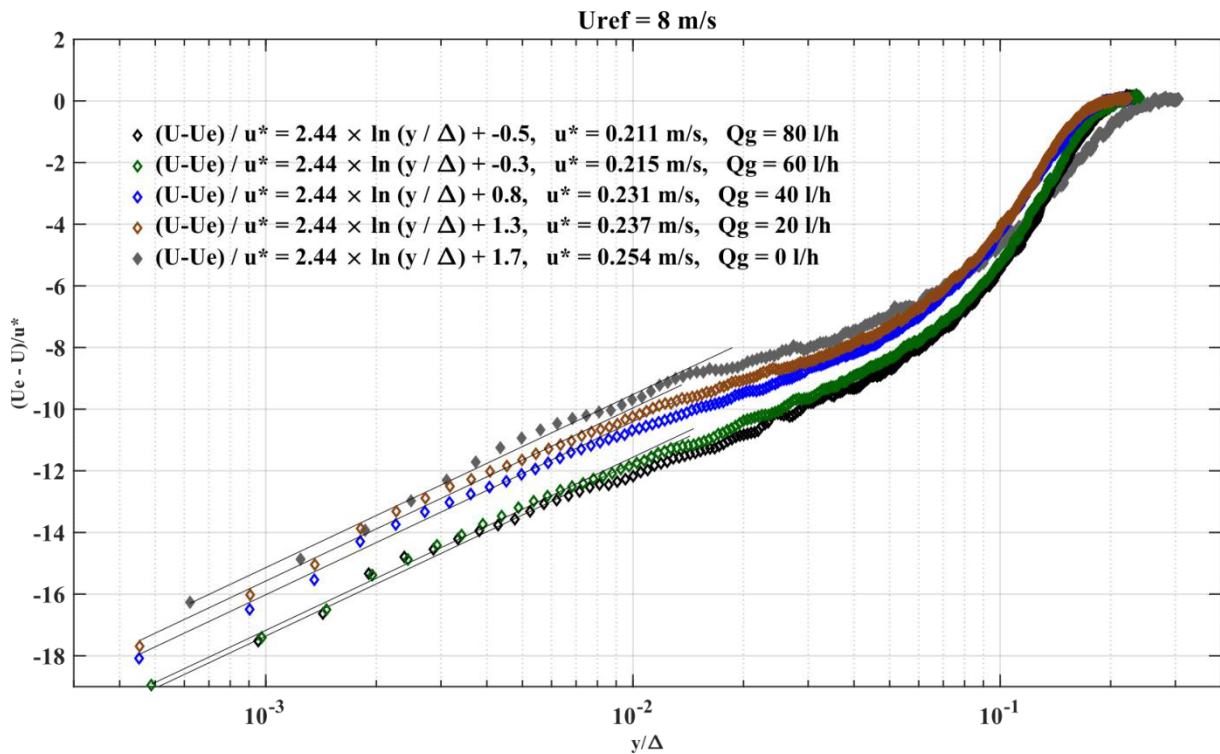


Figure V. 19 Semi-logarithmic plot of mean velocity profiles at $U_{ref} = 8 \text{ m/s}$ for outer variables

The Frictional velocities u^* and the additive constant C are plotted against gas flow rates Q_g at different reference velocities in *Figure V. 20a* and *Figure V. 21* respectively. The evolution of the

additive constant C with the air injection rate follows obviously same trend as the evolution of the friction velocity.

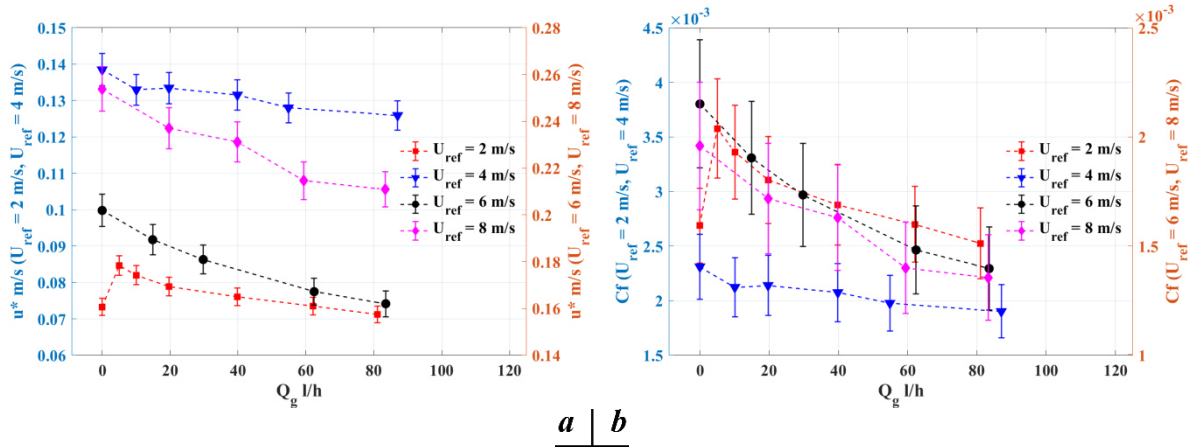


Figure V. 20 Plot versus gas flow rate Q_g of a): friction velocity u^* , b) friction coefficient C_f

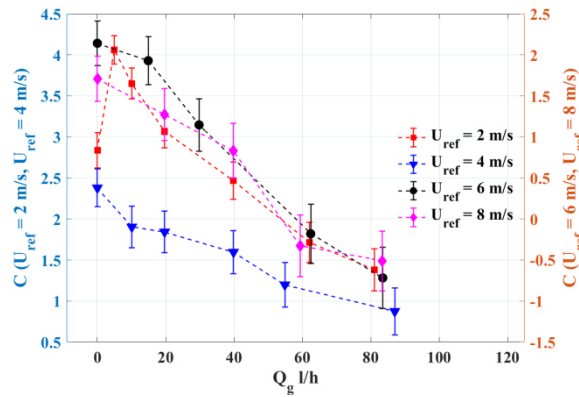


Figure V. 21 Plot of additive constant C versus gas flow rate Q_g

The skin friction coefficient C_f is presented in **Figure V. 20b**. C_f undergoes a variation which comes almost only from the variation in u^* , since U_e seems insensible to gas flow rate.

5.3.3 Integral parameters of the liquid phase flow

The discussion is now focused on the integral parameters of the two-phase flow.

Note that for the specific case: $U_{ref} = 8$ m/s, we will not use the value measured in the single-phase flow as reference value of the integral parameters to compare to the two-phase flow, as the profile of the single-phase flow in the outer region is questionable.

Figure V. 22 shows the evolution of the integral thicknesses δ_3 and δ_4 of the bubbly boundary layer with variation of the air injection rate at different reference velocities. δ_3 and δ_4 are the image of the stream-wise and wall-normal turbulent intensities, integrated upon the boundary layer thickness.

Same trends are obviously observed as for the maxima of U_{rms} , V_{rms} and $-\langle u'v' \rangle$: δ_3 and δ_4 decrease with the air injection rate, for 4, 6 and 8 m/s and for 2 m/s at $Q_g/Q_l < 0.015\%$. For 2 m/s at $Q_g/Q_l > 0.015\%$, δ_3 and δ_4 increase in the two phase flow.

The boundary layer displacement thickness δ^* and the boundary layer momentum thickness θ are plotted against the air injection rate in **Figure V. 23**. Both quantities are scaled by the obstacle height h .

δ^* and θ follow same trends as δ_3 and δ_4 , letting suppose that the turbulent intensity modified by the bubbles drives the displacement and momentum thicknesses of the bubbly boundary layer. The more the bubble additional turbulence, the thicker the boundary layer.

The shape factor H is displayed in **Figure V. 24** as a function of the air injection rate, as well as the *Clauser* parameter G .

Beyond $Q_g = 20l/h$, H decreases with the augmentation of the air injection rate. This comes from an increase of the ratio of momentum flux deficit to the mass flux deficit with the air injection rate.

The *Clauser* parameter grows as the inverse of the friction coefficient. It increases when the air injection rate augments. This is obviously due to the friction reduction enhanced by the increase of the air injection rate. Except at 2 m/s for which the friction coefficient is higher in the two-phase flow than in the single-phase flow, the *Clauser* parameter G is generally increased in the two-phase flow by comparison to the single-phase flow.

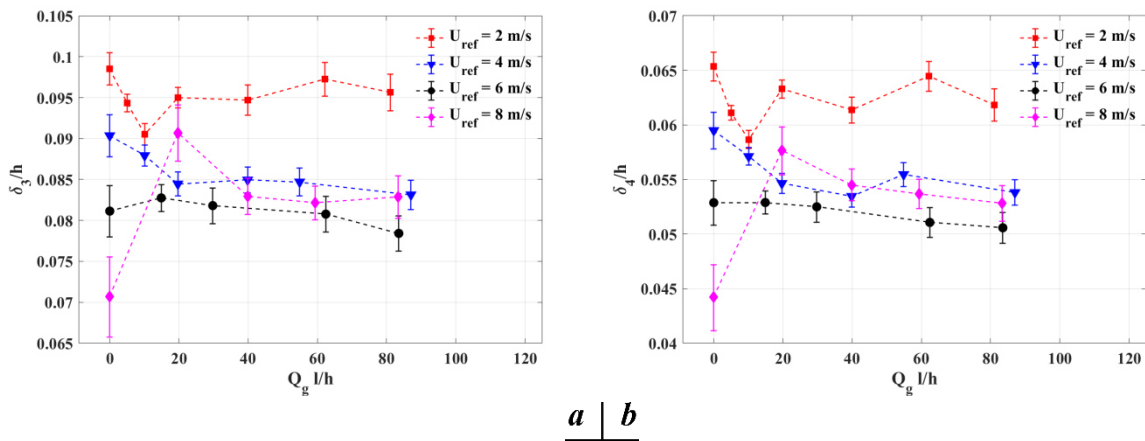


Figure V. 22 Plot versus gas flow rate Q_g of left: integral thickness δ_3 , right: integral thickness δ_4 , both thicknesses scaled by obstacle height h

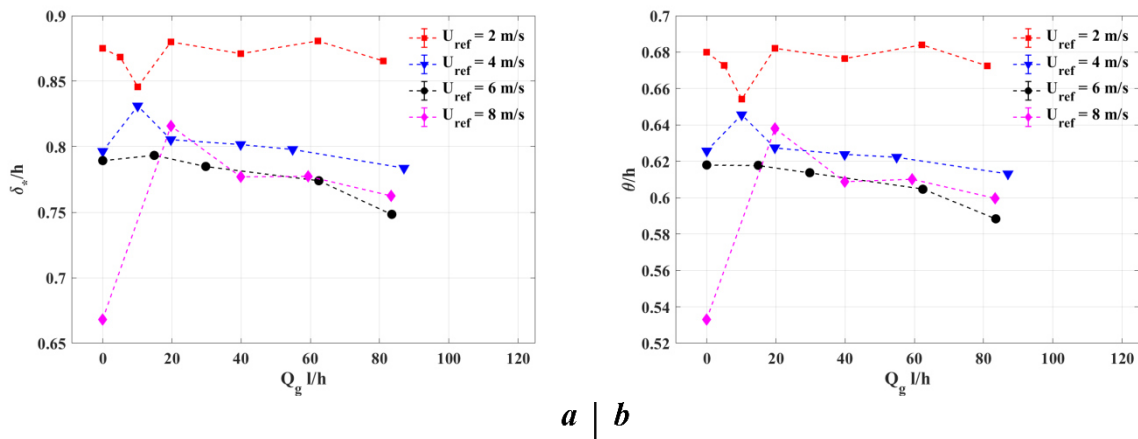


Figure V. 23 Plot versus gas flow rate Q_g of left: displacement thickness δ^* , right: momentum thickness θ , both thicknesses scaled by obstacle height h

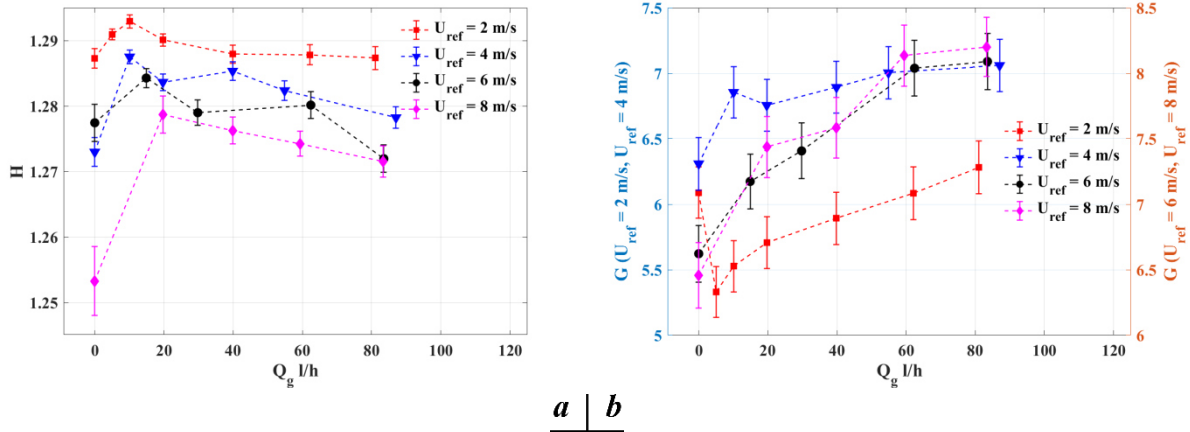


Figure V. 24 Plot versus gas flow rate Q_g of left: shape factor H , right: Clauser parameter G

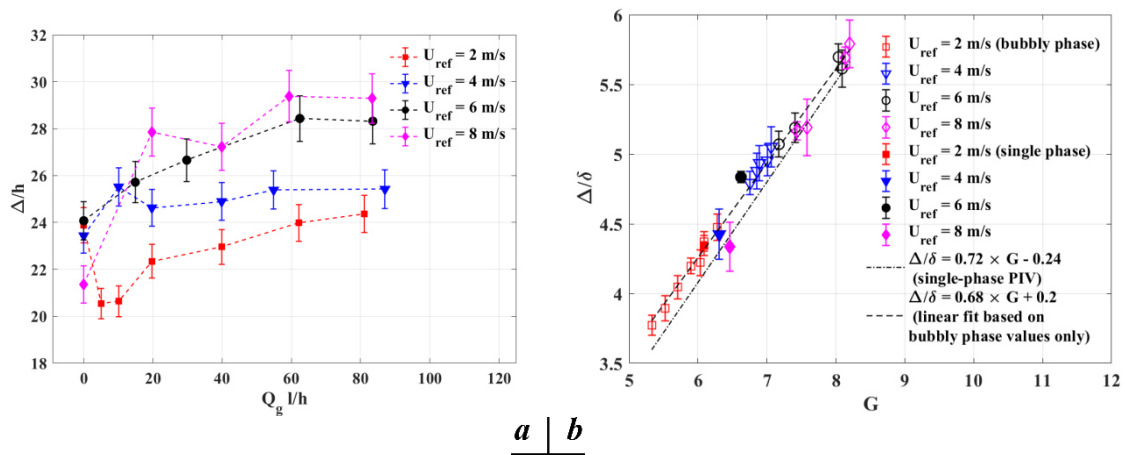


Figure V. 25 Plot of left: Universal thickness Δ scaled by the obstacle height versus gas flow rate Q_g , right: Δ/δ versus G

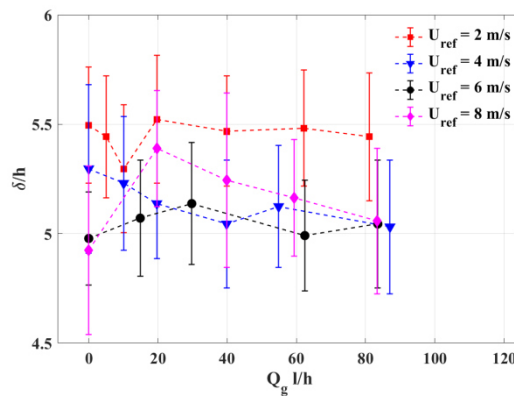


Figure V. 26 Plot of boundary layer thickness $\delta (y_{U=0.99U_e})$ versus gas flow rate Q_g

The evolution of the universal layer thickness Δ versus the air injection rate is shown in **Figure V. 25a**. Also, the ratio of Δ to δ , has been plotted against G in **Figure V. 25b**. The boundary layer δ was defined as the distance away from the wall where 99% of the free stream velocity U_e is reached. Its evolution with regard to the air injection rate is depicted in **Figure V. 26**.

Δ is obviously increased in the two-phase flow; indeed, the universal boundary layer thickness expands with the air injection rate, as expected for friction reduction enhancement.

In the single-phase flow, *Clauser* suggested that Δ/δ has the value 3.6 at constant pressure and Δ/δ remains constant for same pressure distribution. It is seen that the ratios Δ/δ collapses on a linear function of G , as expected in single-phase flow. Moreover, except the operating point at $U_{ref} = 8\text{ m/s}$, $Q_g = 0\text{ l/h}$, which is questionable, points of the single-phase and two-phase flows are aligned on the same curve. The linear regression obtained from *PTV* points of the two-phase flow is displayed on **Figure V. 25b**. *PTV* points are scaled by: $\frac{\Delta}{\delta} = 0.68G + 0.2$. As can be seen, Δ/δ is observed to follow the same trend in both *PTV* and *PIV* data, but the slope is slightly smaller for *PTV* than for *PIV* (*PIV* data $\Delta/\delta = 0.72G - 0.24$, $0 < G < 8.3$).

We can conclude that the bubbly boundary layer has reached equilibrium, with new values of G , function of the air injection rate.

5.4 Discussions

5.4.1 Stream-wise velocity drift between gas & liquid

When comparing the relative velocity between gas-phase and liquid-phase in the stream-wise direction, a “drift” phenomenon is observed. **Figure V. 27** shows the evolution of the mean stream-wise relative velocity profiles $(U_g - U_l)/U_{ref}$ for different reference velocities. Different air injection rates are superimposed. Above a certain distance y_{drift} , the liquid-phase velocity is higher than the gas-phase one ($U_g - U_l < 0$) and the drift velocity increases almost linearly with the distance from the wall. In addition, in this region, for a same reference velocity, the drift velocity between two phases increases as gas rate increases. From the vicinity of the wall up to y_{drift} , except in the very near wall region at $U_{ref} = 2\text{ m/s}$ with $Q_g/Q_l > 0.015\%$ ($20 < y^+ < 60$), the gas-phase velocity is larger than the liquid-phase one ($U_g - U_l > 0$), which means that the wakes of the bubbles is inverted and bubbles push the liquid in the stream-wise direction (*cf. Figure V. 35*).

In the very near wall region, at $U_{ref} = 2\text{ m/s}$ and high volumetric fraction ($Q_g/Q_l > 0.015\%$), profiles of the relative velocity exhibit negative value of $(U_g - U_l)$, which means that the wakes of the bubbles slows down the liquid in the stream-wise direction (*cf. Figure V. 35*).

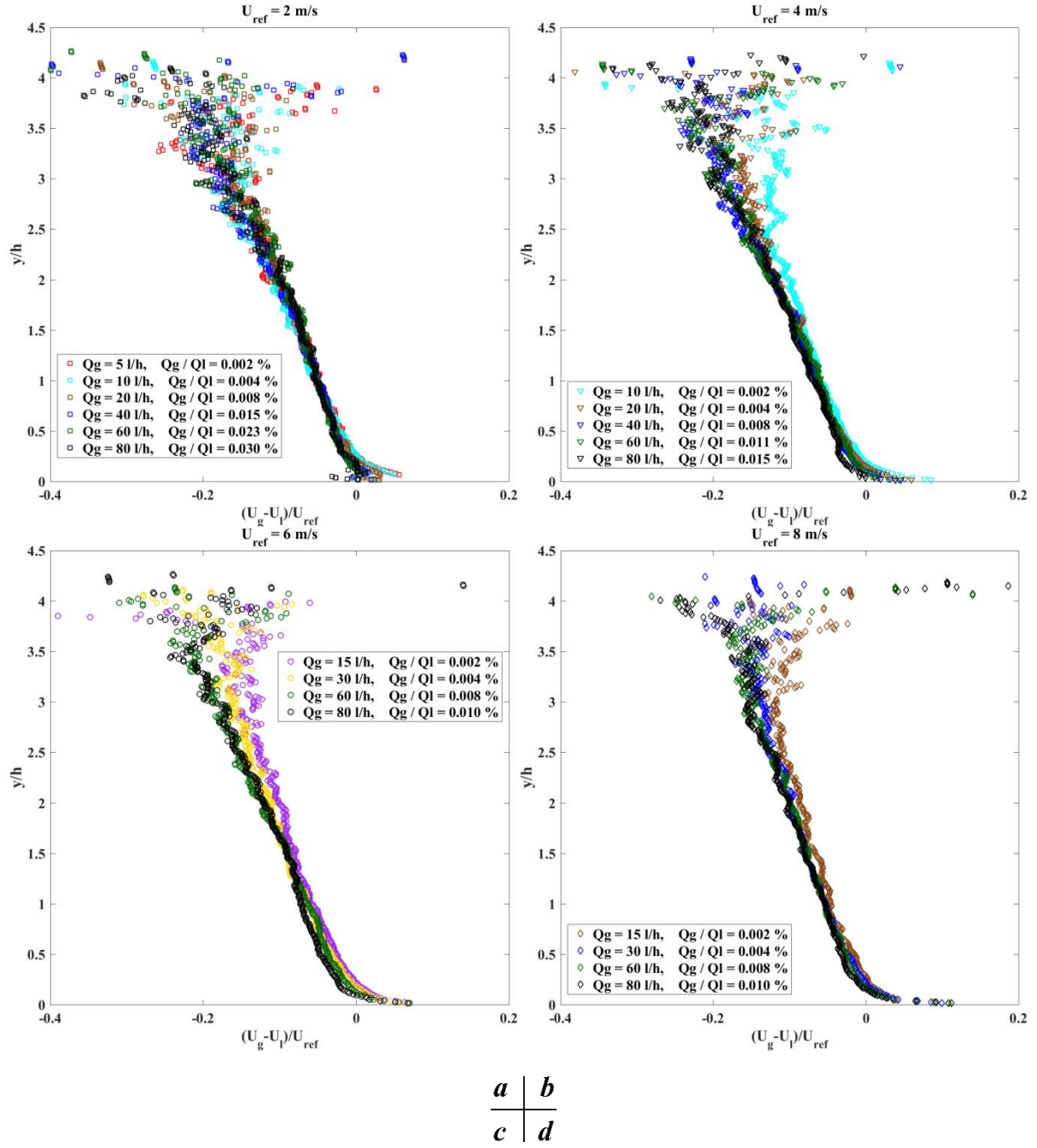


Figure V. 27 Mean stream-wise drift velocity profiles between gas & liquid phases, normalized by the reference velocity U_{ref} (y -coordinate normalized by h) for different air injection rates.

Figure V. 28 shows the evolution of the drift velocity $(U_g - U_l)_{max}/U_{ref}$ measured in the inner region at $y^+ = 50$ with regard to the gas volumetric fraction Q_g/Q_l , the maximum local gas volume fraction α_{v-max} and the dimensionless bubble diameter $\langle d_b \rangle^+$. For a same reference velocity, $(U_g - U_l)_{max}/U_{ref}$ is found to decrease as Q_g/Q_l and α_{v-max} increase for $U_{ref} = 2, 4$ m/s and remains quite insensitive to Q_g/Q_l for higher velocities. Above $\langle d_b \rangle^+ > 80$, the dependency of $(U_g - U_l)_{max}/U_{ref}$ on the volumetric fraction, effective volume fraction and bubble size is not obvious. But for this range of $\langle d_b \rangle^+$ values $(U_g - U_l)_{max}/U_{ref}$ increases as the reference velocity increases (**Figure V. 28c**).

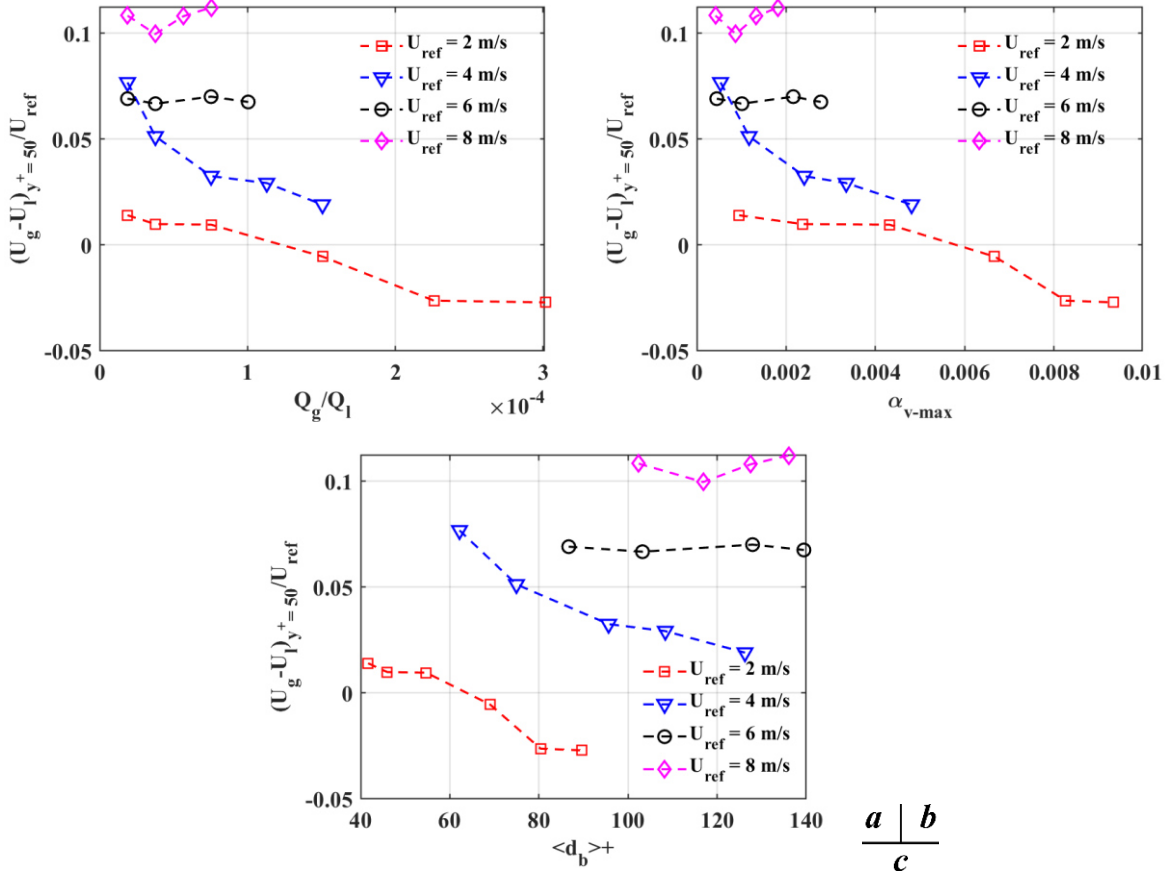


Figure V. 28 Evolution of the near-wall drift velocity between gas & liquid phases ($U_g - U_l$), normalized by reference velocity U_{ref} , measured at $y^+ \approx 50$, with regard to a) gas volumetric fraction Q_g/Q_l , b) near-wall maximum local gas volume fraction α_{v-max} and c) dimensionless bubble diameter $\langle d_b \rangle^+$.

The stream-wise drift velocity $U_g - U_l$, depending on the sign, may induce a wall normal force acting on the bubbles (Lift force) oriented towards or away from the wall. **Figure V. 29** illustrates conceptually the lift force under Magnus effect induced by gas-liquid drift velocity. A bubble traveling downstream that undergoes a mean circulation Γ due to the mean shear flow $\frac{\partial U}{\partial y}$, as represented in **Figure V. 29**, will be subjected to a wall-normal lift force as a function of the incoming flow relative to bubble.

In region ($y < y_{drift}$), where $U_l - U_g < 0$, the lift force pushes the bubble towards the wall except at $U_{ref} = 2$ m/s and $Q_g/Q_l \geq 0.015\%$ in the very near wall region, for which the lift is in competition with buoyancy force and tends to push the bubbles away from the wall. The buoyancy force applied on the bubbles and lift force, when being oriented towards the wall, are both responsible for the bubble driven flow towards the wall that has been evidenced based on V profiles of the liquid phase.

For $y > y_{drift}$, bubbles are driven away from the wall by the lift force. Overall, this creates a divergence effect on bubble wall-normal motion along the y_{drift} line.

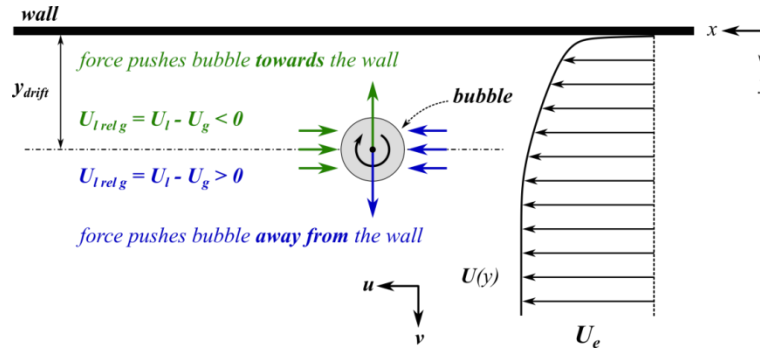
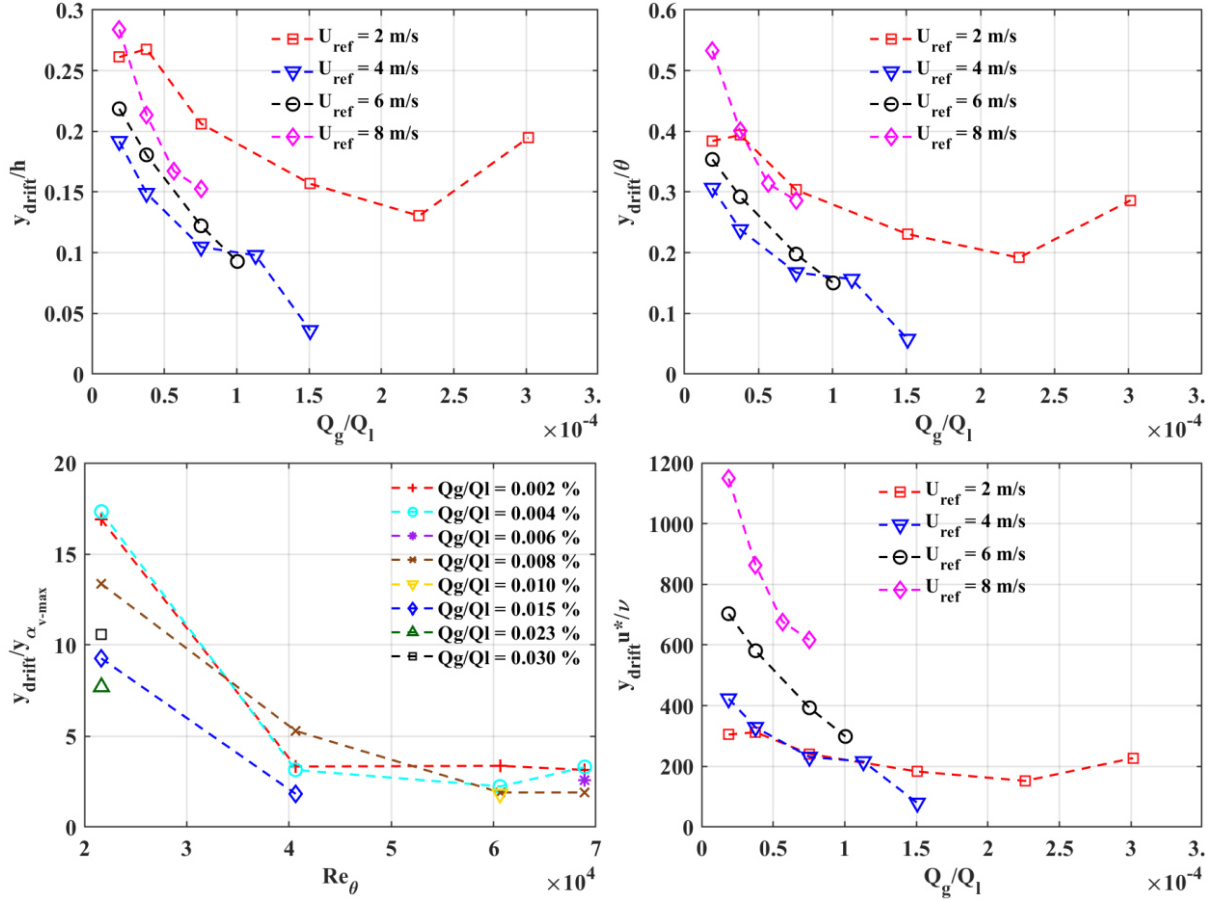


Figure V. 29 Conceptual sketch illustrating drift velocity induced lift exerted on a bubble in the wall normal direction

Figure V. 30 shows the evolution of the y_{drift} value, normalized by different heights, such as h , θ , y_{av-max} and ν/u^* , according to different non dimensional control parameters, such as Q_g/Q_l and Re_θ . Some qualitative remarks can firstly be drawn. y_{drift} decreases as Q_g/Q_l increases for all velocities except for $Q_g/Q_l = 0.03\%$ at 2 m/s (**Figure V. 30a,b**). On the other hand, y_{drift} seems to augment when U_{ref} increases, except for 2 m/s . **Figure V. 30c** shows that, for $U_{ref} \geq 6\text{ m/s}$, y_{drift}/y_{av-max} collapse fairly well ($\frac{y_{drift}}{y_{av-max}} \approx 1.8 - 3.4$) among different gas volumetric fractions Q_g/Q_l . y_{drift}/y_{av-max} decreases greatly from 2 m/s to 4 m/s . For all operating points, we note that the inner bubble region ($y < y_{av-max}$) is included in the region of Lift towards the wall (except at $U_{ref} = 2\text{ m/s}$ and $Q_g/Q_l \geq 0.015\%$ for which the Lift is oriented in the opposite direction).

Figure V. 30d shows that y_{drift} normalized by the viscous length $y_{drift}^+ = y_{drift}u^*/\nu$ follows the same decreasing trend as in **Figure V. 30a,b** as Q_g/Q_l increases, and an increase is observed with respect to U_{ref} for constant values of Q_g/Q_l (except at $U_{ref} = 2\text{ m/s}$ and $Q_g/Q_l \geq 0.015\%$) Overall, as compared to the liquid-phase characteristic regions, y_{drift}^+ shifts from the outer log region or wake region to inner log region, as Q_g/Q_l increases and U_{ref} decreases.



$$\frac{a}{c} \mid \frac{b}{d}$$

Figure V. 30 Evolution with regard to gas volumetric fraction Q_g/Q_l and the *Reynolds* number based on momentum thickness Re_{θ} of the drift y -location, normalized by a) the obstacle height h , b) the momentum displacement θ , c) the y -distance of maximum gas volume fraction $y_{\alpha_{v-max}}$ and d) the viscous length ν/u^* .

For a bubbly mixture, the drag force per unit volume, exerted by the gas phase on the liquid phase, varies with the local gas volume fraction α_v and the stream-wise drift velocity as follows:

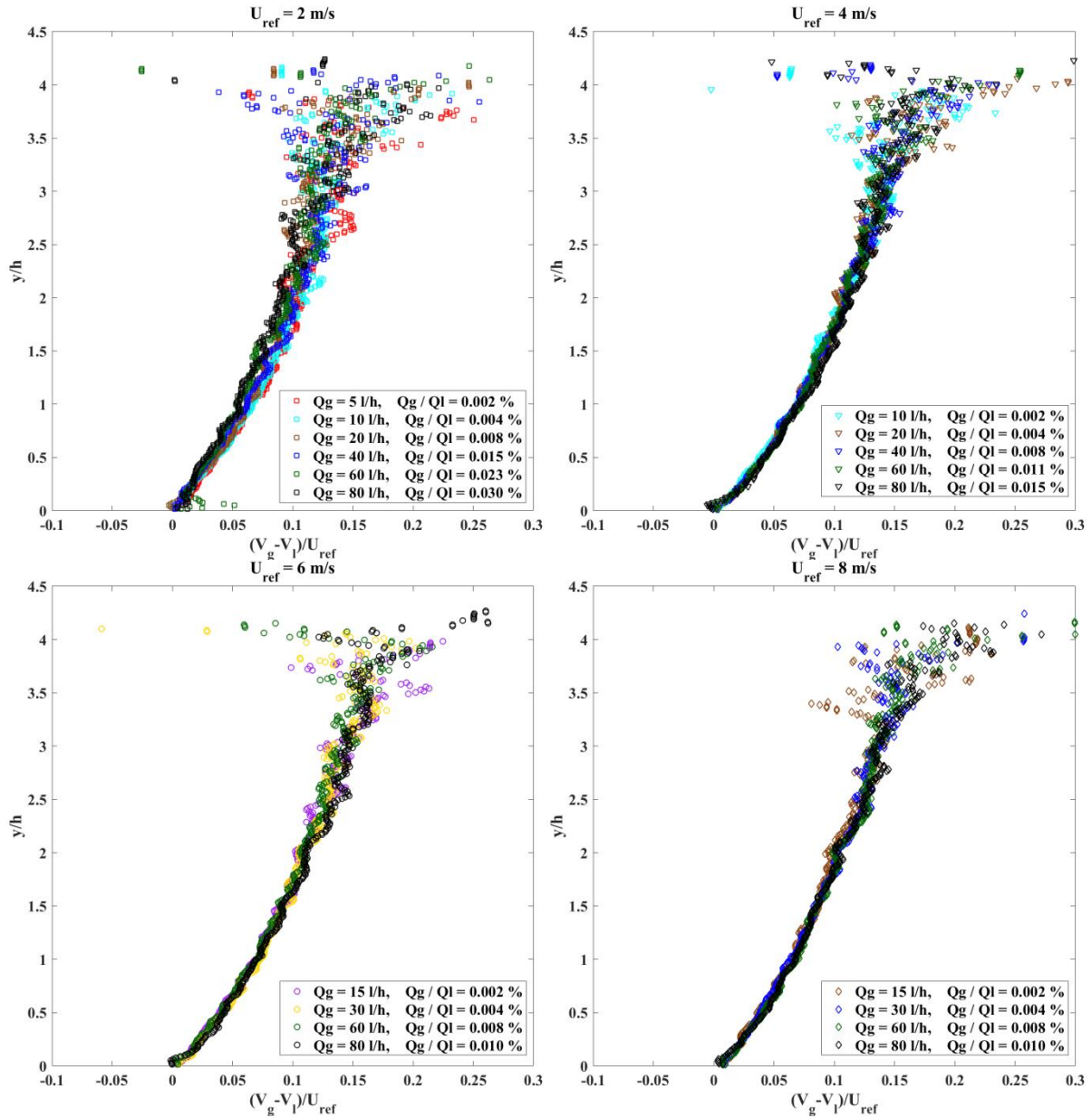
$$f_{Dx} = \frac{1}{2} \rho \frac{3}{2} \frac{\alpha_v}{d_b} C_D |U_g - U_l| (U_g - U_l) \quad 5 - 1$$

where C_D is the drag coefficient of the bubbles.

In the inner bubble layer, except at $U_{ref} = 2$ m/s and $Q_g/Q_l \geq 0.015\%$, this force is expected to be oriented in the stream-wise direction, which tends to increase the stream-wise velocity component of the liquid.

5.4.2 Wall-normal velocity drift between gas & liquid

Figure V. 31 shows the evolution of the mean relative velocity profiles $(V_g - V_l)/U_{ref}$ in the wall normal direction for different reference velocities. Different air injection rates are superimposed. Generally speaking, the gas-phase velocity is seen to be higher than the liquid-phase one for all operating points ($V_g - V_l > 0$) and the drift velocity increases as the wall distance augments. No clear trend with respect to U_{ref} and Q_g/Q_l is observed in the very near wall region ($30 < y^+ < 170$). In this region, the wall normal drift velocity is within the inaccuracy of the measurement.



$$\begin{array}{c|c} a & b \\ \hline c & d \end{array}$$

Figure V. 31 Mean wall normal drift velocity profiles between gas & liquid phases, normalized by the reference velocity U_{ref} (y -coordinate normalized by h) for different air injection rates.

Figure V. 32 illustrates conceptually the lift force under Magnus effect applied on a bubble in the stream-wise direction due to wall normal drift.

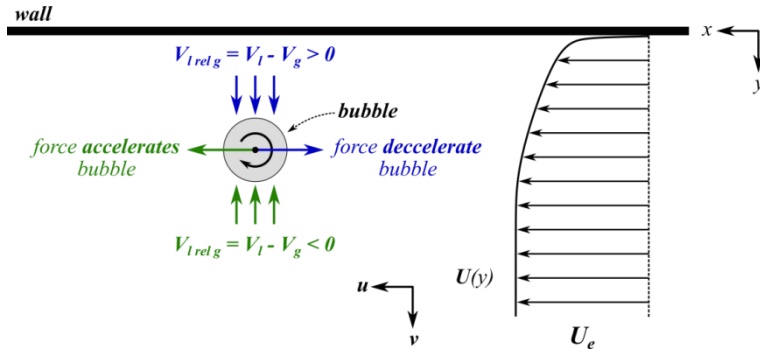


Figure V. 32 Conceptual sketch illustrating drift velocity induced lift exerted on a bubble in the stream-wise direction

Under principle of action-reaction, the lift force per unit volume applied by the gas on the liquid is expressed as follows:

$$f_{Lx} = -\rho\alpha_v C_L (V_g - V_l) \frac{\partial U}{\partial y} \quad 5 - 2$$

with C_L , the lift coefficient of the bubbles. The Lift force applied on the liquid is oriented in the backward direction in most of the boundary layer ($y^+ > 170$).

5.4.3 Non-dimensional analysis of the gain of drag variation

To enable a non-dimensional analysis and comparison between the different flow conditions, the bubble induced drag variation, calculated as the relative variation of the friction coefficient between the single and two-phase flows: DV (%) is plotted versus the volumetric fraction Q_g/Q_l in **Figure V. 33a** and versus the average air volume fraction $\langle \alpha \rangle$ in **Figure V. 33b**.

$$DV (\%) = 100 \frac{C_{f,2\phi} - C_{f,1\phi}}{C_{f,1\phi}} \quad 5 - 3$$

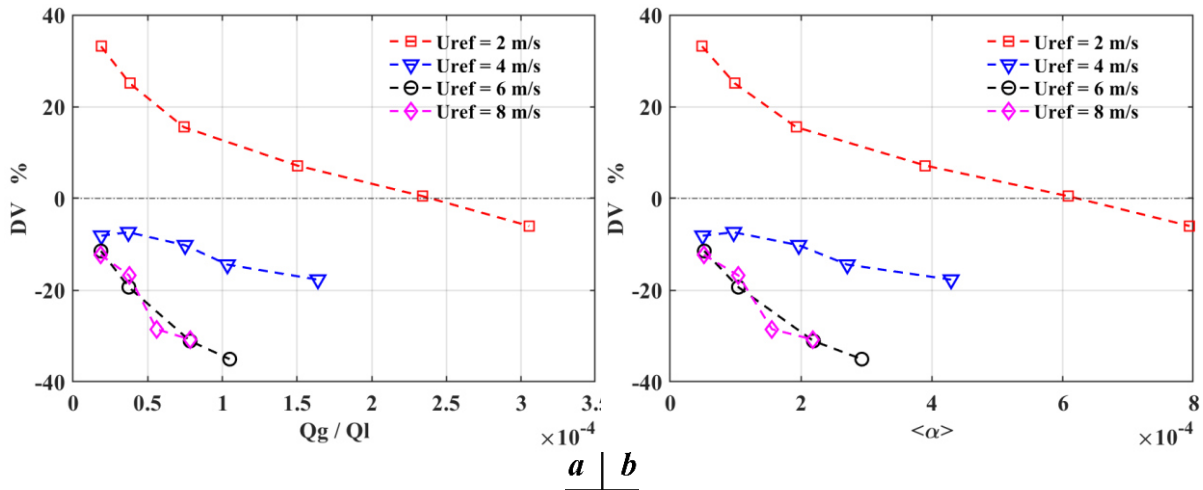


Figure V. 33 Plot of the relative friction reduction versus, a) air volume volumetric fraction, b) average air volume fraction in the boundary layer ($\langle \alpha \rangle$ is the value based on single-phase boundary layer thickness)

$DV < 0$ is associated to drag reduction. At a given velocity, relative drag reduction $|DV|$ encounters a quite linear increase with an increase of the air volumetric fraction. A maximum drag reduction of 35% is achieved at $U_{ref} = 6 \text{ m/s}$ for a volumetric fraction $Q_g/Q_l = 0.01\%$. The drag reduction evolution for $U_{ref} = 8 \text{ m/s}$ is observed to collapse on that for $U_{ref} = 6 \text{ m/s}$, that seems to correspond to a universal family.

The gain factor $DV/\langle\alpha\rangle$ is defined as the ratio of the drag variation per unit average gas volume fraction. In order to distinguish different mechanisms associated with $DV/\langle\alpha\rangle$ modification, the evolution of the gain factor $DV/\langle\alpha\rangle$ has been plotted against Re_θ , Fr_θ , Fr , $\langle d_b \rangle^+$ and We_{u^*} (**Figure V. 33**).

The *Reynolds* number Re_θ illustrates the turbulence effect on $DV/\langle\alpha\rangle$. The Froude number illustrates the ratio of inertia to buoyancy forces. As a reminder, Fr_θ is the Froude number based on momentum thickness, while Fr is the Froude number based on bubble size. The *Weber* number We_{u^*} accounts for the deformability of the bubbles, it is based on bubble size and friction velocity (**Eq. 4 – 8**). Note that We_{u^*} is twice the capillary number Ca (see **Eq. 1 – 28**, when approximating the shear rate γ by $\frac{\tau_P}{\mu}$). $\langle d_b \rangle^+$ illustrates the influence of the bubble size ratio to the length scale of the inner region of the boundary layer .

Considering that the Capillary number is varying from 0.025 to 0.25, bubbles can increase the local viscosity of the liquid (see **Eq. 1 – 27**), but the expected maximum increase in the viscosity is 0.8%. Therefore mechanisms of change in the rheological properties of the liquid are discarded.

At a given air volumetric fraction Q_g/Q_l , an increase in inertia and deformability effects, an increase in turbulence level, as well as a decrease in the gravity effect lead to an augmentation of the gain of drag reduction. This is achieved when increasing the reference velocity. An increase in $\langle d_b \rangle^+$ also results in an augmentation of the gain of drag reduction. This means that the drag reduction is not a direct effect of the bubble size: bubbles don't behave as roughness for the turbulent boundary layer flow but they will interact with the turbulent structures. The best collapse of the gain factor, whatever the value of the volumetric fraction, is obtained for $Fr > 50$ when plotting the gain according to Fr , which means that the ratio of inertia of the liquid to buoyancy of the bubbles has a strong influence on the gain.

The best fit of the gain factor is:

$$\text{For } Fr > 40 \text{ and } \frac{Q_g}{Q_l} \geq 0.004\%, \quad \frac{DV}{\langle\alpha\rangle} = 0.29 \times Fr^2 - 65.79 \times Fr + 1821 \quad 5 - 4$$

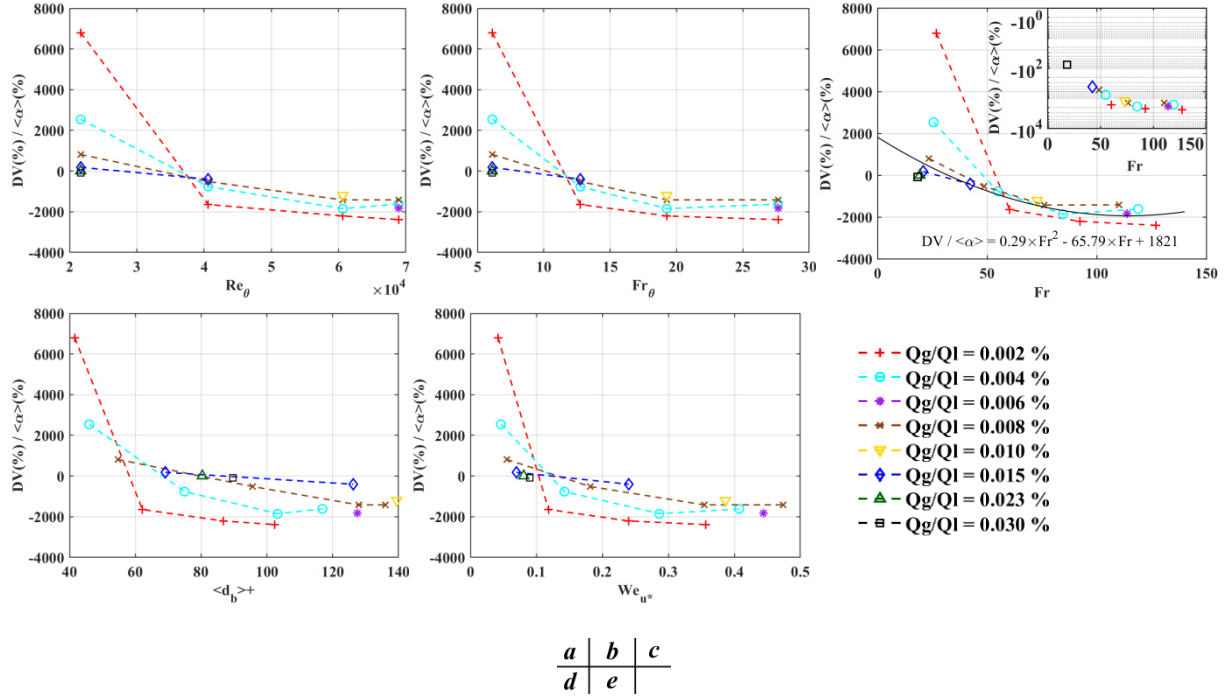


Figure V. 34 Plot of the gain factor, $DV/\langle \alpha \rangle$, in function of Re_θ , Fr_θ , Fr , $\langle d_b \rangle^+$ and We_{u^*} .

5.4.4 Contribution of different mechanisms

When bubbly drag reduction is observed, multiple mechanisms are supposed to be involved.

Despite the fact that it is often difficult to accurately determine all the mechanisms, we try to give an estimation, as an order of magnitude, of the contributions of some of the underlying mechanisms: drag effect, lift effect, modification of the turbulent shear stress induced by the bubbles.

At a first approximation, integration in the wall normal direction from the wall to an upper limit $y_{upper\ limit}$ (in the inner region) of the momentum conservation equation of the liquid phase, in the stream-wise direction, yields the following expression of the bubble induced wall shear stress modification $\Delta\tau_w$:

$$\Delta\tau_w = \Delta\tau_{turbulent}(y_{upper\ limit}) + \int_0^{y_{upper\ limit}} (f_{Dx} + f_{Lx}) dy \quad 5 - 5$$

Where f_{Dx} and f_{Lx} denote the drag and lift forces per unit volume, due to momentum transfer from gas to liquid at the gas-liquid interfaces in the stream-wise direction. This relationship postulates that the phase averaged pressure in the liquid is conservative in the recovery region, as expected in the developing boundary layer of a single-phase flow $(1 - \alpha_v)P_l = P_e(x)$. It also assumes that the external pressure gradient in the bubbly flow is unchanged by comparison to the single-phase flow.

5.4.4.1 Bubble induced Drag effect

As a first attempt to evaluate different contributions, we can consider that the drag coefficient of the bubbles C_D evolves as a function of the *Reynolds* number of the gas phase $Re_b = \frac{|U_g - U_l| d_b}{\nu}$ as:

$$C_D = \frac{J}{Re_b},$$

which makes it possible to linearize the drag force with respect to the drift velocity. Here, J is a constant which can be approximated by 48, in the range of bubbles *Reynolds* numbers considered here (simplification of Moore law, *Moore, 1963*).

The estimated drag modification of the wall shear stress associated with drag effect is given as below:

$$\left. \frac{\Delta\tau_w}{\tau_{w0}} \right|_{Drag} = \frac{3J\nu}{2d_b^2 U_e^2 C_{f0}} \int_0^{y_{upper\ limit}} \alpha_v (U_g - U_l) dy \quad 5 - 6$$

Given that the bubble drag reduction is a near-wall issue, and considering that $y_{upper\ limit}$ must be in the logarithmic region, we have used $y_{\alpha v-max}$ as the integral upper limit for $U_{ref} = 4,6$ end $8\ m/s$ (see **Figure IV. 21** of **Chapter 4.4.5** for more details about the values of $y_{\alpha v-max}$ normalized by the viscous length). For this upper limit, the drag effect tends to increase the local wall shear stress. For $U_{ref} = 2\ m/s$, the integration has been performed over $y_{upper\ limit} = 2 \times y_{\alpha v-max}$ ($y_{\alpha v-max}^+$ being too small ≈ 50).

5.4.4.2 Bubble induced Lift effect

The lift coefficient of a bubble C_L can vary with the vorticity of the liquid phase and the *Reynolds* number of the bubbles Re_b . Nevertheless, as a first attempt to estimate the order of magnitude of the different contributions, we consider $C_L \approx 0.5$, as expected for a bubble in a flow of inviscid fluid.

The modification of the wall shear stress associated with Lift effect is given as below:

$$\left. \frac{\Delta\tau_w}{\tau_{w0}} \right|_{Lift} = -\frac{2}{U_e^2 C_{f0}} \int_0^{y_{upper\ limit}} \alpha_v C_L (V_g - V_l) \frac{\partial U}{\partial y} dy \quad 5 - 7$$

5.4.4.3 Bubble induced modification of the turbulent shear stress

Based on the liquid-phase averaged momentum conservation equations, *Murai et al. (2006)* considered that the turbulent shear stress of the liquid comes from the addition of 3 terms described as follow:

$\tau_{turbulent} = -\rho(1 - \alpha_v)\langle u'v' \rangle_l + \rho\langle \alpha_v'v' \rangle_l U_l + \rho\langle \alpha_v'u'v' \rangle_l$	5 - 8
$\text{term A} \qquad \qquad \text{term B} \qquad \qquad \text{term C}$	

Where α_v' denotes the local gas volume fraction fluctuation.

The component $\rho\langle \alpha_v'v' \rangle_l U$ (*term B*) originates from the correlation between the local volume fraction and the wall-normal liquid velocity fluctuations and is amplified by the mean stream-wise velocity of the liquid U_l . If we consider that the local velocity fluctuations of the gas phase drive the local velocity fluctuations of the liquid, then we expect $\langle \alpha_v'v' \rangle_l < 0$.

$$v_g' > 0 \rightarrow \alpha_v' < 0 \text{ and } v_l' > 0 \rightarrow \alpha_v'v_l' < 0 \quad 5 - 9$$

$$v_g' < 0 \rightarrow \alpha_v' > 0 \text{ and } v_l' < 0 \rightarrow \alpha_v'v_l' < 0$$

This means that the wall normal velocity fluctuations of the gas are expected to decrease the turbulent shear stress and thus the wall shear stress. This can be achieved when the wall normal fluctuating motion of the bubbles interact with the vortical structures in the near wall region. For a channel flow,

Murai et al. (2006) have characterized this term and shown in their experiments that it has same order of magnitude as *term A*, but a sign opposite.

The term $\rho\langle\alpha_v'u'v'\rangle_l$ (*term C*) characterizes the cross-correlation of instantaneous local turbulent stress of the liquid with the fluctuation of the local volume fraction. The turbulent shear stress induced by turbulent bubbles wakes can be included in this term. In theory, if the probability for a bubble to be at a given y position in its upper part of the wake is the same as the one to be in its lower part of the wake, then the wakes are symmetric in the y direction and it leads: $\rho\langle\alpha_v'u'v'\rangle_{l,bubble\ wakes} = 0$. But in the very near wall region, there's only the contribution of asymmetric bubbles wakes.

Figure V. 35 illustrates conceptually the production of bubble wake induced turbulent events. Considering two following cases: **1)** when $(U_g - U_l) > 0$, a wake flow is induced downstream the bubble and the liquid velocity is accelerated locally (**Figure V. 35a**), that results, in the near wall region, in events of $\alpha_v' < 0$ and $u'v' < 0$, thus leading to $\rho\langle\alpha_v'u'v'\rangle_{l-wake} > 0$. **2)** when $(U_g - U_l) < 0$, the wake in front of the bubble decelerates the liquid velocity (**Figure V. 35b**) and leads to the production of events of $\alpha_v' > 0$ and $u'v' > 0$, and leads to $\rho\langle\alpha_v'u'v'\rangle_{l-wake} > 0$.

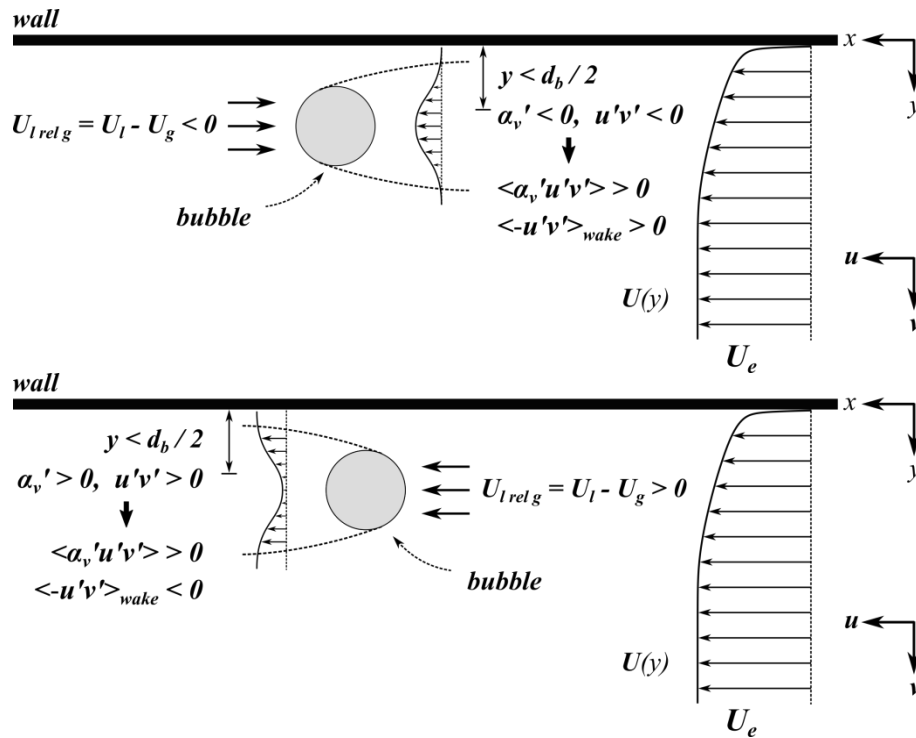


Figure V. 35 Conceptual sketch illustrating stream-wise drift velocity induced bubble wake flow

In their experiment of bubbly channel flow, *Murai et al. (2006)* have observed that the contribution of this term to the total turbulent stress is concentrated near the wall. In their experiment, the contribution of the *term C* is very small by comparison to *terms A* and *B*. Nevertheless, it depends on the magnitude of drift velocity of the gas with respect to the liquid and the bubble size.

The term $-\rho(1 - \alpha_v)\langle u'v'\rangle$, which represents the shear stress induced turbulence modified by local density effects, can further be separated into two sub-components:

$$-\rho(1 - \alpha_v)\langle u'v'\rangle_l = -\rho(1 - \alpha_v)\Delta\langle u'v'\rangle_l - \rho(1 - \alpha_v)\langle u'v'\rangle_0 \quad 5 - 10$$

$\langle u'v' \rangle_0$ stand for the single-phase correlation between the stream-wise and wall normal velocity fluctuations and $\Delta\langle u'v' \rangle_l$ is the bubble-induced variation of this correlation.

In our experiment, the measurement of the liquid phase averaged *Reynolds* stress $\langle u'v' \rangle$ includes both shear stress induced and bubbles wakes induced terms (*term A* \pm *term C* of **Eq. 5 – 8**). Profiles of $\langle u'v' \rangle$ on **Figure V. 10** confirm the contribution of bubbles wake in the inner bubbles layer.

With this approach, we can rewrite the bubble induced variation of the total turbulent shear stress in the following way:

$\frac{\Delta\tau_{turbulent}}{\tau_{turbulent\ 0}} = -\alpha_v + (1 - \alpha_v) \frac{\Delta\langle u'v' \rangle_l}{\langle u'v' \rangle_0} - \frac{\langle \alpha_v'v' \rangle_l U_l}{\langle u'v' \rangle_0} - \frac{\langle \alpha_v' u'v' \rangle_l}{\langle u'v' \rangle_0}$	5 – 11
< 0 sign not known < 0 > 0 for $y < y_{\alpha v-max}$	
< 0 sign not known < 0 ≈ 0 for $y > y_{\alpha v-max}$	
<i>terms A'</i> <i>terms B'</i> <i>terms C'</i> <i>terms D'</i>	

The *term A'* of this last equation is identified as density reduction effect. One can estimate the contribution of the density reduction effect to wall shear stress reduction by using the local gas volume fraction α_v measured at $y_{upperlimit}$.

$\frac{\Delta\tau_w}{\tau_{w0}} \Big _{Density} = -\alpha_{v-y_{upperlimit}}$	5 – 12
< 0	

The remaining term includes the shear stress induced, the bubbles wake induced terms and also the bubble wall normal oscillation induced correlation.

$\frac{\Delta\tau_w}{\tau_{w0}} \Big _{Remaining} = 2(1 - \alpha_v) \frac{\Delta\langle -u'v' \rangle_{l,near\ wall}}{U_e^2 C_{f0}} + 2 \frac{\langle \alpha_v'v' \rangle_l U_l}{U_e^2 C_{f0}} + 2 \frac{\langle \alpha_v' u'v' \rangle_l}{U_e^2 C_{f0}}$ at $y_{upperlimit}$	5 – 13
sign not known < 0 > 0	
(α_v evaluated at $y_{upperlimit}$)	

5.4.4.4 Analysis of the contribution of the different mechanisms to global DV

The contribution to the total variation of the wall shear stress of the remaining effect (**Eq. 5 – 13**) can be evaluated in a qualitative way as:

$\frac{\Delta\tau_w}{\tau_{w0}} \Big _{Remaining} = DV - \frac{\Delta\tau_w}{\tau_{w0}} \Big _{Drag} - \frac{\Delta\tau_w}{\tau_{w0}} \Big _{Lift} - \frac{\Delta\tau_w}{\tau_{w0}} \Big _{Density}$	5 – 14
--	--------

Figure V. 36 summarizes in percent the evolution of above-mentioned effects (density, lift, drag and remaining effects) in fraction of total DV, with respect to the gas volumetric fraction Q_g/Q_l for different reference velocities.

Each figure is divided into a drag decrease contribution zone and a drag increase one, according to the DV fraction sign. The drag decrease contribution zone is located in positive DV fraction region. At 2 m/s , absolute values of DV have been used for normalization as DV changes its sign at $Q_g/Q_l \approx 0.023\%$ and a vertical separation line has been set at this value of the air volumetric fraction.

Generally speaking, the density effect exhibits an overall increase as Q_g/Q_l increases. Under condition of $DV < 0$, the remaining effects are observed to be the main contributor to the total drag reduction, though the contribution of wall normal oscillating motion of the bubbles and are of roughly the order of 100% at 4, 6 and 8 m/s . For these velocities, the maximum fraction of total drag reduction due to density reduction is several%; The bubble-induced lift effect is observed to be a contributor to the total drag decrease for both $DV > 0$ and $DV < 0$ region. In $DV < 0$ regions, its contribution is seen to be quite small ($< 1\%$) to the total drag decrease.

At 4, 6, 8 m/s , the fraction of the drag effect to total DV decreases with increasing Q_g/Q_l , in agreement with the decrease of drift velocity ratio to U_{ref} . For all reference velocities, the contribution of the drag effect is observed to be quite small ($< 1\%$). At 8 m/s , the contribution of density effect compensates the contribution of drag effect.

For $U_{ref} = 2\text{ m/s}$, under condition of total drag increase, the balance between the different mechanisms is different. The remaining effects contribute here to increase the wall shear stress through shear induced turbulence and bubbles wakes (**Figure V. 35a**). In this case, the bubbles vertical fluctuating motion is quite inexistent due to a strong bubbles buoyancy effect (small Froude number $Fr < 30$).

But at $U_{ref} = 2\text{ m/s}$, for $Q_g/Q_l > 0.023\%$, it is interesting to note the contribution of the reversed bubbles wakes near the wall (**Figure V. 35b**), which leads now to global drag decrease through:

-a contribution of drag effect to global drag decrease,

-a wall normal lift force applied on the bubbles oriented away from the wall in competition with buoyancy force that activates wall normal oscillating motion of the bubbles and the contribution of the remaining effect to global drag decrease.

Inversion of the bubbles wakes (from configuration of **Figure V. 35a** to **Figure V. 35b**) occurs at small Froude number ($Fr_\theta < 10$), for high air volumetric fraction, under strong deformation of the bubbles ($We_{u_*} > 0.09$).

In general, we may suggest that the bubble wall normal oscillating motion plays an important role in DV reduction at high Froude numbers.

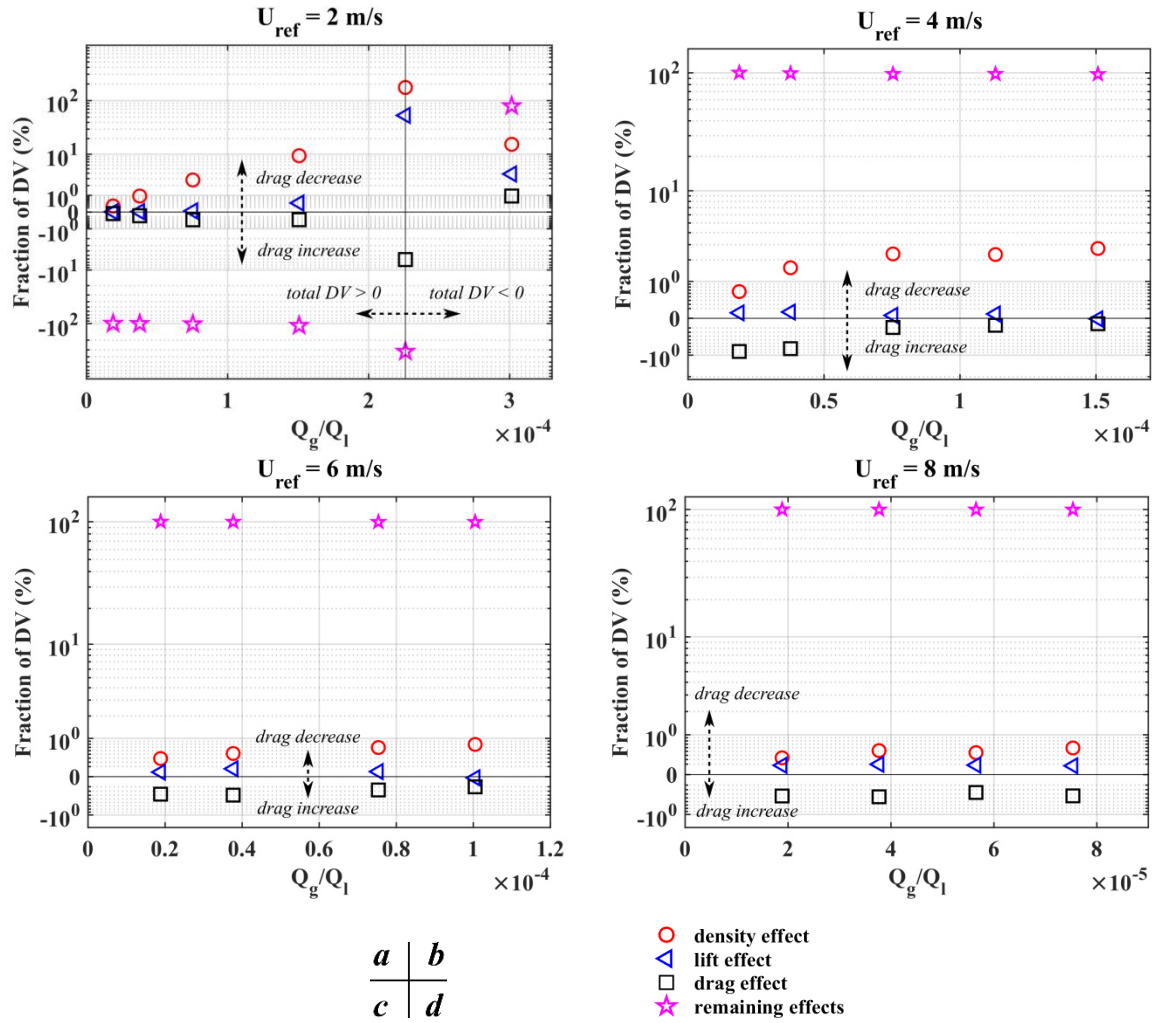


Figure V. 36 Contribution of the different mechanisms to total DV, with respect to Q_g/Q_l

5.5 Conclusion

The liquid-phase flow characteristics measured by *PTV* in the recovery region downward the obstacle have been examined in this chapter.

Mean and fluctuating liquid velocity profiles have been examined for all gas injection rates. An increase of the volumetric fraction is favorable to a bubble induced wall normal driven flow towards the wall, a decrease of the maxima of the *Reynolds* stresses and a shift of the maxima towards the wall. Bubbles move faster than the liquid phase in the stream-wise direction which enhances the gas fraction peak near the wall, as a result of wall normal lift force. Momentum exchange in the stream-wise direction between the gas and liquid phases induces a lift and a drag force that contributes to decrease and increase respectively the stream-wise velocity of the liquid near wall. At 2 m/s, increasing the air volumetric fraction Q_g/Q_l above a critical value of 0.015% leads to opposite trends: in particular the gas phase moves slower than the liquid which leads to reversed bubble wakes and reverse direction of the drag force applied on the liquid.

The logarithmic law of the wall is reported to hold true in the two-phase flow and the friction velocity is observed to exhibit an overall decrease with increasing gas injection rate.

Integral parameters for the liquid-phase flow have been examined. Turbulent intensity thicknesses δ_3 and δ_4 follow the same trends as those for the turbulent stresses maxima and seem to correlate

positively also with the boundary layer thicknesses δ^* and θ : the more the bubble additional turbulence, the thicker the boundary layer. Values of Δ/δ versus G for different gas injection rates and different velocities collapse well on the law of equilibrium boundary layer $\Delta/\delta = f(G)$ established with single-phase *PIV* data, suggesting that bubble injection exhibits a similar effect as an imposed adverse pressure gradient.

As for the drag reduction, a maximum value of 35% is achieved at $U_{ref} = 6 \text{ m/s}$ for a volumetric fraction $Q_g/Q_l = 0.01\%$. The gain factor analysis has brought into light the strong influence of the Froude number.

The stream-wise and wall normal drift velocity profiles between two phases have been examined which has helped us to have a closer view on the different mechanisms associated with drag variation. The bubble-induced modifications on turbulent shear stress decomposition reveal that three other effects play a role in drag variation: density effect which is characterized by near wall local gas volume fraction α_v ; near-wall bubble wake induced turbulent shear stress; bubble wall-normal fluctuating motion induced two phase correlation. It is suggested in our study that the bubble wall normal fluctuating motion should be mainly responsible for the total drag variation. The bubble wall normal fluctuating motion is inhibited by buoyancy effect at small Froude number and promotes drag reduction at large Froude number. The bubble-induced lift and density effects are equally contributors to the drag reduction.

6 General Conclusion

The experimental investigations in this thesis have been made at the French Navy Academy Research Institute. The study is focused on examination of the effect the adverse pressure gradient plays in bubbly drag reduction of reattached turbulent boundary layer flow downstream of a $2D$ surface-mounted squared obstacle with injection of intermediate-size bubbles under favorable.

Firstly, the single-phase velocity field in flow over the obstacle and in downstream wake flow was characterized in the vertical plane over 11 stream-wise stations $x/h = -1.2$ upstream of the obstacle down to $x/h = 38$ in the recovery region using Particle Image Velocimetry. The interrogation window has a dimension of $2.7\text{ mm} \times 1.4\text{ mm}$, with a horizontal and vertical step spacing of $1.4\text{ mm} \times 0.3\text{ mm}$. The wake flow is subjected to a separation and a reattachment due to the strong perturbation induced by the obstacle and the pressure recovery. The Proper Orthogonal Decomposition technique was employed to characterize the energetic & frequential aspect of the flow structure in the recirculation region. Measurements were conducted under 4 main reference velocities ($U_{ref} = 2, 4, 6, 8\text{ m/s}$). At the very last section ($x/h \approx 35$) downstream of the obstacle where multiphase flow measurements were performed, The *Reynolds* number of the single-phase perturbed flow, based on momentum thickness, is varied in the range $Re_\theta = 21662 - 68913$. The non-dimensional pressure gradient β (normalized by the wall shear stress and the displacement thickness) is in the range $[0.39 - 33.55]$. Several observations have been made:

- The recirculation length ($L_R = 12h$) is found to be quite insensible to the reference velocity.
- In the recirculation region, the large vortex traveling frequency varies in a positive almost-linear way with the reference velocity, and the large vortex series contribute up to 18% of the total energy.
- In the recovery region, the universal logarithmic “law of the wall” is confirmed to be valid, even near the reattachment point where steep adverse pressure gradient is still present. The y^+ range of validity extends its upper limit as goes downstream. For a same downstream position, the upper limit range increases as reference velocity increases. Based on this validity, the skin friction coefficient C_f was calculated and a good coincidence was observed with C_f by *Ludwig-Tillmann*’s empirical formula.
- In the very downstream section ($x/h \approx 35$), the mean stream-wise velocity profiles are observed to be *Reynolds*-number dependent in the outer layer ($y/\Delta > 0.1$) but collapse well with the flat plate scaling u^* .
- The scaling of the fluctuating velocity profiles in the inner region is achieved with that proposed by *DeGraaff & Eaton (2000)* which means that a stress equilibrium layer is obtained. The outer region of the *Reynolds* shear stress profiles fails to collapse due to the large eddies persistence.
- Examinations of *Clauser* parameter G and the shape factor H suggest that the flow in the very downstream section ($x/h \approx 35$) has reached equilibrium, though is still subjected to a mild pressure gradient.

A comparison of results obtained in this study has been made with those found in the literature has revealed a good agreement both in mean and fluctuating single-phase velocity profiles and integral parameters.

Secondly, the gas-phase flow characteristics measured in the recovery region ($x/h = 34.3$) downward the obstacle were examined with the help of the Shadowgraphy technique. The spatial integration window has a dimension of $13.6\text{ mm} \times 1.4\text{ mm}$, with a horizontal and vertical step spacing of

General Conclusion

13.6 mm × 0.2 mm. Measurements were performed under the same single-phase flow configurations and with a gas injection rate Q_g varying from 5 l/h to 80 l/h, that gives birth to bubbles of mean diameters varying in the range [40 – 140] viscous length. Several observations have been made:

- The bubble distribution in a recovery region of an obstacle flow can be approximately described by a log-normal law. The bubble mean diameter scaled by the momentum thickness of the single phase flow has shown a power-law-dependency on the global volumetric fraction but remains quite indifferent with regard to the reference velocity.
- The local gas volume fraction profiles for all measuring points have collapsed onto 2 distinct families ($U_{ref} = 2 \text{ m/s}$; $U_{ref} \geq 4 \text{ m/s}$) by using the maximum local volume fraction α_{v-max} and the dimensionless thickness Δ_b , the latter is uniquely dependent on θ and Fr_θ .
- The mean stream-wise and wall-normal gas-phase velocity profiles differ from those of the single-phase flow of the same reference velocity. In the stream-wise direction, in the inner bubbles layer, the gas move faster than the single phase liquid and slower than the liquid phase in the outer bubble layer. In the wall-normal direction, bubbles move faster away from the wall and induce a driven flow that decreases the liquid velocity.
- Air injection rate induce no obvious modification on the gas-phase mean and fluctuating velocity profiles.

Lastly, the liquid-phase flow characteristics measured with Particle Tracking Technique in the same stream-wise position ($x/h = 34.3$) are examined. Several observations have been made:

- The external velocity U_e is quite insensitive to gas injection.
- The logarithmic law of the wall is reported to hold true in the two-phase flow and the log region upper range of validity with respect to yu^*/ν is extended when increasing the gas injection rate. The friction velocity is decreased when increasing the injection rate, except at small Froude numbers and small air volumetric fractions.
- Momentum exchange in the stream-wise direction between the gas and liquid phases induces a lift and drag force that contributes to decrease and increase respectively the near wall stream-wise liquid velocity. The direction of the drag force applied on the liquid is reversed at small Froude number for high air volumetric fraction.
- Examinations focused on other integral parameters such as δ^* , θ , H and G suggest that the boundary layer has reached equilibrium with new values of G , which depends on the air injection rate.
- Based on the examinations of the stream-wise and wall-normal drift velocity between gas and liquid, some mechanisms as regards the bubble induced drag variation have been discussed. It is suggested in our study that the bubble wall normal fluctuating motion should be mainly responsible for the total drag variation. The bubble wall normal fluctuating motion is inhibited by buoyancy effect at small Froude number and promotes drag reduction at large Froude number. The bubble-induced lift and density effects are equally contributors to the drag reduction.

6.1 Recommendations for future investigations

In the framework of bubbly drag reduction in recovery region of an obstacle turbulent flow, some recommendations for future work are presented below:

- The experimental results, coming from this work, can be used for validation of numerical models of two-phase wall-bounded flows with adverse pressure gradients.

General Conclusion

- In this work, the contribution of the different mechanisms to total drag variation has been estimated roughly. A better insight into the different contributions would require a refinement of the hydrodynamic coefficient of the forces applied on bubbles. The drag coefficient and lift coefficient can vary with the local vorticity (*Legendre and Magnaudet, 1998*) and a better correlation with regard to the bubble *Reynolds* number should be investigated. Also, the lift coefficient is sensitive to the vicinity of the wall. Also, the strong deformation of the bubbles at small Froude number in the vicinity of the wall requires better modelization of hydrodynamic forces.
- The wall shear stress was estimated in our study based on the friction velocities, deduced with the help of the logarithmic law of the wall. However, hypothesis have been made that the *von Kármán*'s constant κ remains unchanged under adverse pressure gradient and air injection, which is still questionable. Implementing direct measurement means of wall shear stress may give a more accurate and instantaneous estimation of the bubble induced modification on the flow structures.
- As suggested previously, that the bubble wall-normal fluctuating motion should be of particular importance for drag reduction in the case of an intermediate bubble size, a correct measurement of the instantaneous local gas phase characteristic function is crucial for the quantitative evaluation of this phenomenon, simultaneously with characterization of the instantaneous local velocity field of the liquid. However, with a *2D* Shadowgraphy mean, which integrates over the span-wise direction, it is not possible to measure the local gas phase characteristic in the *PIV* or *PTV* measurement plane of the liquid phase, especially at high values volumetric fractions due to the bubble superposition. Future investigations might be focused on improving the measuring technique (tomo-*PIV* or tomo-*PTV*) or limiting bubble injection in the measurement plane of the liquid phase.
- A wave of gas volume fraction is reported by *Park et al. (2015)* to enhance bubbly drag reduction in a channel flow. One may expect that the same phenomenon should promote drag reduction in our flow configuration. It could be further investigated.
- Helium injection of microbubble is reported to enhance larger drag reduction comparing to air (*Deutsch & Castano 1986*). Injecting other gas than air in our flow configuration might give insight for more indications related to the bubble density effect and *Weber* number effect.

7 Reference

- Angelin-Chaab M., Tachie M. F., PIV Study of Separated and Reattached Open Channel Flow Over Surface Mounted Blocks. *J. Fluids Eng.* vol. 130, 2008
- Antoniou J., Bergeles G., Development of the Reattached Flow Behind Surface-Mounted Two-Dimensional Prisms. *J. Fluids Eng.* vol. 110, pp. 127-133, 1988
- Aubertine C. D., Eaton J. K., Turbulence Development in a Non-Equilibrium Turbulent Boundary Layer with Mild Adverse Pressure Gradient. *J. Fluid Mech.* vol. 532, pp. 345–364, 2005
- Aubertine C. D., *Reynolds* Number Effects on an Adverse Pressure Gradient Turbulent Boundary Layer. doctoral thesis, 2005
- Barnard S. T., Thompson W. B., Disparity analysis of images. *IEEE Trans. Pattern Analysis Machine Intelligence.* vol.2, pp. 333–340, 1980
- Bergeles G., Athanassiadis N., The Flow Past a Surface-Mounted Obstacle. *J. Fluids Eng.* vol. 105, pp. 461-463, 1983
- Bogdevich V. G., Evseev A. R., The Distribution on Skin Friction in a Turbulent Boundary Layer of Water Beyond the Location of Gas Injection. *Investigations of Boundary Layer Control (in Russian).* Thermophysics Institute Publishing House, 1976
- Bogdevich V. G., Malyuga A. G., Effect of Gas Saturation on Wall Turbulence. *Investigations of Boundary Layer Control (in Russian).* Thermophysics Institute Publishing House, 1976
- Bradshaw P. The Turbulence Structure of Equilibrium Boundary Layers. *J. Fluid Mech.*, vol. 29, pp. 625-645, 1967
- Bradshaw P., Wong F. Y., The Reattachment and Relaxation of a Turbulent shear Layer. *J. Fluid Mech.*, vol. 52, pp. 113-135, 1972
- Burgers J. M., The Motion of a Fluid in the Boundary Layer along a Plane Smooth Surface. *Proc. First International Congress for Applied Mechanics, Delft*, pp. 113-128, 1924
- Castro I. P., Haque A., The Structure of a Turbulent Shear Layer Bounding a Separation Region. *J. Fluid Mech.*, vol. 179, pp. 439-468, 1987
- Castro I. P., Relaxing Wakes Behind Surface-Mounted Bbstacles in Rough Wall Boundary Layers. *J. Fluid Mech.*, vol. 93, pp. 631-659, 1979
- Ceccio S. L., Friction Drag Reduction of External Flows with Bubble and Gas Injection. *Annu. Rev. Fluid Mech.*, vol. 42, pp. 183-203, 2010
- Chassaing P., *Turbulence en mécanique des fluides.* Cépaduès-éditions, 2000
- Clark III H., Deutsch S., Microbubble Skin Friction on an Axisymmetric Body under the Influence of Applied Axial Pressure Gradients. *Phys. Fluids A*, vol. 3, pp. 2948-2954, 1991
- Clauser F., Turbulent Boundary Layers in Adverse Pressure Gradients. *J. Aero. Sci.* vol. 21(2), pp. 91-108, 1954

Reference

- Coles D., The law of the wake in the turbulent boundary layer. *J. Fluid Mech.*, vol. 1, PP. 191-226, 1956
- Coles D., The Turbulent Boundary Layer in a Compressible Fluid. Rep. R-403-PR, Rand Corp., 1962
- Colin C., Fabre J., Kamp A., Turbulent Bubbly Flow in Pipe under Gravity and Microgravity Conditions. *J. Fluid Mech.* vol. 711, pp. 469-515, 2012
- Cousteix J., *Aérodynamique : turbulence et couche limite*. Cépaduès, 1989
- Dean R. B., *Reynolds Number Dependence of Skin Friction and Other Bulk Flow Variables in Two-Dimensional Rectangular Duct Flow*. *J. Fluids Eng.* Vol. 100, 1978
- DeGraaff D B., Eaton J. K., *Reynolds Number Scaling of the Flat-Plate Turbulent Boundary Layer*. *J. Fluid Mech.*, vol. 422, pp. 319-346, 2000
- DeGraaff D B., Eaton J. K., *Reynolds Number Scaling of the Turbulent Boundary Layer on a Flat Plate and on Swept and Unswept Bumps*. Report No. TSD-118, Stanford Univ., 1999
- DeGraaff D. B., Eaton J. K., *Reynolds-Number Scaling of the Flat Plate Turbulent Boundary Layer*. *J. Fluid Mech.* vol. 422, pp. 319–346, 2000
- Deutsch S., Castano J., Microbubble Skin Friction Reduction on an Axisymmetric Body. *Phys. Fluids*, vol. 29, 3590, 1986
- Deutsch S., Pal S., Local Shear Stress Measurements on an Axisymmetric Body in a Microbubble Modified Flow Field. *Phys. Fluids A*, vol. 2, 1990
- Dryden H. L., Boundary Layer Flow near Flat Plates. Proc. 4th Int. Cong. Of Applied Mech., Cambridge, pp. 175, 1934
- Dryden H. L., Combined effects of turbulence and roughness on transition. *Z. angeic. Math. Phys.*, 9b, pp. 249-258, 1958
- Einstein A., Eine Neue Bestimmung Der Moleküldimensionen. *Ann. Physik.*, vol. 19, pp. 289–306, 1906
- Elbing B. R., Makiharju S., Wiggins A., Perlin M., Dowling D. R., Ceccio S. L., On the Scaling of Air Layer Drag Reduction. *J. Fluid Mech.* vol. 717, pp. 484–513, 2013
- Elbing B. R., Winkel E. S., Lay K. A., Ceccio S. L., Bubble-Induced Skin-Friction Drag Reduction and the Abrupt Transition to Air-Layer Drag Reduction. *J. Fluid Mech.*, vol. 612, pp. 201-236, 2008
- Elbing B. R., Winkel E. S., Lay K. A., Ceccio S. L., Dowling D. R., Perlin M., Bubble-Induced Skin-Friction Drag Reduction and the Abrupt Transition to Air-Layer Drag Reduction. *J. Fluid Mech.* 612, 201–236, 2008
- Etheridget D. W., Kemp P. H., Measurements of Turbulent Flow Downstream of a Rearward-Facing Step. *J. Fluid Mech.*, vol. 86, pp. 545-566, 1978
- Ferrante A., Elghobashi S., On the Physical Mechanisms of Drag Reduction in a Spatially Developing Turbulent Boundary Layer Laden with Microbubbles. *J. Fluid Mech.*, vol. 503, pp. 345-355, 2004

Reference

- Ferrante A., Elghobashi S., *Reynolds* Number Effect on Drag Reduction in a Microbubble-Laden Spatially Developing Turbulent Boundary Layer. *J. Fluid Mech.*, vol. 543, pp. 93-106, 2005
- Fragos V., Psychoudaki S. P., Direct Simulation of Two-Dimensional Turbulent Flow over a Surface-Mounted Obstacle. *Int. J. Numer. Methods Fluids*, vol. 55, pp. 985-1018, 2007
- Frankel N. A., Acrivos A., The Constitutive Equation for a Dilute Emulsion. *J. Fluid Mech.*, vol. 44, pp. 65-78, 1970
- Fukuda K., Tokunaga J., Nobunaga T., Nakatani T., Iwasaki T., Frictional Drag Reduction with Air Lubricant over a Super-Water Repellent Surface. *J. Mar. Sci. Technol.*, vol. 5, pp. 123-130, 2000
- Gabillet C., Climent E., Coutier Delgosha O., Rapport final de contrat, Projet ANR-12-ASTR-0017, projet F-DRAIHN 'Frictional-Drag Reduction by Air Injection for Naval Hydrodynamics', 2016
- George W., Is there a Universal Log Law for Turbulent Wall-Bounded Flows ? *Phil. Trans. R. Soc. A*, vol. 365, pp. 789-806, 2007
- Hama F. R., Boundary layer characteristics for smooth and rough surfaces. *Trans. Soc. Naval Arch. Marine Engrs.*, vol. 62, pp. 333-358. 1954
- Hara K., Suzuki T., Yamamoto F., Image Analysis Applied to Study on Frictional-Drag Reduction by Electrolytic Microbubbles in a Turbulent Channel Flow. *Exp. Fluids*, vol. 50, pp. 715-727, 2011
- Herring T. E., Norbury J. Some Experiments on Equilibrium Turbulent Boundary Layers in Favorable Pressure Gradients. *J. Fluid Mech.*, vol. 27, 541, pp. 123-347, 1967
- Hinze J. O., *Turbulence*. McGraw-Hill, 1975
- International Maritime Organization, 2019
- Jacob B., Olivieri A., Miozzi M., Campana E. F., Piva R., Drag Reduction by Microbubbles in a Turbulent Boundary Layer. *Phys. Fluids A*, vol. 22, 2010
- Kawahara G., Ayukawa K., Ochi J., Yuasa T., Bursting Phenomena in a Turbulent Square-Duct Flow : Event Detection by the VITA Technique and Quadrant Analysis. *Trans. Jpn. Soc. Mech. Eng. B*. vol. 61, pp. 4290-4296, 1995
- Kawamura T., Fujiwara A., Takahashi T., Kato H., Matsumoto Y., Kodama Y., The Effects of the Bubble size on the Bubble Dispersion and Skin Friction Reduction. 2004
- Kawamura T., Moriguchi Y., Kato H., Effect of Bubble Size on the Microbubble Drag Reduction of a Turbulent Boundary Layer. 4th ASME JSME Joint Fluids Engineering Conference, 2003
- Kitagawa A., Hishida K., Kodama Y., Flow Structure of Microbubble-Laden Turbulent Channel Flow Measured by PIV Combined with the Shadow Image Technique. *Exp. Fluids*, vol. 38, pp. 466-475, 2005
- Klebanoff P. S., Diehl Z. W., Some Features of Artificially Thickened Fully Developed Turbulent Boundary Layers with Zero Pressure Gradient. *NACA Rep.* 1110, 1952
- Kline S. J., *Reynolds* W. C., Schraub F. A., Runstadler P. W., The Structure of Turbulent Boundary Layers. *J. Fluid Mech.*, vol. 30, pp. 741-773, 1967

Reference

- Kodama Y., Hinatsu M., Fluid Dynamics Field- Drag Reduction of Ships. Micro and Nanobubbles, Fundamentals and Applications. Pan Stanford Publishing, pp. 289-300, 2014
- Kowe, R., Hunt, J. C. R., Hunt, A., Couet, B., and Bradbury, L. J. S., The effects of bubbles on the volume fluxes and the pressure gradients in unsteady and non-uniform flow of liquids, International Journal of Multiphase Flow, Vol. 14, No. 5, pp. 587-606, 1988.
- Lecuona A., Nogueira J., AcostaP. A., Rodríguez A., Assessment of Vorticity with Advanced PIV Techniques, Particle Image Velocimetry: Recent Improvements, Springer, pp. 187-197, 2003
- Legendre D., Magnaudet J., The Lift Force on a Spherical Bubble in a Viscous Linear Shear Flow. J. Fluid Mech., vol. 368, pp. 81-126, 1998
- Legendre D., Zenit R., Velez-Cordero J. R., On the Deformation of Gas Bubbles in Liquids. Phys. Fluids, vol. 24, 2012
- Legner H. H., A Simple Model for Gas Bubble Drag Reduction. Phys. Fluids, vol. 27, 1984
- Lu J. C., Fernández A., Tryggvason G., The Effect of Bubbles on the Wall Drag in a Turbulent Channel Flow. Phys. Fluids, vol. 17, 2005
- Ludwig H., Tillmann W., Untersuchungen über die Wandschub-spannung in Turbulenten Reibungsschichten. Ing. Arch. Vol 17, pp. 288-299, 1949
- Lumley J. L., The Structure of Inhomogeneous Turbulent Flows, Atmospheric Turbulence and Radio Wave Propagation, pp. 221–227, 1967.
- Madavan N. K., Deutsch S., Merkle C. L., Reduction of Turbulent Skin Friction by Microbubbles. Phys. Fluids, vol. 27, 356, 1984
- Madavan N. K., Merkle C. L., Deutsch S., Numerical Investigations Into the Mechanisms of Microbubble Drag Reduction. J. Fluids Eng. vol. 107, pp. 370-377, 1985
- Makiharju S., Elbing B. R., Wiggins A. D., Schinasi S., Vanden-Broeck J.-M., Perlin M., Dowling D. R., Ceccio S. L., On the Scaling of Air Entrainment from a Ventilated Partial Cavity. J. Fluid Mech. vol. 732, pp. 47–76, 2013
- Makiharju S., Elbing B. R., Wiggins A., Dowling D. R., Perlin M., Ceccio S. L. Ventilated Partial Cavity Flows at High *Reynolds* Numbers. Int. Conf. on Multi-phase Flows, Tampa, FL, 2010
- McCormick M. E., Bhattacharyya R., Drag Reduction of a Submersible Hull by Electrolysis. Nav. Eng. J., vol. 85, pp. 11-16, 1973
- Meng J. C. S., Uhlman J. S., Microbubble Formulation and Splitting in a Turbulent Boundary Layer for Turbulence Reduction. Advances in Fluid Dynamics, pp. 168-217, 1989
- Moore D. W., The Turbulent Layer on a Spherical Gas Bubble, J. Fluid Mech., vol. 16, pp. 161-176, 1963
- Moriguchi Y., Kato H., Influence of Microbubble Diameter and Distribution on Frictional Resistance Reduction. J. Mar. Sci. Technol., vol. 7, pp. 79-85, 2002
- Morkovin M. V., On the Many Faces of Transition. Viscous Drag Reduction, pp. 1-31, 1969

Reference

- Murai Y., Frictional Drag Reduction by Bubble Injection. *Exp. Fluids*, 55:1773, 2014
- Murai Y., Fukuda H., Oishi Y., Kodama Y., Yamamoto F., Skin Friction Reduction by Large Air Bubbles in a Horizontal Channel Flow. *Int. J. Multiph. Flow*, vol. 33, pp. 147-163, 2007
- Oertel H., Prandtl-Essentials of Fluid Mechanics. *Applied Mathematical Sciences*, vol. 158, 2008
- Oishi Y., Murai Y., Tasaka Y., Yasushi T., Frictional Drag Reduction by Wavy Advection of Deformable Bubbles. *The 6th International Symposium on Measurement Techniques for Multiphase Flows*. 2009
- Olmer N., Comer B., Roy B., Mao X., Rutherford D., Greenhouse Gas Emissions from Global Shipping, 2013-2015, ICCT, 2017
- Paik B. G., Yim G. T., Kim K. Y., Kim K. S., The Effects of Micro-Bubbles on Skin Friction in a Turbulent Boundary Layer Flow. *Int. J. Multiphase Flow*, vol. 80, pp. 164-175, 2016
- Pal S., Merkle C. L., Deutsch S., Bubble Characteristics and Trajectories in a Microbubble Boundary Layer. *Phys. Fluids*, vol. 31, pp. 744-751, 1988
- Park H. J., Repetitive Bubble Injection for Control of Turbulent Boundary Layers. doctoral thesis, Hokkaido Univ. 2016
- Park H. J., Tasaka Y., Oishi Y., Murai Y., Drag Reduction Promoted by Repetitive Bubble Injection in Turbulent Channel Flows. *Int. J. Multiph. Flow*, vol. 75, pp. 12-25, 2015
- Perlin M., Ceccio S. *Mitigation of Hydrodynamic Resistance Methods to Reduce Hydrodynamic Drag*. Singapore: World Scientific, 2015
- Raffel M., Willert C. E., Scarano F., Kähler C., Wereley S. T., Kompenhans J., *Particle Image Velocimetry, a Practical Guide*. Springer, 2018
- Razzaque M. M., Afacan A., Liu S., Nandakumar K., Masliyah J. H., Sanders R. S., Bubble Size in Coalescence Dominant Regime of Turbulent Air–Water Flow through Horizontal Pipes. *Int. J. Multiph. Flow*, vol. 29, pp. 1451-1471, 2003
- Reshotko E., Boundary Layer Stability and Transition. *Annu. Rev. Fluid Mech*, vol. 8, pp. 311-349, 1976
- Reynolds* O., An Experimental Investigation of the Circumstances Which Determine Whether the Motion of Water Shall be Direct or Sinuous, and of the Law of Resistance in Parallel Channels. *Philosophical Transactions of the Royal Society of London*, vol. 174, pp. 935-982, 1883
- Samson A., Sarkar S., Anand K., Experimental Investigation of a Separation Bubble on a Flat Plate with Semi-circular Leading Edge for different *Reynolds* Numbers. 9th International Conference on Heat Transfer, Fluid Mechanics and Thermodynamics, 2012
- Sanders W. C., Winkel E. S., Dowling D. R., Perlin M., Bubble Friction Drag Reduction in a High-*Reynolds*-Number Flat-Plate Turbulent Boundary Layer. *J. Fluid Mech.*, vol. 552, pp. 353-380, 2006
- Schlichting H., *Boundary Layer Theory*. Springer, 1955

Reference

- Schubauer G., Klebanoff P., Investigation of Separation of the Turbulent Boundary Layer. Technical Report 1030, NACA Technical Reports, 1950
- Schultz-Grunow F., Durchflußmeßverfahren für pulsierende Strömungen. Forsch. Ing. Wes. vol. 12, pp. 117-126, 1941
- Serizawa A., Kataoka I., Turbulence Suppression in Bubbly Two-Phase Flow. Nucl. Eng. Des., vol. 122, pp. 1-16, 1990
- Shen X., Ceccio S. L., Perlin M., Influence of Bubble Size on Micro-Bubble Drag Reduction. Exp. Fluids, vol. 41, pp. 415-424, 2006
- Sheng J., Malkiel E., Katz J., Buffer Layer Structures Associated with Extreme Wall Stress Events in a Smooth Wall Turbulent Boundary Layer. J. Fluid Mech., vol. 633, pp. 17-60, 2009
- Sirovich L., Turbulence and the Dynamics of Coherent Structures. I- Coherent structures. II- Symmetries and Transformations. III- Dynamics and Scaling. Quart. Appl. Math., vol. 45, pp. 561-571, 1987
- Skåre P. E., Krogstad P. A Turbulent Equilibrium Boundary Layer Near Separation. J. Fluid Mech., vol. 272, pp. 319-348, 1994
- Song S., Eaton J. K., *Reynolds* Number Effects on a Turbulent Boundary Layer with Separation, Reattachment, and Recovery. Exp. Fluids, vol. 36, pp. 246-258, 2004
- Song S., Eaton J. K., The Effects of Wall Roughness on the Separated Flow over a Smoothly Contoured Ramp. Exp. Fluids, vol. 33, pp. 38-46, 2002
- Spalart P., Direct simulation of a turbulent boundary layer up to $Re_{\theta} = 1410$. J. Fluid Mech., vol. 187, pp. 61-98, 1988
- Spalart P., Watmuff J., Experimental and Numerical Study of a Turbulent Boundary Layer with Pressure Gradients. J. Fluid Mech., vol. 249, pp. 337-371, 1993
- Spalart R. R., Leonard A., Direct Numerical Simulation of Equilibrium Turbulent Boundary Layers. 5th International Symposium on Turbulent Shear Flows, Cornell Univ., Turbulent Shear Flows 5, pp. 234-252, 1987
- Stratford B. S., Beavers G. S., The Calculation of the Compressible Turbulent Boundary Layer in an Arbitrary Pressure Gradient. A Correlation of Certain Previous Methods. ARC RM, 1959
- Taira K., Brunton S. L., Dawson S. T. M., Rowley C. W., Colonius T., McKeon B. J., Schmidt O. T., Gordeyev S., Theofilis V., Ukeiley L. S., Modal Analysis of Fluid Flows: An Overview. AIAA J., vol. 55, 2017
- Tani I., Boundary Layer Transition. Annu. Rev. Fluid Mech, vol. 1, pp. 169-196, 1969
- Tillmann W., British Min. of Aircraft Prod. Volkonrodo Translation MAP-VG 34-45T, 1945
- Tollmien W., Grohne P., Boundary Layer and Flow Control. vol. 2. Pergamon, Oxford, pp. 602-636, 1961

Reference

- Tomiyama A., Celata G. P. Hosokawa S., Yoshida S., Terminal Velocity of Single Bubbles in Surface Tension Force Dominant Regime. *Int. J. Multiph. Flow*, vol. 28, pp. 1497-1519, 2002
- Townsend A. A., Equilibrium Layers and Wall Turbulence. *J. Fluid Mech.*, vol. 11, pp. 97-120, 1961
- Townsend A. A., *The Structure of Turbulent Shear Flow*. Cambridge University Press, 1976
- UNCTAD, *Review of Maritime Transport 2018*, United Nations, 2018
- van den Berg T. H., Luther S., Lathrop D. P., Lohse D., Drag Reduction in Bubbly Taylor–Couette Turbulence. *Phys. Rev. Lett.* Vol. 94, 044501, 2005
- Van der Hegge Zijnen B.G., Measurements of the velocity distribution in the boundary layer along a plane surface. doctoral thesis, 1924
- von Doenhoff A. E., Tetervin N., Determination of General Relations for the Behavior of Turbulent Boundary Layers. NACA Wartime Report 3G13, 1943
- Wilcox D. C., *Turbulence Modeling for CFD*. DCW Industries, 1994
- Wu Q., Pairman D., A Relaxation Labeling Technique for Computing Sea Surface Velocities from Sea Surface Temperature. *IEEE Trans. Geosci. Remote. Sens.* vol. 33, pp. 216–220, 1995
- Zhang J., Gabillet C., Clement A., Billard J-Y., Experimental Investigation of Bubble Induced Modifications of a Turbulent Boundary Layer, 15èmes journées de l’Hydrodynamique, 2016

8 Appendices

8.1 Appendix A. Bubble injection network production drawing archive

The bubble injection network is presented in detail in the below drawing (*Figure A. 1*).

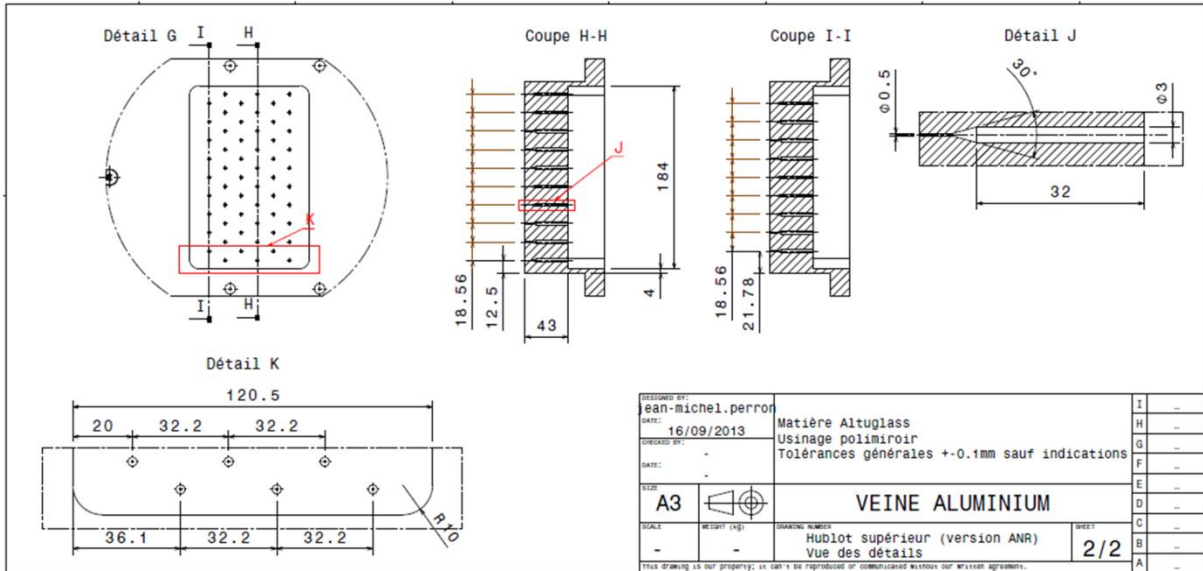


Figure A. 1 Views of the bubble injection network

8.2 Appendix B. Comparison between *PTV* and *PIV* profiles in single phase flow

Replicate measurements have been made with *PIV* and *PTV* techniques on the same viewing section. The reproducibility condition of measurement was to be assessed. **Figure B. 1** shows the time-averaged comparison of the mean stream-wise velocity U profiles obtained both with *PIV* and *PTV* and scaled in by the external velocity U_e at $x/h = 34.3$. Jet induced by the particle injection pushing system has been included in both experiments for comparison.

8.2.1 Mean velocity components

It is shown that U disagrees over a large range of y distance except the last case where $U_{ref} = 8 \text{ m/s}$, although a good agreement is achieved at the first points at the inner region for all velocities. This deficit which happened in the outer region, when it is to be compared to an ordinary boundary layer on smooth wall, could be due to fact that *PIV* fails to predict eddy structures correctly. This last is the main reason why the outer region takes longer time to reach relaxation comparing to the inner one.

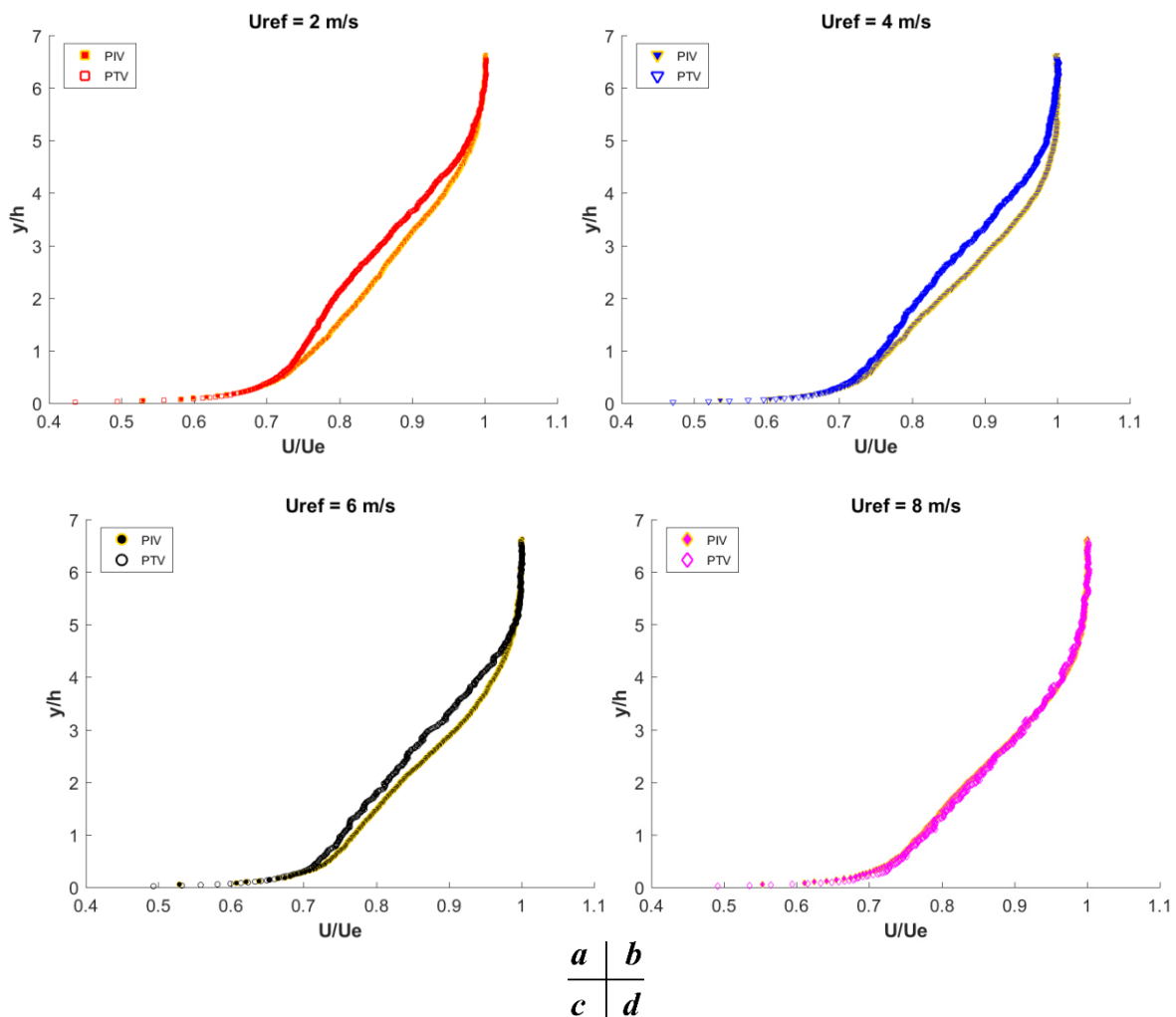


Figure B. 1 Mean stream-wise velocity U profiles normalized by the external velocity U_e . Comparison between *PIV* and *PTV* for the single phase flow at $x/h = 34.3$

Wall normal velocity profiles are plotted in **Figure B. 2**, *PTV* raw data are compared with data obtained by solving the continuity equation using the mean U component values. At lower velocities ($U_{ref} = 2, 4 \text{ m/s}$), no agreement between *PTV* and *PIV* was found from the near wall region up to the outer zone of the boundary layer. For velocities $U_{ref} = 4, 6 \text{ m/s}$, the V in *PTV* remains close to zero

at the near wall region and heads in the negative direction as in *PIV* before swinging towards the positive direction from a y distance roughly equal to the obstacle height.

The *PTV* results from the continuity equation solution, despite the inconsistency with the original *PTV* data, however provide a better global coincidence with *PIV* data, notably the swinging phenomena for $U_{ref} = 4, 6 \text{ m/s}$ disappears totally at a distance $y/h \approx 1.5$.

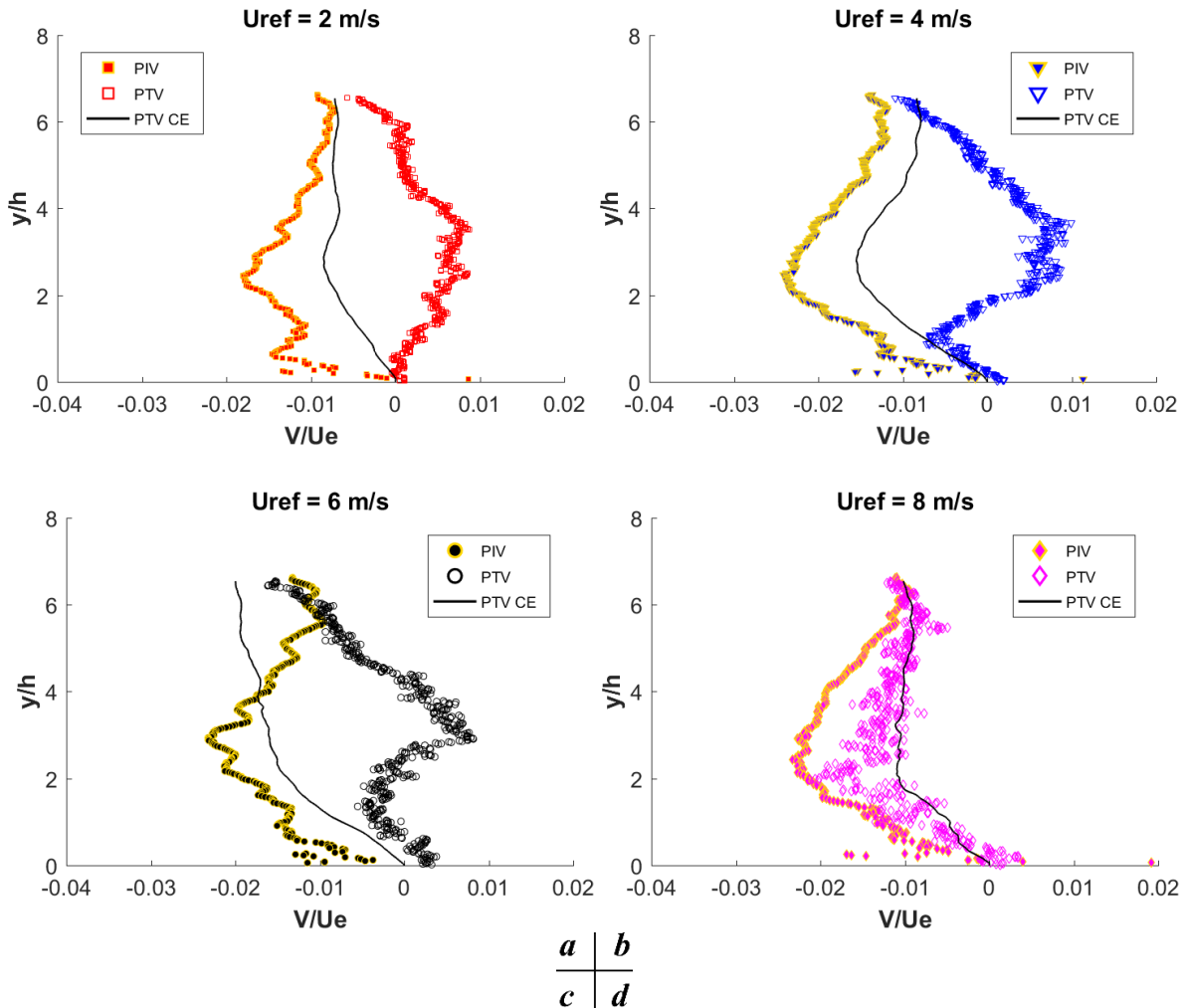


Figure B. 2 Mean wall-normal velocity V profiles normalized by the by the external velocity U_e . Comparison between *PIV* and *PTV* for the single phase flow at $x/h = 34.3$

8.2.2 Reynolds stresses

All *Reynolds* normal stresses, U_{rms} and V_{rms} were equally measured. **Figure B. 3** and **Figure B. 4** show U_{rms} and U_{rms} scaled by the external velocity U_e . The same tendency is observed for all stresses between *PIV* and *PTV*, although the scatter in U_{rms} and V_{rms} is somewhat higher in *PTV* than in *PIV*. This might confirm the underestimation of eddy structures in *PIV*. Generally speaking, the turbulent intensities are higher for *PTV* measurements, as *PIV* underestimate the fluctuating velocities.

Appendices

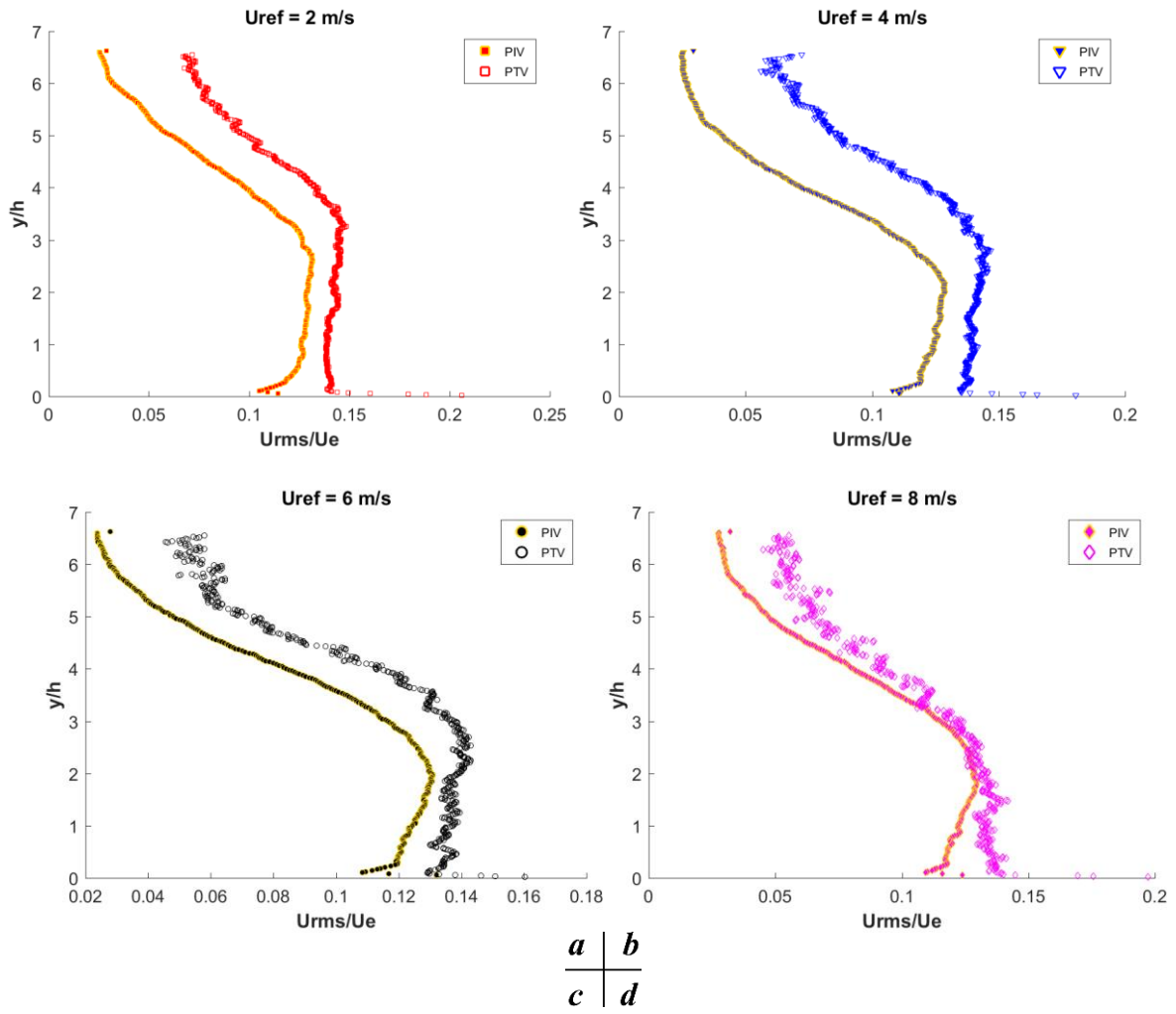
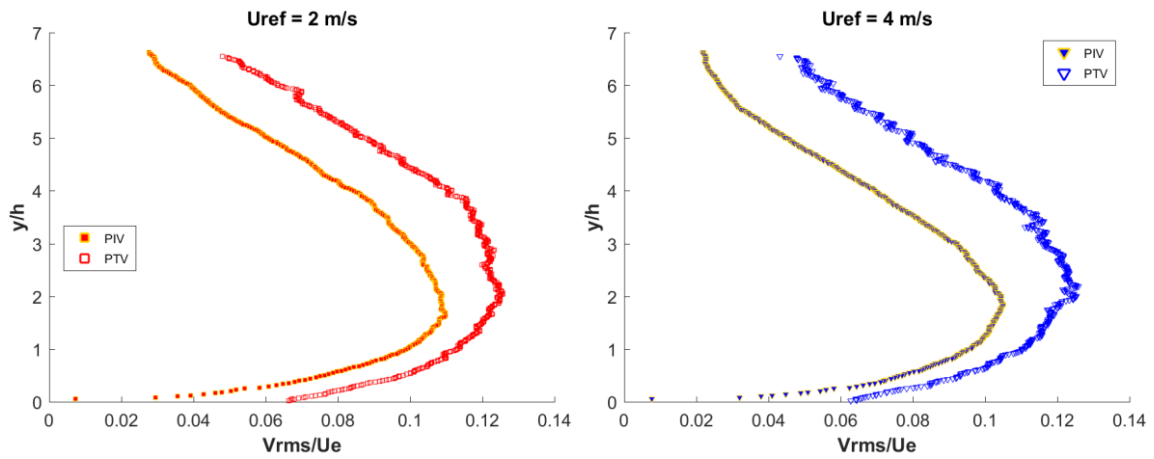


Figure B. 3 U_{rms} profiles normalized by the external velocity U_e . Comparison between PIV and PTV for the single phase flow at $x/h = 34.3$



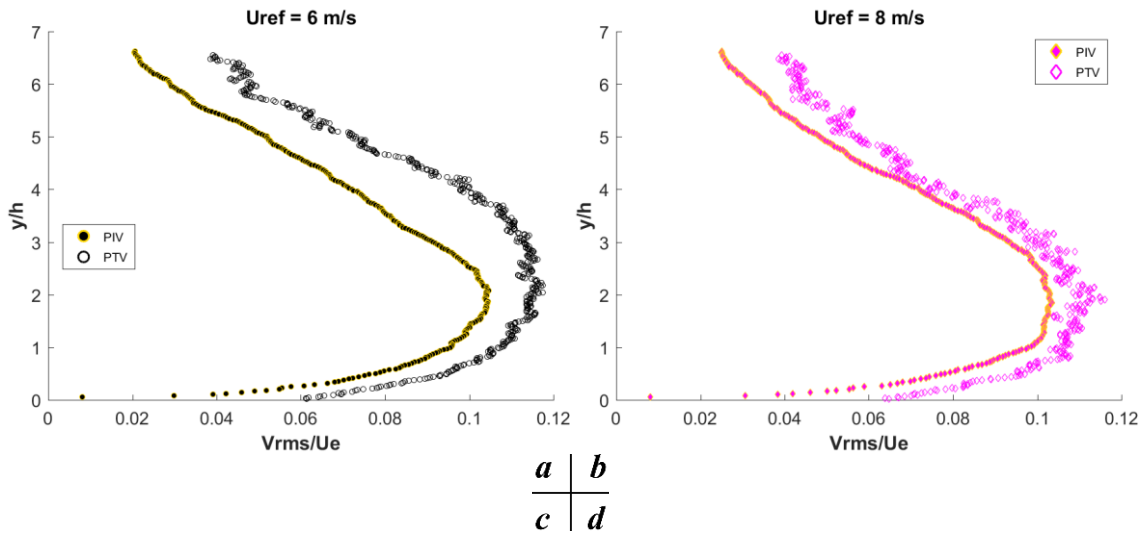


Figure B. 4 V_{rms} profiles normalized by the external velocity U_e . Comparison between *PIV* and *PTV* for the single phase flow at $x/h = 34.3$

Figure B. 5 shows the comparison of *Reynolds* shear stresses between *PIV* and *PTV*. At $U_{ref} = 2 \text{ m/s}$, a plateau-like range of maxima values is found at a wall distance $y/h = 2 - 3$. The maxima-value range reduces into a peak when reference velocity increases.

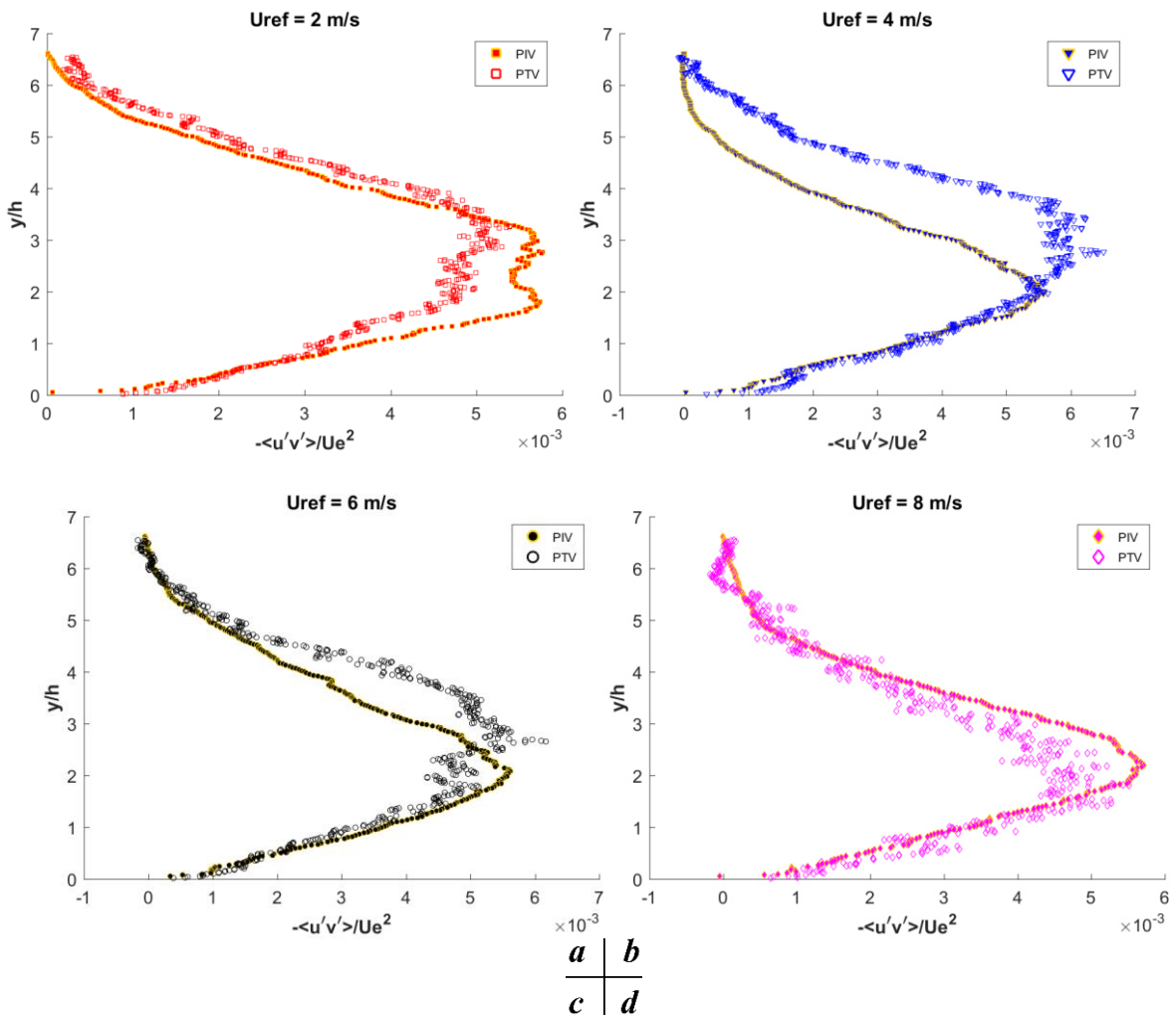


Figure B. 5 $-\langle u'v' \rangle$ profiles normalized by the external velocity U_e^2 . Comparison between PIV and PTV for the single phase flow at $x/h = 34.3$.

8.2.3 Logarithmic law versus inner variables

The frictional velocity u^* , was obtained by applying a least-square fit of the law of the wall. Skåre & Krogstad (1994) suggested that the apparent value of the von Kármán constant κ , decreases as the adverse pressure gradient increases. For the analysis of all single phase flow data, conventional values were used ($\kappa = 0.41, B = 5 \sim 6$). The fit procedure, containing two unknowns u^* and B , was performed manually by finding the optimal range of points aligned in the inner log region. Figure B. 6, Figure B. 7, Figure B. 8, Figure B. 9 show a rather fair agreement of PIV and PTV data both for u^* and B in the inner log region. The large disagreement in the wake part indicates the unsuitable use of viscous scale length ν/u^* to achieve the outer layer similarity.

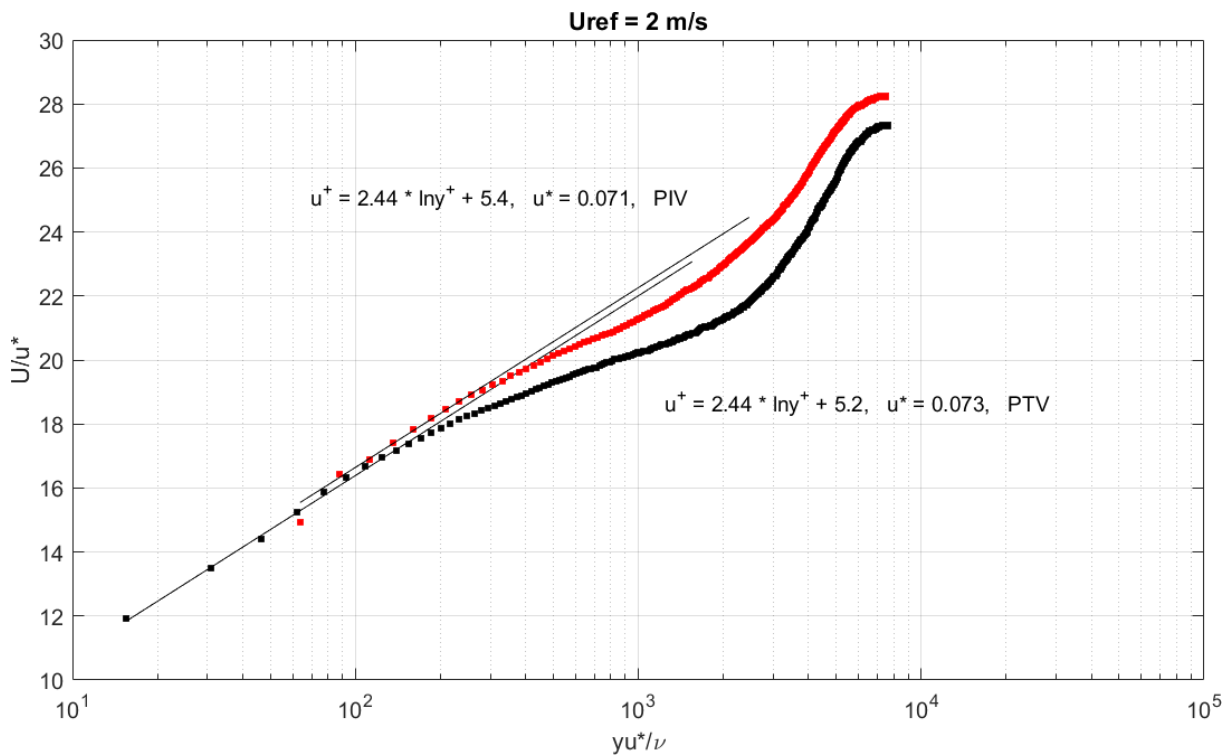


Figure B. 6 Semi-logarithmic plot of mean velocity profile obtained by PTV and PIV at $U_{ref} = 2 \text{ m/s}$

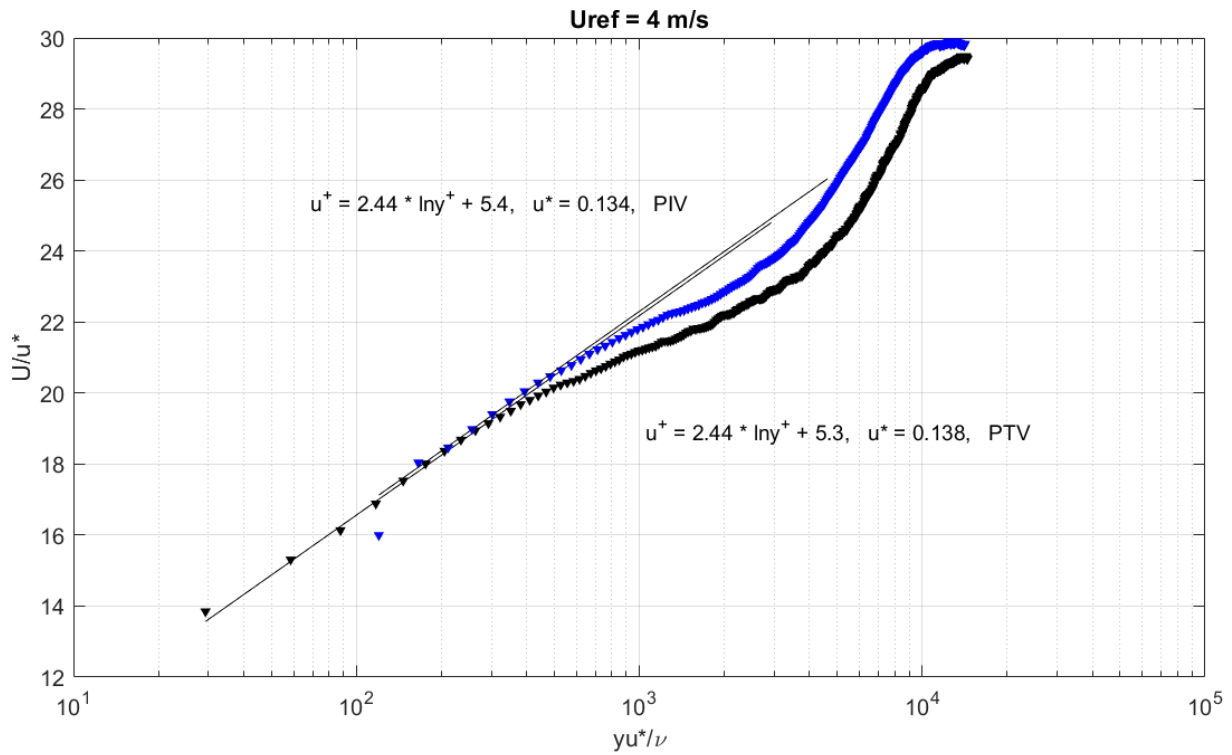


Figure B. 7 Semi-logarithmic plot of mean velocity profile obtained by *PTV* and *PIV* at $U_{ref} = 4 \text{ m/s}$

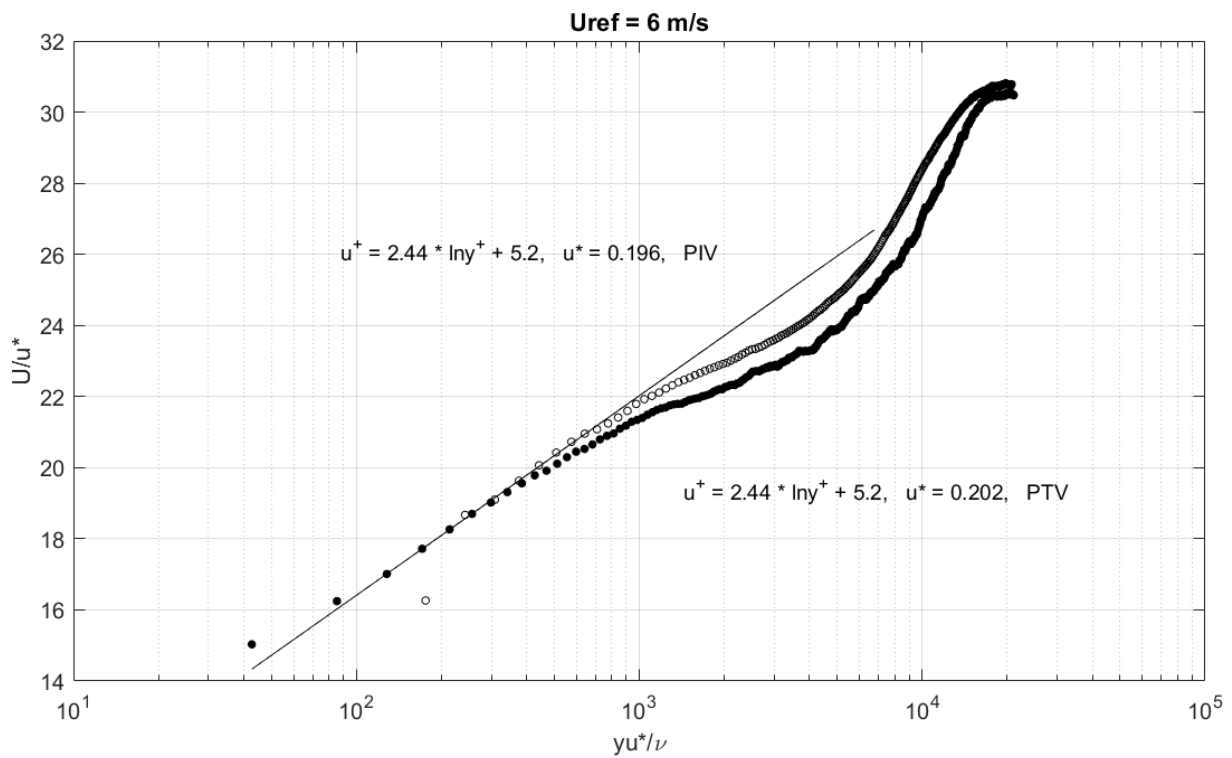


Figure B. 8 Semi-logarithmic plot of mean velocity profile obtained by *PTV* and *PIV* at $U_{ref} = 6 \text{ m/s}$

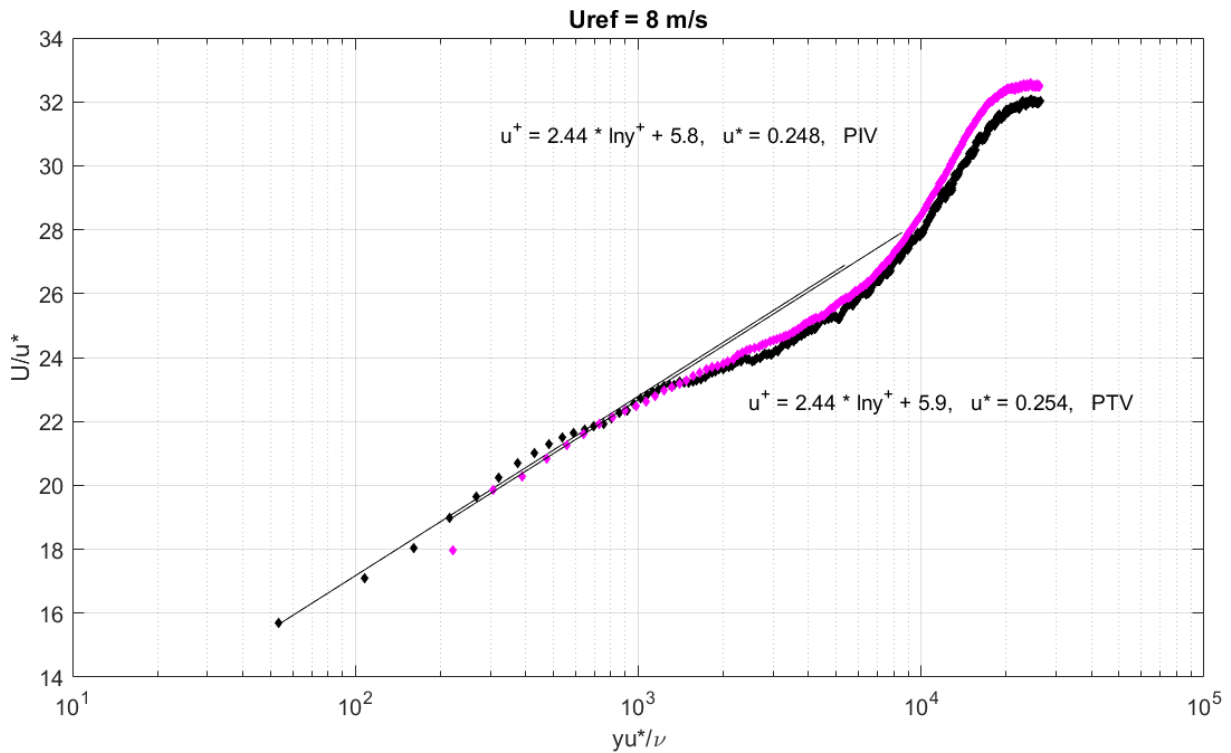


Figure B. 9 Semi-logarithmic plot of mean velocity profile obtained by *PTV* and *PIV* at $U_{ref} = 8 \text{ m/s}$

8.2.4 Logarithmic law versus outer variables

A better similarity is achieved between *PIV* and *PTV* far from the wall once the wall normal distance is scaled by the integral length Δ (Figure B. 10, Figure B. 11, Figure B. 12, Figure B. 13).

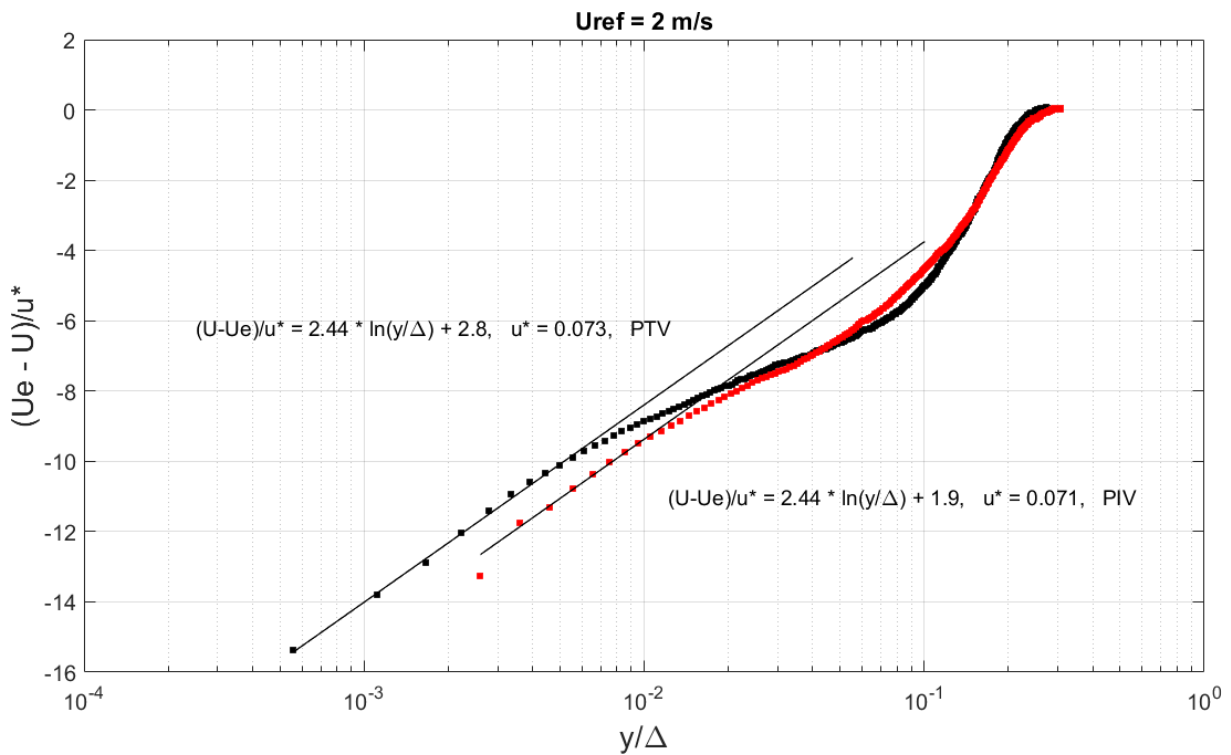


Figure B. 10 Semi-logarithmic plot of mean velocity profile obtained by *PTV* and *PIV* at $U_{ref} = 2 \text{ m/s}$

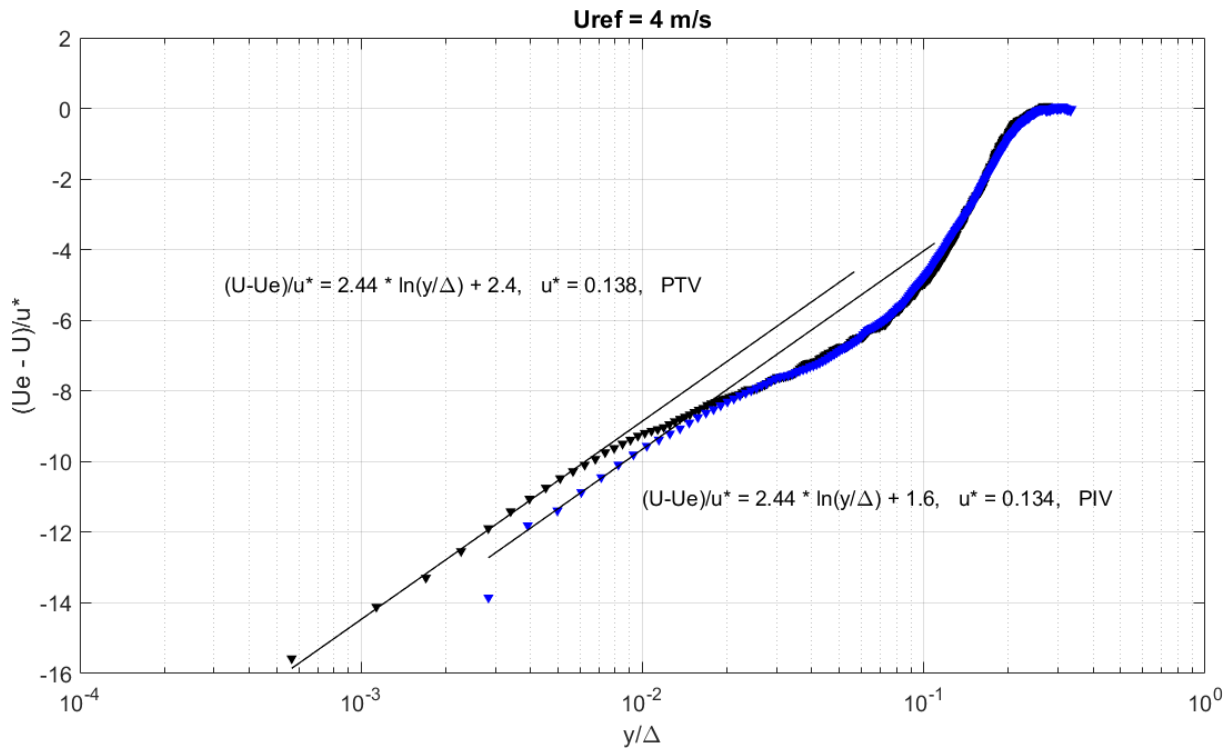


Figure B. 11 Semi-logarithmic plot of mean velocity profile obtained by *PTV* and *PIV* at $U_{ref} = 4 \text{ m/s}$

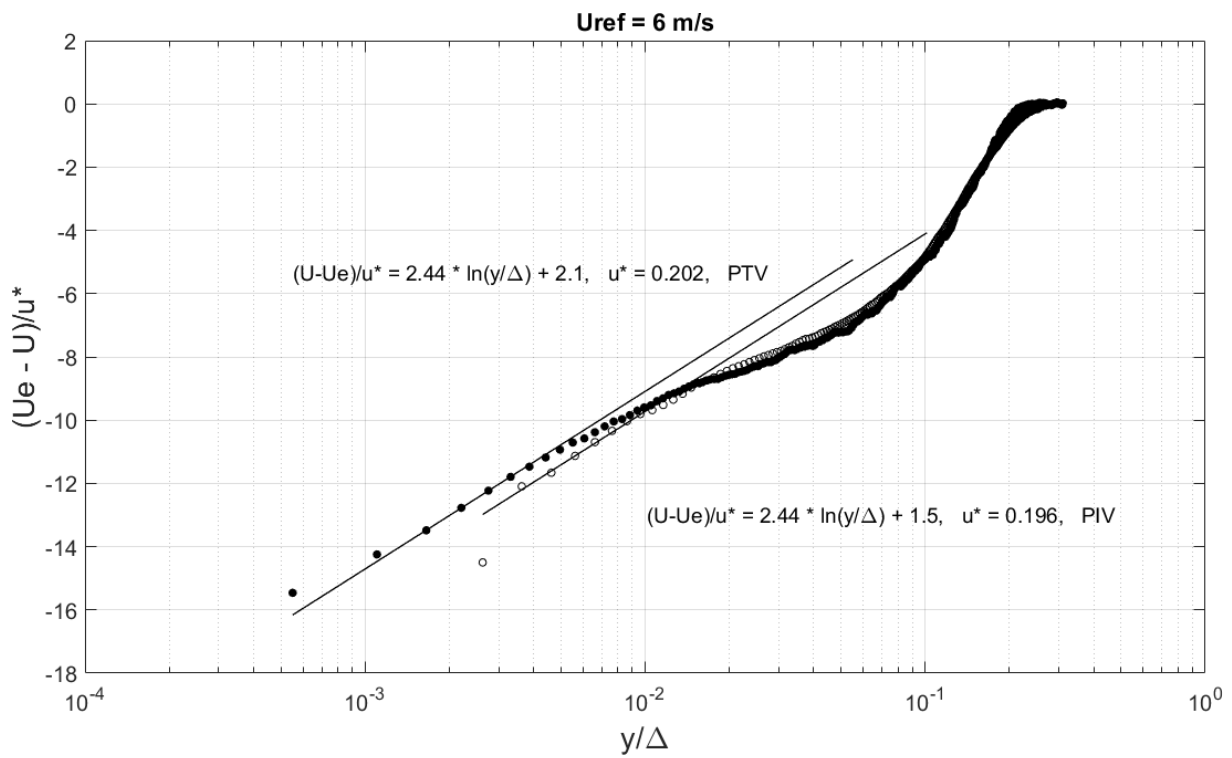


Figure B. 12 Semi-logarithmic plot of mean velocity profile obtained by *PTV* and *PIV* at $U_{ref} = 6 \text{ m/s}$

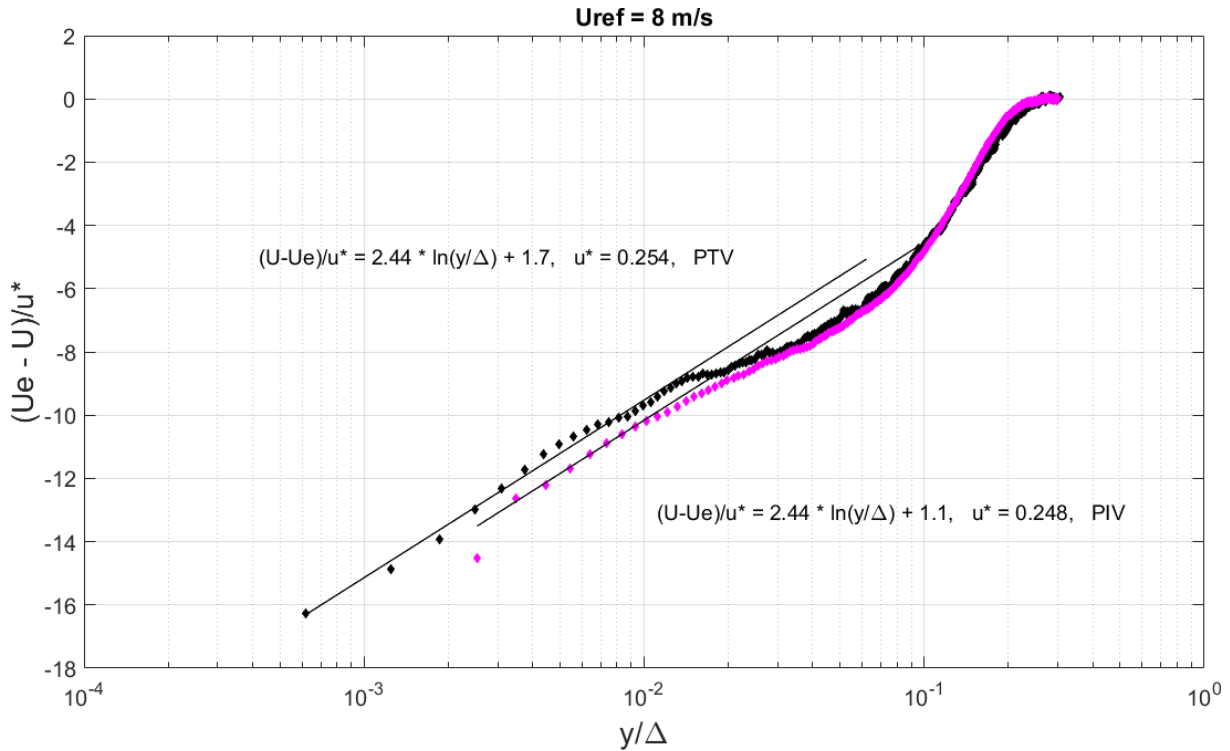


Figure B. 13 Semi-logarithmic plot of mean velocity profile obtained by *PTV* and *PIV* at $U_{ref} = 8 \text{ m/s}$

8.2.5 Comparison of the integral parameters between *PTV* and *PIV*

The integral values for both *PIV* and *PTV* are documented in *Table B. 1*.

An overall excess has been found for values in *PTV* as compared to *PIV*. It is not surprising that similarity is obtained for both u^* and B , as they are the values that are firstly compared in the log-fit procedure. The increase in δ^* and θ seems to be of the same order of magnitude, which results a rather fair agreement in H . The low relative error in *Clauser* parameter G confirmed also that the similarity in flow equilibrium has been obtained.

	U_{ref} [m/s]	C [--]	B [--]	C_f [--]	u^* [m/s]	δ^* [mm]	θ [mm]	H [--]	Δ [mm]	G [--]	Re_θ [--]	U_e [m/s]
<i>PIV</i>	2	1.9	5.4	0.0025	0.071	12.25	9.66	1.27	345.39	5.95	19339	2.01
<i>PTV</i>	2	2.8	5.2	0.0027	0.073	14.01	10.88	1.29	382.12	6.09	21662	2.00
err %		52.4	4.7	6.7922	2.822	14.33	12.58	1.56	10.64	2.32	12	0.50
<i>PIV</i>	4	1.6	5.4	0.0022	0.134	10.64	8.43	1.26	317.35	6.21	33531	4.00
<i>PTV</i>	4	2.4	5.3	0.0023	0.138	12.74	10.01	1.27	374.95	6.31	40623	4.07
err %		50.1	2.2	2.7436	3.352	19.76	18.82	0.79	18.15	1.61	21	1.96
<i>PIV</i>	6	1.5	5.2	0.0021	0.196	11.12	8.81	1.26	342.12	6.40	52920	6.03
<i>PTV</i>	6	2.4	5.2	0.0022	0.202	12.63	9.89	1.28	385.15	6.62	60630	6.16
err %		57.9	0.1	1.8724	2.992	13.62	12.28	1.20	12.58	3.55	15	2.04
<i>PIV</i>	8	1.1	5.8	0.0019	0.248	10.93	8.67	1.26	355.03	6.71	69461	8.04
<i>PTV</i>	8	1.7	5.9	0.0020	0.254	10.69	8.53	1.25	341.61	6.46	68913	8.11
err %		59.2	1.9	3.4123	2.542	2.15	1.61	0.55	3.78	3.74	1	0.84

Appendices

Table B. 1 Relative difference of Integral parameters measured from *PTV* and *PIV* at $x/h = 34.3$ for the single phase flow over the obstacle. Relative difference is calculated following (with jet-without jet)/without jet.

8.3 Appendix C. Publication



Caractérisation expérimentale de l'effet de l'injection de bulles dans une couche limite turbulente

J. Zhang, C. Gabillet, A. Clement et J.Y. Billard

Institut de Recherche de l'Ecole Navale IRENav (EA 3634), CC600, 29240 Brest Naval, Cedex 9

celine.gabillet@ecole-navale.fr

Abstract

Dans le contexte de caractériser les effets de l'injection des bulles de taille intermédiaire dans une couche limite turbulente, nous avons mesuré la vitesse du fluide dans la zone interne de la couche limite dans un écoulement diphasique en utilisant la technique (Particle Image Velocimetry) PIV et (Laser Doppler Velocimetry) LDV. Dans cette étude, nous avons observé l'influence du débit d'injection globale et locale sur l'évolution du profil de vitesse du fluide ainsi que l'évolution des tensions de Reynolds. Les résultats montrent qu'avec une augmentation de la taille des bulles, un déficit de vitesse se manifeste dans la zone logarithmique et un excès de vitesse dans la sous couche visqueuse respectivement causé par un phénomène d'aspiration due à la flottabilité induite par les bulles. Au-delà d'un certain débit d'injection locale, les bulles de sillage sont présentes dans l'écoulement et cela a contribué à une diminution du frottement visqueux et une diminution du frottement turbulent en très proche paroi associé à un effet de soufflage.

1 Introduction

Le développement des navires tout électriques nécessite l'optimisation du système propulsif mais aussi la réduction de la résistance de la carène. Or la résistance de frottement constitue la part la plus importante de la résistance de carène pour des vitesses d'avance faibles à modérées ou de grandes longueurs de coque. Dans ce contexte, l'injection d'air sous la carène est un procédé intéressant qui permet de réduire la résistance de frottement. Ce technique a été étudiée et envisagée pour d'application navale initialement par [McCormick et al. \(1973\)](#). Parmi les différentes configurations possibles (couche de bulles, couche d'air, cavité d'air), la couche de bulles semble être un bon compromis entre efficacité énergétique et tenue à la mer, mais la prédiction des performances est encore difficile [Ceccio \(2010\)](#) et l'extrapolation des résultats de la petite échelle à la grande échelle est discutable [Foeth \(2008\)](#). En effet, les mécanismes physiques mis en jeu sont complexes (réduction de densité effective, effet de compressibilité, effet de glissement entre phases, interactions entre les bulles et la turbulence) et leur compréhension requiert de mener des études académiques [Ferrante et al. \(2004\)](#), [Jacob et al. \(2010\)](#). En particulier, peu d'études expérimentales se sont intéressées aux interactions entre l'écoulement turbulent de proche paroi et des bulles de taille intermédiaire (entre les microbulles et la couche d'air) [Murai et al. \(2007\)](#), [Park et al. \(2014\)](#). Le travail présenté ici s'inscrit dans cette démarche. Afin d'étudier l'effet de l'injection de bulles de taille intermédiaire dans une couche limite turbulente, l'IRENav a réalisé des mesures dans le tunnel hydrodynamique de l'Ecole Navale.

Une vitesse d'écoulement a été testée (2m/s). Le contrôle de la pression d'injection et la modularité du réseau d'injection permettent de contrôler la taille des bulles, et de couvrir une large gamme de taille.

2 Conditions expérimentales

2.1 Dispositif expérimental

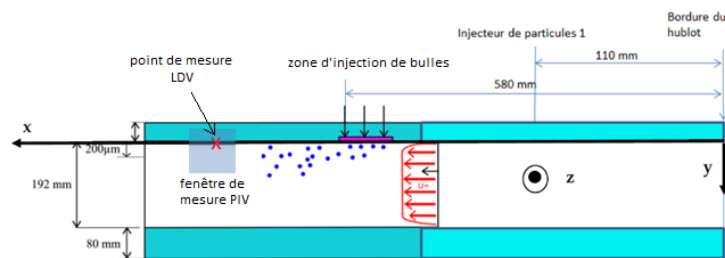


Figure 2.1 vue schématisée de la veine d'essais du tunnel hydrodynamique de l'IRENav

Les mesures ont été réalisées dans le tunnel hydrodynamique de l'Ecole Navale, une vue schématisée de la veine d'essais est présentée **figure 2.1**. La veine d'essais fait 192 mm de haut, par 192 mm de large et par 1m de long. Nous noterons x , la distance longitudinale par rapport à l'entrée de veine, y la distance verticale par rapport à la paroi et orientée vers le bas, et z la position transversale dans la veine.

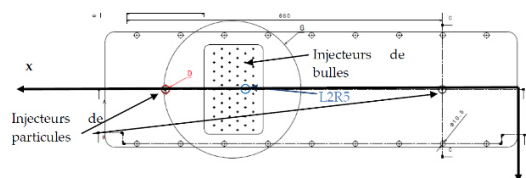


Figure 2.2 vue de dessus du hublot supérieur de la veine d'essais

Des bulles d'air ont été injectées à la paroi supérieure du tunnel à travers un réseau d'injecteurs constitués de 57 capillaires de 180 μm de diamètre situé à 538 mm par rapport à l'entrée de veine.

Une vue de dessus est présentée sur la **figure 2.2**. Le réseau est constitué de 6 lignes transversales de 9 ou 10 capillaires (numérotées de L1 à L6 de l'amont vers l'aval). Chaque capillaire est relié par une vanne tout ou rien, ce qui permet d'avoir le choix des capillaires activés. Nous ajustons à pression d'injection $P \pm 0.03b$, et nous mesurons le débit global injecté dans la veine QG. Nous disposons également de 2 injecteurs qui permettent d'ensemencer l'écoulement en particules.

2.2 Caractéristiques de l'écoulement

Le fluide utilisé est l'eau douce avec la viscosité cinématique $\nu = 1.005e^{-6} \text{ m}^2/\text{s}$. Le tableau suivant **figure 2.3** récapitule les caractéristiques de la couche limite monophasique à $U_e = 2 \text{ m/s}$, U_e étant la vitesse externe à la couche limite, imposée dans la veine. Les caractéristiques sont données à la position longitudinale de l'injecteur de bulles et à la position longitudinale, en aval de l'injecteur de bulles, là où l'ensemble des mesures ont été réalisées en injection de bulles, avant et après abaissement du hublot supérieur.

x(m)/ entrée de veine	δ (m)	U_e (m/s)	H	$Re\delta$	$Re\delta_2$	u^* (m/s)	l_v (μm)
0,505	0,0152	2	1,29	30382	2947	0,083	12
0,747	0,0174	2	1,42	34800	4270	0,079	13
0,705 Hublot supérieur abaissé de 2mm	0.0157	2	1,37	31400	3976	0,082	12

Figure 2.3 Tableau récapitulatif des caractéristiques de la couche limite monophasique ($x=0.505 \text{ m}$ représente la position de la ligne amont d'injection d'air L1, δ est l'épaisseur de couche limite, δ_2 est l'épaisseur de quantité de mouvement, u^* est la vitesse de frottement et l_v l'échelle de longueur visqueuse $=\nu/u^*$, ν : la viscosité cinématique de l'eau)

Une mesure en LDV du profil vertical de vitesse allant de la paroi jusqu'au milieu de la veine a été effectuée à la position longitudinale ($x = 0.705 \text{ m}$) où toutes les mesures en LDV sont effectuées. L'objectif étant de justifier la position de la mesure LDV en monophasique et diphasique en comparant le profil de vitesse obtenu aux lois de vitesse linéaire dans la sous couche visqueuse et logarithmique dans la zone logarithmique **figure 2.4**. La vitesse externe est $U_e = 2 \text{ m/s}$.

On observe un bon accord avec ces deux lois. La loi linéaire est satisfaite jusqu'à $y^+ = 6.9$ et la loi logarithmique est valable jusqu'à $y^+ = 300$.

Une surmontée de vitesse en très proche paroi ($y^+ < 5$) est observée, cela est dû à un fort gradient de vitesse dans la couche limite qui introduit un biais dans la mesure statistique des particules qui traversent le volume de mesure.

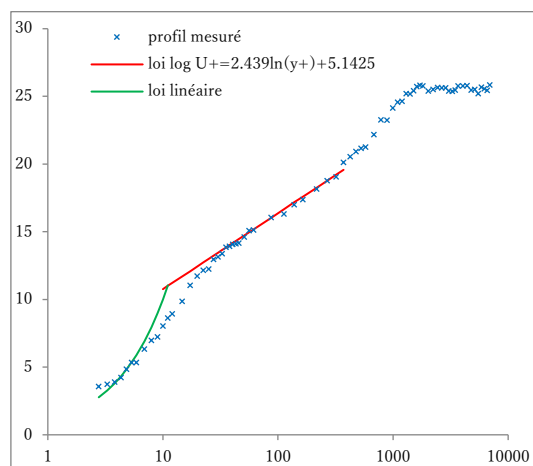


Figure 2.4 profils de vitesse longitudinale moyenne mesurée en monophasique par LDV ($x=0.705 \text{ m}$, hublot supérieur abaissé de 2mm)

L'évolution du nombre de Reynolds de bulles R_{b+} basé sur le rayon de bulles ($R_{b+} = \frac{d_{b+}}{2}$) en fonction du débit d'air par injecteur $\frac{Q_G}{n_{ing}}$ est ensuite étudiée **figure 2.5**. Le nombre de Reynolds de bulles R_{b+} est utile dans le contexte actuel pour caractériser la taille des bulles en moyenne. Nous remarquons qu'au-delà de $\frac{Q_G}{n_{ing}} = 3l/h$, la courbe d'évolution du diamètre de bulles s'aplatit. Cela correspond à un changement de régime de bullage. Au-delà de $\frac{Q_G}{n_{ing}} = 9l/h$, le phénomène du sillage des bulles est observé et la taille des bulles en moyenne diminue.

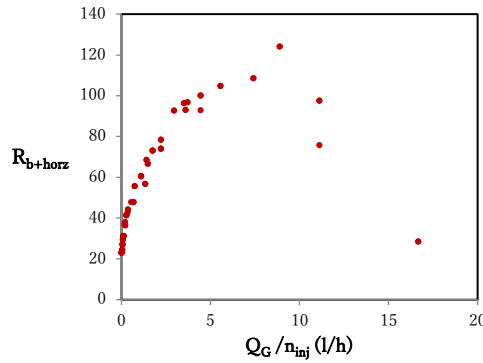


Figure 2.5 influence du débit local sur la taille des bulles et apparition des bulles de sillage

Afin de mieux comprendre l'effet du sillage en fonction de la taille de bulles, une étude statistique sur la distribution des tailles de bulles a été également réalisée **figure 2.6**. Les densités de probabilité du grand axe de bulles ont été calculées avec deux débits d'injection locale ($\frac{Q_G}{n_{ing}} = 3.5l/h$ et $16.7l/h$) en gardant un même ordre de grandeur en débit d'injection globale ($Q_G = 200$ et 150), les lois log normales ont été ensuite tracées à partir des points de mesures obtenus.

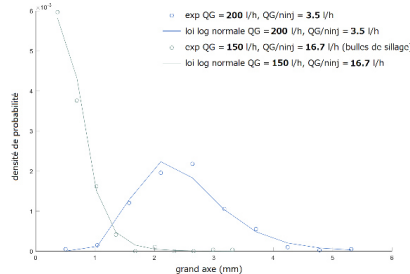


Figure 2.6 l'évolution de la densité de probabilité du grand axe des bulles suivant 2 débit d'injection locale

A $2m/s$, nous illustrons l'influence de l'apparition des bulles de sillage par le décalage de la distribution des tailles de bulles vers les valeurs plus faibles avec l'augmentation de $\frac{Q_G}{n_{ing}}$. A faible débit d'injection locale ($\frac{Q_G}{n_{ing}} = 3.5l/h$), le pic de grand axe en densité de probabilité se trouve dans les environs de $2mm$, dans le cas où le débit d'injection locale est plus élevé ($\frac{Q_G}{n_{ing}} = 16.7l/h$), le pic se rapproche de zéro et se trouve entre 0 et 1 .

3 Techniques expérimentales et traitements spécifiques

3.1 Traitement PIV

Un diagramme schématisé du montage PIV est illustré dans la **figure 3.1**. Une nappe laser est générée dans le plan $x - y$ par un système laser YAG « New wave Solo » d'énergie $30mJ$ de double cavité installée en bas de la veine. Une caméra du type double-trame Flowsense EO4M de la résolution de 12 bits est positionnée en face la nappe laser. La fenêtre de visualisation en x et y est de $63\text{ mm} \times$

63 mm, positionnée à $x = 694 - 757$ mm. Le plan laser est confondu avec le plan $x - y$ illustré dans la **figure 3.1**. L'intervalle de temps entre les pulses dans un doublet d'images est $100 \mu s$.

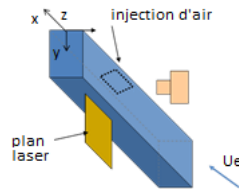


Figure 3.1 diagramme schématisé du montage PIV, x indique le sens de l'écoulement et y est dans la direction normale de la paroi supérieure

Afin de calculer correctement le champ de vitesse de particules d'un écoulement diphasique, il est nécessaire d'identifier les régions occupées par les bulles et de les discriminer avec une série de filtres **figure 3.2** Bröder et al. (2000).

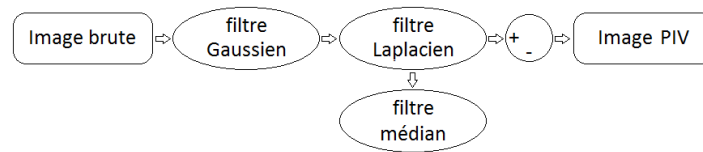


Figure 3.2 processus du prétraitement d'image pour la discrimination de bulles

IPL (Image Processing Library) est un toolbox du traitement d'image dispose par DynamicStudio qui permet d'appliquer sur les images une combinaison de filtres d'une manière séquentielle.

Dans un premier temps, un filtre « Top-hat » est appliqué sur l'ensemble des doublets d'images afin d'éliminer le bruit de fond dans chaque image. Dans le cas de notre étude, les bulles sont principalement concentrées en proche paroi et représentent sur l'image des nuages gris floutes **figure3.3a**. La réfraction de la nappe laser génère parfois les bordures lumineuses sous forme d'anneau à la frontière des bulles avec le fluide, la réflexion de particules voisines sur ces bordures (aussi appelée une particule fantôme) est parfois aussi présente et cela peut fausser les mesures PIV. Un filtre de Gauss 3×3 et de Laplace 3×3 sont donc appliqués pour augmenter le contraste des bordures afin de les éliminer.

Ensuite, un filtre médian 3×3 est appliqué pour ne conserver que la partie grise ainsi que la partie des bordures au sein des bulles dans l'image **figure3.3b**. Une fois terminée, l'image est soustraite de l'image précédente et l'on obtient les images qui ne contiennent que des particules **figure3.3c**.



Figure 3.3 évolution d'une image de bulles et de particules au cours du filtrage

Un post-traitement est mis en place dans le but d'éliminer les vecteurs aberrants **figure3.4a** ainsi que de rendre les données exploitables dans le contexte hydrodynamique.

Nous avons implémenté un critère de validation de vecteur cohérent Westerweel et al. (2005) dans un programme Matlab. Cette méthode consiste à déterminer la fluctuation de vitesse normalisée en calculant la différence entre le vecteur étudié et le médian de vecteurs voisins (matrice 3×3). Le vecteur est éliminé si cette fluctuation dépasse un seuil de validation.

Cependant, à cause de la dimension du filtre, plusieurs vecteurs aberrants résiduels sont observés à la suite du premier passage. Il est donc nécessaire de répéter l'application du filtre deux fois, avec un seuil plus restrictif lors de la première application. Il est ensuite nécessaire de substituer les vecteurs aberrants avec les nouveaux vecteurs « fictifs » afin de ne pas enlever les vecteurs cohérents. Un exemple de résultat de suppression des vecteurs aberrants est montré sur la **figure3.4**.

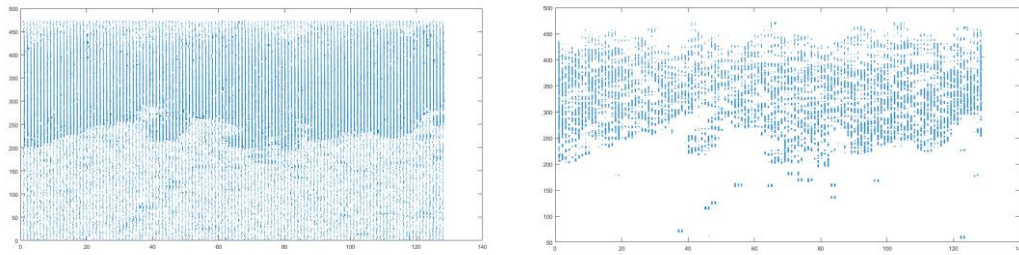


Figure 3.4(a-gauche, b-droite) champ de vitesse PIV avant (a) et après (b) l'élimination de vecteurs aberrants

A l'issue de cette étape, les vecteurs aberrants de vitesses ont disparu considérablement, néanmoins, de nombreux vecteurs cohérents sont également enlevés. L'erreur d'incertitude est donc calculée basée sur le nombre de vecteurs validés à chaque position dans le champ d'écoulement. Voir le chapitre suivant.

3.2 Traitement LDV

Une campagne de mesures LDV a été réalisée dans l'objectif d'observer quantitativement l'influence de la présence des bulles dans la sous couche visqueuse. Un diagramme du montage schématisé est illustré dans la **figure 3.5**. La source laser mono-composante à Argon ionisé est utilisée, le volume de mesure est de dimension $50 \times 50 \times 70 \mu\text{m}^3$ et est situé dans le plan de symétrie à $x = 705 \text{ mm}$. La résolution en translation verticale est $12 \mu\text{m}$ ce qui correspond à $y^+ = 1$.

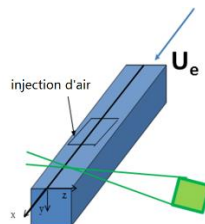


Figure 3.5 diagramme schématisé du montage LDV, le repère reste le même que pour le système PIV

4 Résultats et discussion

4.1 Modification de l'écoulement du fluide par injection des bulles dans la zone logarithmique

4.1.1 Influence du débit global d'injection

Nous avons tracé les profils normalisés en coordonnées de paroi de la vitesse longitudinale moyenne du liquide **figure 4.1a**, de la vitesse verticale moyenne du liquide **b**, de la tension de Reynolds longitudinale **c**, de la tension de Reynolds verticale **d** et du frottement turbulent **e** pour différents débits d'injection globale ($Q_G = 65 \text{ l/h} - 200 \text{ l/h}$) et une même taille moyenne de bulles à 2 m/s ($Q_G/n_{inj} = 3.61 \text{ l/h} - 3.51 \text{ l/h}$). La normalisation est effectuée en utilisant la vitesse de frottement monophasique à 2 m/s et les profils de vitesse en monophasique sont également reportés.

De manière générale, avec l'injection de bulles, nous observons un déficit de vitesse moyenne longitudinale dans la zone logarithmique **figure 4.1a**, le déficit s'accroît lorsque l'injection globale augmente. Un excès de vitesse moyenne longitudinale en proche paroi est respectivement observé **a**, cela peut être expliqué par un débit global d'écoulement constant. Un excès de vitesse moyenne verticale en proche paroi est également observé **b**, qui peut être assimilé à un phénomène d'aspiration de la couche limite dû à la force de flottabilité induite par les bulles.

En comparaison avec l'écoulement monophasique, nous observons un déficit de vitesse fluctuante longitudinale **c**, un excès de vitesse fluctuante verticale **d** et un déficit du frottement turbulent en proche paroi **e**. Ces tendances sont accentuées avec l'augmentation du débit global d'injection d'air.

De manière générale, avec l'injection de bulles, la présence des bulles décorrèle le mouvement fluctuant du liquide en proche paroi. D'autre part, la réduction du frottement turbulent en proche paroi avec les bulles peut être également la conséquence de l'effet d'aspiration induit par la présence des bulles en proche paroi.

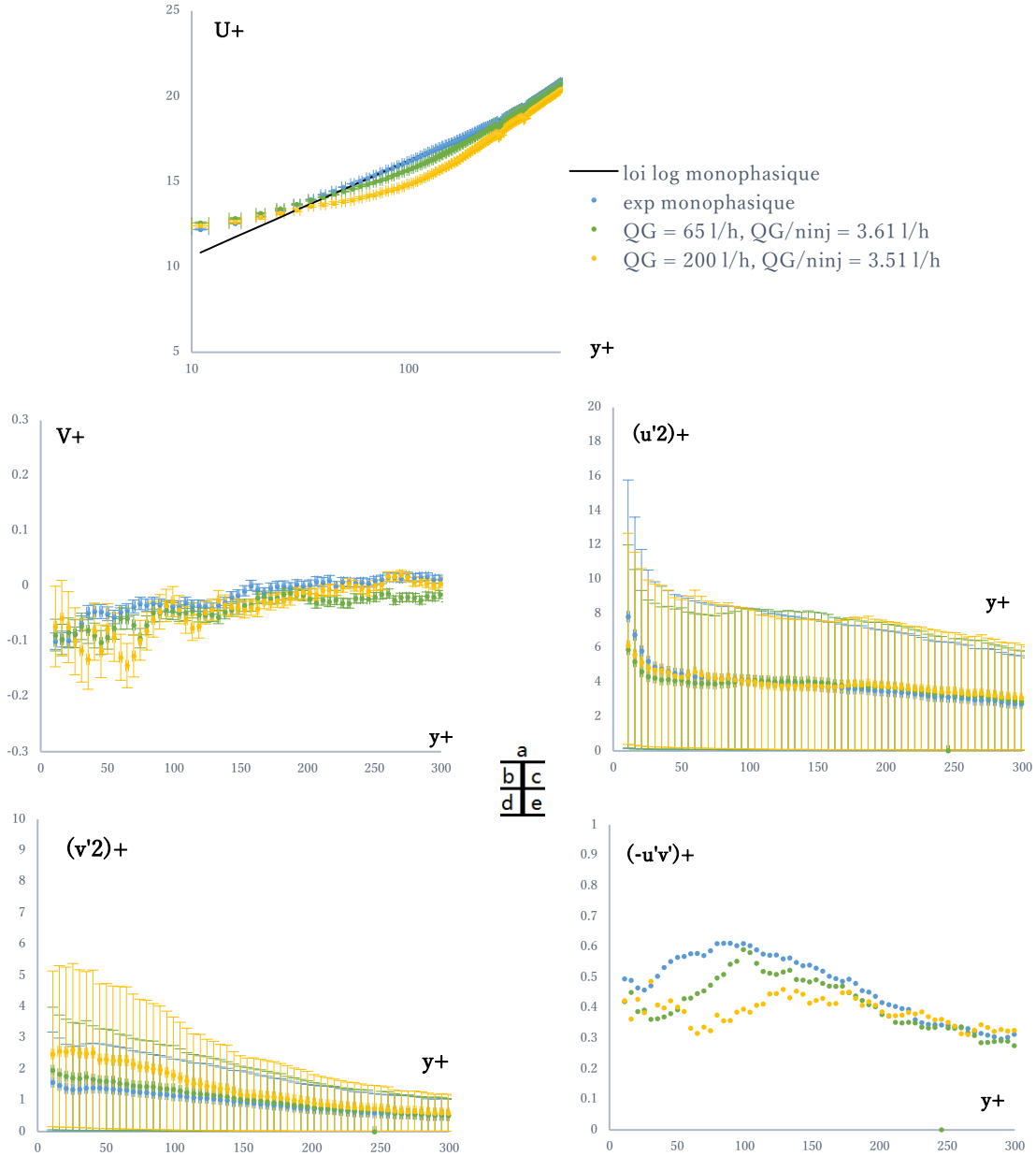


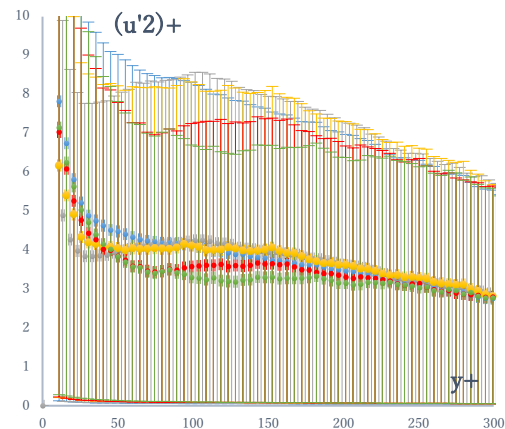
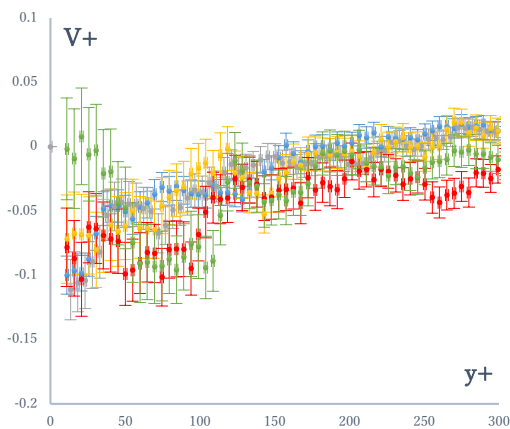
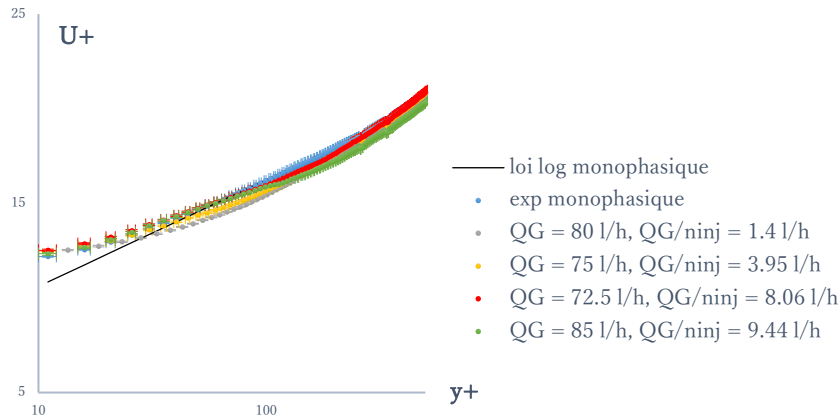
Figure 4.1 influence du débit d'injection globale sur les caractéristiques de vitesse du liquide dans la zone logarithmique à 2m/s

4.1.2 Influence des bulles de sillage

Pour analyser l'influence de la taille des bulles sur le champ de vitesse du liquide dans la zone logarithmique, nous comparons les profils de vitesse pour un même débit global ($Q_G = 72.5 \text{ l/h} - 85 \text{ l/h}$) en faisant varier le débit local ($Q_G/n_{inj} = 1.4 \text{ l/h} - 9.44 \text{ l/h}$) **figure4.2**.

Le déficit de vitesse moyenne longitudinale dans la zone logarithmique diminue avec l'augmentation de l'injection locale Q_G/n_{inj} **a**, c'est-à-dire de la taille des bulles. Par ailleurs, l'amplitude de la vitesse verticale rentrante en proche paroi diminue également **b**. Cependant, nous notons peu d'influence du débit locale Q_G/n_{inj} sur l'amplitude des tensions de Reynolds sauf à l'apparition des bulles de sillage à 2m/s (cas en vert, $Q_G/n_{inj} = 9.44$ l/h) **figure4.2c-d-e**.

A l'apparition des bulles de sillage ($Q_G/n_{inj} = 9.44$ l/h), le déficit de vitesse moyenne longitudinale se décale vers les y_+ croissants et commence à s'accroître à $y_+ = 100$ **a**. Ceci est en accord avec un épaissement de la couche limite avec les bulles de sillage. Par ailleurs, la vitesse verticale tend à s'annuler en proche paroi **b**, comme un effet de soufflage induit par les bulles de sillage. Les valeurs de vitesse verticale rentrante sont décalées vers les valeurs de y_+ croissantes avec présence d'un plateau de vitesse rentrante pour y_+ entre 50 et 100 **b**. Le déficit de la contrainte de Reynolds longitudinale augmente à l'apparition des bulles de sillage et perdure à des distances de la paroi plus grandes qu'en absence de bulles de sillage **c**. Pour la fluctuation de vitesse verticale, l'augmentation de la tension de Reynolds verticale est notable sur toute l'épaisseur de la région interne en présence des bulles de sillage **d**. Avec la génération de bulles de sillage, le frottement turbulent tend à augmenter au voisinage de la paroi, par contre nous avons un déficit de frottement turbulent qui s'étale ensuite sur toute la largeur de la région interne et d'autant plus marqué que les bulles de sillage sont nombreuses **e**.



a
b **c**
d **e**

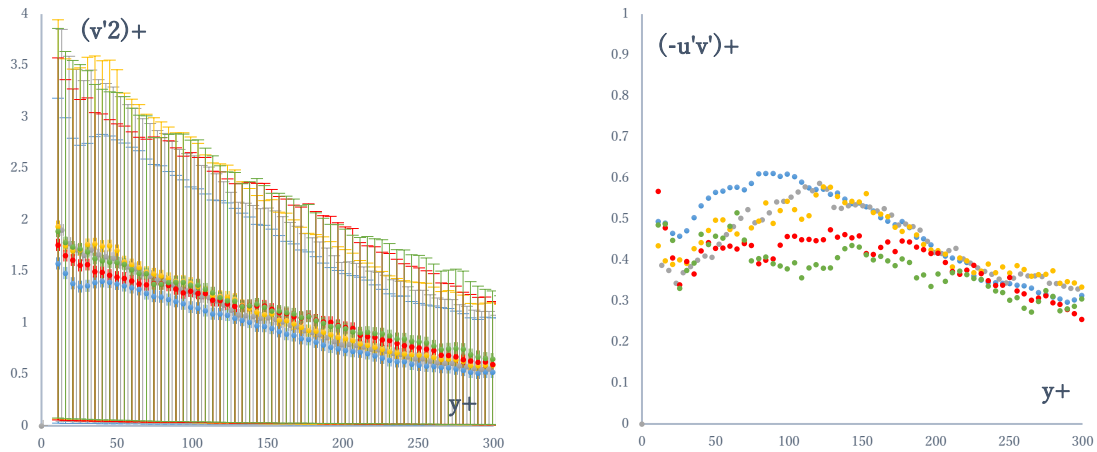


Figure 4.2 influence du débit d'injection locale sur les caractéristiques de vitesse du liquide dans la zone logarithmique à 2m/s

4.2 Influence de l'injection de bulles sur les quadrants des fluctuations de vitesse dans la couche tampon

Un exemple de quadrant des fluctuations de vitesse obtenu par PIV dans la couche tampon en monophasique et diphasique est illustré dans la **figure4.3**. Le champ est divisé en 4 parties selon le signe de la fluctuation de vitesse u' et v' : Le premier quadrant $N1$ ($u' > 0, v' > 0$) contient les événements de la haute vitesse vers l'extérieur de la couche limite, le deuxième quadrant $N2$ ($u' < 0, v' > 0$) correspond aux événements « éjection » de la basse vitesse s'éloignant de la paroi. Le troisième quadrant $N3$ ($u' < 0, v' < 0$) est associé aux événements de la basse vitesse vers l'intérieur de la couche limite et le quatrième quadrant $N4$ ($u' > 0, v' < 0$) correspond aux événements « balayage » de la haute vitesse s'approchant de la paroi. Les événements « éjection » et « balayage » contribuent aux tensions de Reynolds $-\overline{\rho u'v'}$ positives.

Avec l'injection de bulles et si nous augmentons le débit d'air global, nous observons une diminution du nombre d'éjections ($u' < 0, v' > 0$) et une augmentation du nombre d'évènements ($u' > 0, v' > 0$) à 2m/s **figure4.3**.

A 2m/s, l'injection de bulles et l'augmentation du débit d'air global induisent dans la couche tampon une diminution globale des évènements de production de turbulence ($u'v' < 0$), associé à une augmentation globale des évènements de destruction de la turbulence ($u'v' > 0$) **figure4.4**.

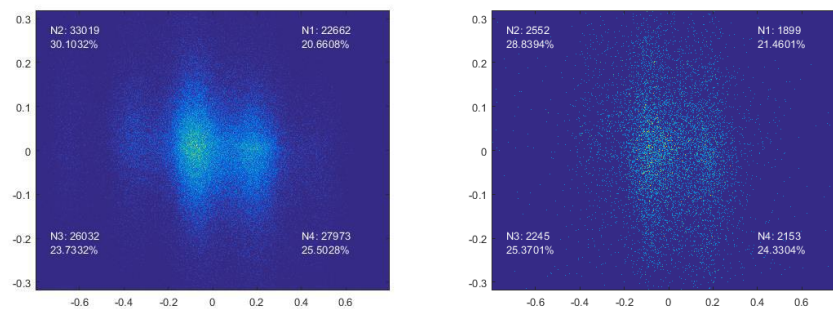


Figure 4.3 quadrants de fluctuations de vitesse mesurées par PIV dans la couche tampon à 2m/s. (a gauche) en monophasique et (b droite) en diphasique avec $Q_G = 200 \text{ l/h}$, $Q_G/n_{inj} = 9.44 \text{ l/h}$

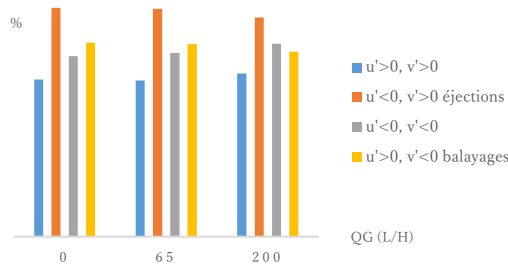


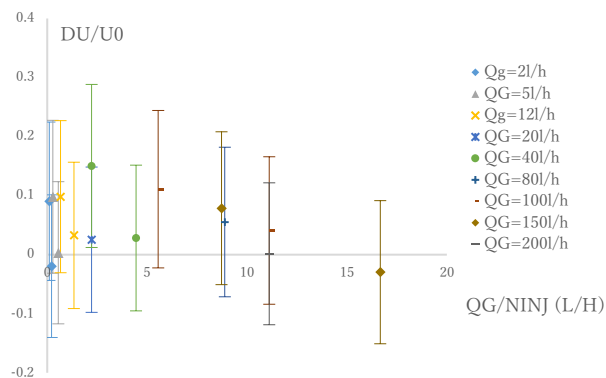
Figure 4.4 influence du débit global d'injection d'air sur la répartition des évènements ($u'v'$) dans les quadrants à 2m/s pour $\frac{Q_G}{n_{inj}} = 0.54 - 0.55 \text{ l/h}$

4.3 Modification de la vitesse longitudinale en zone sous couche visqueuse

La variation relative de la vitesse longitudinale est un autre indice important dans l'estimation de la variation du frottement visqueux en proche paroi induite par l'injection de bulles. Elle est caractérisée par la formule suivante : $\frac{\Delta U}{U_0} = \frac{U - U_0}{U_0}$, où U_0 désigne la vitesse longitudinale moyenne mesurée en monophasique.

Sur la **figure 4.5**, nous avons tracé l'évolution de $\frac{\Delta U}{U_0}$ en fonction du débit d'air rapporté au nombre d'injecteur à 2m/s. Chaque couleur représente un débit d'air global différent. Lorsque l'on trace les grandeurs en fonction du débit d'air rapporté au nombre d'injecteur (débit d'injection locale), cela revient à tracer de manière non linéaire en fonction de la taille des bulles, mais sans biaiser à l'apparition des bulles de sillage.

En absence de la génération de bulles de sillage, la vitesse longitudinale moyenne du liquide dans la sous couche visqueuse augmente due à une accélération du fluide observée dans la zone logarithmique (conservation du débit). A l'apparition des bulles de sillage, la vitesse longitudinale dans la sous couche visqueuse diminue en accord avec un effet de soufflage en proche paroi et un épaissement de la couche limite.



5 Conclusion

Cette étude fournit une base de données expérimentale conséquente de la dispersion active des bulles dans la couche limite pour des bulles déformables, avec fort effet de gravité. Les mesures qui ont été réalisées sont des mesures locales qui reposent sur différentes techniques de mesure qui ont nécessité un développement spécifique conséquent pour le traitement et l'analyse des données.

En dispersion active, nous avons procédé à l'analyse eulérienne des caractéristiques de la phase liquide dans les écoulements diphasiques par mesures PIV en plan vertical, par mesures LDV en un point.

Pour toutes les conditions expérimentales, dans la zone logarithmique, nous avons observé un déficit de vitesse longitudinale du gaz par rapport à la vitesse longitudinale du liquide attendue en écoulement monophasique.

Avec l'injection de bulles, il y a un déficit de vitesse moyenne longitudinale du liquide dans la zone logarithmique, un excès de vitesse moyenne verticale rentrante en proche paroi. La flottabilité induite par les bulles est à l'origine d'un effet d'aspiration de la couche limite en proche paroi de la zone logarithmique qui contribue à diminuer la vitesse fluctuante longitudinale du liquide, à augmenter la vitesse fluctuante verticale du liquide et à diminuer le frottement turbulent du liquide dans cette zone, par comparaison à l'écoulement monophasique.

Cela contribue aussi à décorrélérer le mouvement fluctuant du liquide dans les directions longitudinale et verticale, par transfert de quantité de mouvement entre les phases. L'analyse des quadrants des fluctuations de vitesse du liquide dans la couche tampon a mis en évidence que l'injection de bulles induit une diminution globale des événements de destruction de la turbulence ($u'v' > 0$), en accord avec l'effet d'aspiration induit par les bulles en proche paroi, phénomène d'aspiration qui tend à diminuer la production de turbulence. On note que les tendances observées avec des grosses bulles déformables qui subissent un fort effet de gravité sont différentes des observations obtenues dans le cas de la réduction de traînée par injection de microbulles (Paik et al., 2015)

De manière générale, en absence de génération de bulles de sillage, nous avons observé une augmentation du frottement visqueux dans la sous couche visqueuse. Pour une taille de bulles imposées, toutes ces tendances sont accentuées avec l'augmentation du débit global d'injection d'air.

En dispersion active, l'augmentation de la taille des bulles conduit à une diminution du déficit de vitesse moyenne longitudinale du liquide dans la zone logarithmique et une diminution de l'amplitude de la vitesse verticale rentrante observée en proche paroi, associée à une diminution de l'effet d'aspiration induit par les bulles en proche paroi.

En accord avec la diminution du déficit de vitesse moyenne longitudinale observée dans la zone logarithmique avec l'augmentation de la taille des bulles, on a une diminution de l'excès de vitesse longitudinale du liquide dans la sous couche visqueuse. Cet effet, associé à une diminution de l'aspiration en proche paroi, contribue à diminuer l'excès de frottement visqueux dans la sous couche visqueuse lorsqu'on augmente la taille des bulles.

La vitesse verticale du liquide tend à s'annuler en proche paroi, en accord avec une forte atténuation de l'effet d'aspiration induit par les grosses bulles qui glissent à la paroi. Avec l'apparition des bulles de sillage plus petites, la vitesse de glissement longitudinale entre le gaz et le liquide diminue, ce qui induit une augmentation de la vitesse longitudinale du gaz dans la zone logarithmique, une diminution du déficit de vitesse longitudinale du liquide dans la zone logarithmique et une diminution de l'excès de vitesse longitudinale du liquide dans la sous couche visqueuse, voire un déficit de vitesse longitudinale du liquide dans la sous couche visqueuse.

En conclusion, nous avons mis en évidence deux régimes différents pour l'effet de flottabilité et de déformation des bulles important sur la couche limite :

-Un régime pour lequel, on a plutôt une augmentation du frottement visqueux et une diminution du frottement turbulent en très proche paroi associée à un effet d'aspiration de la couche limite, cela induit un excès du frottement de paroi par rapport à l'écoulement monophasique. Pour ce régime d'écoulement, l'augmentation du débit global d'injection d'air contribue à l'augmentation du frottement de paroi tandis que l'augmentation de la taille des bulles tend à atténuer l'excès de frottement pariétal.

-Un second régime, à l'apparition de petites bulles dans le sillage des grosses bulles déformables, pour lequel on a plutôt une diminution du frottement visqueux et une diminution du frottement turbulent en très proche paroi associée à un effet de soufflage de la couche limite. Cela induit un déficit du frottement de paroi par rapport à l'écoulement monophasique.

Ce deuxième régime n'a jusqu'ici pas été mis en évidence dans l'état de l'art. Il constitue un régime intéressant en termes de rendement hydrodynamique car on a une réduction de frottement pariétal attendue conséquente pour un faible taux de vide global dans la couche limite.

Il est pourtant difficile d'identifier l'influence exacte de la taille de bulles sur le frottement d'une manière quantitative. [Murai et al. \(2007\)](#) ont observé que lorsque nous injectons une grosse bulle déformable à la paroi, le frottement pariétal varie le long de l'interface de la bulle. Ce phénomène s'accroît avec une augmentation de la taille de bulles. [Park et al. \(2015\)](#) ont proposé une technique avec l'injection répétitive de bulles (Repetitive Bubble Injection, RBI). Un essaim de bulles de différentes tailles est généré à chaque pulsation d'injection et une réduction supérieure du frottement pariétal comparée à l'injection continue est observée.

Références

- Bröder, D., Sommerfeld, M., A PIV/PTV system for analyzing turbulent bubbly flows, *Proceedings of the 10th International Symposium Application of Laser Techniques to Fluid Mechanics, Lisbon, Portugal.*, 2000
- Ceccio, S., Friction drag reduction of external flows with bubble and gas injection, *Annu. Rev. Fluid. Mech.*, 42, pp. 183-203, 2010.
- Foeth E. J., Decreasing frictional resistance by air lubrication, 20th International Hiswa Symposium on Yacht Design and Yacht Construction, 2008.
- Ferrante A. and Elghobashi S., On the physical mechanisms of drag reduction in a spatially developing turbulent boundary layer laden with microbubbles, *J. Fluid. Mech.*, 503, pp. 345-355, 2004.
- Jacob B., Olivieri A., Miozzi M., Campana E.F. and Piva R., Drag reduction by microbubbles in a turbulent boundary layer, *Phys. Fluid.*, 22, 115104 pp. 1-11, 2010.
- McCormick, M.E., Bhattacharyya, R., Drag reduction of a submersible hull by electrolysis. *Naval Eng. J.* 85, 11-16, 1973
- Murai Y., Fukuda H., Oishi Y., Kodama Y. and Yamamoto F., Skin friction reduction by large air bubbles in a horizontal channel flow, *Int. J. of Multiphase Flow.*, 33, pp. 147-163, 2007.
- Park H.J., Tasaka Y., Murai Y. and Oishi Y., Vortical structures swept by a bubble swarm in turbulent boundary layers, *Chem. Eng. Sc.*, 116, pp. 486-496, 2014.
- Park H.J., Tasaka Y., Oishi Y., Murai Y., Drag reduction promoted by repetitive bubble injection in turbulent channel flows, *Int. J. of Multiphase Flow.*, 75, pp. 12-25, 2015
- Westerweel J., Scarano F., Universal outlier detection for PIV data, *Exp. In Fluids.*, 39, pp. 1096-1100, 2005

Etude expérimentale de la réduction de traînée par injection de bulles dans une couche limite turbulente décollée redéveloppée

RESUME : Cette étude s'inscrit dans le contexte de la réduction de la résistance visqueuse des carènes de navire par injection de bulles sous la coque. Nous avons réalisé des expériences d'injection de bulles dans la zone de redéveloppement d'une couche limite turbulente décollée. Les expériences ont été menées dans le tunnel hydrodynamique de l'École Navale. Des bulles d'air ont été injectées en aval de la zone de recirculation d'un obstacle bidimensionnel carré monté à la paroi supérieure du tunnel. Le champ de vitesse a été caractérisé par Particle Image Velocimetry (*PIV*) dans le plan vertical de l'amont de l'obstacle et jusque dans la zone de redéveloppement. L'écoulement diphasique à bulles a été étudié pour une position longitudinale située dans la zone de redéveloppement de la couche limite. Les caractéristiques de la phase gazeuse ont été obtenues par visualisations ombroscopiques. La réduction de frottement est observée au maximum de 35% à 6 m/s. Physiquement la présence des bulles entraîne une décorrélation des fluctuations de vitesse longitudinales et normales dans la zone interne et des fluctuations du mouvement des bulles dans la direction normale à la paroi qui peuvent être associées à la modification observée du frottement.

Mots clés : turbulence, obstacle, couche limite recollée, écoulement diphasique, traînée

Experimental Study of the Bubbly Drag Reduction in the Recovery Region of a Separated Turbulent Boundary Layer

ABSTRACT : The bubbly drag reduction in turbulent flow is of significant interest in the naval industry, particularly to reduce the viscous resistance of ships hulls. This thesis is focused on experimental observations of the recovery region of a separated turbulent boundary layer in both single-phase and bubbly flows. The experiments were performed in the Cavitation Water Tunnel of the French Navy Academy Research Institute. Air bubbles of intermediate size (0.4-1.3mm) were injected in the recovery region downstream of the recirculating region of a 2D square obstacle (of height $h = 16$ mm) mounted at the upper wall of the tunnel. The single-phase flow velocity field was characterized in the vertical plane using Particle Image Velocimetry (*PIV*) technique in 11 stream-wise measuring stations from upstream of the obstacle down to the recovery region. The gas-phase velocity field in the vertical plane, the gas volume fraction distribution and the bubble size were characterized by means of Shadowgraphy. A maximum local viscous drag reduction DR of 35% is achieved for 6 m/s. The bubbly drag reduction is promoted by the increase of the velocity and enhanced by increasing the air injection rate. We suggest that bubbles can induce a decorrelation between the stream-wise and wall normal fluctuating velocity in the inner layer, but most of the bubbly drag reduction is attributed to the wall normal fluctuating motion of the bubbles.

Keywords : turbulence, obstacle, reattached boundary layer, bubbly flow, drag

